DELAMINATION GROWTH IN GRAPHITE/EPOXY COMPOSITE LAMINATES UNDER TENSILE LOADING

by

Narendra Venugopal Bhat
B.Tech., Indian Institute of Technology, Bombay, India (1987)
S.M., Massachusetts Institute of Technology, Cambridge (1990)

Submitted to the Department of Aeronautics and Astronautics
in partial fulfillment of the requirements for the degree of

Doctor of Philosophy
in Aeronautics and Astronautics
at the
Massachusetts Institute of Technology
September 1993

Signature of Author ______________________________
Department of Aeronautics and Astronautics
September 27, 1993

Certified by ______________________________
Professor Paul A. Lagace
Thesis Supervisor

Certified by ______________________________
Professor Frederick J. McGarry
Thesis Committee

Certified by ______________________________
Professor Hugh L. McManus
Thesis Committee

Accepted by ______________________________
Professor Harold Y. Wachman
Chairman, Departmental Graduate Committee

DELAMINATION GROWTH IN GRAPHITE/EPOXY LAMINATES UNDER TENSILE LOADING

by

Narendra V. Bhat

Submitted to the Department of Aeronautics and Astronautics on September 27, 1993 in partial fulfillment of the requirements for the Degree of Doctor of Philosophy in Aeronautics and Astronautics.

ABSTRACT

The growth of triangular-shaped delaminations bordered by matrix cracks, defined herein as "compound delaminations", occurring at the free edges of $[\pm15_n]_s$ and $[\pm15_n/0_n]_s$ laminates in static tensile loading was investigated. This triangular compound delamination is the first macroscopic damage observed. Failure of the laminates occurs by unstable growth of these delaminations. The experimental study involved the manufacture of specimens with teflon implants to create an initial delamination configuration with the delamination oriented at 90° to the matrix crack. The delamination front was monitored using strain gages and X-ray radiographs. Growth was observed to occur at the delamination front near the free edge region with no growth at the matrix crack front resulting in the same configuration as observed in originally unflawed specimens. A three-dimensional displacement-based finite element model of the delaminated region was created and the equivalent domain integral was used to determine the energy release rate at the delamination and matrix crack fronts. The energy release rate was predicted to be highest at the intersection of the delamination and the free edge and was lowest at the intersection of the delamination and the matrix crack. The peak energy release rate predicted at the matrix crack front was smaller than that at the delamination front. Growth was simulated in the model by tilting the delamination front about the matrix crack front. The maximum energy release rate along the delamination dropped and became more uniform as the delamination was tilted. These results indicate that the stable delamination configuration observed is formed by the growth of the delamination front at the free edge region in regions of high energy release rate in preference to the growth of the matrix crack resulting in a curved delamination contour. The overall decrease in energy release rate associated with this delamination growth indicates that the resulting curved delamination is a more stable configuration. The failure process in these specimens involves the formation of these stable delaminations, followed by secondary cracking in the plies adjacent to the delamination, and lastly final failure via unstable growth of the entire triangular region to the ends of the specimen.

Thesis Supervisor: Professor Paul A. Lagace
Title: Associate Professor of Aeronautics and Astronautics

ACKNOWLEDGMENTS

As I write this, I realize that the moment has finally arrived to take a glance back at my years at M.I.T and reminisce. During my stay here, I have been educated not only by my Professors but also by my friends and colleagues. I hope to remember all of you in this acknowledgment.

Firstly, my advisor, Paul, to whom I am indebted for several things: encouragement, guidance, friendship, concern, hospitality and for supporting me financially even under the most trying circumstances. I wish him and Robin continued success and happiness in their life. I thank Professors Dugundji and McManus, for having an open door at all times, and I like to think that I have taken advantage of their friendly nature to learn about teaching and research from their knowledge and experience. Thanks to Ping Lee and Debbie for their friendship and being our first line of defense! In the depths of building 37, where I spent most of my time, I have always been thankful for Al's resourceful and friendly presence.

I will through my life, fondly remember the friends with whom I have shared many happy moments during my stay here: Ken Bonello (Bozo!), James Williamson (Bozo's pal!), Claudia Ranniger (the real doc!), Teresa Guy (never over the hill!), Yew Poh Mak (cool 'z hell!), Hiroto Matsuhashi (The Keg!), Mary Mahlar (Hrvd. Sq. party animal!!), Stacy Priest (The Tubeinator!), Steve Thomas (L.A. terror!), Lauren Kucner (go Orioles! Ob: Go Sox!), Rich Kroes (My other place is in Aruba!), Tracy Vogler (Mr. Legs!), Hary Budiman (Dr. Walkman!), Cecelia Parks (Oh! you're such a dork!), Brian Wardle (Steady-B!), Jeff Farmer (Pyro's anonymous), Laura Kozel (Arnie-wannabe), Aaron Bent (Dr.Piezo), Robin Olsson, Taehyoun Kim and

Wai Tuck Chow. And specially to Wilson Tsang (Dr. Ballroom!) and Randy Notestine (Mr.Spelling Bee) for our six years of friendship (and many more years to come) during which they halved my scrrows and doubled my joys. I am confident of their future success. I would like to remember: John Brewer, Doug Cairns, Kevin Saeger, Peter Dunn and special thanks to Pierre Minguet who has been a constant source of advice. Also, my good friends Vishak and Sasi with whom I have have had some great times !

Thanx to the cool 16.62X team of Lisa Cohen and Catherine Downard for providing me with most of my data! And the excellent UROP's without whose help I would never have finished this thesis: Janeen Ault, John Mueller, Andy Melville and Larry Schwartz.

I can never find adequate words to express my gratitude to amma, yogi, and mamama for their love, encouragement and support. My father who had been a constant source of encouragement in his living years, continues to do so in my memory. I have tried to live by the principles that he has taught me and hope to live up to his hopes and aspirations. This is but one small step in that direction... I hope to take many more in the future.

FOREWORD

This work was performed in the Technology Laboratory for Advanced Composites (TELAC) of the Department of Aeronautics and Astronautics at the Massachusetts Institute of Technology. This work was partially sponsored by the Boeing company under Boeing P.O. HN7124.

TABLE OF CONTENTS

TABLE OF CONTENTS

CHAPTER

PAGE

TABLE OF CONTENTS

LIST OF FIGURES

Figure **Page**

LIST OF TABLES

NOMENCLATURE

a	Intrusion of delamination into a specimen
A	Intermediate matrix involving material properties of bimaterials used in the evaluation of the oscillatory singularity
C_{ijkl}	Material stiffness tensor
C_1	Constant used to represent the linear growth criterion based on individual components of energy release rates
C_2	Constant used to represent the quadratic growth criterion based on individual components of energy release rates
E^*	Stiffness of laminate with some interfaces completely delaminated
E_{LAM}	Stiffness of an intact laminated material
E_{LD}	Stiffness of any individual sublaminate formed by delamination of a laminate
f	Integrated value of the shape function, S, at the crack front
G	Total strain energy release rate
G_c	Critical value of total strain energy release rate
G_1	"Mode I" strain energy release rate for materials with oscillatory singularity
G_2	"Mode II" strain energy release rate for materials with oscillatory singularity
G_3	"Mode III" strain energy release rate for materials with oscillatory singularity
G_I	Mode I strain energy release rate for materials without oscillatory singularity
G_{Ic}	Critical value of strain energy release rate in Mode I
G_{II}	Mode II strain energy release rate for materials without oscillatory singularity

NOMENCLATURE

G_{IIc}	Critical value of strain energy release rate in Mode II
G_{III}	Mode III strain energy release rate for materials without oscillatory singularity
G_{IIIc}	Critical value of strain energy release rate in Mode III
H	Intermediate matrix involving material properties of bimaterials used in the evaluation of the oscillatory singularity
$\overline{H}$	Conjugate of H
J	Parameter evaluated by the J-Integral
K	Complex stress intensity factor consisiting of the mode I stress intensity factor as the real part and the mode II stress intensity factor as the imaginary part.
$\overline{K}$	Conjugate of K
K_1	"Mode I" stress intensity factor for materials with oscillatory singularity
K_2	"Mode II" stress intensity factor for materials with oscillatory singularity
K_3	"Mode III" stress intensity factor for materials with oscillatory singularity
K_I	Mode I stress intensity factor for materials without oscillatory singularity
K_{II}	Mode II stress intensity factor for materials without oscillatory singularity
K_{III}	Mode III stress intensity factor for materials without oscillatory singularity
L	Intermediate matrix involving material properties of bimaterials used in the evaluation of the oscillatory singularity
L_d	Length of delamination front
m	number of delaminations adjacent to a matrix crack

NOMENCLATURE

$N(\xi,\eta,\rho)$	Isoparametric shape function used in finite element analysis
r,s,t	local axis system located at intersection of delamination and matrix crack fronts
S	Shape function used in the Equivalent Domain Integral
t_{Lam}	Thickness of undelaminated portion of the laminate
t_{LD}	Thickness of any individual sublaminate formed by delamination of a laminate
U	Strain energy per unit volume
u_j	Component of the displacement vector
u^I	Displacement vector used in the decomposition method to give mode I energy release rate
u^{II}	Displacement vector used in the decomposition method to give mode II energy release rate
u^{III}	Displacement vector used in the decomposition method to give mode III energy release rate
W	Work Density per unit volume
x_1,x_2,x_3	Coordinate axes
x'_1,x'_2,x'_3	Local coordinate system at delamination front
δ	Magnitude of the oscillatory singularity
ε_{ij}	Component of the strain tensor
ε^I	Strain vector used in the decomposition method to give mode I energy release rate
ε^{II}	Strain vector used in the decomposition method to give mode II energy release rate
ε^{III}	Strain vector used in the decomposition method to give mode III energy release rate

NOMENCLATURE

ξ,η,ρ	Coordinate system used in the definition of shape functions of isoparametric elements
σ_{ij}	Component of the stress tensor
σ^{I}	Stress vector used in the decomposition method to give mode I energy release rate
σ^{II}	Stress vector used in the decomposition method to give mode II energy release rate
σ^{III}	Stress vector used in the decomposition method to give mode III energy release rate
μ_j	Characteristic eigenvalues of any material

CHAPTER 1

INTRODUCTION

Graphite/epoxy composites have been widely employed in both the military and commercial aerospace industries. Many of the wide-bodied commercial jets such as the L-1011 and Airbus A-320, have secondary structures made from composite materials. The use of composites in primary structures is also gaining acceptance and the Boeing-777, currently under development, will involve a significant amount of composites in its primary structures, notably the empennage. Some smaller aircrafts, notably the Beechcraft Starship already have a certified all-composite design. Among the newly designed military aircrafts, the F-117 and B-2 Stealth Bomber are most noteworthy for their extensive use of composites. Some of the space applications of composites are in launch vehicles, such as the solid rocket booster nozzles on the space shuttle. Composites are also being used in the design of the space station 'Freedom'. Other industries such as automotive and sporting goods are increasingly using composites.

The use of graphite/epoxy composites in place of conventional metals in the design of structures, requires a rethinking of the design process since the tailoring of the material properties occurs with the design of the structure according to the strength and stiffness requirements of the structure. In many designs utilizing composites the material has been used more like "black aluminum" (or steel) with the conventional design procedures used for metals. Some examples of this can be seen in the tendency towards the use of quasi-isotropic layups to simulate the isotropy of metals, or in the restriction of ply orientations to 0°, 90° and 45°. Such conservative design results in the inefficient use of composites and, given the rather high cost of the material could portray composites as uneconomical and hinder their use in a wide spectrum of applications.

One of the primary reasons for such caution in the design procedure is a lack of thorough understanding of the failure mechanisms of composites. Unlike metals, where there are a few well-defined modes of failure, composites exhibit a wide variety of failure mechanisms such as delamination, matrix cracking, fiber failure, fiber buckling, fiber pullout, sublaminate failure, and sublaminate buckling. These failures could occur individually or in concert with each other, making their analysis a complicated issue. The behavior of each individual mechanism has been examined by several researchers over the years with some success in terms of either prediction, suppression, or circumvention of that failure mode. The area of multiple or compound damage, which is a typical mode of failure seen in many laminates still, is an area of considerable research interest.

Delamination is a mode of failure which is unique to composite structures due to their laminated nature. This failure mode involves the separation of the individual layers which constitute the structure. This failure mode occurs in a thin layer (on the order of a fiber diameter in graphite/epoxy [7]) of matrix material which exists between plies, referred to as the interply matrix layer. This mode of failure initiates due to the presence of out-of-plane stresses that act to separate plies of the laminate [8]. These stresses are referred to as 'interlaminar stresses'. Delamination results in the loss of structural integrity and stiffness, and can reduce the failure stress of composite laminates well below that predicted by in-plane failure criteria [9, 10]. The stage at which delamination occurs within a laminate is dependent on the material properties, geometric characteristics and specifics of loading. Some typical locations where interlaminar stresses occur are free edges, ply dropoffs and fastener locations and these therefore constitute potential sites of delaminations. Delamination is often an intermediate stage in the failure process occurring between matrix cracking and fiber failure leading to overall failure of the laminate.

Delamination is not limited to laboratory type specimens, but manifests itself in typical composite structures as well. Experience in the NASA ACEE program with the composite vertical fin for the L-1011 aircraft indicated that the failure of that part was prompted by delamination[11]. Wilkins [12] says this about the experience of aircraft manufacturers with delamination: "....when test conditions were extended to explore failure mechanisms, delamination is observed to be the most prevalent life limiting growth mode". Therefore, the use of laminated composite media in structures presents the designer with the challenge of understanding this failure mode and effectively designing for it. This requires an understanding of the failure/damage modes, their interactions and their growth.

Some of the typical stages observed in the course of tensile testing of a specimen are shown in Figure 1.1 [1]. The initial failure is usually either the occurrence of delamination in between certain plies (or matrix cracking in some laminates with 90° plies). The final failure of the laminate is usually in-plane failure of some plies. In laminates where delamination initiates at the free edge, the process subsequently results in the development of additional modes, such as matrix cracking in adjoining plies as shown in Figure 1.1. Hence, delamination in association with matrix cracks in adjoining plies is a naturally occurring state in many laminates in static tensile testing and fatigue.

The aim of this thesis is therefore, to provide an understanding of the interaction of delamination with matrix cracking in the overall growth of this

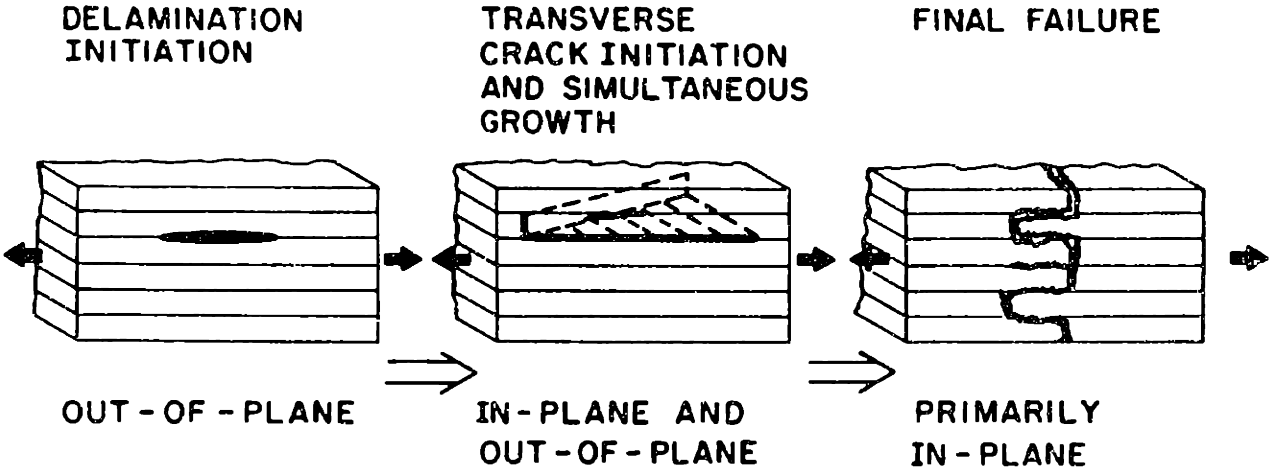

Figure 1.1 Some typical stages observed in the failure process of a composite laminate (*left*) delamination initiation by out-of-plane stresses (*center*) development of additional in-plane and out-of-plane damage (*right*) primarily in-plane failure [1].

damage configuration. The various approaches adopted in the study of fracture in composites and the research done to date on delamination problems and its interaction with matrix cracking are examined in Chapter 2. The previous experimental evidence prompting the current study and the experimental and analytical aspects of the current study are examined in Chapter 3. In Chapter 4, the details of the analytical models and the techniques adopted to obtain the necessary fracture parameters are provided. The manufacture and testing procedure employed for the experimental work are described in Chapter 5. The results of the experiment and the analysis are given in Chapter 6. The mechanisms responsible for the failure process are proposed in Chapter 7. Finally in Chapter 8, the conclusions from the study and recommendations for future research possibilities are discussed.

CHAPTER 2

REVIEW OF PREVIOUS WORK

In the study of failure of composite materials to date, two basic approaches have been adopted. They are the strength of materials approach and the fracture mechanics approach. Several methods have been proposed within these two approaches to study delamination and other damage modes. It has been experimentally observed that delamination and matrix cracking are competing damage modes in terms of their sequence of occurrence. The existence or sequence of occurrence of these are dependent on both the laminate type and on the overall ply thickness. The prediction of initiation as well as growth of intralaminar (matrix) and interlaminar cracks (delamination), or their combination, has been attempted using the above mentioned approaches with varying degrees of success. The limitations of these methods along with the types of problems solved are briefly discussed herein.

2.1 Strength of Materials Approach

There have been several studies applying the strength of materials approach to study the initiation of delamination in a wide variety of composite materials. Interlaminar stresses have been evaluated both by numerical and analytical techniques. The numerical evaluations are mostly based on the finite difference method [8] or the finite element method [13-15] or perturbation methods [16]. Analytical evaluations are based on the force balance method [17] and elasticity solutions [18, 19]. These stresses may then be used in point or average stress criteria to predict delamination initiation.

Various forms of an average stress criterion [20, 21] have been used to predict delamination initiation. For example, the Quadratic Delamination Criterion [20] has been successfully used to predict initiation in a wide variety of graphite/epoxy laminates, when applied in association with interlaminar stresses calculated using the force balance method [17]. The averaging dimension and interlaminar strengths used are found to be material dependent only. There have been however, limited applications of these criteria. Vizzini and Lagace [22] used this approach to predict growth of delamination due to sublaminate buckling under compressive loading. The interlaminar normal stresses ahead of the crack tip were averaged over a small distance and compared with the interlaminar normal strength. The analytical results showed a trend similar to that obtained from experimental data. However, further work needs to be done to examine its applicability to delamination growth problems when the interlaminar shear stresses are also significant.

The strain energy density method [23] is a point energy criterion and has been proposed to predict both initiation as well as growth of delamination and matrix cracks. This approach depends on the strain energy density within a body and assumes that the crack will grow when the critical value of strain energy density is reached at a specific distance ahead of the crack. Both the critical parameters are expected to be material dependent only, but no experimental evidence has been obtained to that effect. This criterion has been successfully applied to predict the unstable growth of matrix cracks in off-axis unidirectional plies. Its use in the prediction of initiation and growth of matrix cracks and delaminations in angle ply laminates has been proposed, but no comparisons have been made with the experimental data to ascertain its applicability.

2.2 Fracture Mechanics Techniques

Fracture mechanics techniques have been widely used to predict the initiation of delamination in composites. The conventional techniques used for crack growth in isotropic materials have been extended to composite materials. This method is based on the Griffith-Irwin crack growth criterion [24, 25] where it is assumed that crack growth occurs when the energy released due to crack growth reaches a critical value. The energy release rate, usually denoted by G, is defined for a virtual crack extension as,

$$G = \frac{\partial(W - U)}{\partial a} \tag{2.1}$$

where a is the crack length, W is the work done by external forces and U is the strain energy in the body.

The growth of a crack occurs when the energy release rate, G, reaches a critical value. This critical value is the rate at which energy is expended in creating new surface as the crack progresses through the material, and is often referred to as the ' fracture toughness' of the material and is denoted by G_c. The basis of fracture mechanics lies in the experimental determination of a realistic single-parameter characterization of the material's resistance to fracture. The criterion for crack growth can be broadly stated as,

$$G = G_c \tag{2.2}$$

These concepts, which have been successfully used in metals, have been applied to predict initiation as well as growth of delamination and matrix cracks in composite laminates. The fracture mechanics approach assumes the existence of flaws within the material, hence the term 'initiation' only implies the growth of these inherent flaws to some predefined size. This size may be defined such that it is detected by some physical means, such as a drop in load carried by the specimen. In the case of delamination problems, G_c is known as the 'interlaminar fracture toughness'. In order for G_c to be a useful parameter, it should be dependent only on the material and not on the laminate lay-up.

In order to describe how the growth of delamination cracks occurs, consider a laminate with a delamination growing from the free edge and extending along the width of the laminate under uniaxial far-field loading as shown in Figure 2.1. Some hypothetical strain energy release rate curves for this problem are shown in Figure 2.2 for different stress levels applied to the laminate. The nature of the curves shown are similar to that obtained by finite element analyses [26]. The crack length a_0 refers to the inherent flaw size within the manufactured material. The various curves represent the hypothetical strain energy release rate that would be obtained from the crack as it progresses through the material when the body is subjected to various levels of far-field stress. The line marked as G_c is the critical value of strain energy for the material and it is assumed to be a known function of the crack length (techniques of obtaining this will be discussed later in this review). At a stress level σ_i, the strain energy release rate available for crack progression is equal to or greater than G_c at all points up to a crack length of a_i and hence the initial flaw can grow up to this size. This process is known as delamination initiation.

The remaining discussion addresses the growth of delamination thus obtained. At the initiation stress σ_i, the G curve dips below the G_c level and any further increase in crack size can only be achieved by incrementing the load level to $\sigma_1$when the crack grows to a size a_1 and is arrested until further increase in load. This represents a post-initiation stable growth phase. This process continues until a crack size of a_u and a load of σ_u where the G curve monotonically increases and is always greater than G_c. This represents the unstable growth phase of the delamination. Alternatively, a crack may also

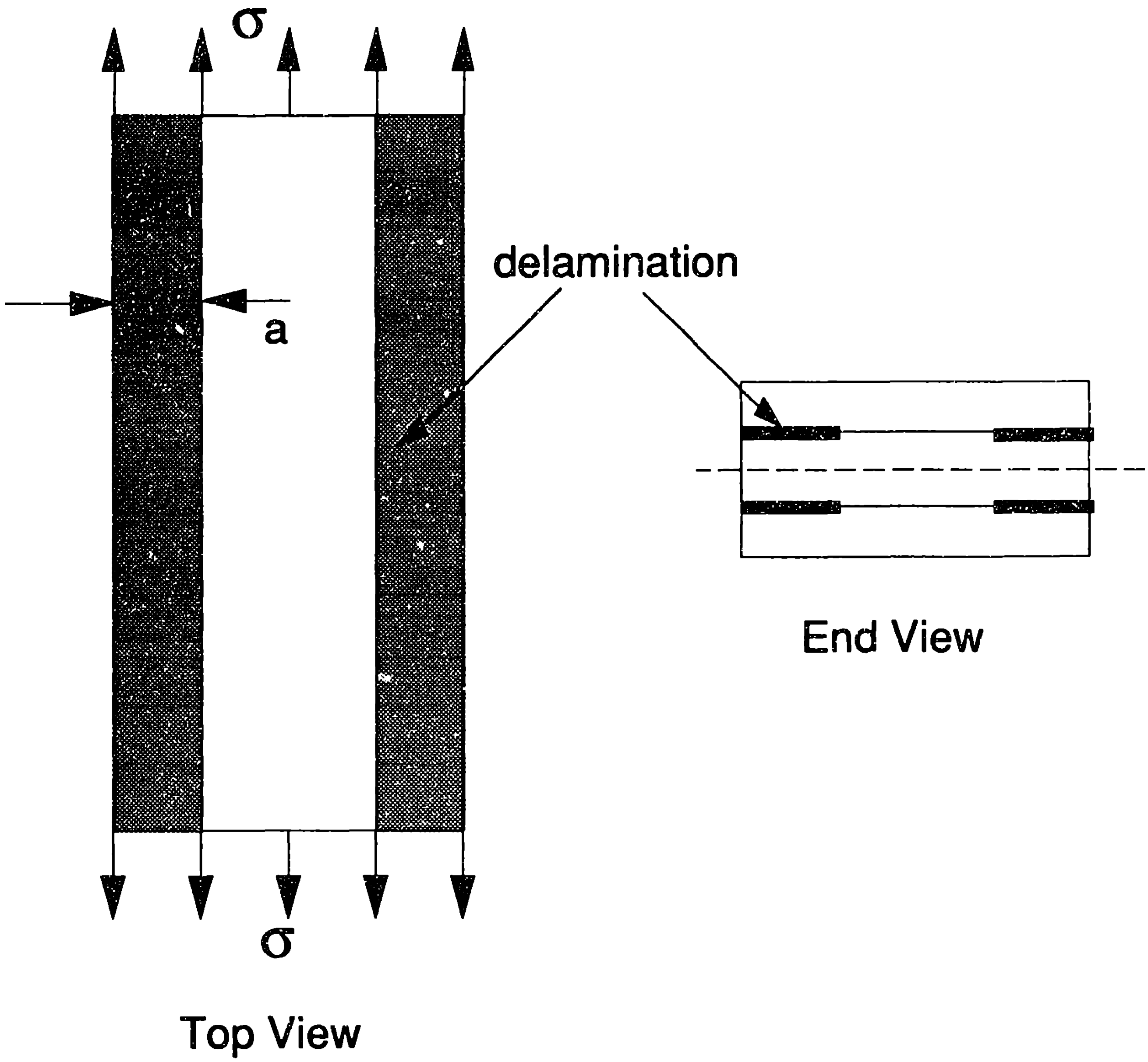

Figure 2.1 Top and end view illustration of a laminate subjected to uniaxial tensile loading and with a free edge delamination of uniform width extending the length of the laminate.

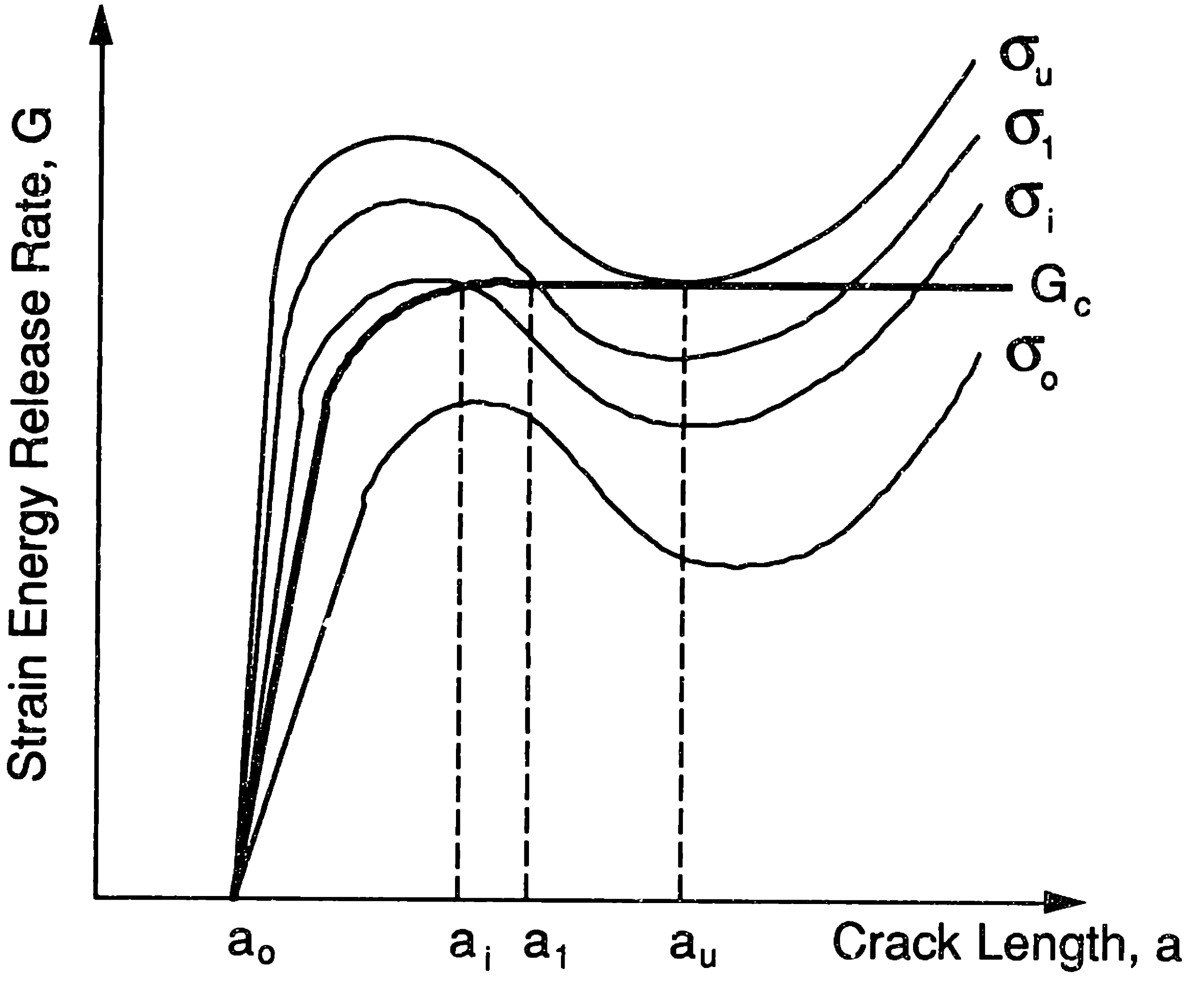

Figure 2.2 Illustration of strain energy release rate and fracture toughness curves for various levels of loading for a uniform width free edge delamination problem.

show no stable growth phase, and this would be represented either by a steadily increasing strain energy release curve or a constant G curve for a given stress level.

The growth of a delamination as described above involves the total strain energy release rate. In classical fracture mechanics, the total strain energy release rate is divided into three components: mode I loading, which accounts for the opening mode of the crack due to the normal stresses on the crack; mode II loading which accounts for the in-plane shearing of the crack; and mode III loading which occurs due to the shear stresses which are out of the plane of the crack (anti-plane shear) and result in the tearing action on the crack face. The deformation of a specimen subjected to such modes is shown in Figure 2.3. The strain energy components of these is henceforth indicated by G_I, G_{II} and G_{III} respectively, and the total strain energy released is denoted by G, where

$$G = G_I + G_{II} + G_{III} \tag{2.3}$$

It has been found in many materials that the 'fracture toughness' may not be adequately described by the total value G_c alone, as distributing the modes in different proportions may lead to different values for the critical strain energy release rate. Various other criteria have been proposed using combinations of G_I, G_{II} and G_{III} to predict mixed mode behavior, rather than the use of total G.

These basic concepts of fracture mechanics have been applied to delamination and matrix cracking problems in composites with the aim to predict the failure load and the mechanisms responsible for the failure process. In the next section, some of the models developed for this purpose, and their limitations, are examined. Comparisons of predictions for growth or failure are made with any experimental results that are available.

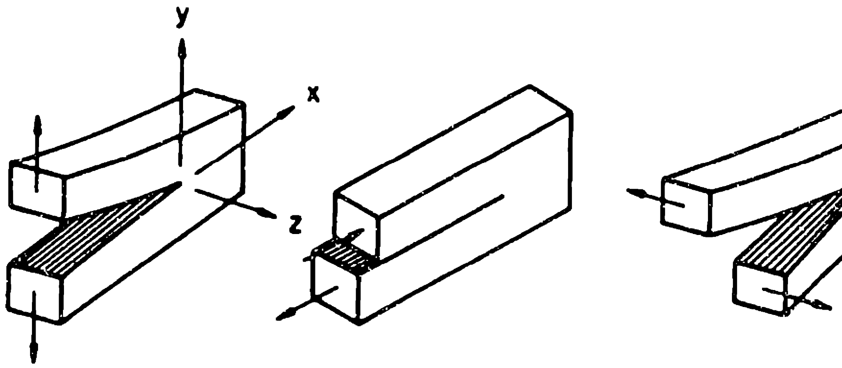

Figure 2.3 Modes of crack surface displacements (*left*) Mode I: symmetric loading, (*center*) Mode II: skew symmetric shear loading and (*right*) Mode III: antiplane shear loading (adapted from [2]).

2.2.1 Previous Study of Delamination Problems

Delamination in composites can be classified into simple or compound delamination problems depending on the physical characteristics of the damage. The classification of delaminations into 'simple' and 'compound' types has not previously been used in the literature, Thus these terms are further defined in this section along with some examples of their occurrence. As a consequence of either delamination state, the laminate may fail in an in-plane manner in locations where the strength of the plies are exceeded either due to the breakdown of combined action or due to stress concentrations caused by the damage and resultant stress redistribution. In either event, the failure occurs earlier than that predicted by a maximum stress or strain criterion for an intact laminate accounting for only in-plane mechanisms.

A simple delamination state refers to the presence of a delamination without matrix cracking in any adjacent plies of the laminate. Some of the models that are examined here address only simple delamination problems. The growth of circular/elliptical delaminations or through-width delaminations under compressive loading has been studied in a few laminates. In the uniaxial tensile loading of composite laminates, the case of the approximately uniform-width, free edge delamination shown in Figure 2.1 has been shown to occur in a few laminates such as $[\pm25/\bar{90}]_s$ graphite/epoxy [27] and $[\pm30/\pm30/90/\bar{90}]_s$ boron/epoxy laminates [28].

A compound delamination involves a delamination coupled with the presence of matrix cracks in adjacent plies of the laminate. Many off-axis composite laminates under tensile loading exhibit compound delamination states at or before failure. In the case of uniaxial tensile loading of graphite/epoxy laminates, two naturally occurring compound delaminations have been observed. The first can be approximated as a uniform delamination extending from the free edge into the laminate guided by matrix cracking in adjacent plies [26, 27] as shown in Figure 2.4(a). In the study of such cases, some researchers have modelled the matrix cracking indirectly by just reducing the modulus of the cracked ply. The resulting problem is then effectively identical to the simple delamination mentioned earlier. The second type of compound delamination observed is a triangular-shaped delamination as shown in Figure 2.4(b) bordered by matrix cracking in adjacent plies [1, 5, 6, 29].

The specific cases of simple and compound delaminations which have been experimentally observed, as well as the analysis adopted for the prediction of their initiation and growth, are briefly discussed here.

Simple delaminations such as through-width delamination [30-32] or approximately circular [33] delaminations occur in composites either under impact loading or due to manufacturing defects. When subjected to compressive loading, the plies on either side of this delamination have been observed to buckle and the delaminations grow as a result of the high crack tip stresses at the delamination front. It has been shown that the mode I strain energy release rate dominates the instability-related delamination growth [32, 33]. The critical value of strain energy in mode I, G_{Ic} has been successfully used to predict the load at which unstable growth of such delaminations begins [32, 33]. Considerable work has been done on this area of growth of delamination due to sublaminate buckling under compressive loads. However, since the area of interest in this thesis is the growth of delamination under tensile loading, this work has not been explored in further detail.

A numerical technique commonly used in analyzing the uniform-width free edge delamination is the quasi-three-dimensional finite element method which implies that there is no change in strain or stress in one direction, hence the problem is not a full three-dimensional problem. This method has been described in further detail in section 2.2.3. Rybicki et al [28] were the first to apply fracture mechanics and experimentally validate this usage to delamination problems in fiber-reinforced composites. A numerical version of the virtual crack closure method was applied in order to evaluate the strain energy release rate of a uniform-width delamination in $[\pm 30/\pm 30/90/\overline{90}]_s$ boron/epoxy laminates. There was no matrix cracking observed and hence this was a simple delamination problem analyzed by a quasi-three-dimensional method. The analytical results predicted stable delamination growth, as was observed experimentally. A constant value of G_c observed during propagation of delamination indicated the possibility of the existence of a critical strain energy rate material parameter. These results led to further investigation of fracture mechanics techniques to predict initiation and growth of delamination in composites.

The same technique has been adopted to predict initiation and growth of compound delaminations of the type shown in Figure 2.4(a) which occur in laminates containing 90° plies subject to uniaxial tension. The matrix cracking occurring in the 90° plies in the early stages of the loading leads to delamination growth in an approximately uniform fashion through the width. Wang et al [26, 27, 34] developed this model to predict delamination and matrix crack initiation and growth in $[\pm 25/90_n]_s$ T300/934 laminates (n=1/2,1,2,3,4,6,8) and the results were compared to the experimental results shown in Figure 2.5 [3, 4]. It is seen from Figure 2.5 that a wide variety of behavior from simple to compound delamination can be obtained by changing ply thickness, n. An important feature of the data is the case of n equal to three, where a sudden drop in the failure and delamination initiation stresses occur and the delamination switches location from the midplane to the 25/90 interface for all subsequent values of n. Using only a single value of G_c for both delamination and matrix crack initiation, the delamination initiation in the laminates where no matrix cracking occurred

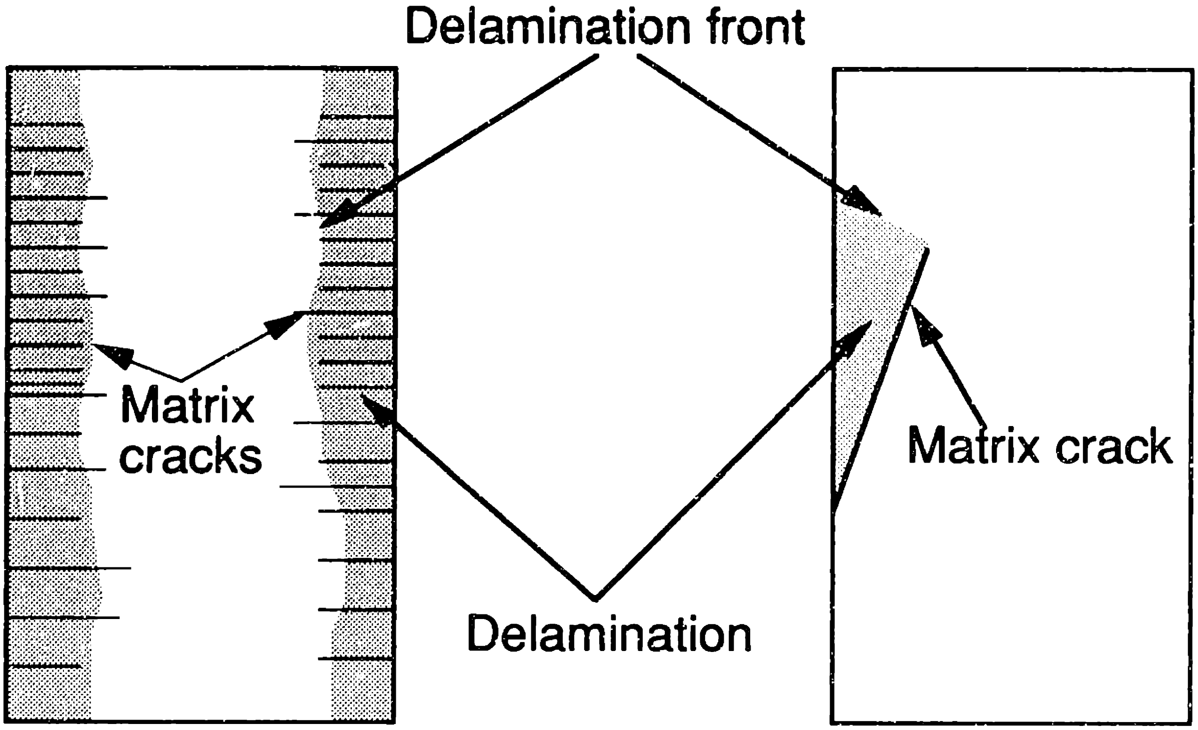

Figure 2.4 Two naturally observed compound delaminations (delamination with matrix crack), under uniaxial tensile test conditions (*left*) uniform-width delamination, and (*right*) triangular-shaped delamination.

(n=1/2,1) and also the initiation of matrix cracking (for n=2,3,4,6,8) in the 90° ply were successfully predicted. In cases where delamination initiation occurred subsequent to matrix cracking, the cracking was only considered indirectly by modelling the cracked 90° ply with reduced modulus properties. However, this approximation was successful in predicting delamination initiation only for laminates with n less than or equal to three. This was attributed to two reasons, the first was that for n greater than three, the delamination became significantly of the mixed mode type and hence for these cases the same value of G_c could not be used to predict it and the individual modes need to be separated and compared individually to critical values or used in a criterion. The second reason is that a reduced modulus was insufficient and three-dimensional modelling was needed to account for the local stress concentrations at the matrix crack(s).

An analytical expression was suggested by O'Brien [35] with an aim to simplify the evaluation of strain energy release rates for the case of a uniform delamination strip. This expression was derived on the basis of a simple rule of mixtures for the global change in stiffness of the laminate when complete delamination has occurred at an interface symmetrically. This expression for G is given as ,

$$G = \frac{\left(E_{lam} - E^{*}\right)}{2} t \, \varepsilon_x^{2} \tag{2.4}$$

where E_{lam} is the modulus of the intact laminate, E* is the modulus of the completely delaminated laminate along one or more interfaces as determined by a rule of mixtures, ε_x is the applied far-field strain and t is thickness of the laminate. While this expression may be evaluated without finite element analysis, it also has the disadvantage that the different modes of strain energy release rate cannot be separated. The strain energy release rate, G, is also seen to be independent of the delamination length, according to equation (4).

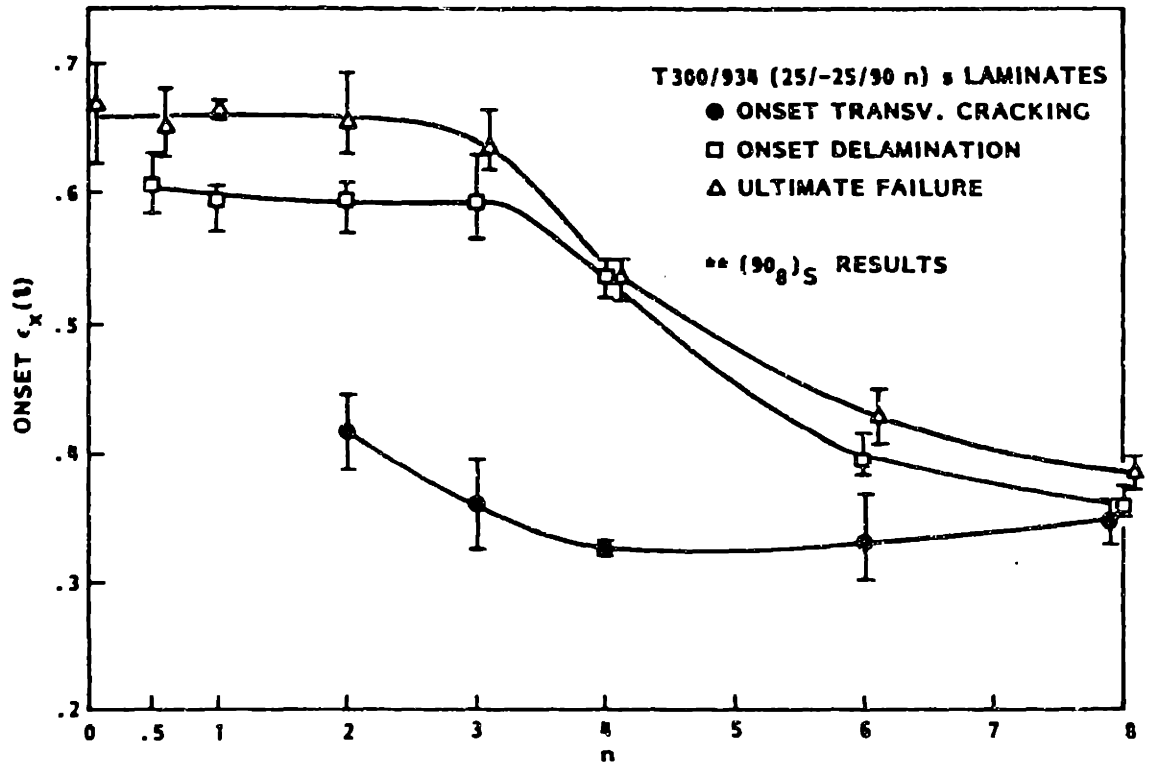

Figure 2.5 Test data for $[\pm 25_n/90_n]_s$ T300/934 graphite/epoxy laminates indicating matrix cracking, delamination initiation and final failure strains [3, 4].

Evaluations by numerical methods for some graphite/epoxy laminates have also borne out the fact that the value of G is almost independent of the crack length. Hence, the form of the curves shown in Figure 2.2 are mostly flat for the case of a uniform free edge delamination except for a small region (on the order of a laminate thickness) near the free edges of the laminate [35] which is the boundary layer region with significant interlaminar stresses. The criterion in equation (2.2) was once again adopted to predict delamination initiation.

Free edge delamination initiation was successfully predicted in $[\pm 45_n/0_n/90_n]_S$ laminates (n=1,2,3), where delamination occurred at the 0/90 interface for all three thicknesses. The effects of altering the relative contributions of the different modes to the total strain energy release rate and its effect on the failure behavior [36] were studied by examining several different layups of the same laminate viz. $[\pm 45/0/90]_S$, $[0/\pm 45/90]_S$ and $[45/0/-45/90]_S$. In all three cases, delamination was seen to occur at the interface of the 90° ply and the rest of the laminate, but no mention was made about any matrix cracking. Therefore, the strain energy release rate according to equation (2.4) is the same in all three cases. Assuming that there exists only a single critical value of G_c, delamination should initiate at the same strain in all three cases, which is not observed experimentally. A finite element model was used to determine the components of the strain energy release rates. The contribution of mode III was negligible in all cases, and the ratio of G_I/G_{II} was different in each case. The results showed that delamination initiation strain values decreased with increasing percentage of mode I. These results indicate that though the global energy release rate based criterion are successful in a few cases to predict delamination initiation, the determination of individual modes is necessary in most cases to predict the observed trends in experimental data.

Compound delaminations of the type shown in Figure 2.4(b) have been observed in certain classes of laminates, such as $[\pm\theta_n/0_n]_s$, $[0_n/\pm\theta_n]_s$ and $[\pm\theta_n]_s$. The free edge delamination is in the form of a triangular shaped region located near the free edge [1, 10] as shown in Figure 2.4(b). It is usually bordered on one side by the free edge and on the second side by a matrix crack. The third side forms the delamination front which, in association with the matrix crack, is seen to grow along the laminate up to failure. This typical damage state occurring in a $[\pm15_n]_s$ laminate is shown in a three-dimensional illustration in Figure 2.6, where the top +15° ply has the matrix crack and the delamination is at the +15/-15 interface. It has seen that the profile of the matrix crack is not a straight line but is curved as shown in Figure 2.6 [5].

In such cases, the quasi-three-dimensional fracture mechanics models can no longer be readily applied to predict either initiation or growth for these cases as this problem cannot be treated as a generalized plane strain problem. Brewer and Lagace [1] attempted to model this form of damage as a modified quasi-three-dimensional problem. The $[\pm15_n]_s$ laminate shown in Figure 2.6 was modelled as a series of quasi-three-dimensional sections along the loading direction and the total strain energy released by the laminate was obtained by adding the contribution of each individual section. They also experimentally monitored the far-field strain level for increasing sizes of the triangular delamination region. These strain levels and delamination sizes were used in the finite element model to obtain the global energy release rate, G, with the intention of finding a trend in the growth as well as the effect on this trend of increasing the effective ply thickness 'n'. As the triangular region grew larger, the strain energy release rate did not reach a constant value of G_c. In fact, no logical trend with increasing delamination size was displayed by the strain energy release rate as obtained from the experimental data. This model ignores

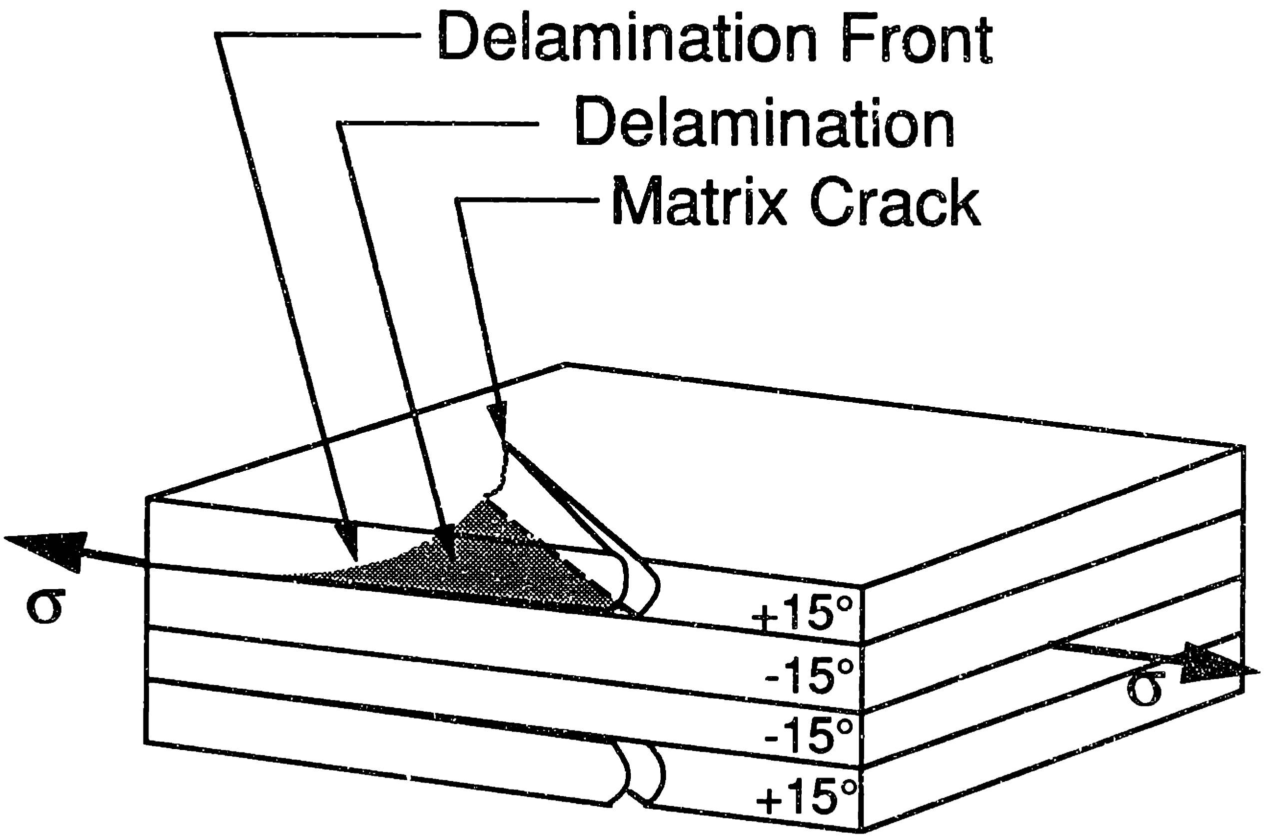

Figure 2.6 Characteristic damage mode observed in some laminates consisting of triangular-shaped delamination bordered by the free edge and a matrix crack.

the specifics of the delamination crack front and the matrix crack tip and evaluates only global energy changes in the laminate. These results indicate that the overall strain energy release rate is not sufficient to examine the behavior of this type of damage configuration and the variation of the strain energy release rate along the delamination front and the matrix crack front may be of key significance in understanding the controlling mechanisms responsible for the growth of this form of damage. An experimental study [6] with only the delamination implants was made, and the matrix crack was seen to appear bordering the delamination before the growth of the delamination occurred. An implanted delamination with a matrix crack bordering the delamination, but extending much beyond the delamination was also tested [6]. In this case, the delamination was seen to extend up to the implanted matrix crack before any damage growth. Both these indicate that neither damage state could grow to failure individually.

Salpekar and O'Brien [37] also modelled a similar damage configuration with the aim of predicting delamination initiation in $[\pm\theta/0]_s$ and $[0/\pm\theta]_s$ laminates. The model was based on the assumption that the delamination grew from a pre-existing matrix crack. They showed that the interlaminar normal stresses at the region of intersection of the matrix crack and the free edges were tensile and hence concluded that the conditions in that region were conducive to the initiation of delamination. They also studied a delamination front growing from the matrix crack with the front parallel to the matrix crack as it grew along the length of the laminate. The results show that the strain energy release rate along the delamination front was large near the free edge, with mode I being the dominant component. Hence, they concluded that the growth of such a delamination from the intersection of the matrix crack and the free edge was feasible. The occurrence of such matrix cracks without delamination were not observed in tensile tests where the only observed form of damage was compound delamination [5]. Radiographic examination under fatigue loading showed some matrix cracks before the formation of delamination [29], but the mechanisms in fatigue could be different from that in static tensile testing.

O'Brien also developed an expression for the energy release rate of a triangular compound delaminations [29] based on the change in the modulus due to the delamination. The model was based on the assumption that the regions near the free edges containing the partial local delaminations act as a system of sublaminates in series and this series system was in parallel with the undamaged laminate. Three possible ways that were visualized for the growing delamination are shown in Figure 2.7. The derived expression showed that the total strain energy release rate of the delamination was not dependent on the shape of the delamination, but was dependent on the intrusion, a, of the delamination as,

$$G=\frac{\varepsilon^2 t_{Lam}}{2m}\left(\frac{L}{a}\right)\left[E_{Lam}-\frac{1}{(Ba+C)}+\frac{Ba}{(Ba+C)^2}\right] \tag{2.5}$$

where,

$$B=\frac{1}{2}\left(\frac{1}{t_{LD}E_{LD}}-\frac{1}{t_{Lam}E_{Lam}}\right)\left(\frac{t}{L}\right) \tag{2.6}$$

and

$$C=\frac{1}{E_{Lam}} \tag{2.7}$$

where E_{Lam} is the modulus of the intact laminate, E_{LD} is modulus of the delaminated sublaminate, L is the length of the specimen, a is the intrusion of the delamination into the specimen, t_{Lam} is the thickness of the specimen, t_{LD} is the thickness of the delaminated sublaminate, ε is the applied far-field strain and m is equal to unity for a single delamination and has the value two for a delamination located symmetrically through the thickness. The E_{LD} of the sublaminate which has delaminated is determined by the detailed expressions derived in reference [29] depending on whether the bending-extension coupling or shear-extension coupling is of importance. The expression in equation (2.5) showed that the global strain energy release rate of the delamination was independent of the shape of the delamination for self-similar delamination propagation, but was dependent on the intrusion into the laminate, and with increasing intrusion the strain energy release rate dropped. The effect of the matrix crack front relative to the delamination was not studied.

Thus, from the review of the previous models it appears that most of the work dwells on the prediction of initiation and growth of simple delamination and certain specific compound delaminations like those shown in Figure 2.4(a). Specifically in the case of such compound delaminations, the matrix cracking occurs first at low load levels due to the presence of 90° plies and the delamination grows subsequently along these matrix cracks. The mechanism of growth is reasonably understood and the impetus lies in the area of prediction of load/strain levels at which such delamination growth occur. The results have shown that even in these cases, the criterion in equation (2.2) has limited success. Individual modes of strain energy release are seen to provide more insight into prediction of the growth process.

In the case of compound delaminations of the type shown in Figure 2.4(b), no models exist to examine the mechanism of the interaction of the delamination front and the matrix crack in the θ° ply. It is evident from the nature of the damage and from previous work that a full three-dimensional model is necessary to examine the mechanisms involved in the growth of this compound delamination and to arrive at successful methods to predict such growth.

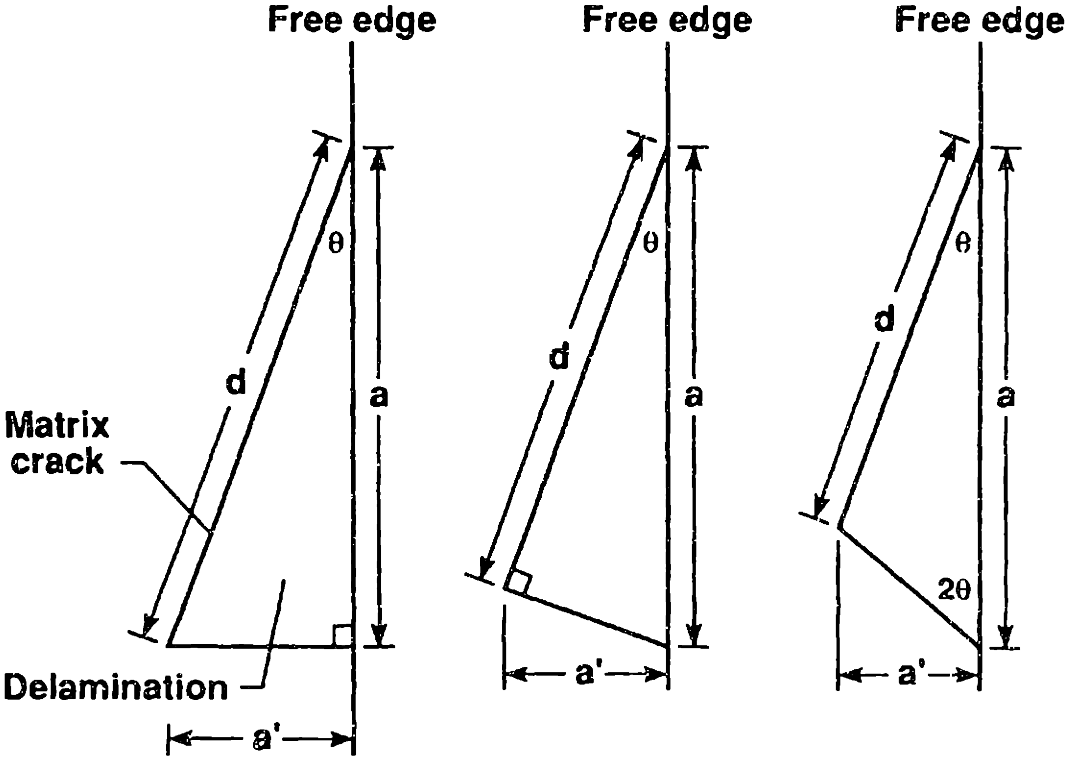

Figure 2.7 Three possible orientations of the delamination in $[0/\pm\theta]_s$ laminates during growth of delamination as suggested by O'Brien [5].

2.2.2 Problems of Bimaterial Interfaces

Experimental investigation of failure of composites in the three different modes of fracture shown in Figure 2.3 have indicated that there is significant difference in the critical values of strain energy release between the three modes. This will be further elaborated in section 2.2.4. Hence, the evaluation of the individual modes becomes necessary to better understand the growth of delaminations. Delamination usually occurs between plies of different materials and therefore typically represents the case of a crack between two different materials. Unlike the cracks in isotropic materials where the modes may easily be separated, the cracks between bimaterials possess some special characteristics which make it difficult to uniquely define the modes. These characteristics as well as their consequences are briefly discussed here.

The behavior of cracks occurring at bimaterial interfaces have been studied since the late 1950's. The bimaterial crack problem was first solved by Williams [38] who showed that the stresses at the bimaterial interface did not just have a singularity of the ($1/\sqrt{r}$) type but also an additional term of the type $r^{i\delta}$ (where $i=\sqrt{-1}$), where δ is the magnitude of the oscillatory singularity. The complex term indicates that the crack opening displacements of the crack surfaces are oscillatory in nature, implying that the crack surfaces interpenetrate each other. Since interpenetration is not physically possible, there is a zone near the crack tip where crack surface contact occurs and, hence, this implies that the linear elastic solution is incorrect in this region.

In the case of isotropic materials, the solution of ($1/\sqrt{r}$) singularity is invalid near the crack tip because the stresses cannot physically approach infinite values and a small nonlinear zone (known as the 'process zone') develops in the vicinity of the crack tip. Consequently the linear elastic solution is not valid near the crack tip. Nevertheless, as long as the process zone remains small relative to the size of the crack, the behavior of the crack is governed by the bulk of the material around it and hence by the stress intensity factor found in the linear elastic solution. This was one of the principal conclusions drawn by Irwin [24] leading to the widespread use of the stress intensity factor and the strain energy release rate after it had been verified by extensive experimentation. Rice [39] suggested that the same reasoning of 'small scale yielding' may be carried over to the bimaterial case when the scale of the contact zone is extremely small compared to the size of the crack length. The conditions for crack growth can then be phrased in terms of the stress intensity factors, K_1, K_2 and K_3 .

These stress intensity factors are very different from the traditional stress intensity factors where, in the isotropic case or a bimaterial case with no oscillatory singularity, the crack opening stresses are a function K_I alone, the crack shear stresses are a function of K_{II} alone and the crack tearing stresses are a function of K_{III} alone. Hence, these stress intensity factors have a one-to-one relation with the type of loading experienced by the crack. In the case of bimaterials with an oscillatory singularity, the crack opening, shearing and tearing stresses are dependent on all three stress intensity factors. Hence, there is no one-to-one relationship between the types of loading experienced by the crack and the stress intensity factors. The stress intensity factors are therefore written as K_1, K_2 and K_3 where, unlike the classical stress intensity factors, the subscripts have nothing to do with the modes. Another interpretation of these new form of stress intensity factors are that the opening and shearing modes are now coupled together and cannot be completely separated. For example, an applied far-field loading of either mode I or mode II induces both mode I and mode II response at the crack tip. The degree of cross-linking is dependent on the magnitude of the oscillatory singularity. Another interpretation of this same effect is that, in the case of isotropic materials, the ratio of the normal to shear stresses is also the ratio of mode I to mode II and is independent of the distance ahead of the crack tip where this ratio is evaluated. But for a bimaterial, this ratio of stresses changes as one moves ahead of the crack tip. It has been suggested by Rice [39] that this ratio can be analytically evaluated at a specific distance ahead of the crack tip, thus requiring a distance parameter to uniquely specify the 'stress intensity factors'. However, this approach has not yet been developed to experimentally classify the fracture toughness of interface cracks in composite materials.

The case of interface cracks between anisotropic bimaterials has also been studied [40-44] to discover that the stress intensity factors need to be defined in a manner similar to that in isotropic bimaterials. Suo [40] has given explicit expressions for the stresses ahead of the crack tip, the crack surface opening displacements, and the total strain energy release rate in terms of the complex stress intensity factors mentioned earlier. These may be used in the study of delaminations as the parameters which control crack growth.

Therefore, no clear cut definitions of modes exist for delaminations between plies of differing orientation. If the oscillatory singularity is found to be small relative to the maximum possible value, then the coupling between the modes is weak and conventional methods may be used with little error to separate the modes. Alternatively, as discussed earlier, the ratio of the stresses at a certain distance ahead of the crack tip may be used to separate the modes. The disadvantage of this method lies in the fact that there are no experimental results currently available regarding the distance at which this ratio needs to be evaluated. Substantial experimentation needs to be done in this area to validate this technique before it can be used.

The approach that may be most suited at the present time for complex delamination problems is the conventional technique for separating the modes.

Since the problem involves a delamination, evaluation of the oscillatory singularity is necessary to determine the severity of the coupling between the various modes. A low degree of coupling between the various modes would imply that the errors in these conventional methods for determining the modes are marginal and the components thus obtained could be used to represent the physical modes of separation in that particular bimaterial problem. This method also enables the comparison of the modes obtained with experimentally determined critical values for these modes to obtain some insight into the mechanisms that may be responsible for the propagation of specific types of delaminations.

2.2.3 Numerical Methods to Evaluate Strain Energy Release Rate

If the techniques of fracture mechanics are to be applied to the delamination problem, the numerical evaluation of the strain energy release rate is an issue which needs to be addressed. In the case of three-dimensional modelling via finite elements, one of the primary requirements is the robustness, as well as efficiency, since computer memory restrictions usually impose limitations on the mesh refinements. Problems where the strain and the cross-section do not vary in one direction are referred to as generalized plane strain/stress problems. In such cases, it is inefficient to use three-dimensional finite elements, as with specially written programs only a two-dimensional cross-section needs to be analyzed. This is accomplished by giving the elements an additional degree of freedom in the direction of loading making it computationally efficient. These are referred to as quasi-three-dimensional problems.

The definition given in equation (2.1) involves the rate of change of energy of the entire body. Irwin showed that the strain energy may be equivalently calculated by considering only the local asymptotic fields around the crack. This approach is known as the Virtual Crack Closure Integral and is an equivalent method for evaluating G,

$$G = \lim_{\Delta a \to 0} \frac{1}{\Delta a} \int_0^{\Delta a} \sigma_{ij}(r) u_j(\Delta a - r) dr \tag{2.8}$$

where σ_{ij} are the stresses ahead of the crack tip, u_j are the crack opening displacements behind the crack tip and r is the distance measured ahead of the crack tip in its plane. The crack is assumed to grow in a self-similar fashion. Hence, Δa is a small crack extension measured along the direction of the crack length.

Three-dimensional and quasi-three-dimensional finite elements have been used by the majority of researchers to evaluate the strain energy release rate and its components for cracks in composites. The Virtual Crack Closure Technique and J-Integral Approach (discussed later) are the two basic techniques used to evaluate strain energy release rate in linear elastic materials. The Virtual Crack Closure Technique has been the most widely used in evaluating the strain energy release rate at the tip of a delamination. The expression shown in equation (2.8) is modified as follows,

$$G = \frac{1}{\Delta a}\left(F_x(r)\, u_x(-r) + F_y(r)\, u_y(-r) + F_z(r)\, u_z(-r)\right) \tag{2.9}$$

where the crack tip element is of size Δa; F_x, F_y and F_z are the nodal forces within this element at a distance 'r' ahead of the crack tip; and u_x, u_y and u_z are the crack opening displacements behind the crack tip. A two-dimensional version of this is shown in Figure 2.8. There have been many versions of this method currently in use though the basic premise remains the same as that of equation (2.8). One such improvement is the use of singular elements which are typically used along the crack front to model the ($1/\sqrt{r}$) type of singularity at the crack tip enabling the evaluation of the strain energy release rate with coarse meshes. This, however, ignores the $r^{i\delta}$ type of oscillatory singularity mentioned earlier. The separation of modes is also easily possible as the three individual terms in equation (2.9) evaluate the contributions due to opening (G_I), shearing (G_{II}) and tearing modes (G_{III}), respectively. However, three-dimensional formulations of this approach are not available in the literature to the best of this author's knowledge. The typical approach in three dimensions is to measure the forces ahead of the crack tip and then to extend the crack and measure the crack-opening displacements at the same location and use them in equation (2.9). This approach, though adopted by some researchers in the analysis of three-dimensional problems [37] may be uneconomical as the scale of the problem increases since two runs of the problem are necessary to obtain G.

It has been suggested in some recent review papers [45, 46] that the J-Integral approach may give fairly accurate measures of G along three-dimensional crack fronts in an efficient manner. As originally formulated, the J-Integral is a closed contour integral in two dimensions (or a surface integral in three dimensions), which, in the case of linear elastic solids, is equal to G, and is evaluated along any contour around the crack tip as,

$$G = \int_{\Gamma} \left(W n_1 - \sigma_{ij} \frac{\partial u_i}{\partial x_1} n_j \right) ds \tag{2.10}$$

where Γ is the path around the crack tip where this integral is evaluated, W is the strain energy density, and n_1 is a component of the normal to the contour surface.

Surface integrals are cumbersome to evaluate numerically, hence this definition has been modified to a volume integral form by the application of the

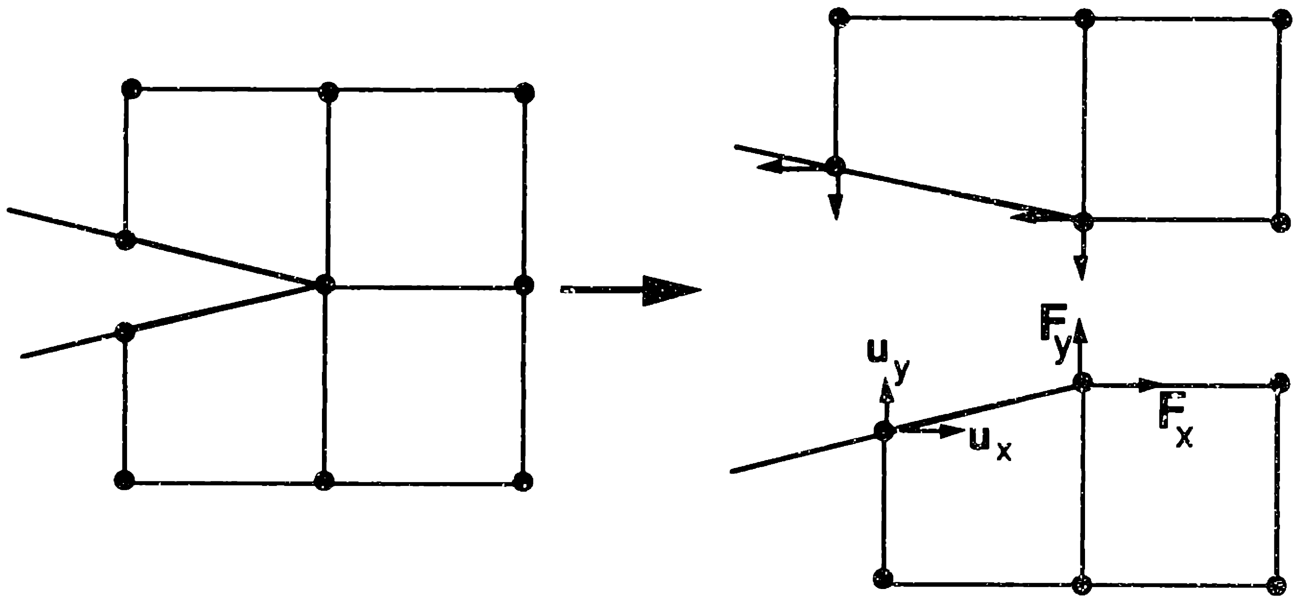

Figure 2.8 Nodal forces ahead of the crack tip and crack opening displacements behind the crack used in the virtual crack closure method.

divergence theorem. The resulting integral is called the 'Equivalent Domain Integral'. This method has been successfully applied to a wide variety of three-dimensional problems [47-49]. In this case, only the total strain energy release rate is obtained and, in order to obtain the individual components, a 'decomposition method' has been suggested [47, 50]. The decomposition method requires a symmetric mesh around the crack tip so that the displacement, stresses, and strains in the region around the crack tip can be easily obtained at mirror image points on either side of the crack tip. The crack tip load data is then broken down into three components. The first component consists of only those types of displacement, stresses, and strains which can cause a mode I type of loading on the crack, i.e. the loading on the regions above and below the crack are mirror images of each other and can hence only 'open' the crack but cannot 'shear' or 'tear' the crack. The second component consists of only those loading which can cause a mode II type of behavior, i.e. the loading above and below the crack are anti-symmetric to each other in a manner to cause a pure shearing (in-plane) deformation of the crack. The third component consists of only those loading which can cause a mode III type of behavior, i.e. the loading above and below the crack are anti-symmetric to each other so that they cause a pure tearing (out-of-plane) deformation of the crack. Once these individual components of loading have been determined, the equivalent domain integral may be used with the symmetric part of the loading to provide the value G_I. When used with the anti-symmetric parts, the integral provides values for G_{II} and G_{III}. Thus, the components of the loading provide the modes of the strain energy release rate. Although the components of the strain energy release rate can be determined, these are not unique for bimaterial interfaces.

The oscillatory characteristics of the singularity at bimaterial interfaces are reflected in the numerical evaluation of the individual modes of the strain energy release rate and cause these values to not be uniquely determined. It is seen from equation (2.8) that Irwin's definition of the virtual crack closure method requires a value for Δa, and in finite element evaluations it generally refers to the size of the crack tip element. It has been shown by Raju [51] and subsequently by Sun [52] that choosing different values for Δa results in different values for G_I, G_{II} and G_{III}, although the total G is unaffected. With increasing values of Δa, the values of the modes have almost constant values, but as the crack tip element size grows smaller, considerably different values may be obtained. The constant values attained for larger values of Δa occur because the solution for stress and strain have been averaged over a distance large enough to eliminate the effects of the oscillations. The physical ramifications of the components thus obtained are still a much debated issue. The total G, which is a sum of G_I, G_{II} and G_{III}, however, does not vary with the size of the crack tip element.

Therefore, the approach that seems most efficient for three-dimensional problems is a volume or domain based J-Integral approach along with a decomposition method for mode separation purposes.

2.2.4 Failure Criteria

Once the strain energy release rate and its modes have been determined for any crack problem, the next step is to use them in the prediction of the growth process. The prediction of failure can be divided into two parts, the first one being the failure criterion itself and the second is the technique of obtaining the parameters within the failure criterion.

Several failure criteria for the fracture mechanics methodology have been proposed and used for delamination and matrix crack problems in composites. The simplest criterion adopted was shown in equation (2.2) and this was used to successfully predict delamination within a certain class of laminates with varying ply thickness [35]. Experimentally, no single value of G_c was seen to be valid across different layups or for different mode ratios. Other similar criteria involve individual modes instead of the total G,

$$G_I = G_{Ic} \quad or \quad G_{II} = G_{IIc} \quad or \quad G_{III} = G_{IIIc} \tag{2.11}$$

According to equation (2.11), whichever mode satisfies the criterion first will be responsible for the failure. The mode I version of equation (2.11) has been validated in the case of delamination propagation under compressive loading, where the mode I dominates. The mode II and mode III versions have not been tested.

Several mixed mode growth criteria have been proposed to predict the growth of delaminations under mixed mode (mode I & mode II only) conditions. The criteria that are proposed are based on data available either from tensile tests of off-axis unidirectional ply specimen, with a crack parallel to the fiber direction [53, 54], or by some form of a mixed-mode bending specimen [55, 56]. Many of these criteria are power laws whose indices are determined by curve fits to the data and are generally restricted to mode I and mode II only [15]. A general form of the criterion is,

$$\left(\frac{G_I}{G_{Ic}}\right)^m + \left(\frac{G_{II}}{G_{IIc}}\right)^n + \left(\frac{G_{III}}{G_{IIIc}}\right)^q = 1 \tag{2.12}$$

where m, n and q are dependent on the material and have been determined for some graphite/epoxy and graphite/PEEK systems [15]. To the best of the author's knowledge, no data is available for the mixed-mode case involving mode III, although it has been shown to be the dominant mode in the case of free-edge delamination in some laminates [42].

Once a criterion is adopted, the values of the parameters G_{Ic}, G_{IIc} and G_{IIIc}

need to be determined. There are several tests which have been developed for this purpose, the double cantilever beam (DCB) specimen [12] and modified versions of that [57] for mode I behavior; the edge notch flexure (ENF) specimen, the cracked lap shear (CLS) specimen [12], and the three rail shear test [54] for mode II behavior; and the Arcan specimen [58], the edge delamination test (EDT) specimen [35], the four point bend (FPB) specimen [59] and Sandwiched Brazil Nut specimens [60] for mixed mode behavior. There are very few results available to determine the mode III behavior. Donaldson [61] used the DCB specimen loaded in the tearing mode to determine G_{IIIc}. This specimen is known as the split cantilever beam specimen.

Delamination in most cases is seen to occur at the interfaces between dissimilar plies, but most of the tests mentioned earlier determine the critical values for G_I, G_{II}, and for the mixed mode G, by causing and propagating a delamination between similar plies, usually 0° or 90° plies. There have been some attempts to extend the tests such as the DCB to examine multidirectional laminates [62] with little success due to wandering of cracks to different interfaces.

There are several sets of data available for various fiber/matrix systems with considerable difference even for similar fiber/matrix systems. In the case of Mode I testing via the DCB specimen and the EDT specimens, the variation in G_{Ic} for T300/5208 system ranges from 80 to 240 J/m^2 and the G_{IIc} data for the T300/5208 system vary from 150 to 1200 J/m^2 [63]. The methods for calculating these from the basic measured data vary from the use of simple formulae based on compliance measurements to detailed finite element analysis. Furthermore, the use of the basic data changes depending upon what is regarded as "initiation". The variations in mode I data are attributed to various phenomenon [64], such as the method used to make the starter crack, crack wandering and fiber bridging. When the specimens used for mode I testing consist of several identical plies, nesting or intermingling of plies occurs and there may be no distinct interlaminar layer available for delamination propagation. The crack then weaves between layers of fibers causing these bridges. Thicker specimens are seen to contribute more to fiber bridging and hence give increasing G_{Ic} values with increasing crack length [65]. Similarly in the case of mode II test results, crack surface friction and the type of starter crack are issues currently of concern [64, 66]. In the case of mode II, it has been shown that scaling the specimens results in different values of G_{IIc} [67].

Most research on delamination growth in fiber reinforced composites is centered around the application of G_I, G_{II} and G_{III} to identify modes of failure. However, there has recently been work done on glass to epoxy interfaces [68, 69] where the new definition of stress intensity factors (K_1, K_2 and K_3) for bimaterial interfaces discussed in the earlier section has been used. However, this data is for cracks between two isotropic materials and is not directly applicable to laminated composites. No such data is available for delaminations in any composite materials.

2.3 Summary

The strength of materials approach has been successful in the prediction of delamination initiation but has not yet been widely applied to crack growth problems in composite materials. The method first needs to be tested for predicting growth of cracks in cases such as double cantilever beam specimens or other such problems where adequate amounts of experimental data is available. This basic groundwork would be needed before a criterion based on the strength of materials could be validated and applied to compound delamination problems.

The fracture mechanics method has been long established to work in the case of isotropic materials even for complex crack configurations with the aid of parameters such as the stress intensity factors and strain energy release rates. The methods of evaluation of these parameters around the crack tip have also been well-established, even in the case of three-dimensional problems. In the case of delamination growth, this method has shown some success in predicting the growth of circular delaminations and free edge delaminations. The inadequacy of this approach lies primarily in the lack of a universal mixed mode criterion. In spite of this, it has been shown that the method is capable of predicting trends in the data and also in serving as a technique for recognizing incipient crack growth .

The problem of compound delamination has not been adequately tackled thus far in literature. This involves both in-plane damage/failures and out-of-plane damage/failures and hence the relative importance of either mode along with their interaction needs to be determined. The evidence so far indicates that this problem is still a research issue which needs to be addressed.

CHAPTER 3

PROBLEM DEFINITION

In this chapter, the mechanics of the triangular-shaped compound delamination are explored in the light of the detailed experimental evidence available from the previous work done in this area as described in Chapter two. The issues for further research in this area are identified and the experimental and analytical procedures adopted to pursue them are outlined.

3.1 Mechanics of Compound Delaminations: Current Status

The research on triangular-shaped compound delaminations has been mostly carried out on the $[\pm\theta_n]_s$, $[\pm\theta_n/0_n]_s$, and $[0_n/\pm\theta_n]_s$ families of laminates. The subscript n is a discrete number indicating the number of plies of the same angle that have been layed together to form an 'effective ply', and the resulting thickness is known as the effective ply thickness. These types of delaminations are observed under tensile loading, for values of θ between 0° and 30° [1, 9, 29, 70]. As a consequence of the delamination, the failure stresses of these laminates fall considerably below predictions made via in-plane failure criteria [9]. Further investigations have been carried out with values of θ equal to 15°, 20°, 25° and 30° and for values of n ranging from to 2 to 8 [1, 5, 29] in order to examine the growth of the triangular-shaped delaminations in these laminates from initiation to unstable growth (failure). The effect of ply thickness on this process has also been considered.

In all these families of laminates, the experimental data consistently indicates that the first stable mode of damage visible by radiographic examination is a triangular compound delamination with a curved delamination front and bordered by a matrix crack as shown in the X-ray radiographs in Figure 3.1 [6]. In the case of $[\pm15_3]_s$ specimens, the delamination was observed to be at the +15/-15 interface and the matrix crack was in the surface +15° ply [6]. Though this observation was not made earlier, the current author notices, from the observation of these specimens, that the delamination is located symmetrically through the thickness for the $[\pm15_n]_s$ laminates. The $[\pm15_n/0_n]_s$ laminates also show an almost identical stable damage mode consisting of cracking in the top +15° plies and delamination at the +15/-15 interface [6]. In this case, the delamination is not always symmetric through the thickness. The $[0_n/\pm\theta_n]_s$ laminates show an identical delamination configuration at the $+\theta/-\theta$ interface located symmetrically through the thickness. However, the matrix cracking in this case is not in the surface plies, but in the central $[-\theta_{2n}]$ sublaminates [5, 6]. There was no consistency in the size (areas) of the delaminations observed in the various laminates. In the case of $[\pm15_3]_s$ and $[\pm15_n/0_n]_s$ laminates, the size of the delaminations that are first observed via X-ray radiographs are generally smaller than in the case of the $[0_n/\pm15_n]_s$ laminate.

The formation of these triangular delaminations during testing was usually accompanied by a loud click and a drop in the load [6]. On further loading, this primary mode of damage was generally followed by the formation of matrix cracks in the plies neighboring the delamination, henceforth this is referred to as "secondary cracking". In the case of $[\pm15_3]_s$ and $[\pm15_n/0_n]_s$ laminates, the secondary matrix cracks usually formed as tangents to the curved delamination front at the free edge region in the -15° sublaminates, as shown in Figure 3.2 [6]. In the case of the $[0_n/\pm\theta_n]_s$ laminates, it cannot be conclusively said that the matrix cracking occurred tangential to the delamination front. However, these cracks still originate in the region where the delamination front

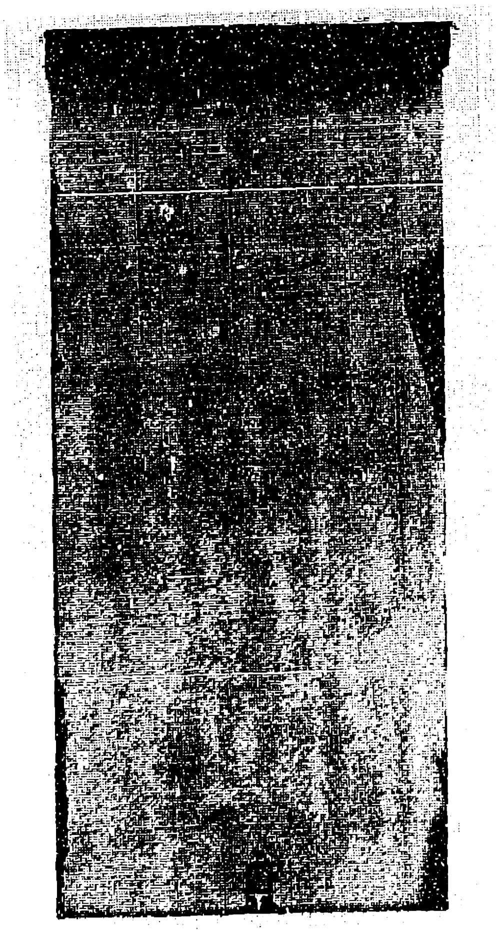

Figure 3.1 X-ray picture showing triangular compound delamination with a curved delamination front observed in $[\pm\theta_n]_s$, $[\pm\theta_n/0_n]_s$ and $[0_n/\pm\theta_n]_s$ laminates at the +θ/-θ interface [6].

meets the free edge as shown in Figure 3.2 [5, 6].

In all three families of laminates, the original triangular delamination with the matrix crack propagated to the ends of the specimen and were stopped when they encountered the loading grips. This was usually accompanied with a significant (40%-50%) drop in load carried by the specimens and this was regarded as final failure of the specimen. A typical delamination which has grown to the loading tabs is shown in Figure 3.3 [6]. The delaminated region in all the cases had considerable secondary matrix cracking, as seen in Figure 3.3, which may have occurred either during, or subsequent to, final failure of the specimen as defined earlier.

The initial triangular delamination usually occurred at or above 95% of the failure load in the case of the $[\pm 15_3]_s$ laminate. In the case of the $[\pm 15_n/0_n]_s$ and the $[0_n/\pm 15_n]_s$ laminates, the delaminations occurred at about 80-90% of the final failure load [6]. The final failure load in these latter two laminates was higher due to the presence of the 0° plies which carried substantial load even after the initial delamination and loss of load-carrying capability in the cracked and delaminated +15° or -15° plies.

In certain laminates, it has been observed that delamination initiates at the free edge. This first mode of damage can be observed only by microscopic examination. Subsequently, the triangular-shaped compound delamination with a curved front and an adjoining matrix crack is the first stable mode of damage that is macroscopically visible. This is further strengthened by an earlier study discussed in Chapter 2 [6]. In this study, only one form of damage was implanted into specimens, i.e. either delamination alone or a matrix crack alone. Loading of these specimens resulted in the formation of the complementary form of damage such that the end result was the formation of a triangular-shaped compound delamination of a configuration similar to that observed naturally.

No further information is available regarding the development of the initial microscopic delamination into this macroscopic damage.

On further loading, the existing damage excites secondary matrix cracking in adjoining plies and this overall damage subsequently propagates to the ends of the specimen resulting in significant amounts of delaminations within the specimen, recognized as final failure. Some of the issues pertaining to this failure are further identified in this section. Further work needs to be done to resolve these issues in order to provide a better understanding of the reasons for the occurrence and propagation of the observed damage mode.

A previous analysis based on the global energy release rate of specimens with triangular delaminations was discussed in Chapter two. This work concluded that there was no difference in the global energy release rate for different orientations of the delamination front, relative to the matrix crack, as shown in Figure 2.7 [29]. The local effects along the delamination front were not considered and the global energy release rate refers to the total energy released for the growth of the entire triangular delamination region. However, delaminations of various orientations are seldom found in the experiments involving these laminates. Therefore, one of the issues that needs to be addressed is the stability of the observed delamination contour and the mechanisms involved in the growth of the delamination into this configuration from its initiation configuration.

In order to further examine this, a greater detail in the modelling is necessary to determine the differences between the various delamination orientations on a local level, rather than at a global level. This requires a three-dimensional model of the delamination front in order to obtain the distribution of the energy release rate and the individual modes of the

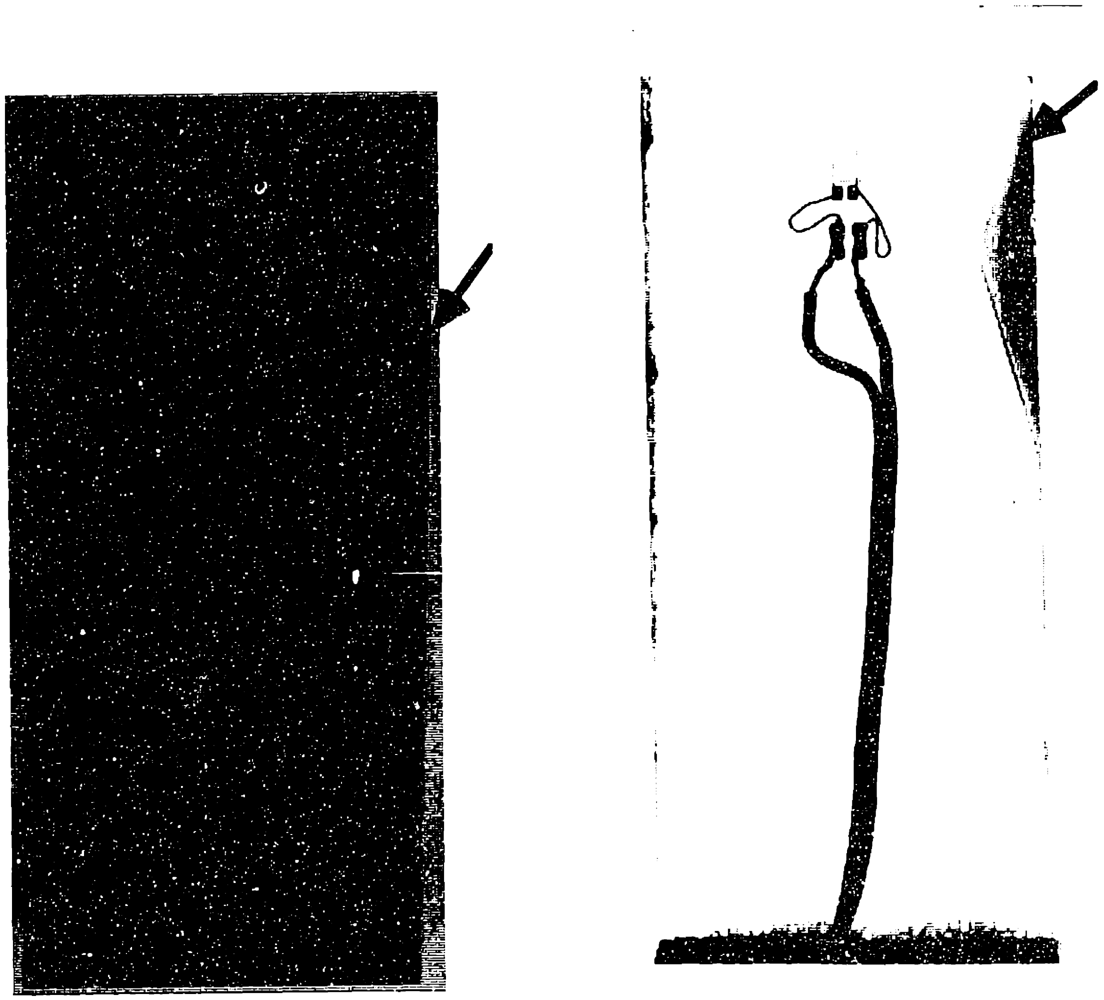

Figure 3.2 Secondary matrix cracking observed (*left*) in the $[-\theta_n]$ sublaminates in $[\pm\theta_n]_s$ and $[\pm\theta_n/0_n]_s$ laminates and (*right*) in the $[+\theta_n]$ sublaminates near the delaminated region in $[0_n/\pm\theta_n]_s$ laminates [6].

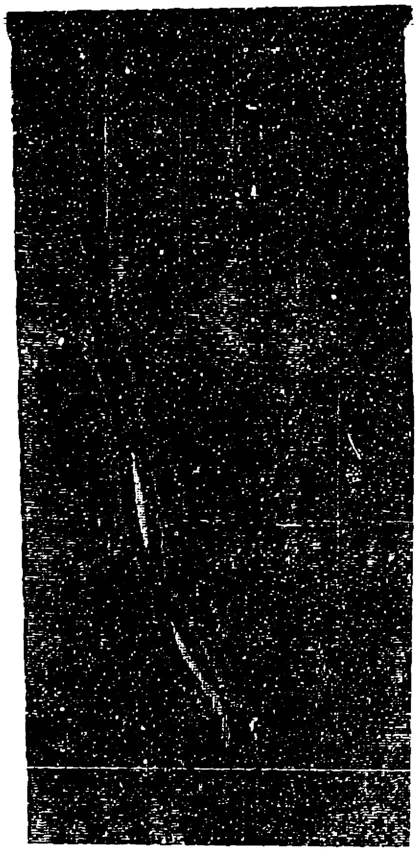

Figure 3.3 X-ray photograph after failure, showing delamination propagation along with secondary matrix cracking observed in $[\pm\theta_n]_s$, $[\pm\theta_n/0_n]_s$ and $[0_n/\pm\theta_n]_s$ laminates [6].

delamination along the delamination front. The delamination front within this model will be oriented at different angles to the matrix crack in an attempt to simulate the growth of the delamination. Since the fracture mechanics approach is adopted in the current study, the distribution of strain energy release rate is used to determine the patterns of growth. Such growth is likely to occur in regions where the energy release rate exceeds a critical value and this could result in a delamination with a different orientation. The examination of the strain energy release rate may also help to identify the mechanisms involved in the arrest of the delamination growth in the form of the experimentally-observed delamination contour.

The second issue that needs investigation is the interaction between the delamination and the matrix cracking in this configuration. Since the triangular delamination region including the matrix crack propagates as a 'unit', the relative importance of the matrix crack and the delamination front in the propagation needs to be determined to ascertain whether one of these two damage types, or their interaction, is responsible for the unstable growth of this damage configuration. In order to examine this, it is necessary to model both the delamination front and the matrix crack front. Any such model necessarily involves a three-dimensional modelling of the damage state.

For small delamination sizes, subsequent to the formation of the triangular-shaped delamination, the secondary damage is seen to occur in the vicinity of the triangular delamination. No other isolated matrix cracks are visible anywhere within the laminate. This suggests that the causes of these matrix cracks are related to the stress state around the delamination front. It is likely that as the delamination front changes orientation, the stress state becomes conducive to the formation of secondary matrix cracks in those plies. One of the benefits of the three-dimensional model is the ablility to examine such stress states in the vicinity of the delamination front for different delamination orientations.

These issues provide a breakdown of the problem of final failure via propagation of the triangular-shaped compound delamination into key stages. An understanding of each individual issue via analytical and experimental modelling would provide an insight into the mechanisms responsible for each stage of the growth as well as the relative importance of the component damage modes.

3.2 Proposed Method of Study

In order to address these issues, a model of the initial damage state is necessary. Ideally, the initiation of either the delamination or the matrix crack would be a convenient point to start the analysis. However, the order in which these occur is still a debated issue. In the case of some laminates mentioned earlier, the occurrence of delamination prior to matrix cracking has been observed [6]. However, a finite element analysis performed for $[0/\pm\theta]_s$ laminates suggests the feasibility of delamination arising from matrix cracking [5], although no experimental evidence is available in quasi-static tensile testing to show that matrix cracks occur prior to delamination. The existence of a matrix crack without delamination is show in the case of tensile fatigue loading. It is likely that the mechanisms responsible for initiation could vary with laminate angles and effective ply thickness and with types of loading, hence it would be impossible to generalize the occurrence of one specific mode as the starting point. The existence of flaws near the free edges of the laminate may also play an important part in causing either the delamination or matrix crack to occur first. Hence, this thesis will not go into the details of the initiation of the delamination and matrix cracking. This has been discussed at length in reference [71]. The starting point for the current study is the presence of both the matrix crack and delamination. The delamination front is assumed to initially be at right angles to the matrix crack. The configuration size is defined by its intrusion, a, which measures the length of the damage extending along a normal to the free edge. This configuration is illustrated in Figure 3.4. This situation is not identical to that observed naturally, but is meant to represent a possible stage in the growth towards the naturally occurring contour.

Another aspect of the damage observed from radiographs and micrographs, is that the delamination front as well as the matrix cracks are curved in these laminates. In the case of matrix cracks, it is important to distinguish the crack profile from the crack front. In order to distinguish between these two terms, an example of a penny-shaped crack is shown in Figure 3.5. The straight lines seen on the plane PQRS normal to the crack is the crack profile. The curve seen on the section A-A, which slices through the crack, is known as the crack front. In the case of the laminate families discussed earlier, the shape of the matrix crack front is not known, however, the crack profile is almost parabolic at the free edge as illustrated in Figure 2.6 [5]. Since this geometry is still not properly documented, the matrix crack front and the crack profile will be modelled as straight lines, normal to the interface of the laminate, as shown in Figure 3.6. As mentioned in Chapter two, the delamination front is also curved in the regions close to the free edge. However, for simplicity, the present study will also approximate the delamination front as a straight line, as in previous studies [29] .

The study is separated into the experimental and analytical parts, described in succeeding sections, along with their particular objectives.

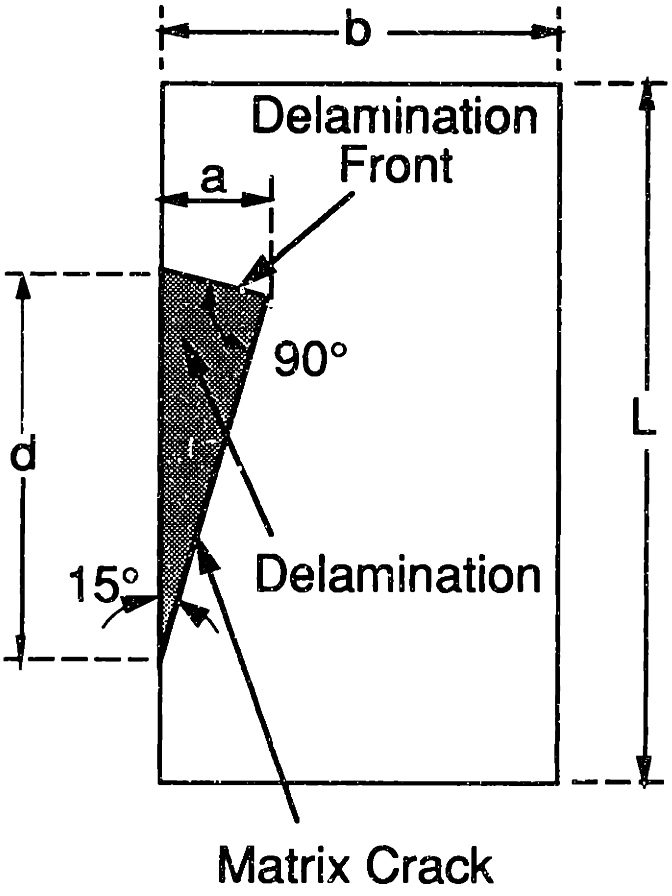

Figure 3.4 Top view of the delamination front used as the initial configuration in the present analysis of growth of the compound delamination.

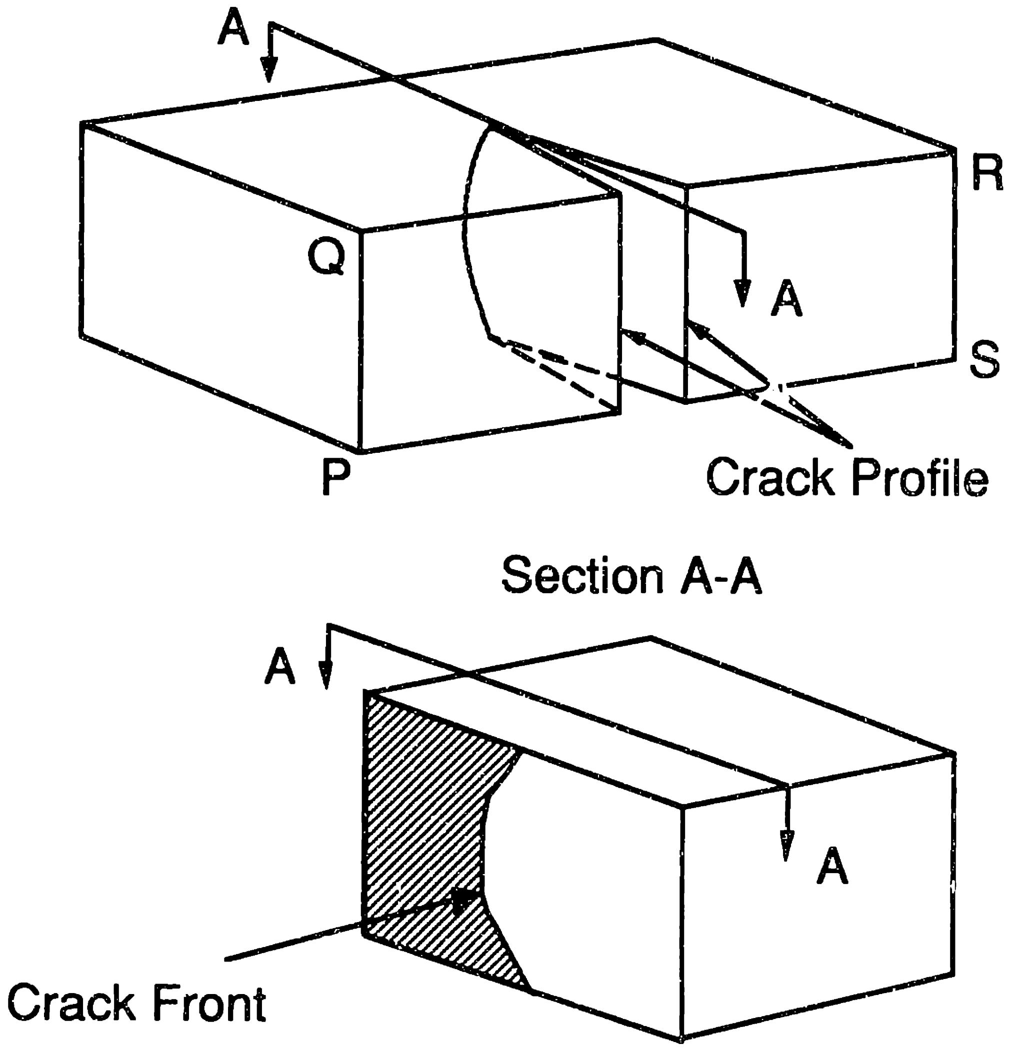

Figure 3.5 Definition of a crack front and crack profile in the case of a penny-shaped crack.

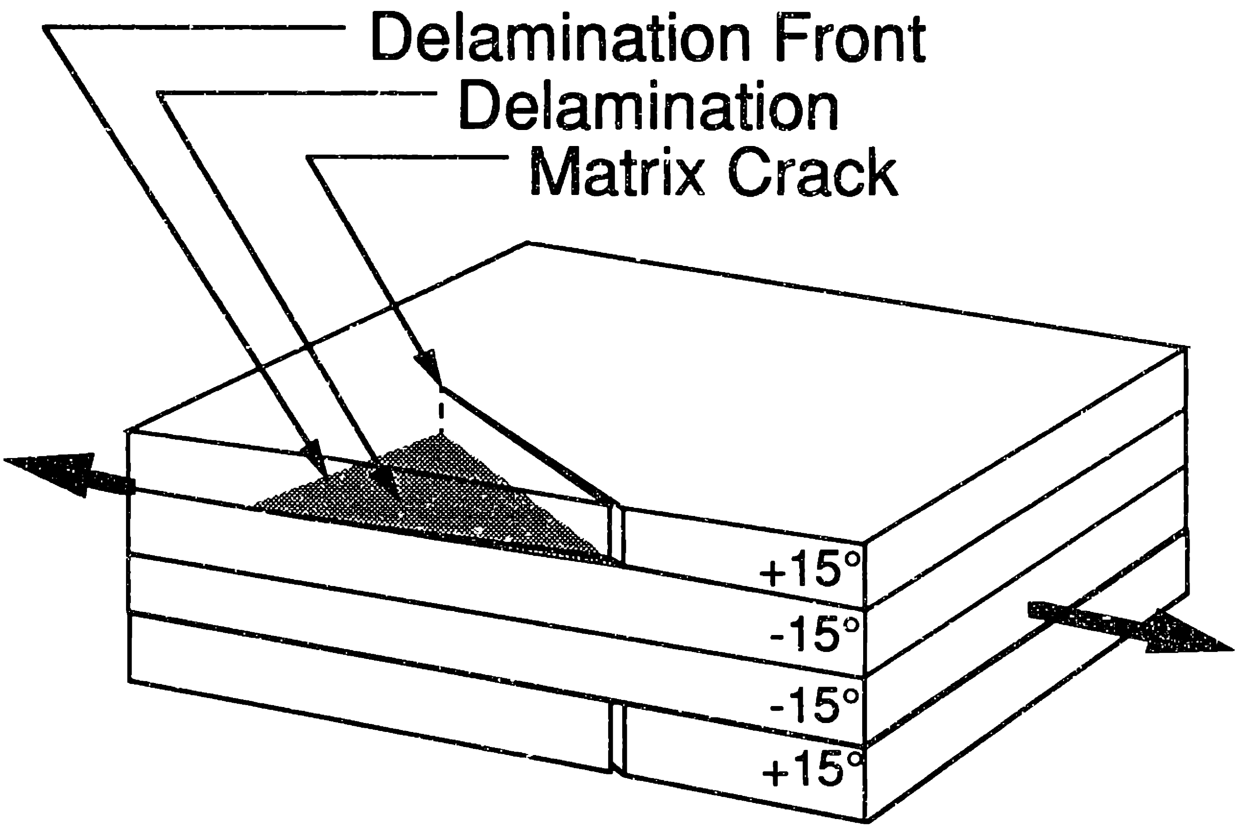

Figure 3.6 Model of the delamination and matrix crack adopted for the current study approximating the delamination front and the matrix crack front and profiles as straight lines.

3.2.1 Experimental Study

The objective of the experimental study is to examine the growth of the damage state from the initial assumed configuration, shown in Figure 3.4, to that observed naturally. This includes the examination of the relative growth tendencies of the triangular delamination and the matrix crack bordering it. The local behavior of the matrix crack tip and the delamination front are monitored for changes in local strains via strain gages placed strategically on the specimen.

The laminates adopted for the current study are made from AS4/3501-6 graphite/epoxy. The layups chosen are $[\pm 15_2]_s$ and $[\pm 15_n/0_n]_s$ with n equal to 2, 3, 5. These laminates are chosen because virgin specimens of $[\pm 15_n/0_n]_s$ and $[\pm 15_3]_s$ have been tested earlier [6]. The naturally occurring delaminations at different stages of the growth process in these specimens have been documented and therefore these specimens will be used to study the growth behavior of artificially-created delaminations which resemble the initial configuration chosen for the present study. The virgin specimens of the $[\pm 15_2]_s$ layup are not available from earlier tests . These have therefore been tested in the current study. Furthermore, the $[0_n/\pm 15_n]_s$ laminates were not chosen because the intact 0° plies on the surface make it difficult to monitor the internal damage. Additionally, the frictional effect between the intact outer plies and the delaminated internal plies introduces another uncertainty in the interpretation of the experimental results and in the analysis of this configuration.

In order to simulate the occurrence of the delamination and associated matrix crack, the $[\pm 15_2]_s$ and $[\pm 15_n/0_n]_s$ laminates were implanted with teflon pieces during the layup of the laminate and then cured. The manner in which the teflon pieces were placed before the curing of the specimens is shown in Figure 3.7. The presence of the teflon piece prevents the bonding of the plies, or regions of plies, in contact with the teflon. When cured, the teflon piece can be removed and it leaves behind a simulated triangular-shaped compound delamination. The resulting laminate conforms to the initial configuration discussed earlier and shown in Figure 3.4.

The naturally occurring delaminations are seen to be quite small in the case of the $[\pm15_3]_s$ laminate, as shown in the radiograph in Figure 3.8. However, implanting of such small delaminations, as well as the monitoring of the growth of such delaminations via radiographs or strain gages, is extremely difficult. Therefore, 10 mm intrusions were utilized in all $[\pm15_2]_s$ and $[\pm15_n/0_n]_s$ laminates that were implanted. The delamination may be conceptually divided into three regions: A, B and C as shown in Figure 3.9. Regions A and C are boundary layer regions affected by the free edge and the matrix crack, respectively, and any steep gradients in stresses, strains, energy release rates etc. manifest themselves in these regions. Region B basically does not have any gradients along the delamination front. Thus, enlarging the delamination size does not significantly affect regions A and C, but has the effect of enlarging region B. However the stresses in this region are virtually unaffected. Therefore, even though the dimensions of the delaminations that are implanted within the laminate are different from those that occur naturally, it includes all the important regions of interest and must behave in a manner similar to that occurring naturally.

Strain gages were placed along the delamination front and along the matrix crack tip to monitor any change in strain in the local region due to the propagation of either the delamination or the matrix crack. A typical coupon specimen with the implanted delamination and the strain gages is illustrated in Figure 3.10. The manufacturing and testing procedures for these specimens is discussed further in Chapter five. Radiographs of the specimens are also taken

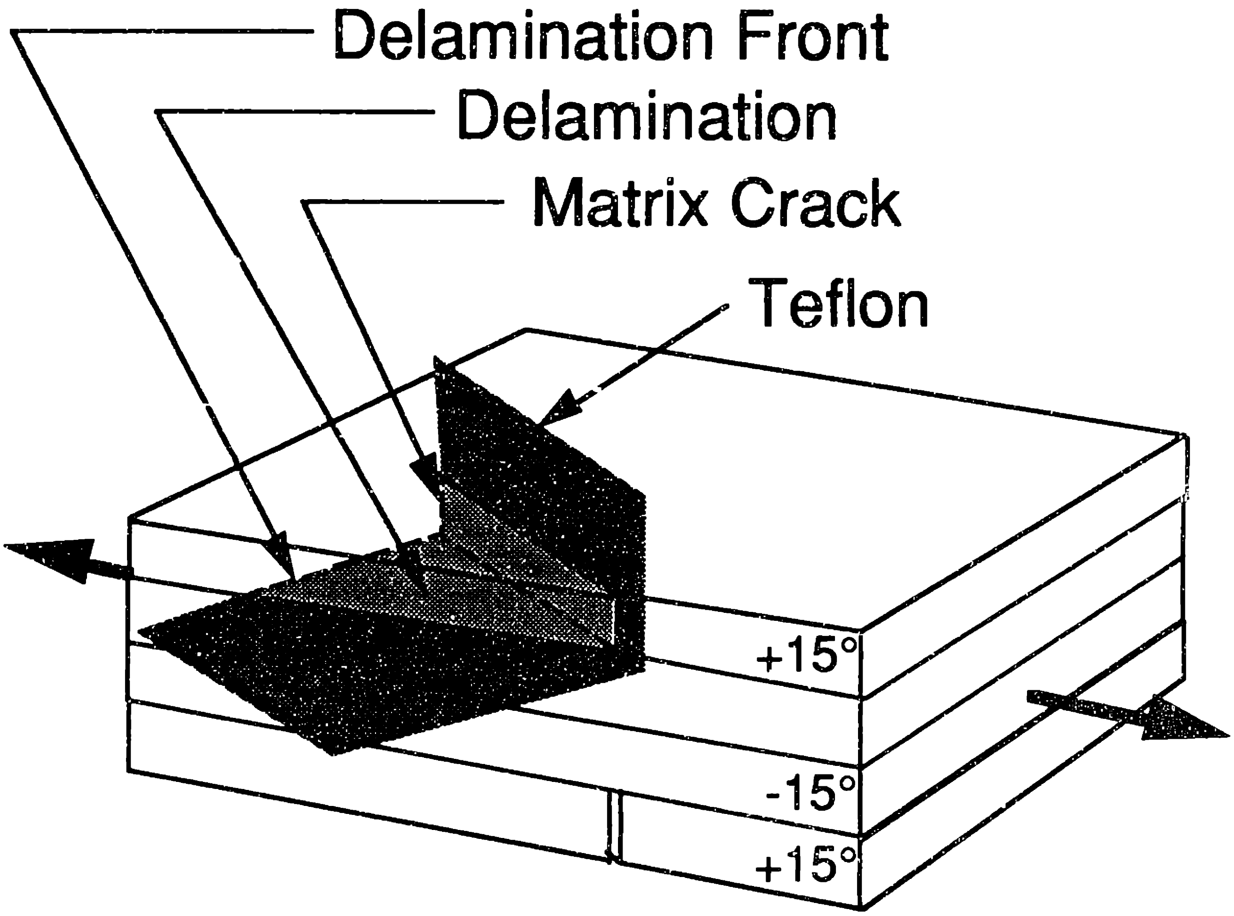

Figure 3.7 Placement of teflon piece before curing of the laminate to simulate delamination and matrix crack.

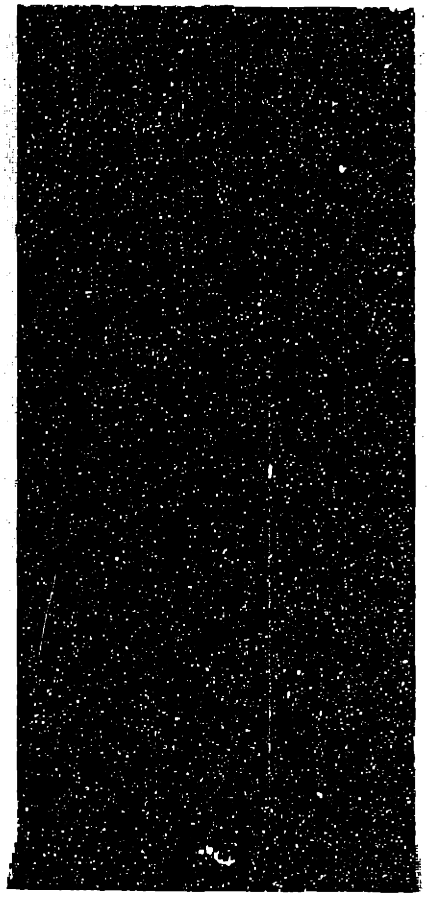

Figure 3.8 Radiograph of triangular-shaped compound delaminations in $[\pm15_3]_s$ laminate [6].

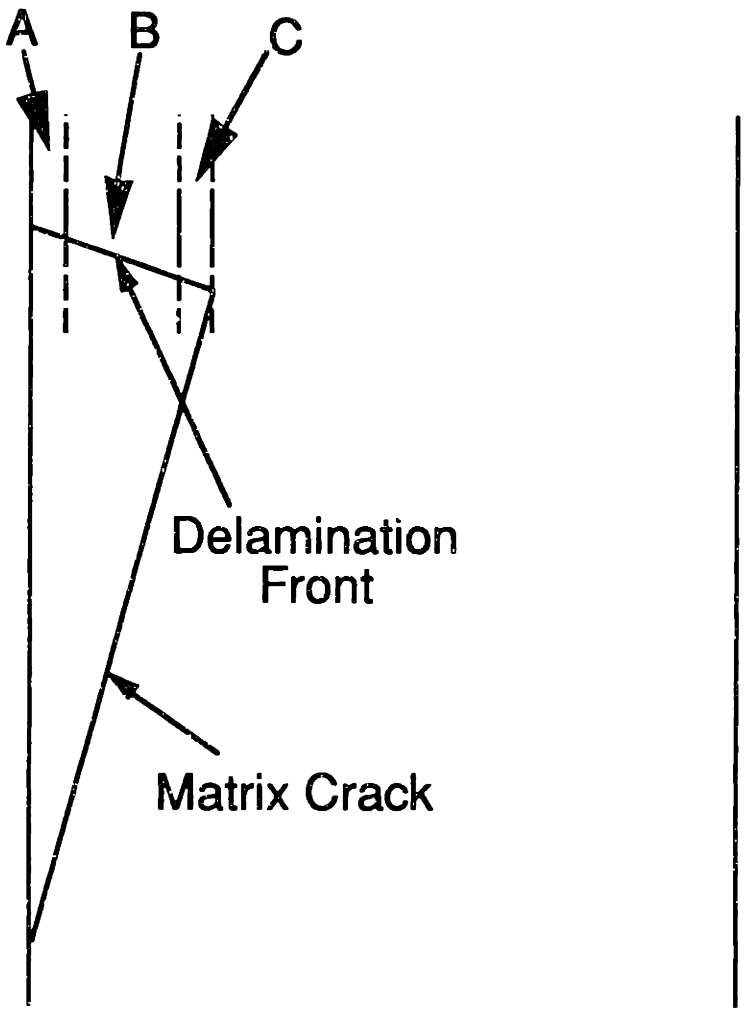

Figure 3.9 Illustration of three regions A, B and C, spanned by the delamination front representing respectively the boundary layer region at the free edge, the intermediate region and the boundary layer region at the matrix crack.

at predetermined load levels to monitor changes in the implanted damage.

The strain data obtained from the gages located at the delamination front and the matrix crack front was used to find changes in the local strain due to the propagation of the respective crack fronts. It is expected that any such changes would register as kinks or distortions in the strain data. This strain data is used to further support the radiographic evidence in determining whether one damage front has a preference to grow over the other.

In summary, the experimental data collected from radiographic examination and from the strain gages should help to resolve the issue of whether the growth of the delamination is possible from the initial configuration. In the event that this growth occurs, the relative importance of the delamination front (or regions along the delamination front) to that of the matrix crack will be identified. Such growth data would also help to establish the tendency of the delamination to grow into the naturally observed configuration, identifying that this is a possible mechanism by which the delamination grew into the naturally observed state.

3.2.1 Analytical Study

The objective of the analytical portion of the study is to determine regions where growth is likely to occur from the initial configuration, and the mechanisms by which this occurs. A fracture mechanics approach is adopted and strain energy release rates along the delamination and matrix crack fronts are used to measure the ability to grow, as discussed in Chapter two. A complete model of the compound delamination requires the modelling of the delamination crack front as well as the matrix crack tip. Since this requires a three-dimensional modelling, three-dimensional finite elements are used in the current study to capture the details of interest.

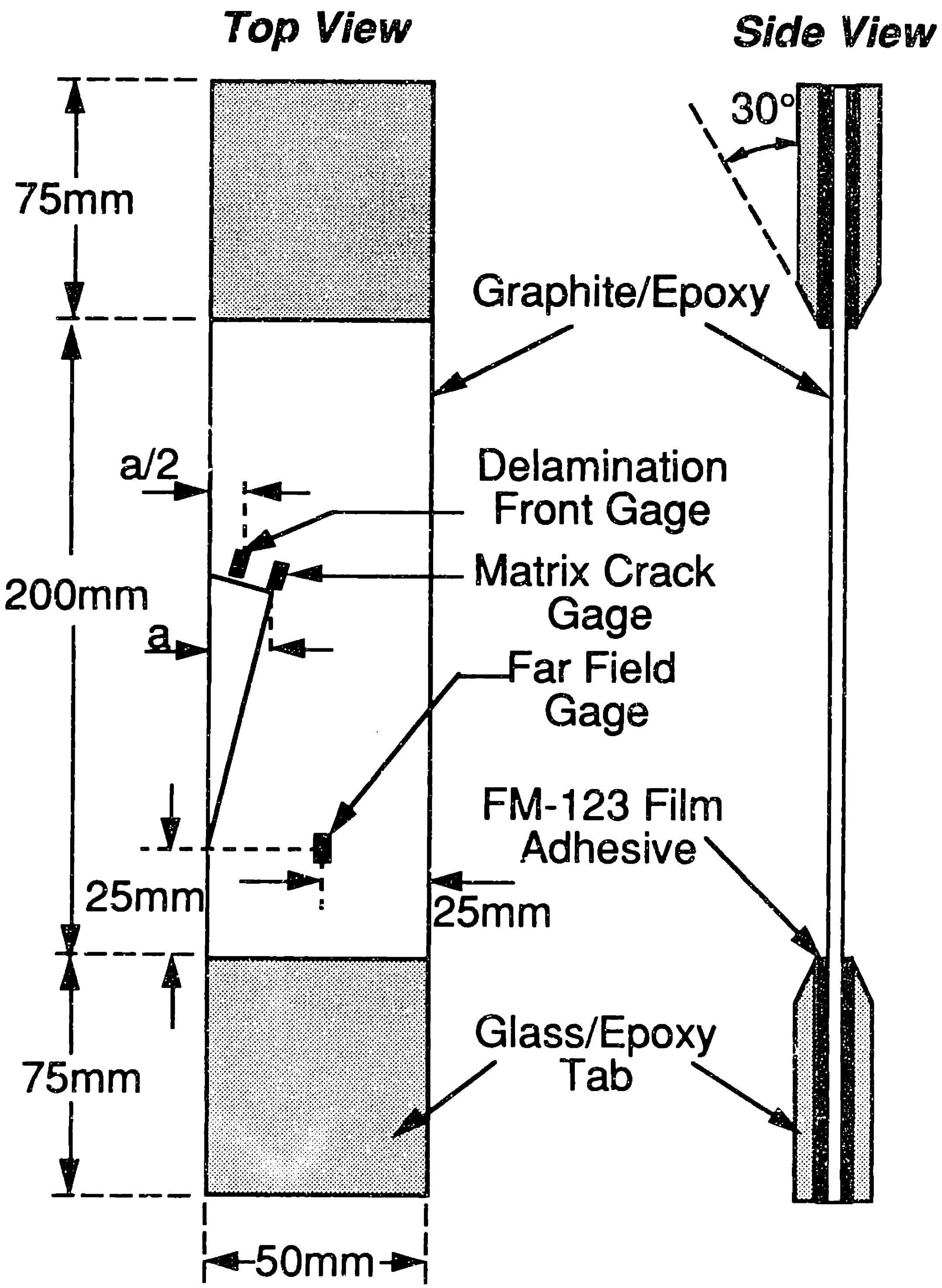

Figure 3.10 Illustration of typical implanted coupon specimen with strain gages at the delamination front, matrix crack front and far-field.

The analytical study starts from the initial configuration shown in Figure 3.4. The strain energy release rate is evaluated along the delamination front and the matrix crack front using the Equivalent Domain Integral. The individual components of the strain energy release rate are obtained from the decomposition method. The limitations of using the decomposition method for delamination problems are discussed later in this section. The crack front with the highest strain energy release rate is expected to grow in preference over regions of lower strain energy. Such growth could result in a curved crack front. However, in the present study such a crack front is approximated by a straight line for ease of computation. The initial configuration of the delamination front is taken to be 90° to the matrix crack as shown in Figure 3.4. Subsequent orientations are taken at 105° and 120° as a simulation of the process of growth of the delamination into the naturally observed configuration. The changes in the strain energy release rate and its components at different orientations of the delamination would also provide insight into the mechanisms responsible for causing a stable configuration. These parameters are also evaluated along the matrix crack front for the different delamination orientations. This helps to determine whether the matrix crack front has an increasing tendency to grow with the changes in the delamination front.

An attempt is also made to examine the tendencies of the delamination to excite secondary damage in neighboring plies. The experimentally observed secondary cracking has been seen to occur in the intact plies neighboring the delamination. Hence, all the components of the in-plane stresses in the neighborhood of the delamination are examined to assess the change in the stress state due to changes in the orientation of the delamination. The initiation of the secondary matrix crack could have occurred from any location in the neighborhood of the delamination. Since no experimental evidence is available to suggest the actual region of origin of these cracks, the stresses are examined at the free edge region where the effects of the change in delamination orientation can be conveniently observed. It is expected that an increase in the stresses in this area may accompany the changing delamination orientation, making this region more prone to secondary matrix cracking.

The $[\pm15_2]_s$ laminate is chosen for the finite element model. The symmetry observed in the delamination pattern along with the smaller number of plies make it an attractive choice for the analysis. The detailed reasons for this laminate choice are described in section 4.1. The delamination in these laminates is located at the +15°/-15° interface and the strain energy release rate along the delamination front is generally mixed-mode in nature. The variation of the total strain energy release rate and the individual modes along the delamination front both need to be evaluated, to determine any change in the total strain energy release rate or its mode mixity as the delamination grows and changes its orientation from the initial assumed configuration.

Since the delamination is a crack at the interface of two different anisotropic materials, there does not exist a unique definition of the 'modes' as discussed earlier in section 2.2.2. The stresses at the tip of the delamination crack exhibit an oscillatory singularity in addition to the square root singularity seen in isotropic materials. The magnitude of this oscillatory singularity determines the extent of coupling at the delamination tip between the various stresses. As a consequence of this coupling between stresses, there is no unique single parameter which controls the behavior of each individual stress, and hence there is no unique definition for the modes. However, to provide an understanding of the delamination behavior, two methods have been adopted to separate the modes in the present study. The first is known as the decomposition method and the second is known as the crack opening displacement approach.

The decomposition method is conventionally used in isotropic materials. It ignores the presence of the oscillatory singularity, and separates the modes by breaking the stresses, strains and displacement near the crack tip region into symmetric and antisymmetric components. Using the analogy of isotropic materials, the symmetric components are considered to provide the crack opening modes (mode I) and the antisymmetric components are considered to provide the shearing (mode II) and tearing (mode III) modes.

The crack opening displacement approach, which has been developed in this study, does not ignore the presence of the oscillatory singularity. The crack opening displacements behind the crack front are used to compute the stress intensity factors and these are then used to obtain the stress state ahead of the crack tip [40]. The ratio of the normal stresses to the in-plane shear stresses ahead of the crack tip is taken to be the mode ratios (mode I to mode II) and the ratio of the normal stresses to the out-of-plane shear is taken to be the other mode ratio (mode I to mode III). The presence of the oscillatory singularity causes these ratios to be different at different distances ahead of the crack tip. Hence, a distance ahead of the crack tip must be chosen to determine these ratios. However, the crack opening displacement approach may also be used by approximating the oscillatory singularity to zero. In this case, the modal ratios obtained are independent of the distance ahead of the crack tip. This process of ignoring the oscillatory singularity is an approximation that is valid in cases where the oscillatory singularity is small. The current study uses the crack opening displacement approach both by utilizing the oscillatory singularity as well as by assuming it to be zero. This provides a new perspective on the separation of modes ahead of the delamination front.

A theoretical solution exists for the global energy released in a free edge delamination. Hence, the case of a simple delamination at the free edge in a $[0_2/90_2]_s$ laminate is studied using both the decomposition approach and the crack opening displacement approach and the results from the two methods are compared to theory. This example is also used to examine the differences between the modes of strain energy release rate predicted from different approaches. However, no theoretical values of modes exist for comparison.

Since the previous problem involves only orthotropic plies, another more general laminate, $[\pm75_2]_s$ was chosen for a similar study, to compare the results obtained by the two approaches. In this case, no theoretical results exist for either the total energy release rates or the individual modes and hence this serves as a check of consistency between the various approaches, rather than a validification of the approaches themselves.

In summary, the analytical study provides information regarding the changes in the total strain energy release rate of crack fronts with differing orientations. It also provides the individual modes and the changes observed for different orientations of the crack. This should provide insights into the mechanisms responsible for causing the stable configuration of the delamination during its growth. The strain energy release rate at the delamination front may be compared to that at the matrix crack front to determine which may be responsible for the growth to failure. A method known as the crack opening displacement approach is developed to enable a new method for mode separation in delamination problems with the option of either utilizing or neglecting the oscillatory singularity.

The experimental study and the analytical study are together aimed at resolving the issues posed in section 3.2. Both these studies start with the same initial configuration for the triangular-shaped delamination. The analysis provides a numerical estimate of the parameters controlling the growth of such initial delamination configurations and also provides insight into possible mechanisms by which any such growth is likely to occur. The experiments are expected to provide a qualitative validation of these analytical results with radiographs of any actual growth from the initial delamination configuration. The analysis also compares the energy release rate at the delamination and the matrix crack fronts to determine the relative importance of these two crack fronts. Strain gages are utilized in the experiments to monitor the growth of the delamination and the matrix crack and determine which of the two propagates first from the initial configuration. Though no quantitative estimates of the growth are obtained, the experiments will help to determine if growth does actually occur where it is predicted to occur.

CHAPTER 4

ANALYSIS METHODOLOGY

The details of the different analysis methods used to evaluate the strain energy release rate are examined in this chapter along with the finite element modelling procedure adopted for the compound delamination. In order to validate the programs that were developed for the analysis, a verification problem has been solved.

4.1 Finite Element Model of the Compound Delamination

The triangular compound delamination is analyzed with the aid of the finite element method using the software ADINA® (Automatic Dynamic Incremental Nonlinear Analysis) [72]. This software has a pre-processor, called ADINA-IN®, which was used to create the mesh. However, since this pre-processor produces several groups of elements and joins them together, some programs had to be written by the author to check whether different regions had been appropriately connected to each other. A three-dimensional model of the laminate was made using 20-noded isoparametric brick elements, shown in Figure 4.1 with three displacement degrees of freedom per node. The degrees of freedom are extensional displacement along the x, y and z directions designated as u_1, u_2 and u_3. These elements have been used extensively in previous models of composite laminates [37, 73, 74]. The model consisted of 5100 elements and had about 65,000 degrees of freedom.

The laminate analyzed was the $[\pm15_2]_s$ laminate with an effective ply thickness of 0.268 mm. Only one quarter of the laminate was modelled implying

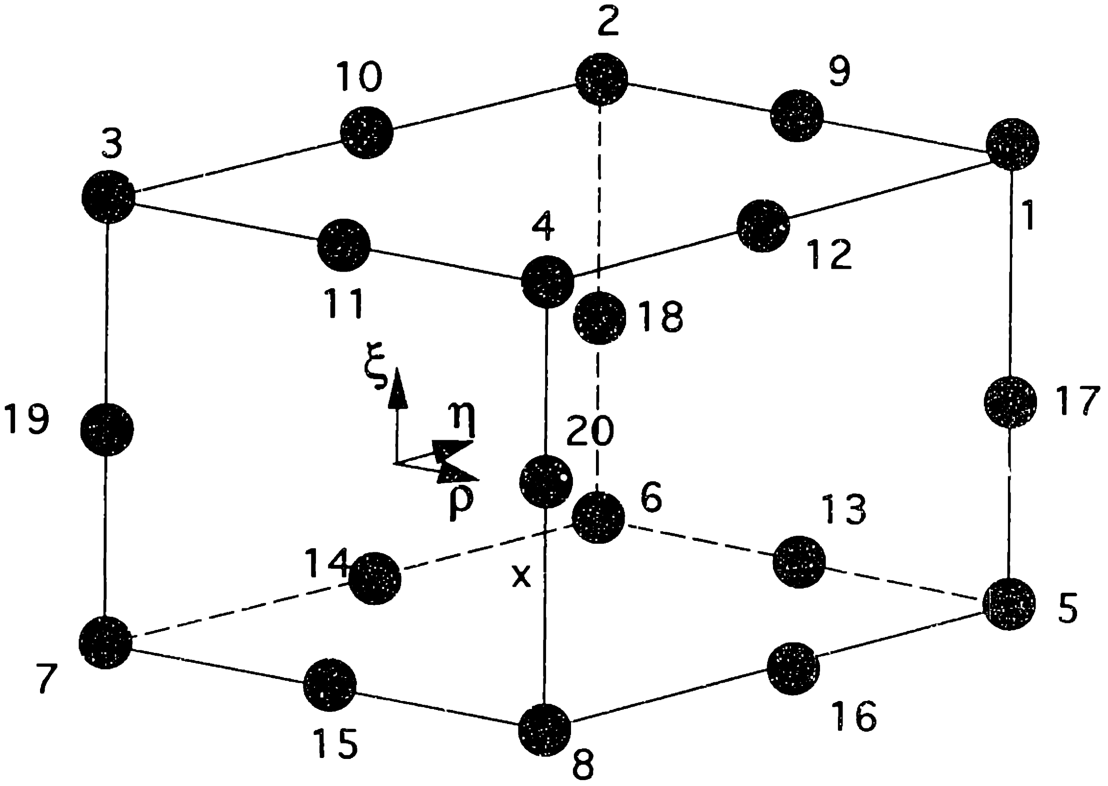

Figure 4.1 Twenty-noded isoparametric brick element, with three degrees of freedom per node, used in the finite element analysis.

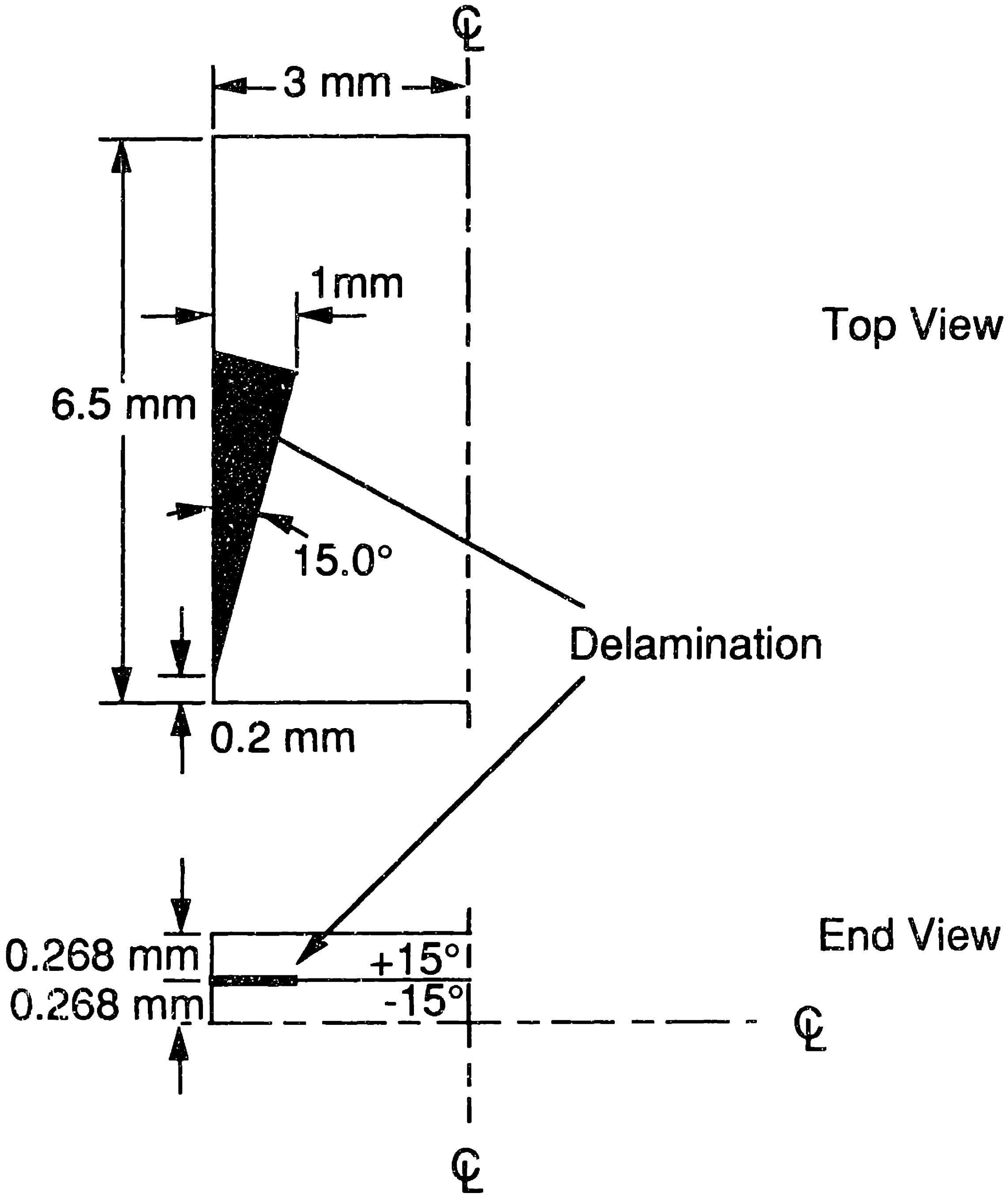

Figure 4.2 Dimensions of the quarter model of the triangular-shaped compound delamination in a $[\pm 15_2]_s$ laminate used in the finite element analysis.

the presence of four symmetrically located triangular compound delaminations at the +15/-15 interfaces, as shown in Figure 4.2 along with the dimensions of the model. Since the distribution of the strain energy release rate was needed along the delamination front as well as along the matrix crack front, the mesh was refined locally in these regions. There are twenty elements along the delamination front and six elements along the matrix crack front within the +15° ply. These six elements through the thickness of the +15° ply were local to the region around the matrix crack tip and were gradually reduced in number at regions away from the crack tip to one element through the thickness at the outer boundaries of the model. This was done in order to reduce the elements in the far-field regions where the stress gradients are not steep and the stresses approach classical laminated plate theory values. The -15° ply has only four elements through the thickness, since no matrix cracks are assumed to exist within this ply and these elements were reduced to a single element through the thickness at the outer boundaries in the same manner as the meshing in the +15° ply. In order to obtain accurate results with finite elements in regions of steep stress gradients, the aspect ratio of the elements must be less than approximately four or five. In the model, the aspect ratio of the elements was preserved to within these limits in regions near the delamination and matrix crack front where steep stress gradients were expected. The aspect ratios were relaxed to ten or larger in regions with insignificant gradients.

The smallest elements are in the ring around the crack tip where the brick elements are 0.01mm by 0.01mm normal to the crack and are of various widths along the crack front ranging from refined at the free edges and near the matrix crack front with aspect ratios of about unity, to slightly coarser in the middle of the delamination front with aspect ratios of about two or three, as seen from the mesh in Figure 4.3. The loading on the laminate is imposed in the form of a

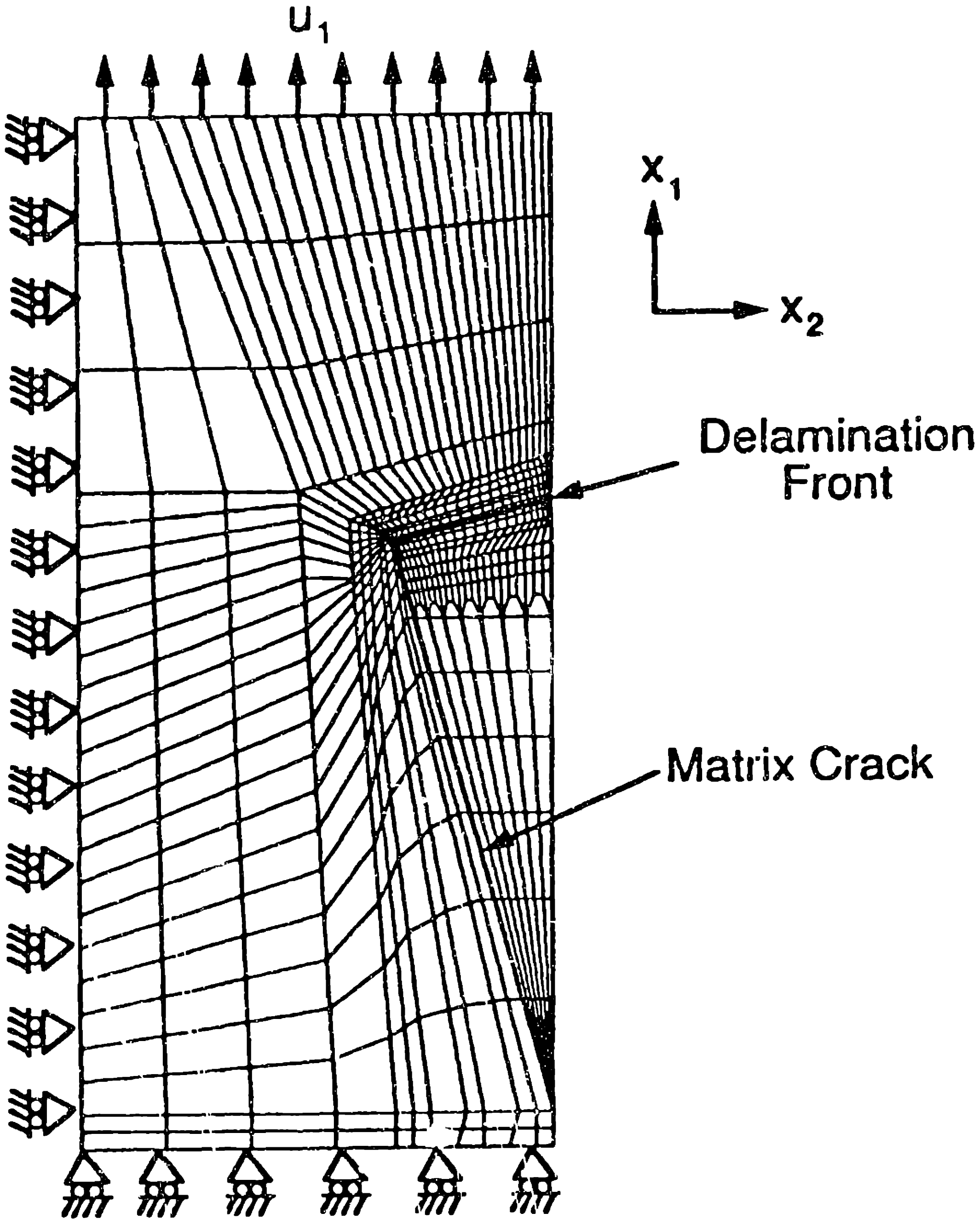

Figure 4.3 Planar representation of the mesh used in the analysis of a $[\pm 15_2]_s$ laminate with applied loading and boundary conditions.

uniform displacement along the top surface. Boundary conditions consistent with symmetry assumptions mentioned earlier are also imposed on the model as shown in Figure 4.3. The location of the delamination and the matrix crack front are shown in the three-dimensional outline drawing of the finite element model in Figure 4.4.

Three different orientations of the delamination front are examined relative to the matrix crack and these are shown in Figure 4.5 along with dimensions of the model and the size of the intrusion. The intrusion of the delamination in the finite element model was chosen to be 1 mm. This distance is greater than three effective ply thicknesses away from the free edge. Thus, the delamination spanned the region from the free edge with highly gradient interlaminar stresses to areas outside the boundary layer where the interlaminar stresses are negligibly small. The delaminations observed to occur naturally in these class of laminates are about 3 to 4 mm wide. Modelling of such large delamination fronts would require the model to have a much larger size in-plane, but would not change dimensions out-of-plane. Therefore, this would require a significant increase in the number of elements but would not provide any additional information since the delamination spans the same three important regions shown in Figure 3.9. Region A is affected by free edge interlaminar stresses, region C is affected by the presence of the matrix crack and region B is the intermediate region. On increasing the delamination intrusion, regions A and C, which are 'boundary layer' regions, do not change significantly. Hence, only the size of region B increases. Since the crack tip parameters are relatively uniform in region B, increasing its size does not provide any additional information regarding the delamination front. Therefore, the delamination was restricted to a smaller size in the currrent model.

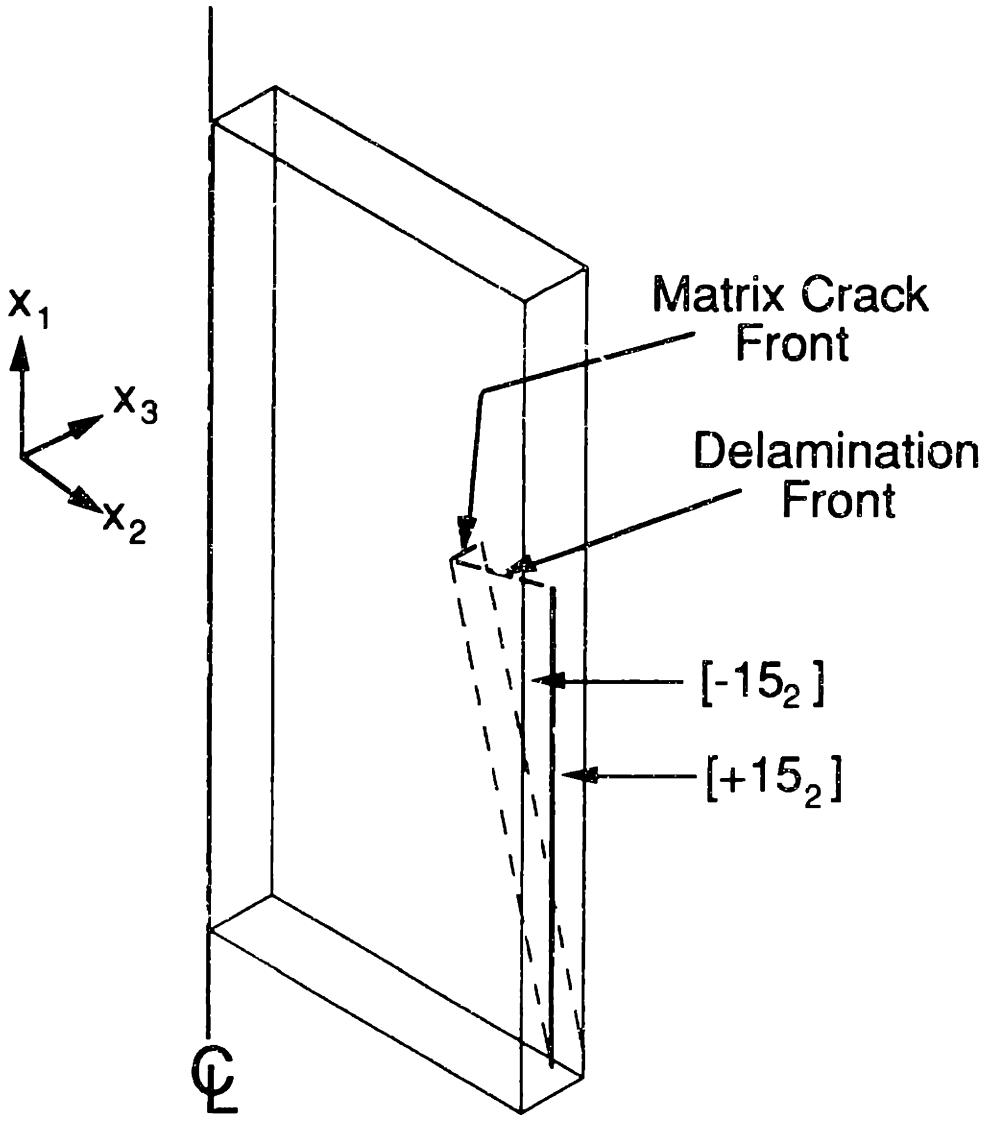

Figure 4.4 Outline of the finite element model indicating the location of the delamination and the matrix crack.

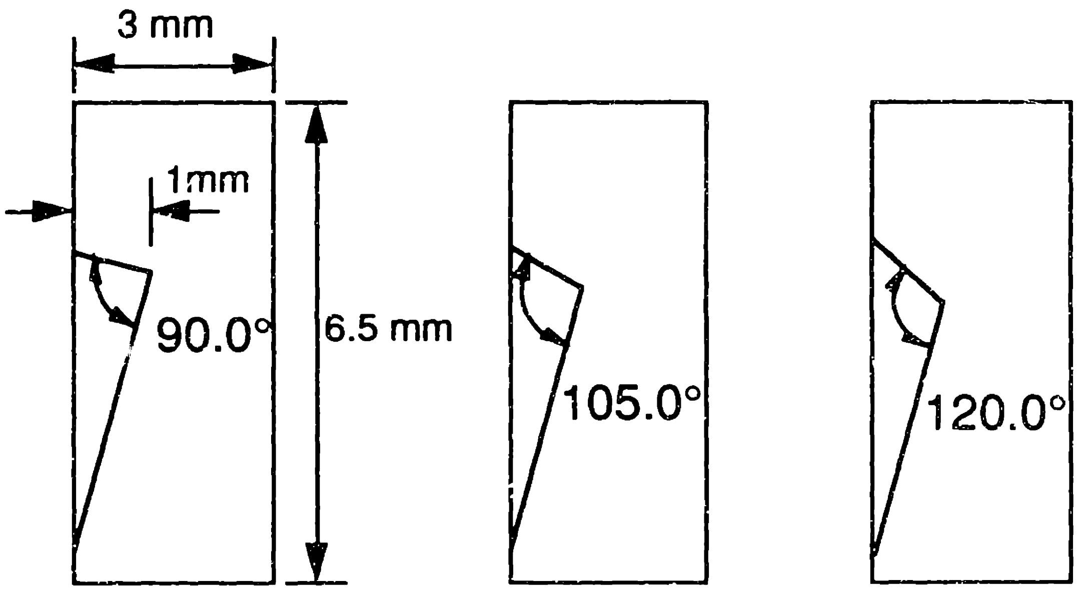

Figure 4.5 Three cases modelled using the finite element model with differing orientation of the delamination front relative to the matrix crack: (*left*) 90°, (*center*) 105°, and (*right*) 120°.

The meshing at the delamination and the matrix crack front is critical, since the stresses in these regions are singular and hence have steep gradients. Quarter-point singular elements have typically been used at the crack front to model the $1/\sqrt{r}$ singularity [45]. In the case of the delamination front, there exists both the $1/\sqrt{r}$ singularity and an additional oscillatory singularity. These singular elements cannot, however, capture the oscillatory part of the singularity.

There are two mesh choices available along the crackfronts: the crack front could be surrounded by a square ring of four brick elements or by a circular ring consisting of several prism-shaped elements (brick elements with one side collapsed) as shown in Figure 4.6. The ring of prism-shaped elements is advantageous in terms of the increased element concentration at the crack front. It has also been shown that this type of element has a $1/\sqrt{r}$ singularity throughout the element and hence efficiently models the stresses around the crack tip. However, the compound delamination problem involves the intersection of two cracks and requires that the ring of elements around the delamination front be able to merge into the ring of elements around the delamination front. If prism-shaped elements are used, then the mesh is geometrically incompatible at regions of crack intersection. To avoid this problem, the configuration of four brick elements at the crack tip has been used in the current analysis.

The brick element has two disadvangtages in this case. One, the number of crack tip elements are restricted to four, hence a dense mesh in the immediate vicinity of the crack front is not possible. Two, the quarter-point brick element has a $1/\sqrt{r}$ singularity not within the entire element, as in the case of the collapsed brick element, but only in the vicinity of the crack front [45]. However, the intersection of cracks does not present a problem in this case as is shown by

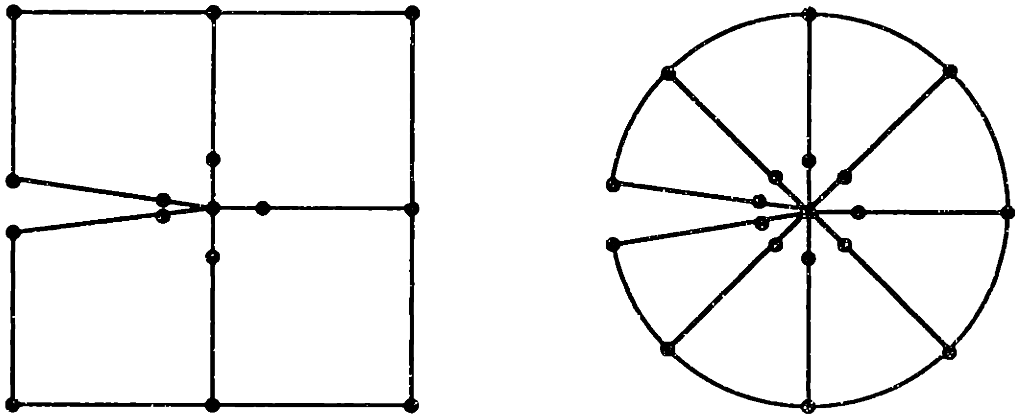

Figure 4.6 Illustration of two possible meshes around the crack front: (*left*) a square ring of four brick elements and (*right*) a circular ring of prism-shaped elements.

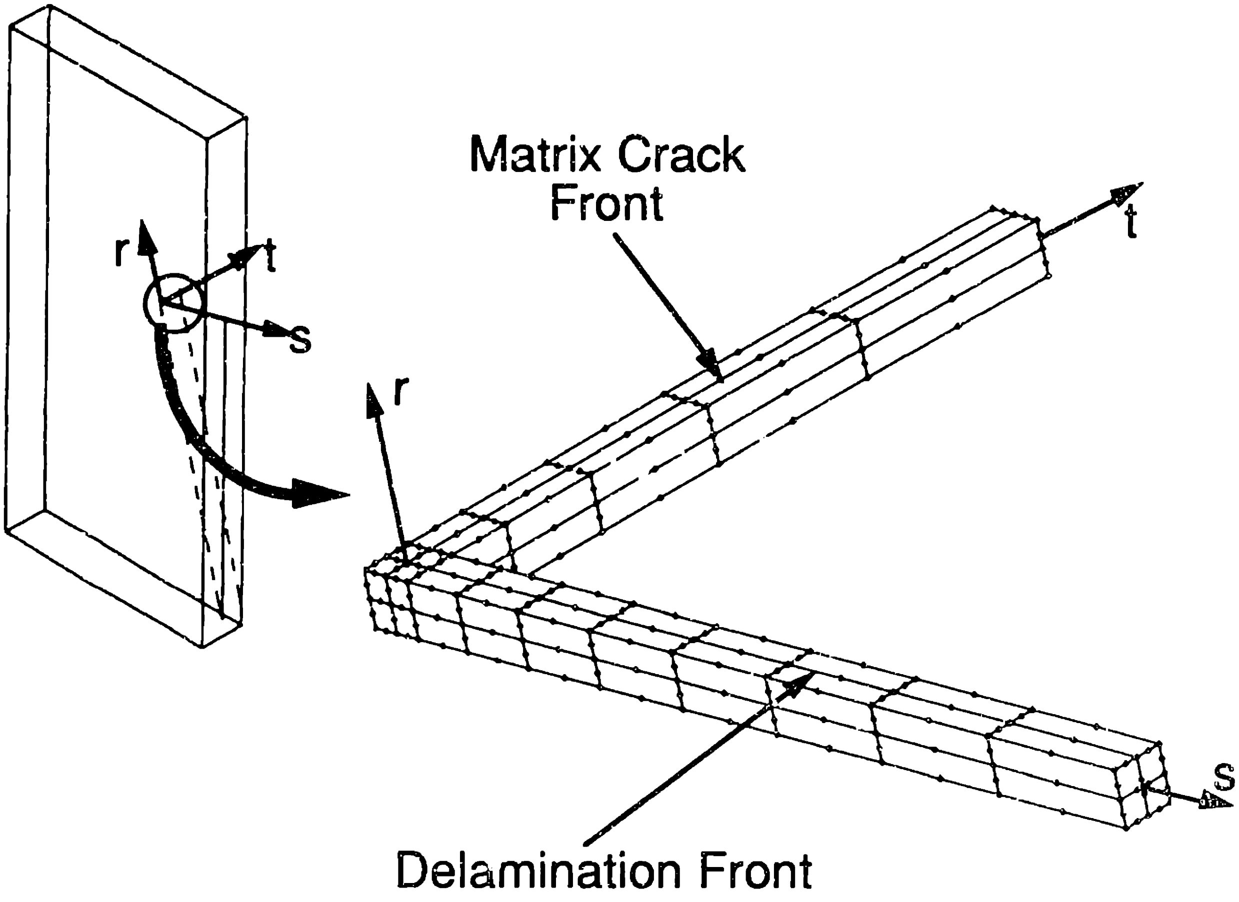

Figure 4.7 Compatible intersection of the rings of elements along the delamination front and along the matrix crack front (r-s-t are local coordinates to help identify the orientation of the mesh).

their geometric compatibility in Figure 4.7. A local coordinate system (r,s,t) has been defined in Figure 4.7 to help identify the orientation of the crack tip rings within the model. In this figure, the mesh along the delamination front has been terminated after a few elements for convenience of presentation. The ring consists of four brick-shaped elements which surround the mesh. In the endview (along either the s- or t-axis) these rings would appear like the ring of brick elements shown in Figure 4.6. The symmetry of the mesh around the crack tip allows convenient application of the decomposition method, which demands mesh symmetry to separate the modes.

The model was executed on the CRAY-YMP at the MIT Supercomputer facility. A typical run requires about three hours of CPU time. The post-processing was done with the ADINA-PLOT post-processor and also with some programs written by the author to isolate the stresses, strains and displacements at the crack front. A program was also developed to use the equivalent domain integral technique to obtain the strain energy release rate around the crack front. The equivalent domain intergral along with the decomposition technique used to separate the modes are briefly described in the next section.

4.2 Techniques for Evaluating Strain Energy Release Rate

Two methods for evaluating the strain energy release rate are described here. The first is based on the J-integral technique and is called the equivalent domain integral. It is the method which is used in association with a decompostion technique to obtain the total energy release rate and the individual energy release rates in isotropic material. The second method is based on the crack opening displacement behind the crack tip which is used to obtain the stress intensity factors. These are then used to obtain the strain energy release rates

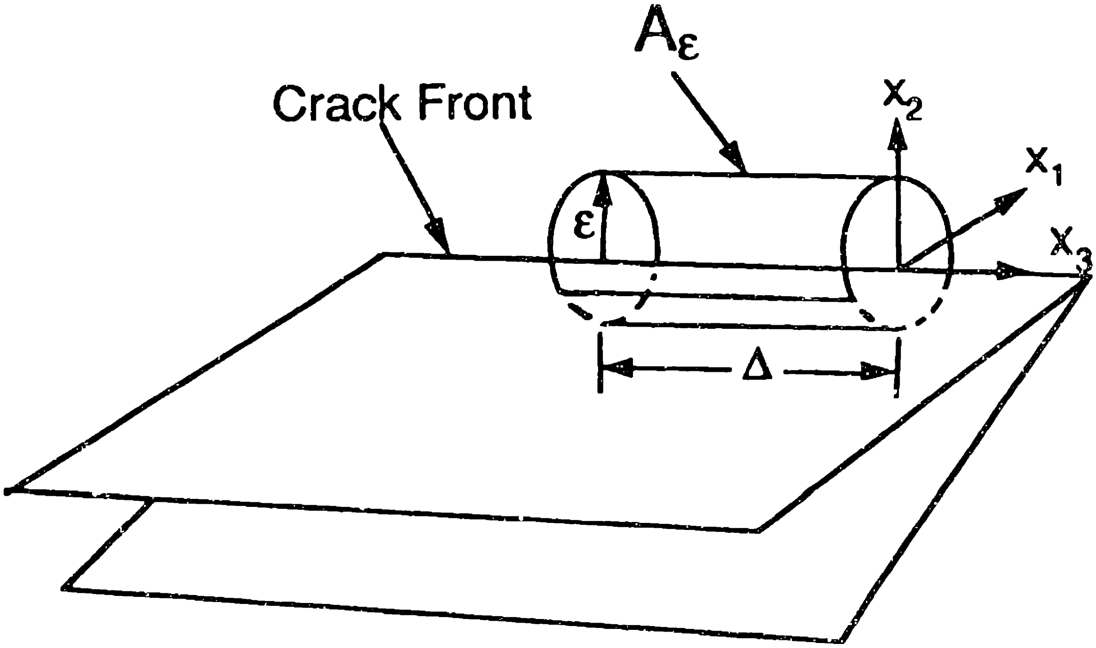

Figure 4.8 Illustration of the coordinate system adopted for the evaluation of the J-Integral along the crack front, along with the surface on which it is evaluated.

and the individual modes. The coordinates x_1, x_2 and x_3 are defined locally at the crack (or delamination) front, as shown in Figure 4.8. The x_3-axis is located along the crack front, and the x_2 and x_1-axes are located such that they measure the crack opening and shearing distances along them respectively. These coordinates are used in the evaluation of the crack tip parameters.

4.2.1 Equivalent Domain Integral (EDI)

The J-Integral, as originally formulated in two-dimensions, is a path-independent integral around the crack tip. The strain energy density and work done by tractions on any path around the crack tip are used to obtain a crack tip parameter, J. This parameter J is equal to the strain energy release rate, G, in the case of linear elastic bodies. The J-integral is convenient for crack tip analysis in two dimensions because it requires only a line integral. However, in three-dimensional problems, it requires the evaluation of a surface integral. Evaluation of surface integrals requires the evaluation of normals to the surface and hence are computationally quite difficult and unwieldy. Therefore, alternate forms of this integral have been proposed for ease of computation. In references [47, 49, 50], the J-integral has been modified into a volume integral, also known as a domain integral, through the use of the divergence theorem and hence the name Equivalent Domain Integral (EDI). The EDI formulation is computationally very efficient compared to the J-integral formulation. It is also much preferred over the virtual crack extension technique since it does not require the crack to be incremented in order to evaluate the strain energy release rate.

In the case of two-dimensional problems, the crack tip is represented by a single point where the stresses are singular. Therefore, only one value of strain energy release rate exists at that point. In the case of linear elastic problems, this may be evaluated using the J-Integral as,

$$J = G = \int_{\Gamma_\varepsilon} \left[W n_1 - \sigma_{ij} \frac{\partial u_i}{\partial x_1} n_j \right] d\Gamma \tag{4.1}$$

where Γ_ε is a contour of radius ε around the crack tip, n_1 is the component of the normal in the x_1-direction to the surface Γ_ε and W is the work energy density defined as,

$$W = \int_0^{\varepsilon_{ij}} \sigma_{ij}\, d\varepsilon_{ij} \tag{4.2}$$

In three dimensions, however, there is a crack front as opposed to a point and hence, there is a line singularity along the crack front instead of the point singularity observed in two dimensions. Therefore, in a manner similar to the two-dimensional case where the G was evaluated at the singular point, viz. the crack tip, in the three-dimensional case there is a distribution of strain energy release rate along the crack front. In order to obtain the G distribution along the three-dimensional crack front like the one shown in Figure 4.8, the crack front is broken down into discrete bits of infinitesimal length Δ, in each of which G is evaluated. The three-dimensional J-integral is defined over one such length of the crackfront, Δ in Figure 4.8, as,

$$\int_\Delta G\, dx_3 = \lim_{\Delta \to 0} \left[\lim_{\varepsilon/\Delta \to 0} \int_{A_\varepsilon} \left[W n_1 - \sigma_{ij} \frac{\partial u_i}{\partial x_1} n_j \right] dA \right] \tag{4.3}$$

where A_ε is a surface of radius ε around the crack front, Δ is the small limiting unit of length along the crack front where this surface integral is evaluated, and the remaining parameters have the same definition as in the two-dimensional case in equation (4.1). Equation (4.3) has two limits imposed on it, the first one is on Δ such that, in the limit, a continuous distribution of G may be obtained. The second limit is on the ratio (ε/Δ) and this restriction arises because the crack front presents a line of singularities, while the original definition of the path-independent integral shown in equation (4.1) was for a point singularity. In the case of a line of singularities, there is an additional effect of one singularity on the line affecting the adjacent singularity. In order to reduce the effect of the adjacent singularities on the region of the crack under consideration, a restriction is placed on the radius of the ring ε. Therefore, in three dimensions, the J-Integral is path independent only to a limited extent. Henceforth, these limits on ε and Δ will not explicitly be shown for convienience of presentation.

In order to convert this surface integral into an EDI, the strain energy release rate is assumed to be constant along the small length Δ of the delamination front considered in equation (4.3). Both sides of the equation are multiplied by a shape function, S. This shape function has different values at different nodes. Hence, it multiplies the displacements at these nodes by different values, simulating a virtual displacement in these nodes. This process therefore simulates the virtual crack displacement approach without having to actually open up the crack physically. The rigorous proof of this has been given in [75]. The resulting equation is,

$$G\,f = \int_{A_\varepsilon}\left[Wn_1 - \sigma_{ij}\frac{\partial u_i}{\partial x_1}n_j\right]S\,dA \tag{4.4}$$

where,

$$f = \int_{\Delta} S\,dx_3 \tag{4.5}$$

Another ring, A, larger than A_ε is selected, as shown in Figure 4.9, such that the S-function goes to zero on the outer ring and on the sides of the cylindrical surface with areas A_1 and A_2 shown in Figure 4.9. These conditions may be thought of as the boundary conditions to be satisfied by the S-function. Therefore, this method is similar to other methods in mechanics based on the principle of virtual work, where any virtual displacement satisfying the geometric boundary conditions may be used to obtain solutions to problems.

Since S is identically zero on the area A, equation (4.4) can be rewritten as,

$$G\ f = -\int_{A}\left[Wn_1 - \sigma_{ij}\frac{\partial u_i}{\partial x_1}n_j\right]S\,dA + \int_{A_\varepsilon}\left[Wn_1 - \sigma_{ij}\frac{\partial u_i}{\partial x_1}n_j\right]S\,dA \qquad (4.6)$$

or writing it as a single integral,

$$G\ f = -\int_{A-A_\varepsilon}\left[Wn_1 - \sigma_{ij}\frac{\partial u_i}{\partial x_1}n_j\right]S\,dA \qquad (4.7)$$

This integral is over the surface area, A-A_ε, which encloses the annular volume V-V_ε around the crack front. On application of the divergence theorem [50], equation (4.7) gets converted to a volume integral over the volume V-V_ε and the integral may then be written as,

$$G f = -\int_{V-V_\varepsilon}\left[W\frac{\partial S}{\partial x_1} - \sigma_{ij}\frac{\partial u_i}{\partial x_1}\frac{\partial S}{\partial x_j}\right]dV - \int_{V-V_\varepsilon}\left[\frac{\partial W}{\partial x_1} - \frac{\partial}{\partial x_j}\left(\sigma_{ij}\frac{\partial u_i}{\partial x_1}\right)\right]S\,dV \qquad (4.8)$$

In order to convert equation (4.8) into the equivalent domain integral, some relations that are necessary are the equations of equilibrium without body forces:

$$\frac{\partial \sigma_{ij}}{\partial x_j} = 0 \qquad (4.9)$$

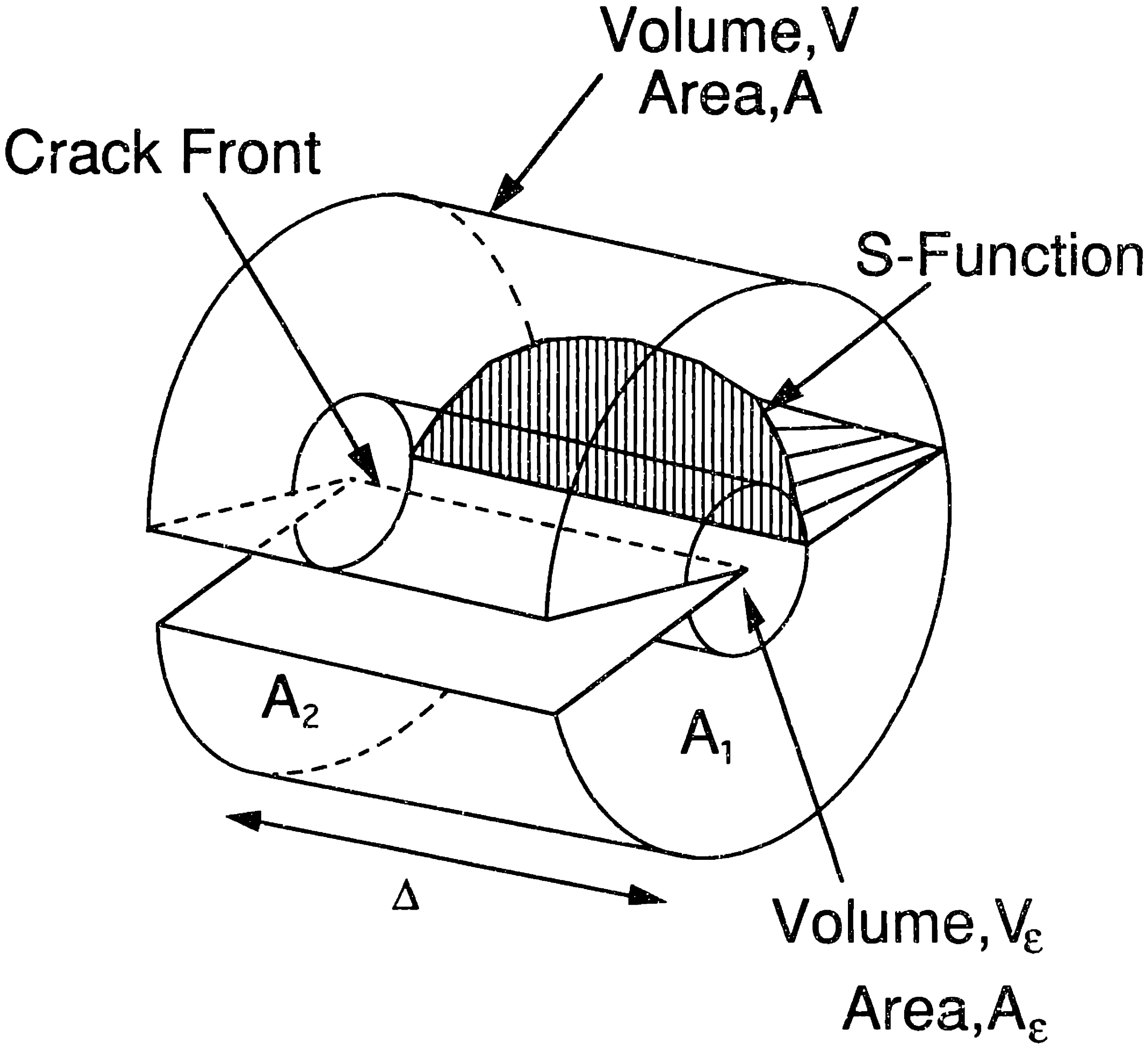

Figure 4.9 Illustration of the annular region used in equivalent domain integral along with a typical S-function used for analysis.

and the definition of stress in terms of the work energy density,

$$\sigma_{ij} = \frac{\partial W}{\partial \varepsilon_{ij}} \tag{4.10}$$

This latter equation is evident from equation (4.2). These relations are then used in the second integral in equation (4.8) to prove that it reduces to zero. The differentials are first evaluated to give:

$$\frac{\partial W}{\partial x_1} - \frac{\partial}{\partial x_j}\left(\sigma_{ij}\frac{\partial u_i}{\partial x_1}\right) = \frac{\partial W}{\partial \varepsilon_{ij}}\frac{\partial \varepsilon_{ij}}{\partial x_1} - \sigma_{ij}\frac{\partial}{\partial x_1}\left(\frac{\partial u_i}{\partial x_j}\right) - \frac{\partial \sigma_{ij}}{\partial x_j}\frac{\partial u_i}{\partial x_1} \tag{4.11}$$

Equation (4.10) is substituted into the first term and the third term of equation (4.11) is zero by comparing it with equation (4.9). The second term may be expressed in terms of strain, thus yielding:

$$\frac{\partial W}{\partial \varepsilon_{ij}}\frac{\partial \varepsilon_{ij}}{\partial x_1} - \sigma_{ij}\frac{\partial}{\partial x_1}\left(\frac{\partial u_i}{\partial x_j}\right) - \frac{\partial \sigma_{ij}}{\partial x_j}\frac{\partial u_i}{\partial x_1} = \sigma_{ij}\frac{\partial \varepsilon_{ij}}{\partial x_1} - \sigma_{ij}\frac{\partial \varepsilon_{ij}}{\partial x_1} = 0 \tag{4.12}$$

This leaves G, from equation (4.8), in terms of a single integral known as the equivalent domain integral (EDI),

$$G = -\frac{1}{f}\int_{V-V_\varepsilon}\left[W\frac{\partial S}{\partial x_1} - \sigma_{ij}\frac{\partial u_i}{\partial x_1}\frac{\partial S}{\partial x_j}\right]dV \tag{4.13}$$

This is the final form of the EDI that has been used in this work for evaluating the strain energy release rate. This integral gives only the total strain energy release rate and has to be used in association with some other method to obtain the individual modes.

In the finite element formulation, the volume V_ε is reduced to zero, implying that the volume $V\text{-}V_\varepsilon$ will consist of all the crack tip elements where equation (4.13) is evaluated. As mentioned earlier, this volume consists of the four elements adjacent to the crack tip and, therefore, the outer surface of the

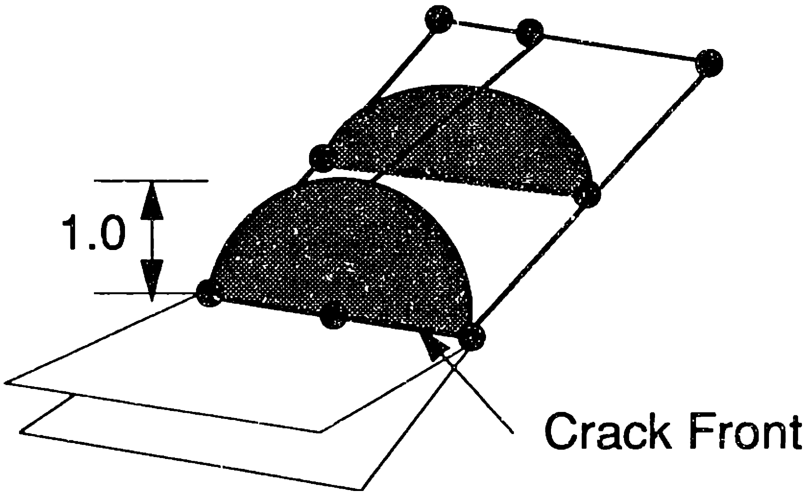

Figure 4.10 Illustration of S-function, used in the analysis, on one of the faces of a typical brick element surrounding the crack front.

cylinder shown in Figure 4.9 is the outer surface of these elements. The length Δ then refers to the width of the ring of elements surrounding the crack front. The shape function used for all calculations was of the form shown in Figure 4.10. It has been shown [47, 50] that there is no significant difference between the various shape functions that may be used as long as they satisfy the boundary conditions mentioned earlier. The S-function chosen for this study is shown relative to the nodes of the crack tip element in Figure 4.9. It has the value of unity at one node along the crack front, and is zero at all other nodes of the element. It was chosen over other shape functions due to its simplicity. The S-function was interpolated using the nodal values and the same interpolation functions as used for the 20-noded brick elements in the finite element model. Thus, the S-function may be expressed in terms of the nodal values as,

$$S = \sum_{i=1}^{20} s_i N_i(\xi, \eta, \zeta) \tag{4.14}$$

where ξ, η and ζ are the isoparameteric coordinates used in the shape functions for the 20-noded brick element.

The EDI in equation (4.13) is evaluated using the FORTRAN-77 program given in Appendix A. The details followed in the programming procedure are those given in references [47, 50] which have been used here without changes.

4.2.2 Decomposition Method

This method is used in association with the equivalent domain integral, EDI, to separate the individual modes from the total strain energy release rate, G. The decomposition method splits the stress, strain and displacement data, in the volume around the crack front, into symmetric and antisymmetric components which are used in the EDI to obtain the individual modes.

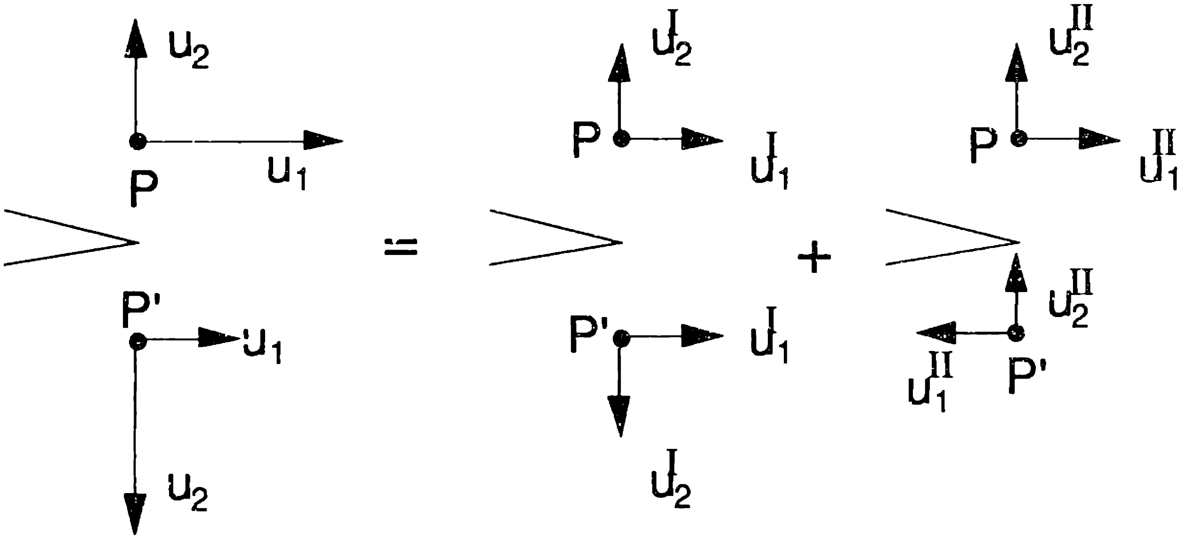

Figure 4.11 Two-dimensional illustration of the decomposition technique for the displacements using two symmetric points, P and P', relative to the crack front.

The method involves the use of data at symmetric points above and below the crack front, necessitating a symmetric mesh in that region. The displacement data at two symmetric points, shown as P and P' in Figure 4.11, may be manipulated to split them into three components. For simplicity, these are shown in Figure 4.11 for a two-dimensional case. In three dimensions, the components are as follows:

$$\begin{aligned}\{u\} &= \{u^{I}\} + \{u^{II}\} + \{u^{III}\} \\ &= \frac{1}{2}\begin{Bmatrix} u_{1P} + u_{1P'} \\ u_{2P} - u_{2P'} \\ u_{3P} + u_{3P'} \end{Bmatrix} + \frac{1}{2}\begin{Bmatrix} u_{1P} - u_{1P'} \\ u_{2P} + u_{2P'} \\ 0 \end{Bmatrix} + \frac{1}{2}\begin{Bmatrix} 0 \\ 0 \\ u_{3P} - u_{3P'} \end{Bmatrix}\end{aligned} \tag{4.15}$$

The superscripts are used to refer to the modes, (i.e. I refers to mode I etc.) to which these displacements contribute. In a similar fashion, the stress data may be split into three modes:

$$\begin{aligned}\{\sigma\} &= \{\sigma^{I}\} + \{\sigma^{II}\} + \{\sigma^{III}\} \\ &= \frac{1}{2}\begin{Bmatrix} \sigma_{11P} + \sigma_{11P'} \\ \sigma_{22P} + \sigma_{22P'} \\ \sigma_{33P} + \sigma_{33P'} \\ \sigma_{12P} - \sigma_{12P'} \\ \sigma_{23P} - \sigma_{23P'} \\ \sigma_{13P} - \sigma_{13P'} \end{Bmatrix} + \frac{1}{2}\begin{Bmatrix} \sigma_{11P} - \sigma_{11P'} \\ \sigma_{22P} - \sigma_{22P'} \\ 0 \\ \sigma_{12P} + \sigma_{12P'} \\ 0 \\ 0 \end{Bmatrix} + \frac{1}{2}\begin{Bmatrix} 0 \\ 0 \\ \sigma_{33P} - \sigma_{33P'} \\ 0 \\ \sigma_{23P} + \sigma_{23P'} \\ \sigma_{13P} - \sigma_{13P'} \end{Bmatrix}\end{aligned} \tag{4.16}$$

just as the strain data may also be split to give:

$$\begin{aligned}\{\varepsilon\} &= \{\varepsilon^{I}\} + \{\varepsilon^{II}\} + \{\varepsilon^{III}\} \\ &= \frac{1}{2}\begin{Bmatrix} \varepsilon_{11P} + \varepsilon_{11P'} \\ \varepsilon_{22P} + \varepsilon_{22P'} \\ \varepsilon_{33P} + \varepsilon_{33P'} \\ \varepsilon_{12P} - \varepsilon_{12P'} \\ \varepsilon_{23P} - \varepsilon_{23P'} \\ \varepsilon_{13P} - \varepsilon_{13P'} \end{Bmatrix} + \frac{1}{2}\begin{Bmatrix} \varepsilon_{11P} - \varepsilon_{11P'} \\ \varepsilon_{22P} - \varepsilon_{22P'} \\ 0 \\ \varepsilon_{12P} + \varepsilon_{12P'} \\ 0 \\ 0 \end{Bmatrix} + \frac{1}{2}\begin{Bmatrix} 0 \\ 0 \\ \varepsilon_{33P} - \varepsilon_{33P'} \\ 0 \\ \varepsilon_{23P} + \varepsilon_{23P'} \\ \varepsilon_{13P} - \varepsilon_{13P'} \end{Bmatrix}\end{aligned} \tag{4.17}$$

It has been shown [76] that the values of u^I, σ^I and ε^I may be substituted into equation (4.13) to obtain the mode I component (G_I) of the energy release rate.

The process may be repeated with the other two components to obtain G_{II} and G_{III}, respectively. Hence, the decomposition method is a computationally advantageous way of obtaining the strain energy release rate.

One of the cracks of interest in this study is a delamination crack between dissimilar plies of the material. It has been stated [48] that this approach may not be used for separation of modes in a bimaterial problem since the three modes cannot be obtained by using the individual components of displacements and stresses due to the oscillatory singularity as mentioned earlier. That is, in general each of the three modes of the strain energy release rate is related to all of the displacements, stresses and strains,

$$G_I, G_{II}, G_{III} = f\left(u^I, u^{II}, u^{III}, \sigma^I, \sigma^{II}, \sigma^{III}, \varepsilon^I, \varepsilon^{II}, \varepsilon^{III}\right) \tag{4.18}$$

This inability to apply the decomposition method is true for bimaterials with oscillatory singularities. However, if the material constants for the bimaterials satisfy some constraints, as described in the next section, there are no oscillatory singularities at the crack tip. It has been shown that in such a case, the stresses in each individual material may be obtained by pretending that the whole plate is made of that material alone [77]. The absence of the oscillatory singularity implies that there is a unique definition for the individual modes. It is shown in Appendix B that for such a bimaterial case with no oscillatory singularity, the decomposition method is capable of performing the mode separation correctly. Hence, the generalization that the decomposition method does not work for any bimaterial interfaces is not entirely true.

There are almost no naturally occurring bimaterial combinations where the oscillatory singularity is perfectly zero. But many problems have very weak oscillatory singularities relative to the maximum possible oscillatory singularity of 0.175 which occurs when one of the bimaterials is perfectly rigid [39]. In the present study, the decomposition method of mode separation has been extended further to include such cases. This assumption inherently implies that the coupling between different modes is small and may hence be neglected and the problem treated as that of a bimaterial without any oscillatory singularity. Thus, there are some errors introduced by this approximation and the exact magnitude of this error introduced cannot be determined because there exist no 'correct' or 'ideal' values to which these modes may be compared.

4.2.3 Crack Opening Displacement (COD) Approach

As is obvious from the preceeding discussions, the presence of oscillatory singularities is still a much discussed and debated issue in the case of bimaterial problems. A mode separation technique which accounts for this singularity is proposed and utilized in a delamination problem here. It is based on the analytical results developed for stresses and the crack opening displacements for a crack located at the interface of two anisotropic materials [40]. These analytical results are applicable to the general case of delaminations in composites.

The process starts with the evaluation of the oscillatory singularity. This may be performed with the aid of a formulation known as the Lekhnitskii-Eshelby-Stroh (LES) formulation, after the three researchers who independently arrived at this approach [40]. This approach is briefly described here.

The constitutive law for a generally anisotropic material can be written as:

$$\sigma_{ij} = C_{ijkl}\varepsilon_{kl} = C_{ijkl}\frac{\partial u_k}{\partial x_l} \tag{4.19}$$

This equation may be substituted into the equilibrium equation without body force, i.e. equation (4.10). This results in the equilibrium equation in terms of the displacement, known as the Navier-Cauchy equations:

$$C_{ijkl}\frac{\partial^2 u_k}{\partial x_j \partial x_l} = 0 \tag{4.20}$$

If only the simpler case of a generalized plane stress or plane strain is considered, then the solution to equation (4.20) is of the form [44]:

$$u_i = 2Re\left[\sum_{j=1}^{3} A_{ij} f_j\left(x_1 + \mu_j x_2\right)\right] \tag{4.21}$$

and the resulting stresses of interest are of the form,

$$\sigma_{2i} = 2Re\left[\sum_{j=1}^{3} L_{ij} f_j'\left(x_1 + \mu_j x_2\right)\right] \tag{4.22}$$

where μ_j, A_{ij} and L_{ij} need to be determined. Equation (4.21) may be substituted into equation (4.20) and under generalized plane strain assumptions, the resulting equation is:

$$\left[C_{i1k1} + \mu_j(C_{i1k2} + C_{i2k1}) + \mu_j^2 C_{i2k2}\right]A_{kj} = 0 \tag{4.23}$$

This is an eigenvalue problem where the eigenvalues μ_j may be determined by setting the determinant of the matrix in equation (4.23) to zero:

$$\left|C_{i1k1} + \mu_j(C_{i1k2} + C_{i2k1}) + \mu_j^2 C_{i2k2}\right| = 0 \tag{4.24}$$

When equation (4.24) is expanded, it results in a sixth-order polynomial which has no real roots. If the roots are distinct, then they are seen to be three pairs of complex conjugate roots. The three μ_j with the positive imaginary parts are chosen (their conjugates may be chosen also without any difference). The A_{ij} are also determined from equation (4.23) since they are the eigenvectors associated with the μ_j. Since the A_{ij} determine the displacements in equation (4.21) and the L_{ij} determine the stresses through equation (4.22) using the A_{ij} , they are related through the constitutive relations as:

$$L_{ij} = \sum_{k=1}^{3}\left[C_{12k1} + \mu_j C_{12k2}\right]A_{kj} \tag{4.25}$$

Assuming that the roots of Equation (4.24) are positive definite, a hermitian matrix, H, may be defined for later use as follows,

$$H = i\left(A L^{-1}\right)_{material 1} - i\left(A L^{-1}\right)_{material 2} \tag{4.26}$$

where A and L are square three by three matrices whose components are A_{ij} and L_{ij} respectively. Since only the constitutive properties of the two materials have been used so far, the matrix H involves the bimaterial elastic constants. As shown further on, this matrix H is an indicator of the existence of any oscillatory singularity at any bimaterial interface.

In order to obtain the magnitude of the oscillatory singularity, the nature of the stresses of interest and the functions are assumed to be of the form,

$$\sigma_{2j} = w\left(x_1 + \mu_j x_2\right)^{-\frac{1}{2}+i\delta} \tag{4.27}$$

where w is a constant and δ is the oscillatory singularity. Both these values need to be determined. This solution is compatible with the form of σ_{2j} that was assumed earlier in equation (4.22). This solution has both the $1/\sqrt{r}$ singularity as well as the oscillatory singularity, δ, and this determines the exact nature of the function $f(x_1+\mu_j x_2)$ in equation (4.22) except for a constant, w. The displacements can be expressed in terms of both w and δ using equation (4.21). In order to obtain the value of δ, the stresses and the displacements are matched at the interface of the bimaterials. This procedure can be seen in detail in reference [40, 44] . This matching of the stresses and diplacements results in the following eigenvalue problem,

$$\overline{H}\, w = e^{2\pi\delta} H\, w \tag{4.28}$$

where the overbar implies the complex conjugate and $e^{2\pi\delta}$ is the eigenvalue in equation (4.28) and w is the eigenvector. It can be seen in Equation (4.28) that if H is a real matrix, i.e.

$$\overline{H} = H \tag{4.29}$$

then the oscillatory singularity, δ, is zero. This is the condition that needs to be satisfied by the material properties of the bimaterial to have no oscillatory singularity.

If the matrix H is real, then there are no oscillatory singularities and the stresses and displacements have only a $1/\sqrt{r}$ singularity as in the case of isotropic materials and the stresses at the crack tip can be expressed as,

$$\begin{Bmatrix} \sigma_{21} \\ \sigma_{22} \\ \sigma_{23} \end{Bmatrix} = \frac{1}{\sqrt{2\pi r}} \begin{Bmatrix} K_{II} \\ K_{I} \\ K_{III} \end{Bmatrix} \tag{4.30}$$

and the displacements behind the crack tip can be expressed as,

$$\begin{Bmatrix} \Delta u_2 \\ \Delta u_1 \\ \Delta u_3 \end{Bmatrix} = \sqrt{\frac{2r}{\pi}}\; H \begin{Bmatrix} K_{II} \\ K_{I} \\ K_{III} \end{Bmatrix} \tag{4.31}$$

where the K's are the classical intensity factors. The total strain energy release rate can thus be obtained by using equations (4.30) and (4.31) in Irwin's virtual crack closure integral, equation (2.8) discussed in Chapter two. The resulting expression for G is,

$$G = \frac{1}{4}\{K_{II} \quad K_{I} \quad K_{III}\}\, H \begin{Bmatrix} K_{II} \\ K_{I} \\ K_{III} \end{Bmatrix} \tag{4.32}$$

However, if the condition in equation (4.29) is not satisfied, then an oscillatory singularity, δ, also exists along with the $1/\sqrt{r}$ singularity and three distinct pairs of eigenvalues and corresponding eigenvectors exist which are of the form,

$$(\delta,\{w_1\})\,;\,(-\delta,\{\overline{w}_1\}) \text{ and } (0,\{w_3\}) \tag{4.33}$$

These satisfy the three conditions,

$$\overline{H}w_1 = e^{2\pi\delta}Hw_1 \tag{4.34a}$$

$$\overline{H}\overline{w}_1 = e^{2\pi\delta}H\overline{w}_1 \tag{4.34b}$$

and

$$\overline{H}w_3 = Hw_3 \tag{4.34c}$$

Thus, the stresses may be obtained from equation (4.27), by substituting the values of w and δ shown in equation (4.33). Since there are three pairs of values, the complete solution is a sum of all the three individual values and the stresses are expressed as:

$$\begin{Bmatrix} \sigma_{21} \\ \sigma_{22} \\ \sigma_{23} \end{Bmatrix} = \frac{1}{\sqrt{2\pi r}}\left[(K_1 + iK_2)r^{i\delta}\begin{Bmatrix} w_1 \end{Bmatrix} + (K_1 - iK_2)r^{-i\delta}\begin{Bmatrix} \overline{w}_1 \end{Bmatrix} + K_3\begin{Bmatrix} w_3 \end{Bmatrix}\right] \tag{4.35}$$

where K_1, K_2 and K_3 are constants which are called the stress intensity factors, but not in the same sense as the classical stress intensity factors, K_I, K_{II} and K_{III} which determine the individual modes of fracture. The value r is the distance ahead of the crack tip in the plane of the crack.

Once the stresses are obtained, the displacements may be obtained by using the stresses in the constitutive laws in equation (4.19) and integrating them. The crack opening displacements are given by:

$$\begin{Bmatrix} \Delta u_1 \\ \Delta u_2 \\ \Delta u_3 \end{Bmatrix} = \left(H + \overline{H}\right)\sqrt{\frac{r}{2\pi}}\left[\frac{Kr^{i\delta}}{(1+i2\delta)\cosh\pi\delta}\begin{Bmatrix} w_1 \end{Bmatrix} + \frac{\overline{K}r^{-i\delta}}{(1-i2\delta)\cosh\pi\delta}\begin{Bmatrix} \overline{w}_1 \end{Bmatrix} + K_3\begin{Bmatrix} w_3 \end{Bmatrix}\right] \tag{4.36}$$

where Δu_j is the crack opening measured at any distance r, measured along the crack, behind the crack tip. It represents the difference in the displacement between the top face of the crack and the bottom face of the crack as follows:

$$\Delta u_j = \left(u_j\right)_{top} - \left(u_j\right)_{bot} \tag{4.37}$$

Using a finite element analysis, the crack opening displacements could be obtained for any point behind the crack front. The accuracy with which these crack opening displacements are obtained is a function of the mesh refinement. If these crack opening displacements are then substituted into equation (4.36), they result in a three-by-three matrix equation, which may be solved for the three unknowns, K_1, K_2 and K_3. It should be noted that the units of these stress intensity factors are very strange, and depend on the value of δ. In general the units are of the type: stress*(length)$^{0.5-i\delta}$

The subscripts used for the stress intensification factors have no relation to the modes, and, as can be seen from equation (4.35), if the vectors w_1 and w_3 are fully populated, then all the stresses are related to all the stress intensity factors. If both materials are identical to each other, then δ is zero and the following eigenvectors are obtained when equation (4.28) is solved:

$$w_1 = \begin{Bmatrix} -0.5i \\ 0.5 \\ 0 \end{Bmatrix} \tag{4.38a}$$

$$\overline{w}_1 = \begin{Bmatrix} 0.5i \\ 0.5 \\ 0 \end{Bmatrix} \tag{4.38b}$$

and

$$w_3 = \begin{Bmatrix} 0 \\ 0 \\ 1 \end{Bmatrix} \tag{4.38c}$$

This simplifies equation (4.35) to that in the case of isotropic materials,

$$\begin{Bmatrix} \sigma_{21} \\ \sigma_{22} \\ \sigma_{23} \end{Bmatrix} = \frac{1}{\sqrt{2\pi r}} \begin{Bmatrix} K_2 \\ K_1 \\ K_3 \end{Bmatrix} = \frac{1}{\sqrt{2\pi r}} \begin{Bmatrix} K_{II} \\ K_I \\ K_{III} \end{Bmatrix} \tag{4.39}$$

where each stress is associated with the classical stress intensity factor. In the case of arbitrary anisotropic bimaterials, however, the eigenvectors are usually fully populated and hence all the stress intensity factors are related to all the stresses.

The total G may be obtained by using the stresses given in equation (4.35) and the displacements given in equation (4.36) in Irwin's virtual crack closure integral, equation (2.8) discussed in Chapter two. The resulting G is given by:

$$G = \frac{w_1\left(H+\overline{H}\right)w_1\left|K_1{}^2+K_2{}^2\right|}{\left(4\cosh^2\pi\delta\right)} + \frac{1}{8}w_3^T\left(H+\overline{H}\right)w_3K_3^2 \tag{4.40}$$

This G may be compared to that obtained by another independent method such as the EDI. This is only an indirect check that determines whether the K_1, K_2 and K_3 obtained by using the crack opening displacements provide a reasonable estimate of the total G. The validity of the actual values of K_1, K_2 and K_3 cannot be determined from currently known methods.

Thus far, the total G has been obtained, however the individual modal components of this need to be defined. In the case of isotropic materials, the mode ratios may be classifed as a ratio of the normal stresses to shear stresses and, from equation 4.39, two such ratios can be defined,

$$\psi = tan^{-1}\left(\frac{\sigma_{21}}{\sigma_{22}}\right) = tan^{-1}\left(\frac{K_{II}}{K_I}\right) \tag{4.41}$$

The inverse tangent is used so that the ψ spans from 0° to 90° for loading cases ranging from mode I to mode II. Similary, another ratio may be defined as,

$$\phi = tan^{-1}\left(\frac{\sigma_{23}}{\sigma_{22}}\right) = tan^{-1}\left(\frac{K_{III}}{K_I}\right) \tag{4.42}$$

where ϕ also spans from 0° to 90° for loading cases ranging from mode I to mode III. In the case of bimaterials, however, due to the presence of the $r^{i\delta}$ term, the ratio of σ_{21}/σ_{22} and σ_{23}/σ_{22} vary depending on the distance ahead of the crack tip and do not reduce to simple forms as in the isotropic cases shown in equations (4.41) and (4.42).

This new definition of modes has been proposed in reference [39] and may be written as:

$$\psi = tan^{-1}\left(\frac{\sigma_{21}}{\sigma_{22}}\right)_{r=r_0} \tag{4.43a}$$

$$\phi = tan^{-1}\left(\frac{\sigma_{23}}{\sigma_{22}}\right)_{r=r_0} \tag{4.43b}$$

where r_0 is a distance measured ahead of the crack tip in the plane of the crack. It could be a distance characteristic of the fracture process itself. If the stresses from equation (4.35) are substituted into equations (4.43a,b), then it is seen that these ratios are functions of the distance ahead of the crack tip and the modes vary depending on the distance ahead of the crack tip. If the critical value of G changes for different mode ratios, then a surface defines the failure criterion, and it can be expressed as:

$$G_c = G_c(\psi, \phi, r_o) \tag{4.44}$$

With this particular definition, a crack will start to grow when the total G reaches a critical value. But, this critical value is a function of the modes, and the characterizing distance at which these modes are determined.

These new definition of modes, ψ and ϕ, have been used to separate the modes in a free edge delamination problem in a $[0_2/90_2]_s$ laminate solved in the next section as an example. The mode ratio is evaluated for different values of r_0 and is then compared to the modes obtained by the decomposition method.

4.3 Verification Problem and Comparison of Methods

The equivalent domain integral approach and the crack opening displacement approach are compared here by using two example problems. The first example is that of a free edge delamination in a $[0_2/90_2]_s$ laminate. This problem has a theoretical solution for the total strain energy release rate, G. Therefore, the results obtained by the EDI and COD methods may be compared to a known solution. This serves as a verification problem only for the total G. The comparison of individual modes as obtained by the two methods is also performed, but no theoretical solutions are available for comparison.

Another approach adopted for separation of modes uses the COD approach but neglects the small oscillatory singularity observed and obtains the individual modes. These modes are compared to the modes obtained by the EDI approach.

The second example studied is that of a $[\pm 75_2]_s$ laminate where the loading was normal to the delamination front. This example was chosen because, unlike the earlier example, this is not an orthotropic laminate, but an example of a more general laminate. In this example, the oscillatory singularity is once again shown to be small and hence is neglected. The results for the total G and the individual modes obtained by the EDI and the COD approaches are compared but no theoretical solution is available for comparison in this case.

4.3.1 Delamination in $[0_2/90_2]_s$ laminate

The comparison of the results by the two methods was performed on the problem of a simple free-edge delamination in a $[0_2/90_2]_s$ laminate loaded in tension with a far-field strain of 1% (10^4 μstrain) for which a theoretical solution was available. The material used in the analysis is AS4/3501-6 and the properties of the material are listed in Table 4.1 [78]. The length, L, was chosen to be 2 mm; the width of the model, b, was 3 mm; and the delamination crack length, a, was 1 mm. The delamination length was more than three effective ply thicknesses from the free edge of the laminate and hence the delamination front

Table 4.1 Material Properties of AS4/3501-6[a] Graphite/Epoxy

Property	Value
E_{11}	138 GPa
E_{22}	9.81 GPa
E_{33}	9.81 GPa
G_{12}	6.0 GPa
G_{1z}	6.0 GPa
G_{2z}	4.8 GPa
ν_{12}	0.3
ν_{1z}	0.3
ν_{2z}	0.57
t_{ply}	0.134 mm

[a] As reported by Weems [78]

is in the region where the total strain energy release rate, G, can be predicted by the theoretical global energy release rate model discussed in Chapter two [36].

A three-dimensional finite element model of this problem is shown in Figure 4.12 only one quarter of the laminate is modelled due to the symmetry. The finite element model uses twenty-noded brick elements with three degrees of freedom per node. The region around the crack tip, with a refined mesh, is shown in Figure 4.13. The crack front has four singular brick elements surrounding it and the refined meshing is intended to capture the steep stress gradients in that region. In order to study the effect of the size of the elements at the delamination front on the different parameters evaluated, two different crack tip element sizes were chosen. Square crack tip elements, seen in Figure 4.13, with sides a_0 equal to a/50 and a/100, were used in the analysis.

Since the laminate is orthotropic, there is no difference in the behavior of any particular section in the loading (x_3) direction. Therefore, the problem is a quasi-three-dimensional problem and the results that are presented are valid for any point along the delamination front. This fact was borne out by the model, where no changes in any parameter was observed at different points along the delamination front.

The objective of this exercise was twofold. The first objective was to use the EDI and COD approaches to obtain the total G and compare the results to some theoretically known solution. The second objective was to obtain the oscillatory singularity and determine how the modes obtained by the decomposition method differed from the modes obtained by the COD approach. As described in the earlier section, the modes defined by the COD approach could have different values at different distances ahead of the crack tip depending on the magnitude of the oscillatory singularity.

The total strain energy obtained by the EDI and the COD approach for the

Table 4.2 Values of total G^a (J/m^2) for the case of a $[0_2/90_2]_s$ laminate with simple delamination at the 0/90 interface

Method	Crack Tip Element Size (a_0)	
	a/50(=0.02 mm)	a/100(=0.01 mm)
EDI	9.48 (-1.8%)[b]	9.42 (-2.4%)
COD[c]	9.39 (-2.7%)	9.10(-5.7%)

[a] G_{theory}=9.65 J/m^2

[b] Values in parentheses are percentage differences from theoretical results

[c] The crack opening displacements are evaluated at a_0

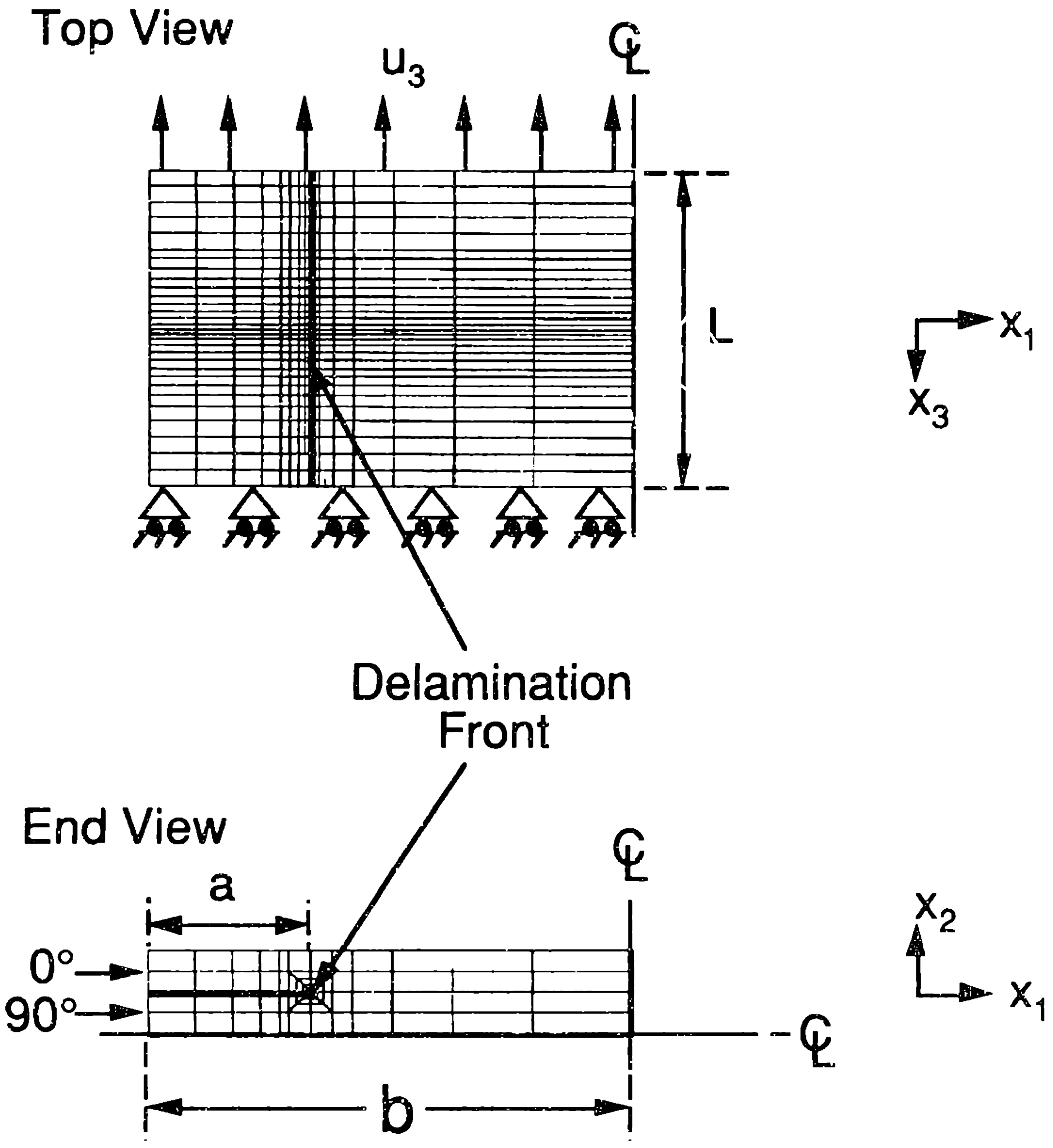

Figure 4.12 Quarter model used in the finite element analysis of a $[0_2/90_2]_s$ laminate with a delamination at the 0/90 interface.

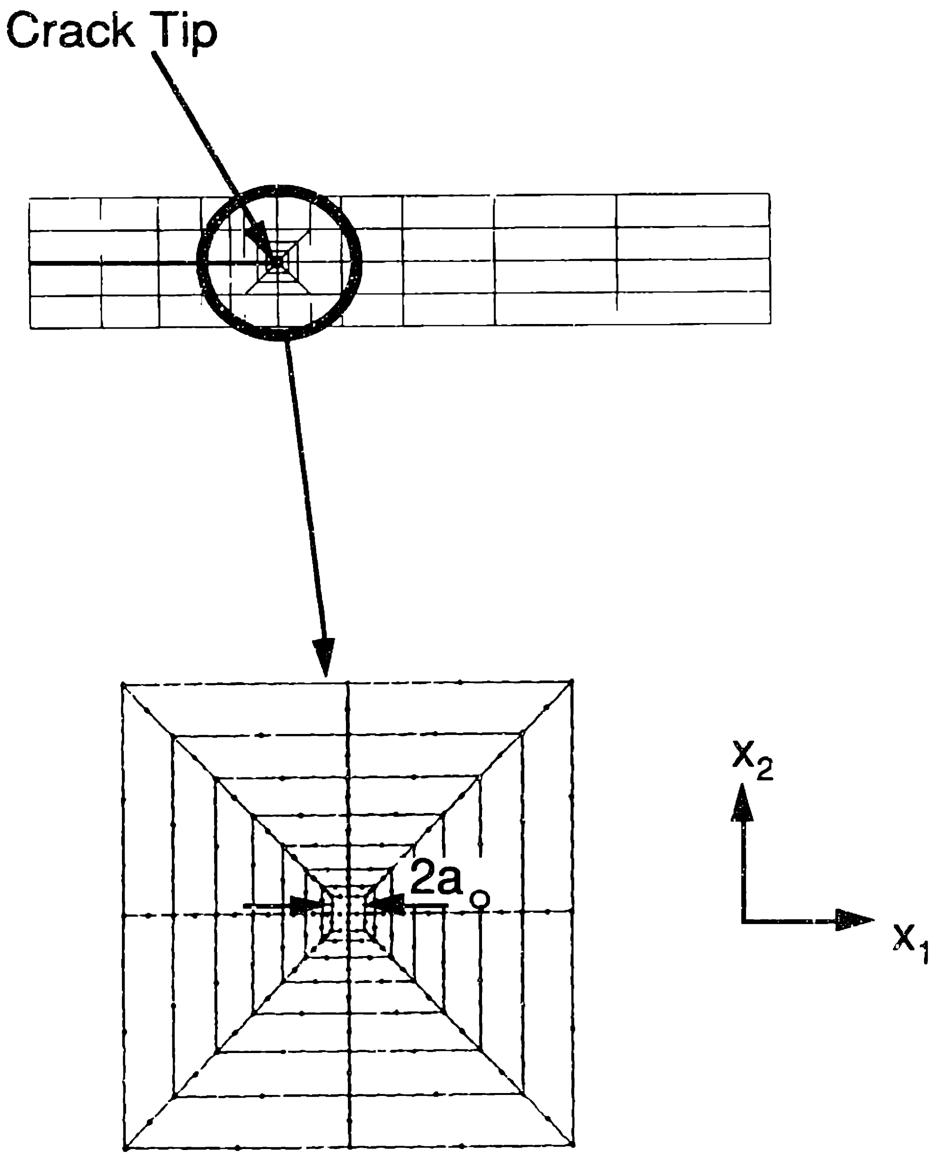

Figure 4.13 Illustration of finite element mesh in the region of the crack tip for $[0_2/90_2]_s$ case, showing four singular brick elements at the crack tip.

two crack tip element sizes are shown in Table 4.2. The theoretical value of the total strain energy release rate, as obtained by using equation (2.4), is 9.65 J/m^2.

It is necessary in the COD approach to use crack opening displacement data to evaluate the stress intensity factors K_1, K_2 and K_3, and consequently the G. Such data can be evaluated at any distance behind the delamination front. However, since the displacement data is available only at the nodal points and since the mesh was refined near the crack tip, the data from the nodes in that region was more accurate. Thus the displacement data at the edge of crack tip elements, i.e. at a distance a_0 behind the delamination front, was used.

Ideally in the case of the EDI method, there should be no discernible change in the total G with differing cracktip element sizes. However, there are minor differences (approximately 2 to 3%) observed here. In the case of the EDI, the use of smaller elements is expected to give a better approximation to the J-Integral shown in equation (4.3) as discussed section 4.2.1. However, the results in Table 4.2 indicate that slightly better results are obtained for larger element sizes. While the reason for this is unclear, one possible reason is that the brick-shaped element does not have the $1/\sqrt{r}$ singularity throughout the laminate and this could affect the way the EDI is evaluated.

The total G obtained by the COD approach has more error than observed in the EDI method. Since the COD approach uses just the displacement at one point behind the crack tip to determine G, this larger error is to be expected. In order to improve these results, a considerable increase in the mesh density is required. Note that the results presented in Table 4.2 are not for different mesh densities, but for different crack tip element sizes only.

For the EDI approach, the decomposition method is used to separate the modes in the conventional fashion. The results are shown in Table 4.3. In order to have a consistent method of comparing mode ratios between the EDI method and

Table 4.3 Mode ratios obtained by the EDI approach for the case of a simple delamination in a $[0_2/90_2]_s$ laminate

Crack tip element size	G_1 (J/m^2)	G_2 (J/m^2)	G_3 (J/m^2)	$\psi = tan^{-1}\left(\sqrt{G_2 / G_1}\right)$
a/50 (=0.02 mm)	5.77	3.65	0	32°
a/100 (=0.01 mm)	5.65	3.83	0	34°

the COD method, the parameter ψ is redefined here in terms of G. In the case of isotropic materials or bimaterials without oscillatory singularity, the strain energy release rate components are related to the stress intensity factors:

$$G_I \propto K_I^2 \tag{4.45a}$$

$$G_{II} \propto K_{II}^2 \tag{4.45b}$$

$$G_{III} \propto K_{III}^2 \tag{4.45c}$$

Using these equations and equation (4.41), the ratio ψ is defined in terms of components of energy release rate as:

$$\psi = tan^{-1}\left(\frac{K_{II}}{K_I}\right) = tan^{-1}\left(\sqrt{\frac{G_{II}}{G_I}}\right) \tag{4.46}$$

In the present case, an oscillatory singularity exists but its presence is ignored in using the decomposition method. The outcomes of this mode separation process are designated as G_1, G_2 and G_3 to indicate that they are only approximate modes. A definition similar to that in equation (4.46) has then been used to define the mode ratio shown in Table 4.3:

$$\psi = tan^{-1}\sqrt{\frac{G_2}{G_1}}$$

There is a small difference (3%-5%) between the modes obtained from the two different crack tip element sizes. Part of this difference could be attributed to the fact that the total G itself has changed with different element sizes and part of it could be attributed to the presence of the oscillatory singularity. The tearing mode, G_3, is identically zero as expected.

In order to use the COD method, the oscillatory singularity, δ, first needs to be evaluated. The properties of AS4/3501-6 given in Table 4.1 are used to obtain the H matrix and then δ , w_1, and w_3 using the procedure described in section 4.2.3. The H matrix for the [0/90] interface with the ply properties of AS4/3501-6 is as follows:

$$H=\begin{bmatrix} 2.148 & 0.473i & 0 \\ -0.473i & 3.165 & 0 \\ 0 & 0 & 3.727 \end{bmatrix} 10^{-10} \tag{4.47}$$

In evaluating H all the modulus properties of the 0° and 90° ply are in N/m^2, but no units are presented here for terms in the H matrix, since it involves complex numbers and units have little meaning. It is evident from equation (4.47) that the matrix H is not real and hence does not satisfy equation (4.29). Therefore, a crack at the 0/90 interface has an oscillatory singularity δ which is equal to 0.058 and the eigenvectors described in equation (4.31a,b,c) are:

$$w_1=\begin{Bmatrix} -0.5i \\ 0.41 \\ 0 \end{Bmatrix} \tag{4.48a}$$

$$\overline{w}_1=\begin{Bmatrix} 0.5i \\ 0.41 \\ 0 \end{Bmatrix} \tag{4.48b}$$

and

$$w_3=\begin{Bmatrix} 0 \\ 0 \\ 1 \end{Bmatrix} \tag{4.48c}$$

Equation (4.48a,b,c) may be compared to equation (4.38a,b,c) and it is observed that the vectors w_1 and w_3, which appear in the expression for stresses, are not much different from those for an isotropic body for this delamination crack. The existence of the oscillatory singularity at the interface couples the stresses σ_{22} and σ_{21} at the crack tip as shown in equation (4.35). The second term in the w_1 vector reflects this fact as it is different from 0.5, the value expected in isotropic materials. The presence of the δ in the equation for the stresses will couple these stresses together. Once again, the tearing mode, indicated by σ_{23}, is identically zero. This implies that there is no tearing effect on the crack tip.

The crack opening displacements were used in equation (4.36) to obtain the stress intensity factors. These stress intensity factors are given in Table 4.4. The units of the stress intensity factors are strange due to the presence of the oscillatory singularity and the values obtained for K_1, K_2 and K_3 are meaningless by themselves. They only have meaning as used to evaluate the stresses using equation (4.35) and the mode ratio, using equation (4.43a).

The mode ratio can be plotted for different distances ahead of the crack tip. The presence of the oscillatory stresses implies that very near the crack front, the stresses are oscillatory in nature and hence the linear elasticity solution is not valid there. Hence finding the ratio, ψ, in that region is meaningless. This ratio, ψ, must be evaluated in regions where the physical process of fracture actually occurs, although in this case such regions are not exactly known. Therefore, the mode ratio is evaluated for a wide range of distances ahead of the crack tip and the results are shown in Figure 4.14.

These results show that the mode ratio as measured by this technique show a significant change over the region spanning from close to the crack tip (microscopic) to several fiber thicknesses (macroscopic). Within this region, it is not possible to characterize a single mode ratio for this delamination. It must also be noted that in crossing across these order of magnitude scales, the manner in which the material is analyzed must also significantly change. In the case of the microscopic length scales, the model would have to distinguish between the fiber and the matrix, and a homogenized composite property is meaningless at that level. Therefore, only the results beyond r greater than 10^{-5}m are considered. At scales which are of the order of five to ten fiber diameters, the material may be treated as a homogenized material and the current analysis is

Table 4.4 Stress intensity factors[a], K_1, K_2 and K_3, for the case of a simple delamination in a $[0_2/90_2]_s$ laminate obtained by the COD approach

Crack Tip Element Size	K_1 (MPa $m^{1/2-i\delta}$)	K_2 (MPa $m^{1/2-i\delta}$)	K_3 (MPa $m^{1/2-i\delta}$)
a/50 (=0.02 mm)	0.4223	0.05004	0
a/100 (=0.01 mm)	0.4165	0.04162	0

[a] crack opening displacement data at distance a_0 behind crack are used.

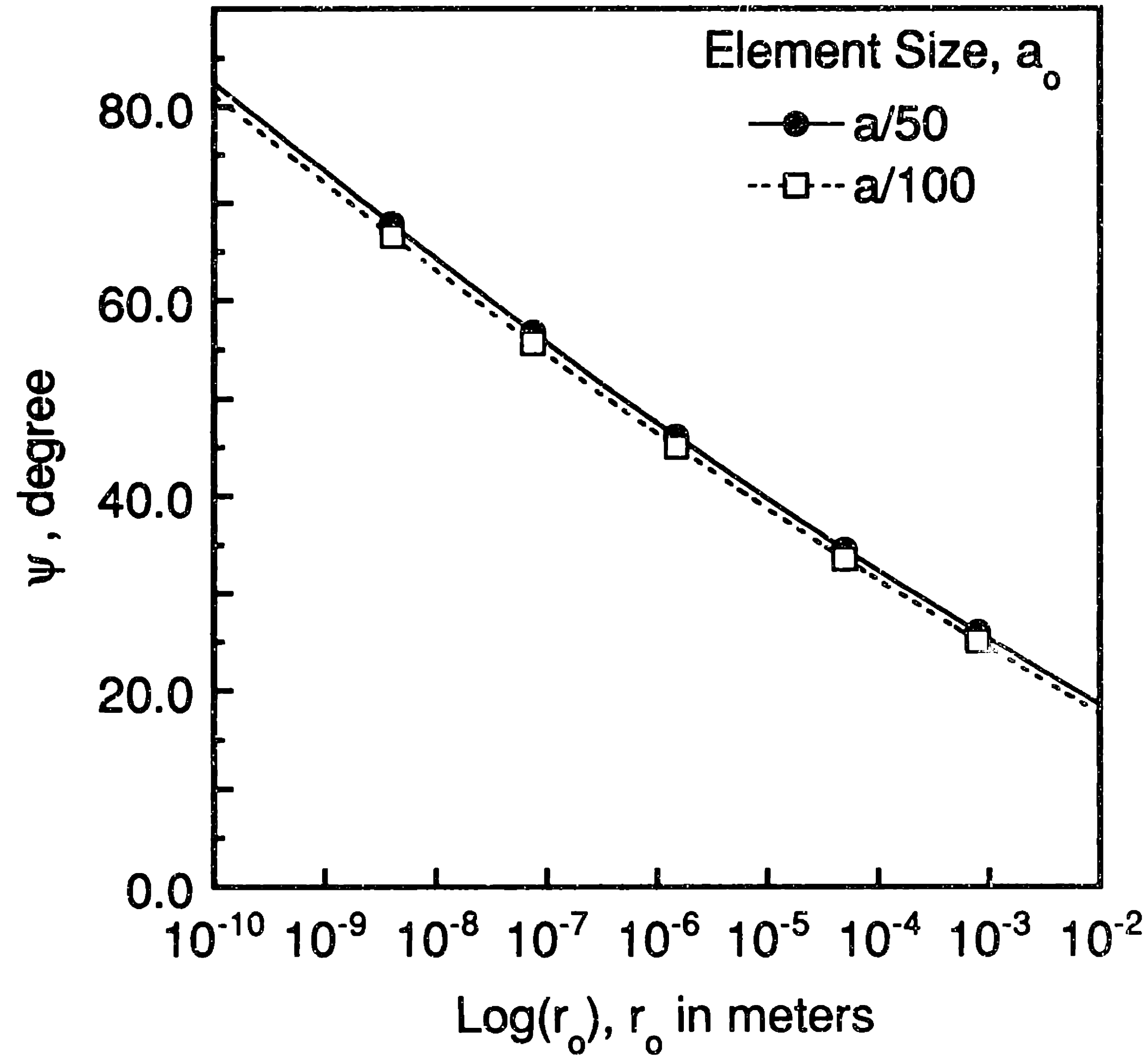

Figure 4.14 Variation of the mode ratio calculated via the COD approach, defined as the ratio of the stresses at different distances ahead of the delamination tip, for the case of a $[0_2/90_2]_s$ with a simple delamination at the 0/90 interface.

valid over those regions. It is, however, difficult to recognize any relationship between these mode ratios and that obtained by the EDI.

However, another option that is available to evaluate the modes by the COD approach is to assume that δ is small and therefore set it to zero before K_1, K_2 and K_3 are evaluated. This also implies that the H matrix must be considered to be real in order to be consistent with the assumption that the oscillatory singularity is zero, as was discussed earlier and shown in equation (4.29). Therefore after eliminating the imaginary terms from the H matrix, equation (4.47) reduces to:

$$H = \begin{bmatrix} 2.148 & 0 & 0 \\ 0 & 3.165 & 0 \\ 0 & 0 & 3.727 \end{bmatrix} 10^{-10} \frac{m^{3/2}}{N} \tag{4.49}$$

Since the matrix is real, it now has well defined units. With the oscillatory singularity set to zero, the modes are not coupled and three unique modes can be defined for this case. The crack opening displacements behind the crack, and the H matrix given in equation (4.49) were used in equation (4.31) to obtain the stress intensity factors K_1, K_2 and K_3 pertaining to these modes. These stress intensity factors were then used in equation (4.32) to obtain the total energy release rate and, since the H matrix is diagonal, the expression for G, the total strain energy release rate, can be separated into three parts: the ones involving K_1, K_2 and K_3 are called G_1, G_2 and G_3, respectively. These modes are given in Table 4.5 and they are seen to be similar to those obtained by the EDI method.

These results indicate that there is a similarity between the modes obtained by the EDI method and those obtained by assuming the absence of an oscillatory singularity in the COD method. However, this does not indicate the validity of either method, but only implies a consistency in the results obtained by using the two methods.

Table 4.5 Mode ratios obtained by the COD approach for the case of a simple delamination in a $[0_2/90_2]_s$ laminate (with $\delta = 0$)

Crack tip element size	G_1 (J/m^2)	G_2 (J/m^2)	G_3 (J/m^2)	$\psi = tan^{-1}\left(\sqrt{G_2 / G_1}\right)$
a/50 (=0.02 mm)	5.38	3.89	0	36°
a/100 (=0.01 mm)	5.41	3.57	0	33°

4.3.2 Delamination in a $[\pm 75_2]_s$ laminate

The previous example was that of a delamination in an orthotropic laminate. In order to study the behavior of a delamination in a more general laminate, the mesh shown in Figure 4.12 was used, initially, in representing a $[\pm 15_2]_s$ AS4/3501-6 laminate. However, on analyzing the loading of this laminate, the results indicated that the surfaces of the delamination would interpenetrate each other. This is physically impossible since there would be contact at the crack faces. This makes the problem nonlinear and, hence, quite complex.

Therefore, this problem was altered such that the same mesh with different boundary conditions was adopted to prevent crack surface interpenetration. The problem now being solved was not that of a free edge delamination, but that of a laminate with its delamination front located normal to the loading direction as illustrated in Figure 4.15. The material properties from the preliminary analysis were retained, and the loading direction was rotated by 90° resulting in a $[\pm 75_2]_s$ laminate relative to the loading direction. Since the laminate is symmetric, only a half model is used, as shown in Figure 4.16. The central $[-75_2]_s$ sublaminate is clamped and the $[+75_2]$ sublaminates are left unconstrained. Unlike the earlier problem of a $[0_2/90_2]_s$ laminate, which was a quasi-three dimensional problem, this is a full three-dimensional problem since this laminate is not orthotropic. Although this problem does not represent any useful physical situation, it is useful in the assessment of the analytical methodology because the deformation, as shown schematically in Figure 4.15, occurs without any problems associated with crack surface interpenetration. This model is thus used to compare the results for the energy release rate by the EDI and the COD approaches.

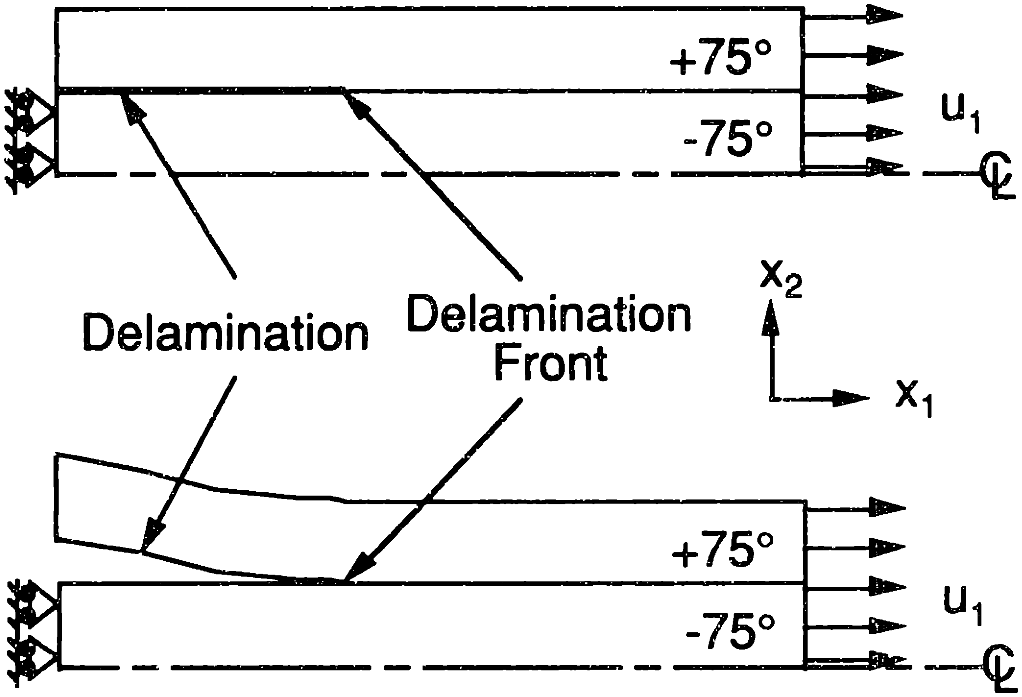

Figure 4.15 Illustration of delaminated [±75_2]$_s$ laminate loaded normal to the delamination front in the (*top*) undeformed configuration, and (*bottom*) deformed configuration.

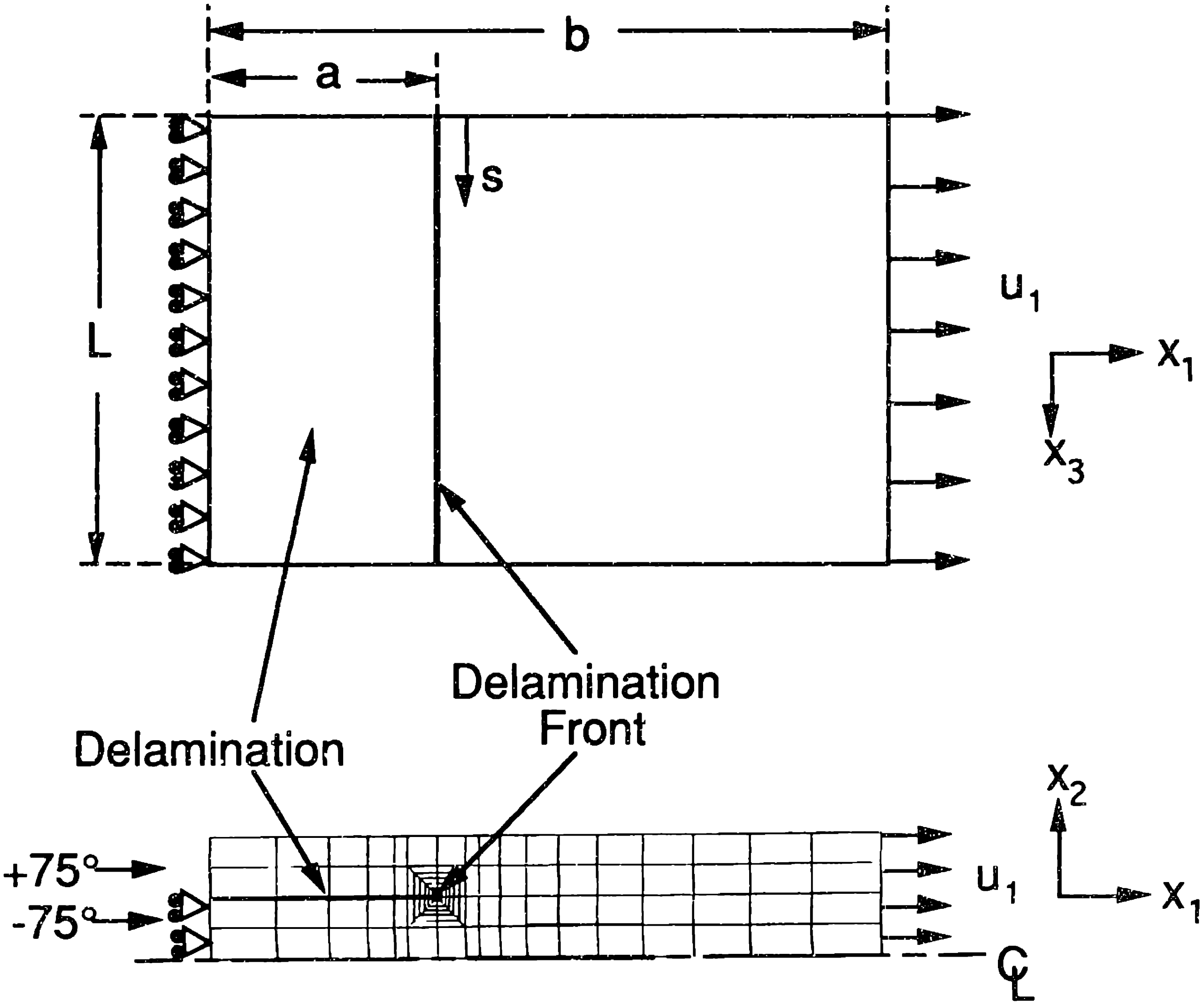

Figure 4.16 Illustration of the finite element model used in the $[\pm75_2]_s$ laminate with loading normal to the delamination front.

The H matrix for the +75/-75 interface is given by,

$$H = \begin{bmatrix} 0.993 & 0 & 0 \\ 0 & 2.855 & -0.126i \\ 0 & 0.126i & 3.468 \end{bmatrix} 10^{-10} \tag{4.50}$$

It is evident from equation (4.50) that the matrix is not real and hence does not satisfy equation (4.29). Therefore, an oscillatory singularity exists for a crack at the +75/-75 interface and its value can be evaluated using equation (4.28). The value of δ is found to be equal to 0.013. Since the oscillatory singularity is small, it is set equal to zero and consequently the H matrix consistent with this assumption is as follows,

$$H = \begin{bmatrix} 0.993 & 0 & 0 \\ 0 & 2.855 & 0 \\ 0 & 0 & 3.468 \end{bmatrix} 10^{-10} \tag{4.51}$$

The cases with a real H matrix were discussed in section 4.2.3 and it was shown that three unique modes could be defined for this case. The crack opening displacements were used in equation (4.31) to obtain the stress intensity factors pertaining to these modes. These stress intensity factors were used in equation (4.32) to obtain the total energy release rate and, since the H matrix is diagonal, the expression for G is made up of only three terms each involving one of the stress intensity factors. These are the individual modal energy release rates. The results for the total G and the individual modes are compared with those obtained by the EDI method.

The total strain energy release rate obtained by the EDI is compared with the two COD results (viz. with the δ equal to 0.013 and with δ set to zero) in Figure 4.17 where the results are presented along the coordinate, s, which is measured along the delamination front. It is seen that the total energy release rate by the COD approach is quite close to that obtained by the EDI approach.

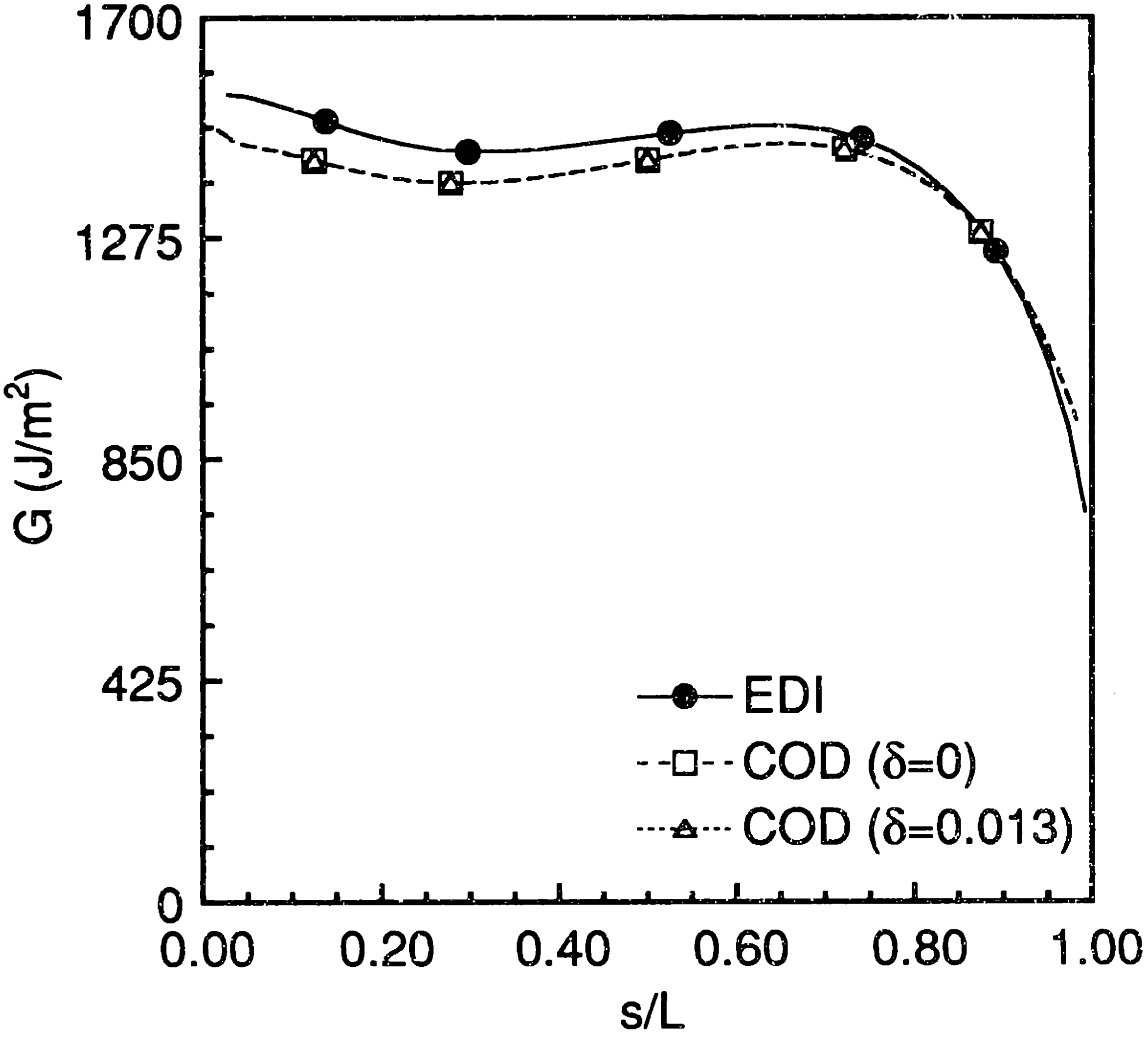

Figure 4.17 Total strain energy release rate along the delamination front for the case of a delaminated $[\pm 75_2]_s$ laminate.

Also, there is almost no difference observed in the total energy release rate between the two results obtained via the two COD approaches.

The individual modes are presented in Figure 4.18, 4.19 and 4.20. While there is no significant difference between the mode II energy release rate obtained by the EDI and the COD approaches, the oscillatory singularity affects the magnitudes of mode I and mode III as the results by the COD approach not match those by the EDI approach. In the case of mode I, the results by the EDI approach are larger than the COD results. In the case of mode III, the results obtained by the COD approach are larger. However, the trends shown by the individual modes obtained by the two methods are very similar.

The current research on the issues involved in mode separation is not sufficient to conclusively determine the practical use of the new definition of the mode ratios nor is it sufficient to determine what the relationship of these modes is to the modes determined by the conventional methods. However, as is seen from the two examples in cases where the oscillatory singularity is small, the mode ratios separated by the conventional method are very similar to that obtained by the COD approach if the oscillatory singularity is forced to zero in the COD approach. This, however, does not validate either method but implies consistency between the results by the various methods. No validification is possible due to a lack of theoretical definitions for the modes.

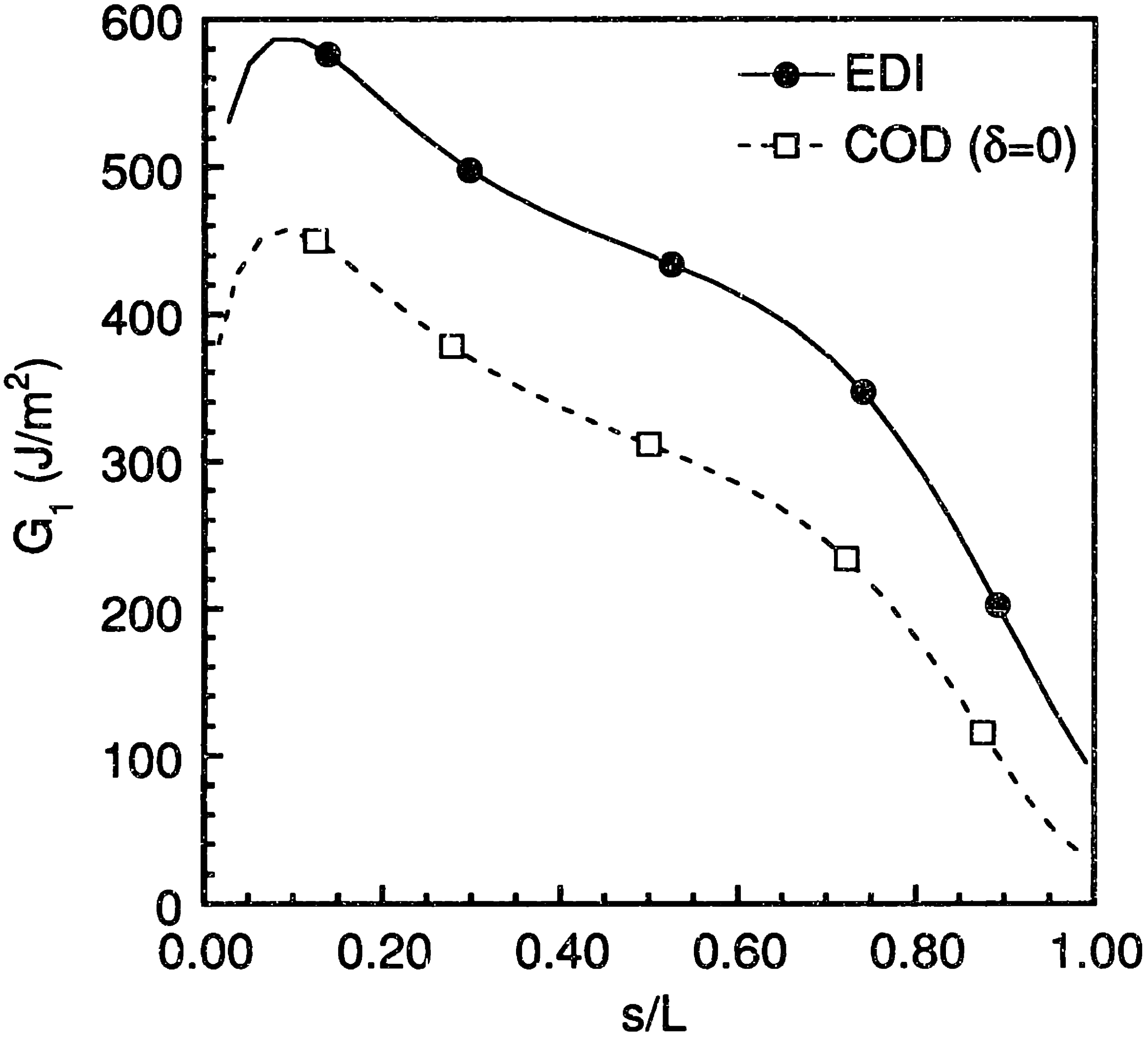

Figure 4.18 Mode I energy release rate along the delamination front obtained by the EDI approach and the COD approach with δ set equal to zero for the case of a delaminated $[\pm 75_2]_s$ laminate.

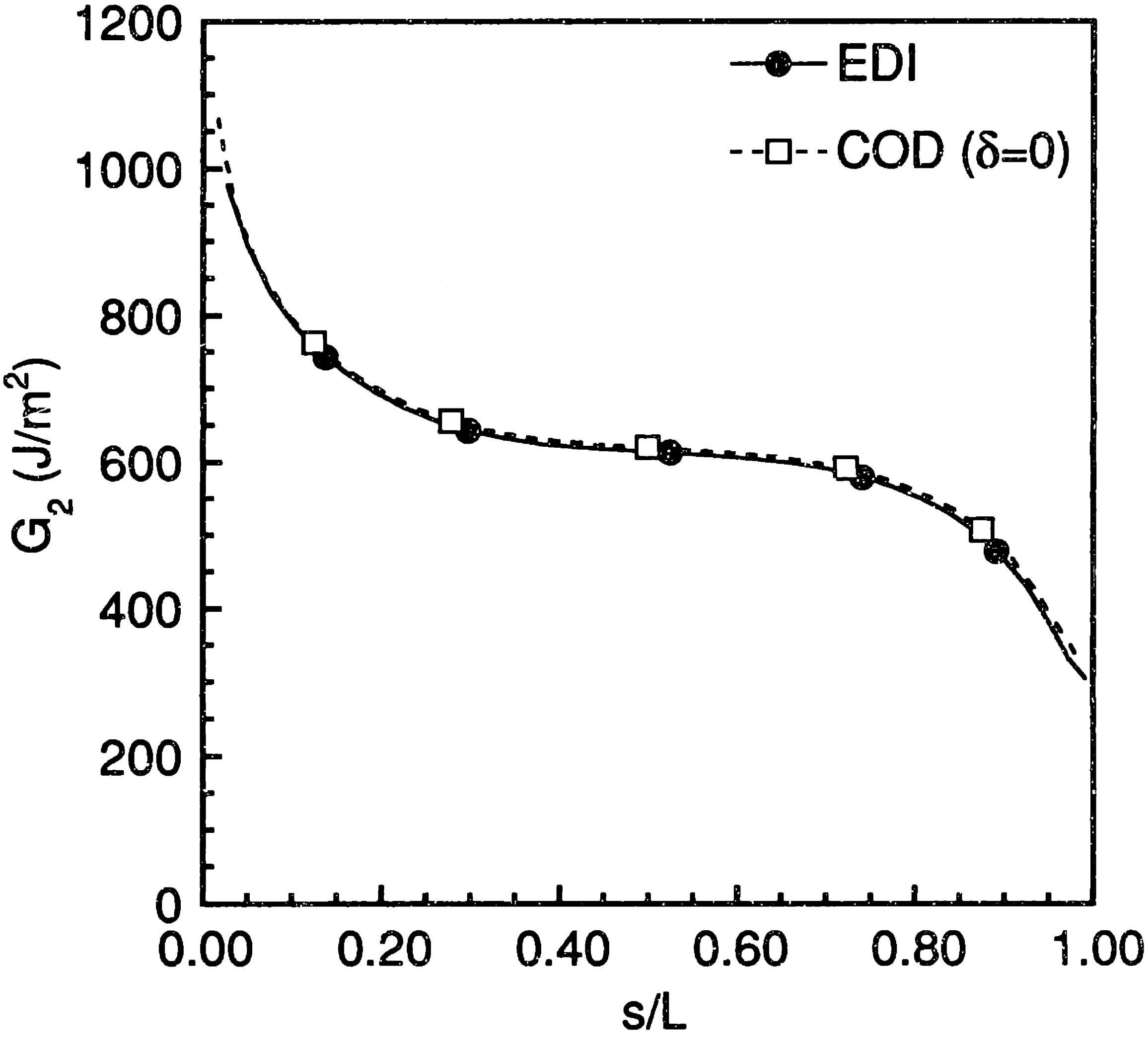

Figure 4.19 Mode II energy release rate along the delamination front obtained by the EDI approach and the COD approach with δ set equal to zero for the case of a delaminated $[\pm 75_2]_s$ laminate.

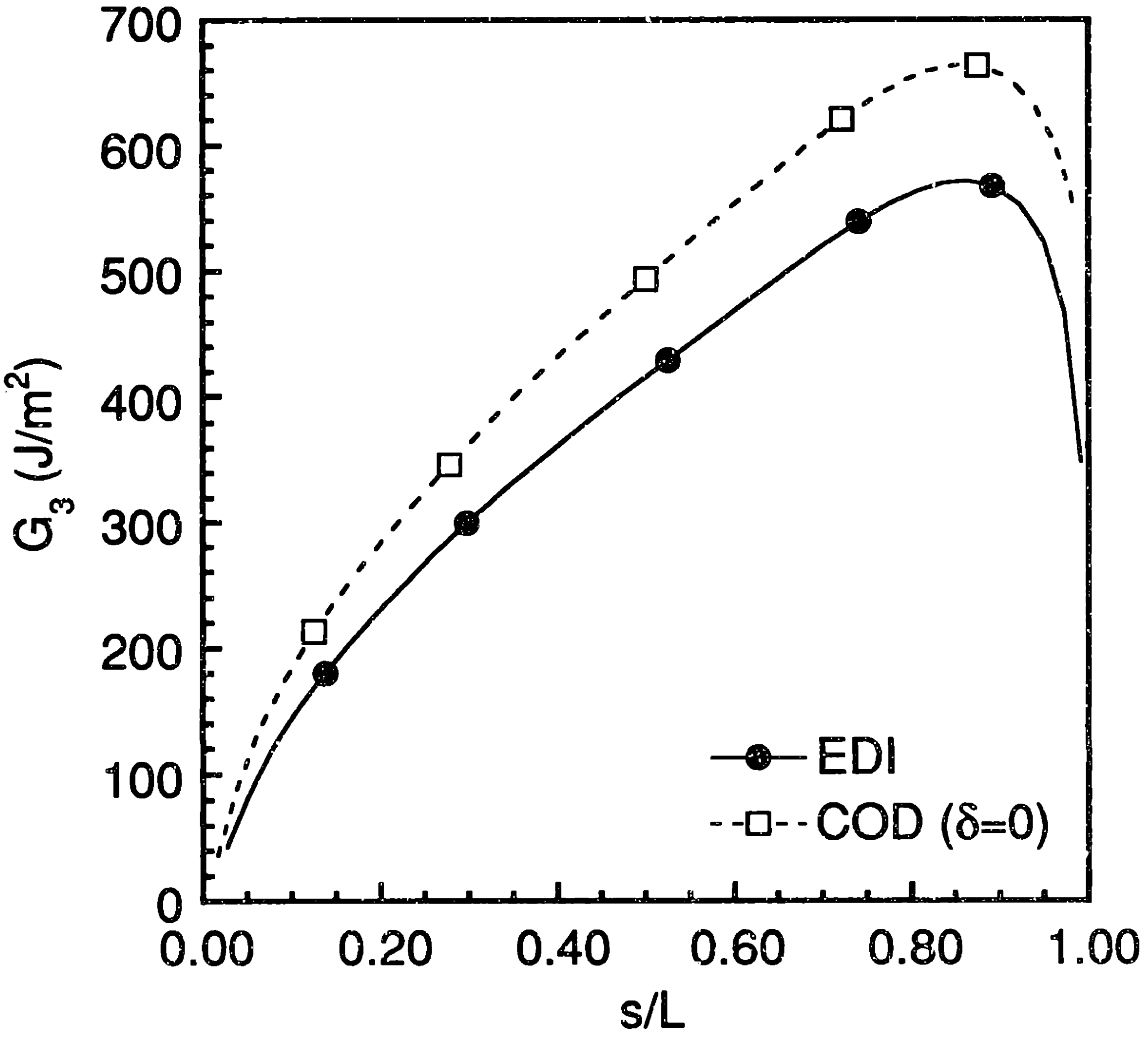

Figure 4.20 Mode III energy release rate along the delamination front obtained by the EDI approach and the COD approach with δ set equal to zero for the case of delaminated $[\pm 75_2]_s$ laminate.

CHAPTER 5

EXPERIMENTAL METHODOLOGY

The experimental program involves the manufacture and testing of AS4/3501-6 graphite/epoxy coupons of two types. The first type of specimens are unflawed specimens, and the second type have teflon strips implanted within them in order to simulate a delamination bordered by a matrix crack. The objectives of the experiments are to monitor the growth of the delamination and matrix cracks from the initial implanted configuration. Strain gages and X-ray radiography are used to trace any changes from the initial configuration.

The laminates manufactured for the current study are $[\pm 15_n/0_n]_s$ specimens with implants (with n equal to 2, 3 and 5) and both unflawed $[\pm 15_n]_s$ specimens and those with implants (with n equal to 2). No unflawed specimens of the $[\pm 15_n/0_n]_s$ specimens were manufactured because these specimens have been tested in earlier studies and adequate data such as failure stresses, strains and X-ray radiographs of damage states are available. The complete test matrix for this study is shown in Table 5.1.

5.1 Manufacture of Specimens

The unflawed specimens were constructed using the basic procedures developed at TELAC [79]. The second type of specimens were specialized with delaminations created in them. They therefore required some modifications of the basic procedures.

5.1.1 Layup Procedure

The unidirectional graphite/epoxy arrives from the manufacturer in rolls

Table 5.1 Test Matrix Used in Experimental Study

Type of Specimens	Laminate	Number of Specimens
Unflawed	$[\pm15_2]_s$	5
Implanted (10 mm)	$[\pm15_2]_s$	4
	$[\pm15_2/0_2]_s$	3
	$[\pm15_3/0_3]_s$	3
	$[\pm15_5/0_5]_s$	3

of semicured preimpregnated tape or "prepreg". The unidirectional graphite/epoxy rolls are 305 mm wide (12 inches nominal). The epoxy material is B-staged and is therefore stored at or below -18°C. Before prepreg is prepared for curing, it is allowed to warm up to room temperature for 30 minutes in a sealed bag to minimize condensation.

The prepreg is cut into individual plies and laid up into laminates in a "clean room". The temperature in this room is kept below 25°C and the relative humidity is kept low. Rubber gloves are worn during the cutting and laying up procedures to avoid contamination of the ply surface.

The standard TELAC manufacturing procedure involves the layup of 305mm by 350 mm laminates which are cured and subsequently cut into five coupons of size 50 mm by 350 mm. Razor blades and precisely-milled aluminum templates covered with guaranteed non-porous teflon (GNPT) are used to cut the prepreg into individual plies. Angle plies of unidirectional prepregs are cut with the help of trapezoidal templates. These are then cut in half such that the two halves can be put together to form a 305 mm by 350 mm rectangular ply with a precise angular orientation of the fibers such that there is only a matrix joint where the two halves meet. Hence, there are no fiber breaks in the resulting plies. The region of the joint then becomes indistinguishable from the remaining ply after the curing process.

The plies are stacked in a jig which allows precise alignment. The jig is made of an aluminum plate with two aluminum beams attached to it to form a 90° corner. Plies are carefully positioned into the corner of the jig. This "good corner" is used as the reference corner in later steps in the manufacturing procedure. The plies are tacky enough at room temperature to stick together and maintain proper fiber orientation.

The manufacture of the second type of specimens, which were implanted with teflon to create a delamination and matrix crack, differs only at this particular stage from the conventional manufacturing procedure. First, a collection of plies of the same orientation are layed up together. These are known as 'sublaminates' since they may be put together to form the complete laminate. The sublaminates are then cut into four pieces of 70 mm width each. The matrix crack was made along the fiber direction in the necessary sublaminate with a razor blade at a distance of 145 mm from one of the ends of the specimens as shown in Figure 5.1. The intrusion of the delamination at this stage was set at 20 mm. This allowed acheivement of the desired 10 mm intrusion upon cutting 50 mm wide coupons out of these 70 mm wide specimens. In the case of $[\pm 15_n/0_n]_s$ laminates, the matrix crack was placed only in one of the $[+15]_n$ sublaminate. In the case of the $[\pm 15_2]_s$ laminates, the matrix crack was placed in both the $[+15]_2$ sublaminates.

In order to create the delamination, a rectangular piece of teflon is placed underneath the sublaminate with the matrix crack. One of the edges of the teflon piece is located at the region where a delamination front is required, and another part of the teflon is pulled up from under the sublaminate and through the matrix crack as shown in Figure 5.2. The excess teflon material is wrapped around the triangular region and held in place by a piece of flash tape as shown in Figure 5.2. The flash tape ends up above the top surface of the laminate, on the teflon piece. The remaining procedure of layup is identical to that of the conventional specimens, with the individual sublaminates being layed up with the help of the aluminum jig discussed earlier. This procedure results in four specimens of size 70 mm by 305 mm.

Both sides of the laminates thus formed are covered with a sheet of "peel-ply" material. The peel-ply is a porous nylon material which protects the laminate surface before milling. The peel-ply extends approximately 50 mm past

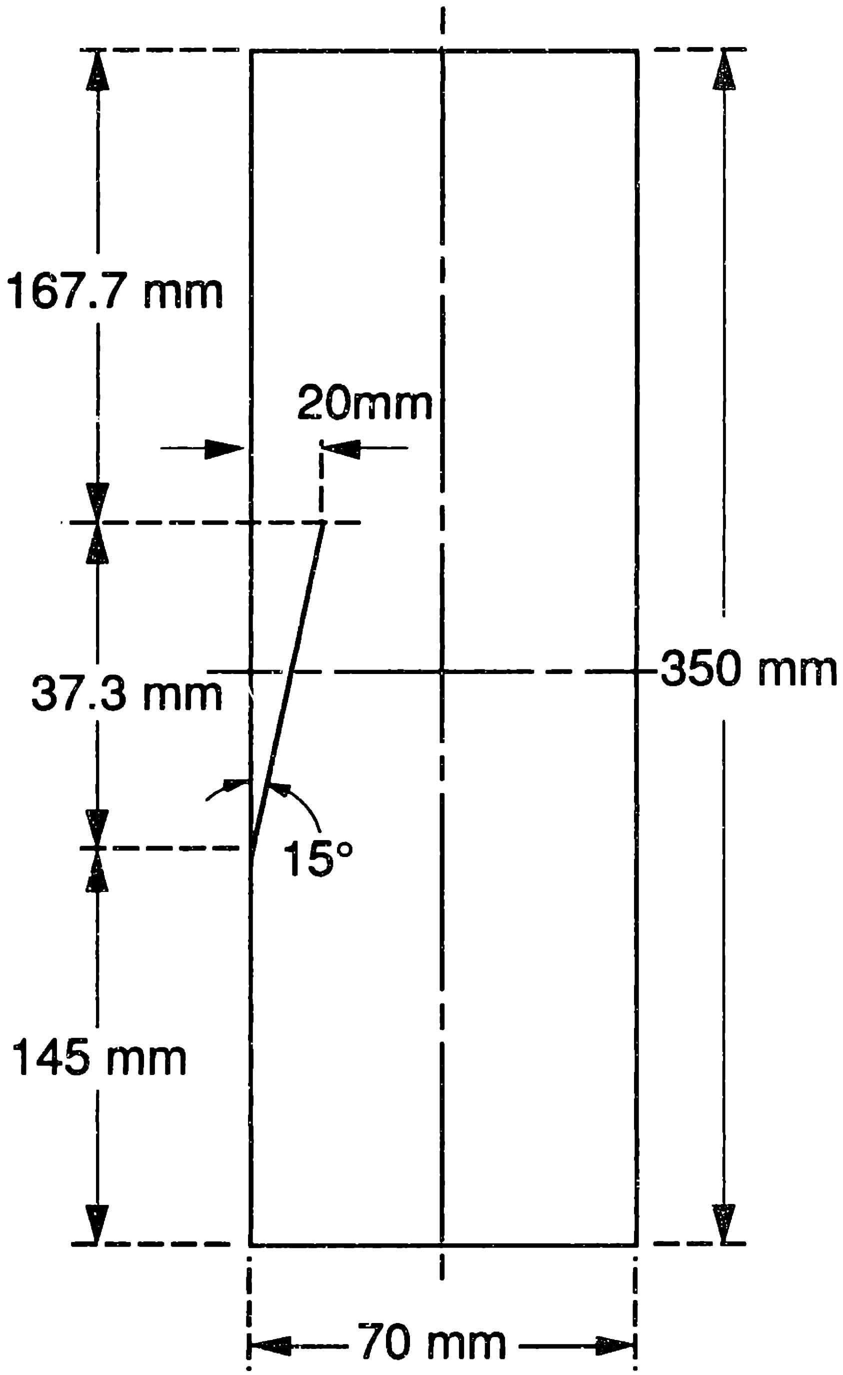

Figure 5.1 Dimensions and location of the matrix crack cut in the $[+15_n]$ sublaminate.

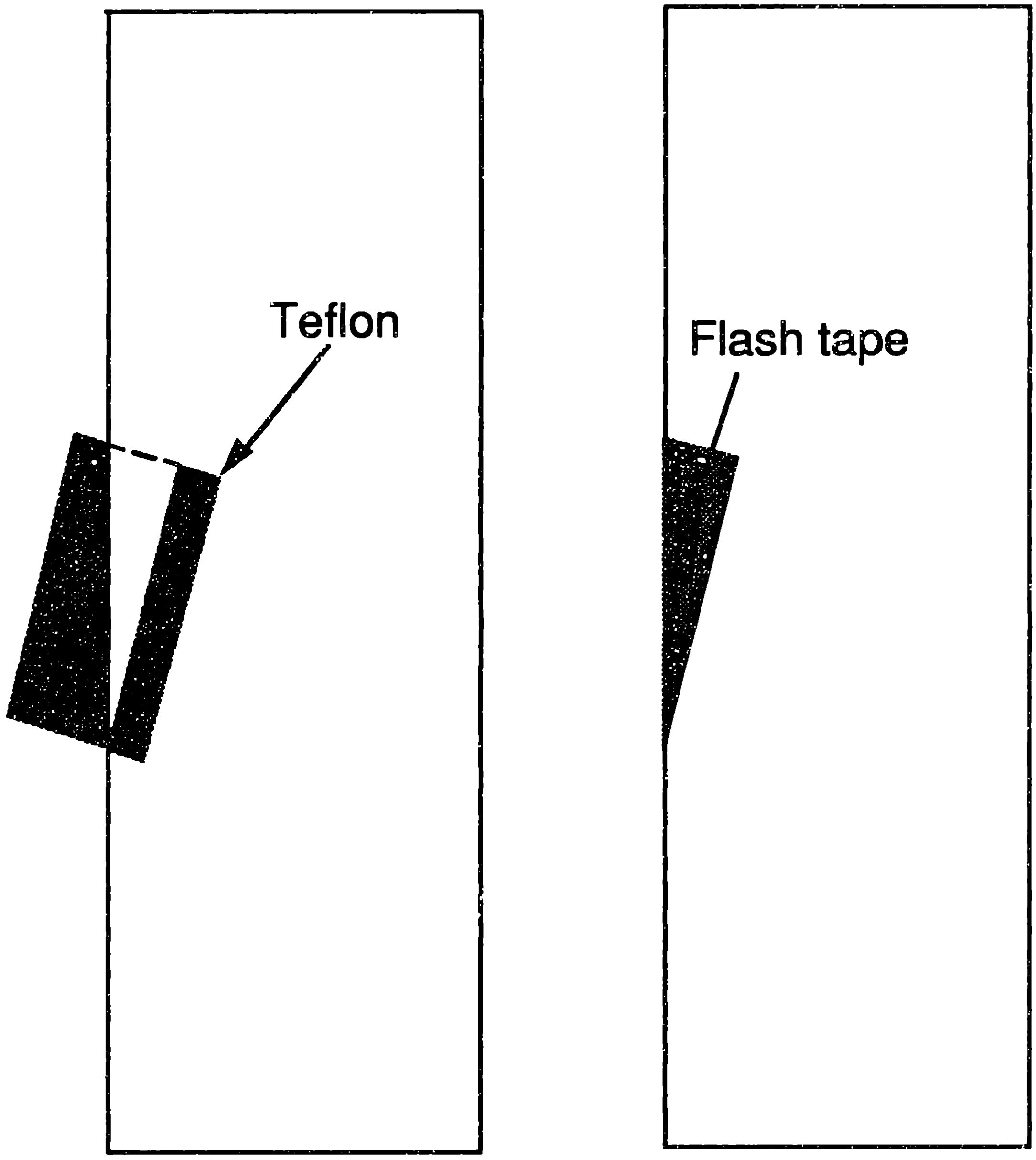

Figure 5.2 Placement of the (*left*) rectangular piece of teflon in the laminate and (*right*) folding the excess teflon piece to form the delaminated region.

the end of the laminate opposing the good corner. It is trimmed on all other sides to fit the laminate exactly.

5.1.2 Cure Procedure

The curing of the specimens involves setting up the cure assembly on the caul plate. The assembly includes coverplates, cork dams and a variety of other cure materials. A schematic of a cross-section of the cure assembly is shown in Figure 5.3.

The cure plate is a flat aluminum plate, 6.3 mm thick, and having two 12.7 mm diameter holes drilled at each end with appropriate plumbing installed to allow a vacuum to be drawn over the plate during a cure. The plate is coated with a mold release agent and covered with a sheet of GNPT. Aluminum dams with a "T" shape are positioned on the GNPT and held in position with pressure sensitive tape. These dams are also coated with a mold release agent. Two types of top plates were used depending on the size of the composite laminate being cured. For the 70 mm by 350 mm coupons, individual top plates were used for each coupon and the individual coupons were separated with corprene rubber ("cork") dams. The larger composite plates which were 305 mm by 350 mm, were cured using a single large top plate of appropriate size. The corner formed by the aluminum dams is the location of the good corner of the laminate.

The laminate is surrounded by several "curing materials" during the preparation for curing. First, a slightly oversized sheet of GNPT is placed in the curing area. Then the laminate covered with peel-ply is positioned with the reference corner placed in the corner formed by the aluminum dams. An oversized sheet of porous teflon is placed on top of the laminate. Precisely cut layers of a paper bleeder material are then positioned in the curing area. One layer of bleeder material is used for every two plies in the laminate. An

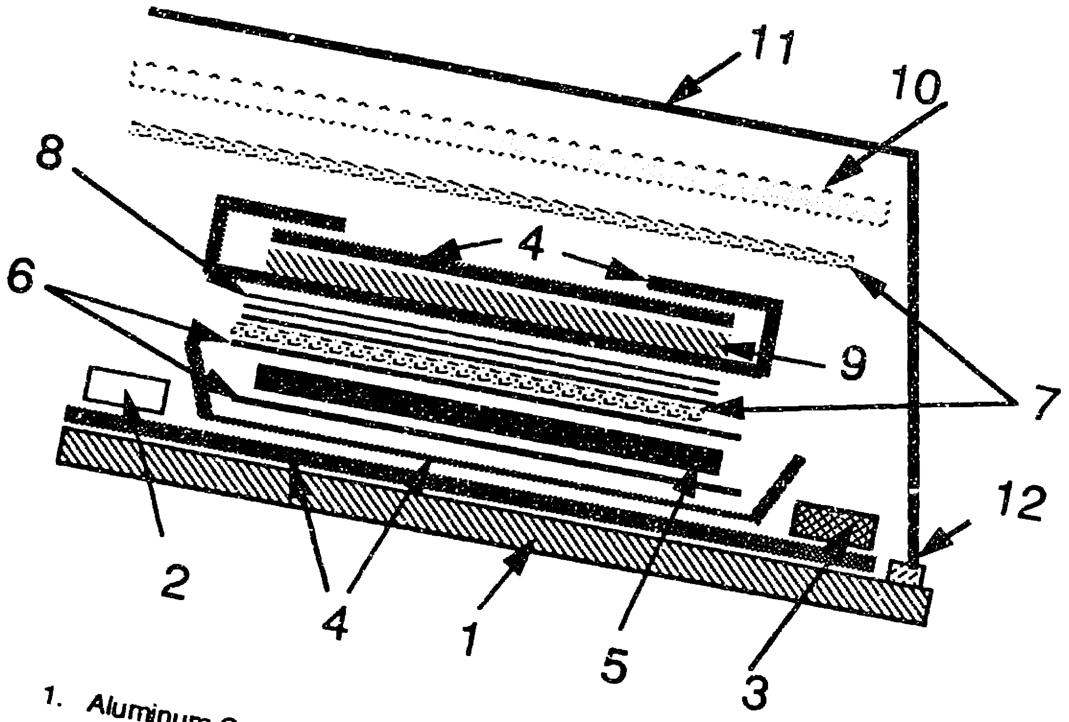

1. Aluminum Caul Plate coated with mold release
2. Aluminum Dams
3. Corprene (Cork) dams
4. "Guaranteed" Non-Porous Teflon
5. Laminate
6. Peel-Ply
7. Porous Teflon
8. Paper Bleeders
9. Aluminum Top Plate
10. Fiberglass Airbreather
11. Vacuum Bagging
12. Vacuum Tape

Figure 5.3 Cross-sectional view of the cure assembly.

oversized sheet of GNPT is placed on top of the bleeder. An aluminum top plate is coated with a mold release agent and placed on top of the GNPT.

After all the laminates to be cured are prepared in a similar manner, the cure assembly is covered with a large sheet of porous teflon and a sheet of fiberglass fabric. The fiberglass serves as an "air breather", providing a path for air and volatiles to be drawn to the vacuum hole and out of the system during the cure. The assembly is then surrounded with a vacuum tape sealant and covered with a high temperature vacuum bag.

The curing is done in an autoclave at an applied pressure of 0.59 MPa (85 psig). A vacuum is drawn on the plate through the vacuum holes. The nominal value of the vacuum is 760 mm (30 in) of mercury pressure differential below atmospheric pressure.

The cure is a two-stage process. The first stage is a one-hour "flow stage" at 117°C. The 3501-6 epoxy is at its minimum viscosity at this temperature. This facilitates the flow or "bleeding" of excess epoxy into the bleeder plies which in turn assures proper bonding of the plies and aids in the removal of voids by vacuum and pressure. The second stage is a two-hour "set stage" at 177°C. The polymer chains in the epoxy complete most of their cross-linking during this stage. Heat-up and cool-down rates are in the range of 1 to 3°C/min to avoid thermal shocking of the composites. An eight-hour postcure at 177°C in an unpressurized oven is used to drive the cross-linking process to completion. The cure cycle is shown schematically in Figure 5.4.

5.1.3 Preparation of Coupon Specimens

The resulting cured plates are 305 mm by 350 mm and the individually cured specimens with implants are 70 mm by 350 mm. These cured parts are milled to final dimensions with a water-cooled diamond blade. The specimens with implants were scribed to mark a 50 mm wide and 350 mm long specimen, with the desired 10 mm intrusion of the teflon strip within the specimen as indicated schematically in Figure 5.5. The matrix crack in the $[+15]_n$ sublaminate is visible on the top surface of the laminate. Hence, the measurement of the intrusion can be obtained relative to the matrix crack front. The specimens were then milled along these scribe lines. In some specimens with implants, the teflon strips could be removed. However, in specimens where the teflon offered considerable resistance to removal, or tore into pieces, no further effort was made to remove them.

After the specimens were cut to the required size, thickness and width measurements were taken from the test section of each coupon at the marked points shown in Figure 5.6. Thickness measurements were taken at 9 points with a digital micrometer and width measurements were taken with calipers at three points along the length of the specimen. The location of the measurement points in the case of the implanted specimens was moved so that no points fell on or within the implanted region as shown in Figure 5.6.

The measured thicknesses are used as quality control checks to enable a rough estimate of the epoxy content left within the ply. For purposes of stress calculations, however, the nominal thickness (0.134 mm) of the specimens have been used. The average thickness of the unflawed $[\pm15_2]_s$ specimens were about 3% above the nominal thickness. The average thicknesses of the $[\pm15_2]_s$ specimens with implants were about 3% below the nominal thickness, respectively.

The loading tabs used in the coupon specimens are made from $[0/90]_{ns}$ cross-ply laminates of Scotchply 1002 fiberglass/epoxy. These are obtained as precured 380 mm by 610 mm sheets of various thicknesses. The thickness of the tabs that were chosen was based on standard TELAC procedure. These

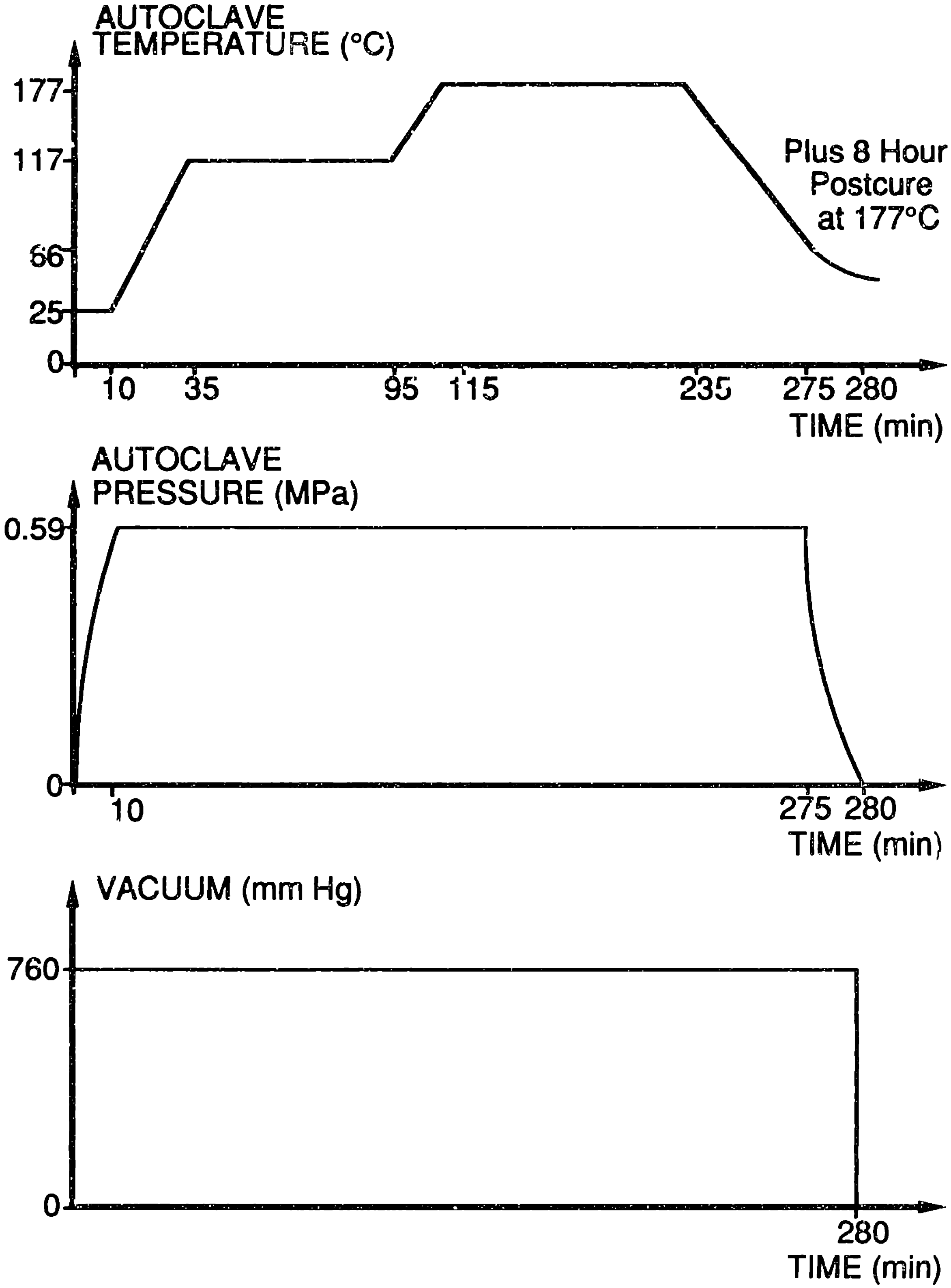

Figure 5.4 Cure cycle for AS4/3501-6 graphite epoxy.

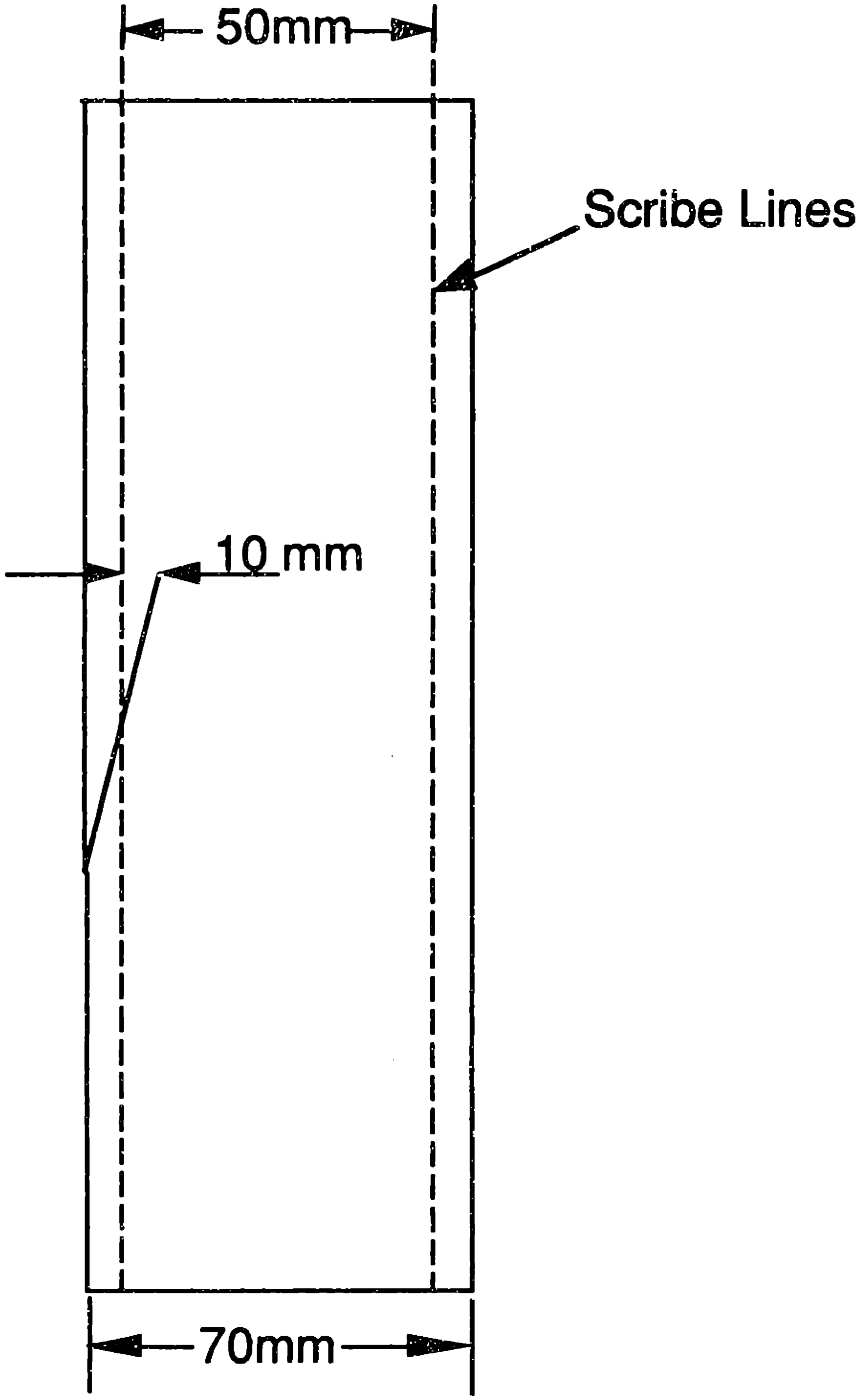

Figure 5.5 Illustration of scribe lines for milling of the laminate down to the required coupon size.

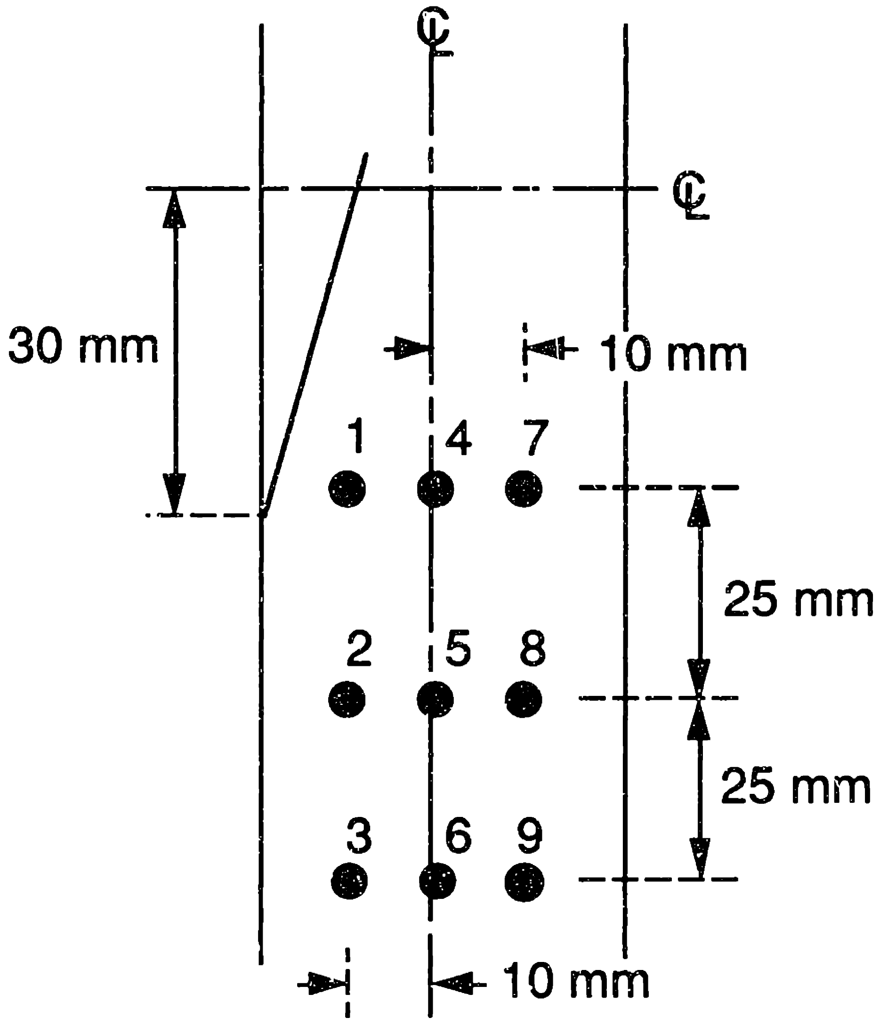

Figure 5.6 Location of specimen width and thickness measurements.

fiberglass/epoxy sheets were cut into rectangular pieces 75 mm long and 50 mm wide and these pieces beveled on a belt sander to a 30° angle so that the tabs, when placed on the test specimens, would taper towards the test section, as shown in Figure 3.9. These loading tabs were bonded to the specimens with FM-123 film adhesive from American Cyanamid. The FM 123-2 film adhesive was cured in the autoclave using the cure assembly shown in Figure 5.7. Steel cover plates 380 mm long were used to help apply even pressure over the tab. The adhesive was cured at 107°C for two hours, with an external pressure of 0.069 MPa plus a 30 mm Hg vacuum. This provides the recommended 0.35 MPa pressure on the bond surfaces given the ratio of pressure surface to bond surfaces.

The final step in the specimen preparation procedure was the instrumentation of the specimen with strain gages. All unflawed specimens were outfitted with two primary strain gages at the center of the test section, one aligned with the longitudinal (loading) axis, the other aligned with the transverse axis. These gages provide the longitudinal and transverse strains used to calculate the elastic constants of the specimen. The standard strain gage configuration is shown in Figure 5.8. In the case of the specimens with implants, the gages needed to measure far-field strain are located at the bottom of the specimen as shown in Figure 3.9. Large strain gages of the type EA-06-125AD-120 manufactured by Micro Measurements were used for measuring the far-field strain data.

In addition to the far-field gages, the specimens with implants also had strain gages located at the delamination and matrix crack fronts. In the case of the $[\pm 15_n/0_n]_s$ laminates, the strain gages were placed at a distance of 5 mm and 10 mm from the free edges of the laminates. These gages were of the type EA-06-031DE-120 which are small gages manufactured by Micro Measurements.

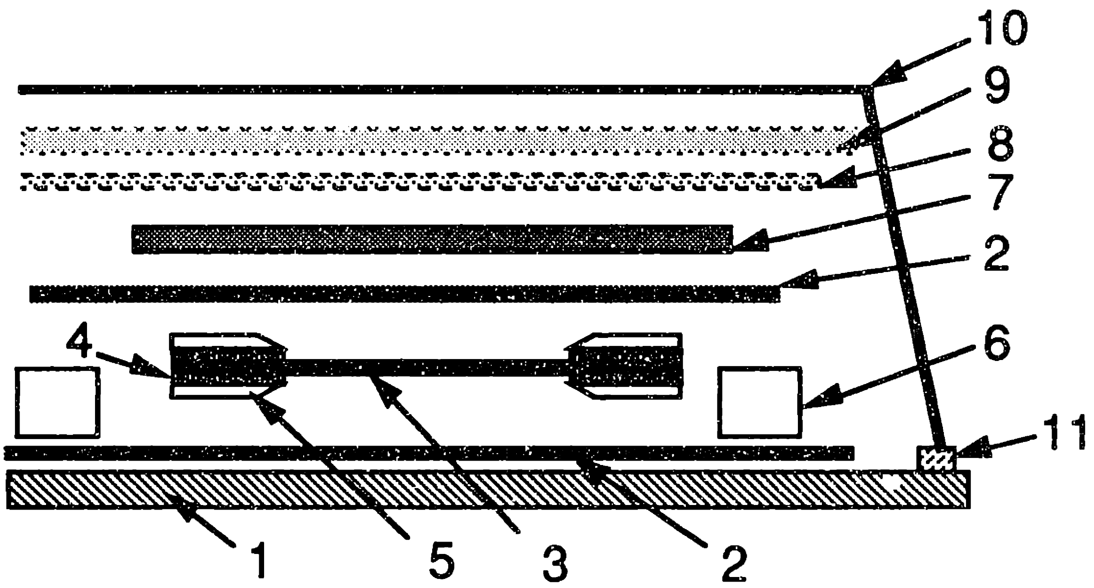

1. Aluminum Caul Plate
2. "Guaranteed" Non-Porous Teflon
3. Specimen
4. FM123-2 Film Adhesive
5. Fiberglass/Epoxy Loading Tab
6. Support Tabs
7. Steel Cover Plate
8. Porous Teflon
9. Fiberglass Airbreather
10. Vacuum Bagging
11. Vacuum Tape

Figure 5.7 Cure assembly cross-section for a tab-bond cure.

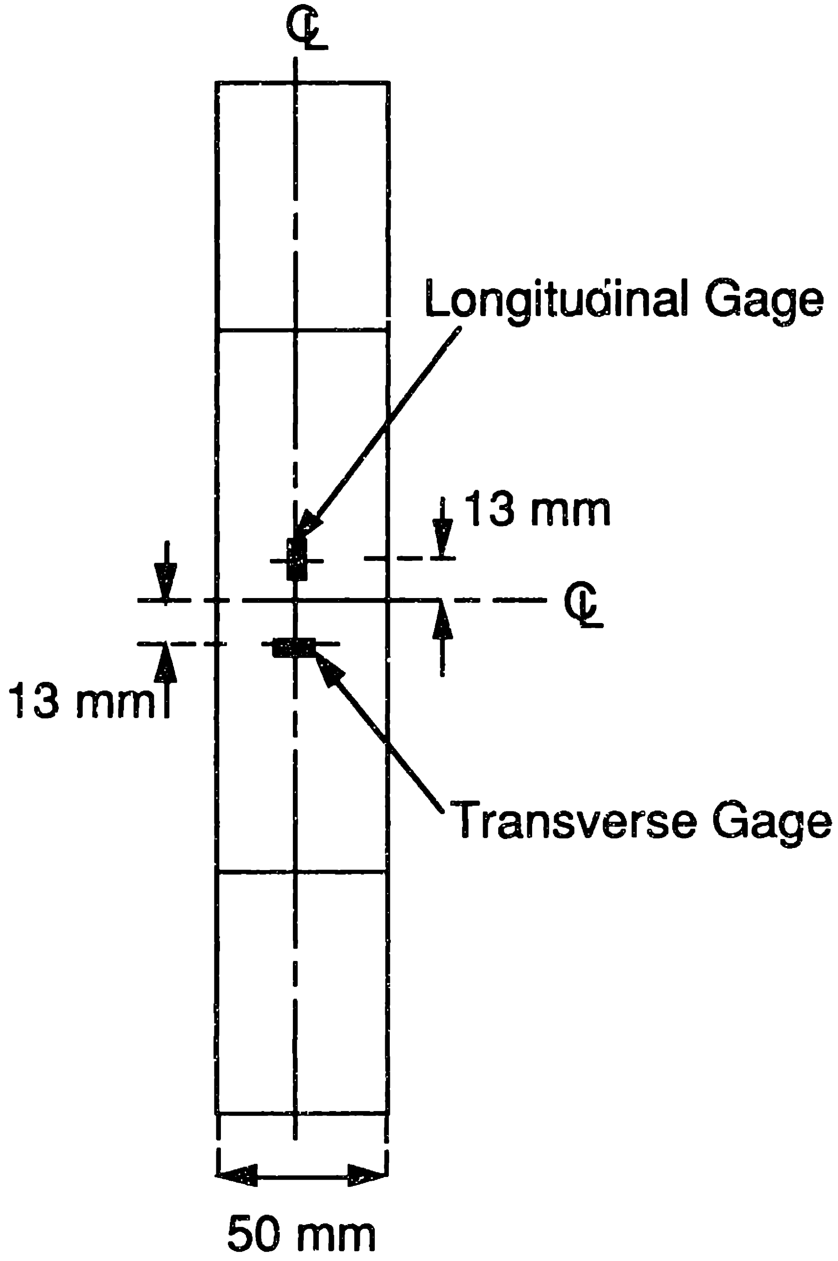

Figure 5.8 Location of strain gages on unflawed specimens.

The gages at the delamination front and the matrix crack front were oriented along the direction of the loading axis. The gages in the $[\pm15_2]_s$ specimens, were placed slightly differently based on the experience and results obtained from the testing of the $[\pm15_n/0_n]_s$ specimens. The strain gages at the delamination front in the $[\pm15_2]_s$ laminates were relocated to be as close to the free edge as possible as shown in Figure 5.9 as this was the location where initial growth was detected in the $[\pm15_n/0_n]_s$ specimens. The gages at the matrix crack tip were tilted so that they were aligned along the axis of the matrix crack, as this enabled the placement of the gage closer to the tip of the matrix crack. Since the delamination was implanted symmetrically in the $[\pm15_2]_s$ laminates, the strain gages were also located symmetrically on both faces of the laminate.

5.2 Testing Method

The testing system used in this investigation consists of an MTS 810 hydraulic test machine interfaced with a Macintosh computer equipped with an Analog-Digital board. The testing machine has a capacity of 100,000 pounds (445kN) and is equipped with hydraulic grips. The computer is set up for data acquisition.

5.2.1 Basic Test Procedure

At the beginning of each test, the specimen was placed in the testing machine and gripped at its upper end only, with the lower grip being placed, but not closed, around the lower end of the specimen. This is defined as the zero strain condition. A machinist's square is used to ensure that the longitudinal axis of the specimen was parallel to the loading axis by using one edge of the specimen and the upper grip of the machine as references for the square. In the unloaded condition, the load and strain channels are zeroed and all active strain gage conditioners balanced and calibrated. Calibration of the strain gage

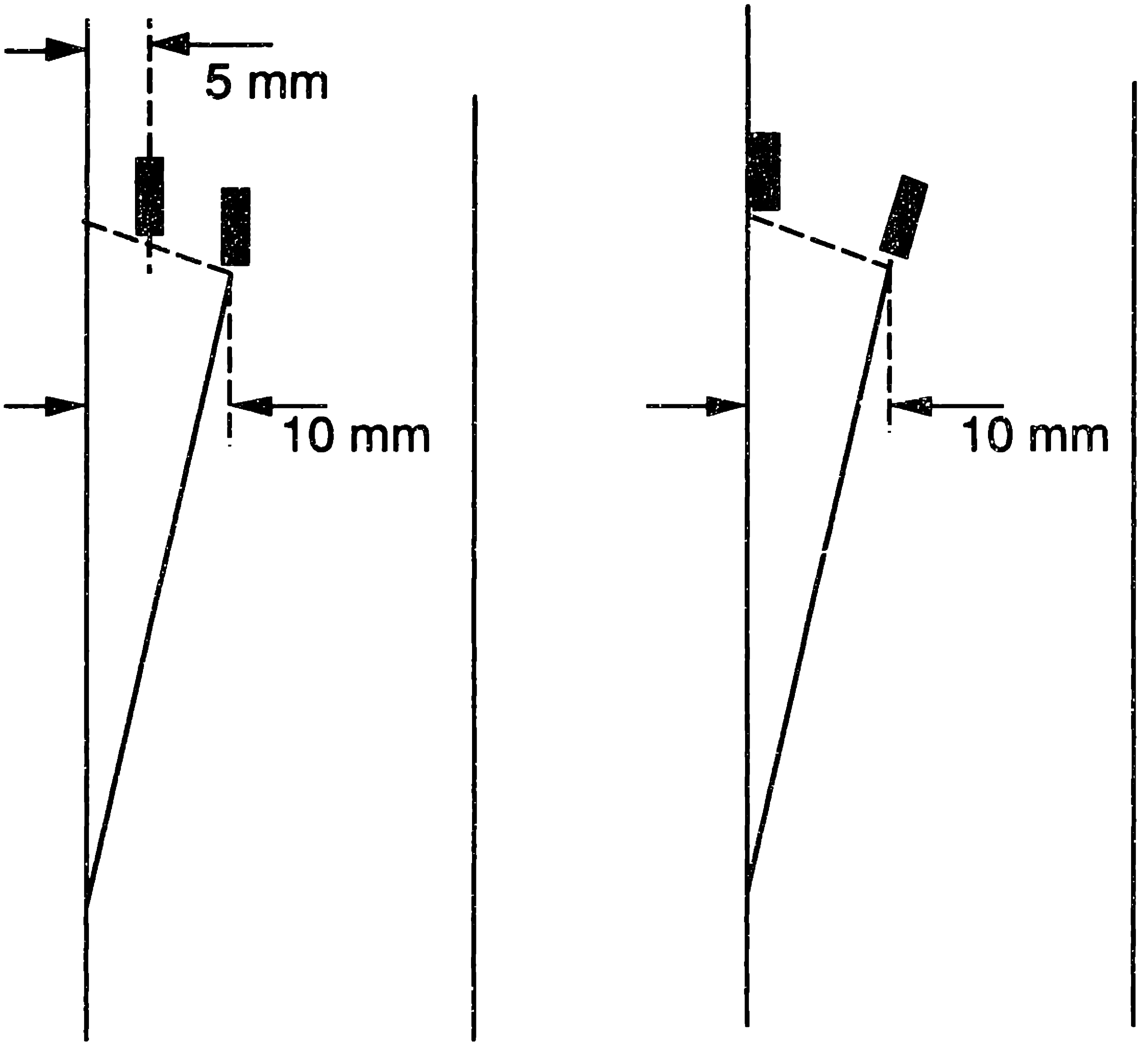

Figure 5.9 Location of strain gages on (*left*) $[\pm 15_n/0_n]_s$ specimens and (*right*) $[\pm 15_n]_s$ specimens.

conditioners was accomplished by placing a precision decade resistor in parallel with the active gage to simulate a strain of a certain magnitude, then adjusting the conditioner gain until the computer read the desired value. After all calibration is complete, the lower grip was closed. The specimens were loaded at a constant stroke rate of about 1.09 mm/min, producing a strain rate of approximately 5000 microstrain/min which is similar to standard tests. The resolution of the raw data obtained from the computer was 12.5 microstrain for strain, and 48.5 pounds (215.7 N) for load. The resolution of the load data depends on the load range used, which in turn was governed by the maximum expected failure load. The expected failures in the present study were under 20,000 pounds, and hence the machine was set to 20% of its load capacity. The data files also contain marks which were inserted manually whenever any visible or audible damage was detected during testing.

One specimen of each type was tested monotonically to failure at a stroke rate of 0.38 mm/minute. This stroke rate was rather slow and was chosen to avoid any rate effects on the specimens during testing. The results from this data was used to determine the points at which the tests of the remaining specimens were to be stopped for X-ray examination. These points are determined so that the tests would be halted in order to take X-ray radiographs in between any points of nonlinearity or kinks observed in the load versus strain data of all the gages. The specimens were unloaded for X-ray examination and, after taking the X-ray radiographs, the specimens were reloaded. This process was repeated until the failure of the specimens and usually resulted in three to four stops before final failure.

5.2.2 Dye Penetrant-Enhanced X-radiography

The study of delamination growth and final failure requires that the damage state be nondestructively monitored over a series of tests. The method used for monitoring delamination growth is dye penetrant-enhanced X-radiography. The dye penetrant used is di-iodobutane (DiB), which is a liquid. DiB is applied to the free edge of a specimen with a cotton swab and in the case of specimens with implants, a syringe is used to inject it inside the delaminated region. In the case of unflawed specimen, it is done after a test while the specimen is at half the maximum stroke level. But in the case of implanted specimens, it was done after removing the specimen from the testing machine. Since the delamination was open and the DiB seeped in quite easily. The DiB has a low viscosity and can seep into delaminated regions via capillary action.

After DiB has been applied, the specimen is removed from the testing machine. The location of the DiB can be detected from the radiographs. The X-ray machine used in this investigation is a Scanray Torrex 150D X-ray Inspection Device. The machine is used in "timed radiation" (TIMERAD) mode. An unexposed sheet of black and white instant film is placed on a sensor in the X-ray chamber. The film used is 100 mm by 125 mm (4 in by 5 in nominal) Polaroid PolaPan instant sheet film type 52. The portion of the specimen to be X-rayed is placed on top of the film. The door to the X-ray chamber is closed and the X-ray generator is activated. When the sensor detects a certain quantity of radiation, the X-ray generator is shut off. The quantity of radiation detected by the sensor is set to between 230-260 mR (milliRoentgens) depending on the level of contrast desired.

The film can be developed using a standard Polaroid camera back. The resulting X-radiograph essentially shows three shades of gray. The region of the film which is not shielded by any portion of the specimen is mostly white. The region under the undelaminated section of the laminate is a medium gray. This results from the fact that the specimen absorbs a significant portion of the X-rays passing through it. The delaminated region shows up in dark gray. This is due to the fact that the thin layers of DiB in the delaminations absorb a large fraction of the X-rays passing thorough them.

The X-ray radiographs are presumed to represent the approximate location of the delamination front, matrix crack front and any other form of damage where the DiB may seep in, such as additional matrix cracking that may occur.

5.2.2 Data Reduction

The raw data files, as created by the data acquisition program, contain the load in pounds, stroke in inches, and strain in microstrain. The first step in data reduction is to snip off extraneous data points which were recorded after final failure of the specimen or before loading of the specimen began. The failure loads, stroke and far-field strain of the specimen are recorded from the data files.

With the data reduced to the required form, the elastic modulus and the Poisson's ratio are determined from linear regressions of the appropriate stresses and strain. In these cases, a special program was used to determine the linear regions of maximum correlation, with the elastic constants being taken as the slope of the first significant linear region [80]. Plots of the stress-strain data are also used to determine whether any changes in strain are observed in the gages ahead of the delamination and the matrix crack.

CHAPTER 6

RESULTS

The results for the $[\pm15_n/0_n]_s$ and $[\pm15_2]_s$ laminates obtained from the testing of the unflawed specimens and those with implants are described. In section 6.1 of this chapter, the experimental results are presented. The results obtained from the analysis of the finite element model of the $[\pm15_2]_s$ laminate are presented in section 6.2.

6.1 Experimental Results

The results are divided by laminate type. The results for the $[\pm15_n/0_n]_s$ specimens are presented in subsection 6.1.1 and the results for the $[\pm15_2]_s$ specimens are presented in subsection 6.1.2.

6.1.1 $[\pm15_n/0_n]_s$ laminates

The $[\pm15_n/0_n]_s$ specimens with implants were the first to be tested. The modulus data of these specimens are presented in Table 6.1. The theoretical modulus as computed from classical laminated plate theory using the basic material properties listed in Table 4.1 is 125 GPa for unflawed specimens of this type. The average modulus for the $[\pm15_2/0_2]_s$ specimens is 123 GPa which is similar to this theoretical value with a difference of only 5% between the two despite the presence of the delamination. The average moduli of the $[\pm15_3/0_3]_s$ specimens and the $[\pm15_5/0_5]_s$ specimens are 114 GPa and 117 GPa which are very close to each other and these deviate from the theoretical value by about 7%. The coefficients of variation for these laminates are less than 4%. These moduli may be compared to the data available from previous research on

Table 6.1 Moduli[a] and failure stresses and strains for $[\pm 15_n/0_n]_s$ specimens implanted with triangular-shaped delaminations of 10 mm intrusion.

Laminate	Specimen	Modulus (GPa)	Failure Strain (μstrain)	Failure Stress (MPa)
$[\pm 15_2/0_2]_s$	1	125	7140	861
	2	120	7180	837
	3	125	6380	785
	Average	123 (2.3%)[b]	6900 (6.5%)	828 (4.7%)
$[\pm 15_3/0_3]_s$	1	110	6380	689
	2	115	5540	663
	3	118	6090	718
	Average	114 (3.5%)	6003 (7.1%)	690 (4.0%)
$[\pm 15_5/0_5]_s$	1	119	4890	541
	2	117	4320	505
	3	116	4150	474
	Average	117 (1.3%)	4453 (8.7%)	507 (6.6%)

[a] Theoretical value obtained via classical laminated plate theory is 125 GPa

[b] Numbers in parentheses are coefficients of variation.

unflawed laminates, presented in Table 6.2 [6]. The average modulus for the unflawed laminates are 122 GPa, 123 GPa and 117 GPa, respectively, which are very similar to the values obtained for the specimens with implants.

The failure stresses and strains for these specimens are also listed in Table 6.1. These are the maximum stresses and strains attained by the specimen after which there was an abrupt drop in the load to 50% or lower of the maximum load carried. This was defined as the failure of the specimen. The failure stresses and strain of the specimens with implants may be compared to the data available from previous research on unflawed laminates, presented in Table 6.2 [6]. The difference in the failure strains between the unflawed specimens and the specimens with implants is 9% or less for the laminates with n equal to two and three. In the case of the laminate with n equal to five, the specimens with implants failed at strains which were about 21% lower than that of the unflawed specimens. The presence of the secondary matrix cracking observed in the cured laminate in the -15° plies may be one reason for their premature failure.

The stress-strain data for the different specimens with far-field gages, delamination front gages and matrix crack front gages are presented here. The arrows placed in the graphs indicate the first sign of a discontinuity observed in the linear behavior of the data obtained from the delamination front and matrix crack front gages. These discontinuities indicate the possibility that there is an alteration in the characteristics of the region around the delamination and matrix crack front most likely associated with damage growth.

The first specimen of each laminate type was tested monotonically to failure as described in Chapter five. The second and third specimens of each laminate type were loaded to about 60% of the failure stress as obtained from the first specimen. Subsequently they were incrementally tested with X-ray radiographs

Table 6.2 Failure stresses and strains for $[\pm15_n/0_n]_s$ specimens unflawed specimens [6].

Laminate	Modulus (GPa)	Growth to Tab Strain (μstrain)	Growth to Tab Stress (MPa)	Failure Strain (μstrain)	Failure Stress (MPa)
$[\pm15_2/0_2]_s$	122	6355	713	6355	747
$[\pm15_3/0_3]_s$	123	5004	603	5997	642
$[\pm15_5/0_5]_s$	117	4824	567	5626	618

[a] Theoretical value by classical laminated plate theory is 125 GPa

taken at intervals of 100 MPa, at which the testing was stopped. For all the cases tested here, if delamination growth occurred, it was always observed in the X-ray radiographs taken before the final failure of the specimen occurred. Hence, in the case of these specimens there are two sets of stress-strain data presented: the first is the loading penultimate to failure, where discontinuities are observed in the data obtained from the strain gages, and the X-rays indicate growth of the delamination front; the second set represents the data when the specimen is loaded to failure .

The stress-strain data for the first specimen of the $[\pm15_2/0_2]_s$ implanted laminate is shown in Figure 6.1. The gage at the delamination front has a discontinuity in the data before any other gage as indicated by the arrow in Figure 6.1 at approximately 635 MPa. It, however, continues to register data till about 735 MPa when the strain level drops drastically indicating that some changes have occurred in the damage state along the delamination front. The latter discontinuity is registered by all the other gages including the far-field gage indicating that the change in damage configuration is significant enough to affect the global behavior. There are small discontinuities observed in the data obtained from the strain gage located at the matrix crack front. However, this latter gage continues to register strain almost up to the failure load of the specimen. Since this specimen was monotonically tested, there are no X-ray radiographs of the delamination.

The stress-strain data for the second specimen is presented in Figures 6.2 and 6.3 for two consecutive tests, i.e. the test which precedes failure and the test at which failure of the specimen takes place, respectively. The X-ray radiographs taken in between these two consecutive tests are shown in Figure 6.4. The same is repeated here for the third specimen of this type. Figures 6.5 and 6.6 are for consecutive tests of these specimens and the X-ray radiographs taken in between

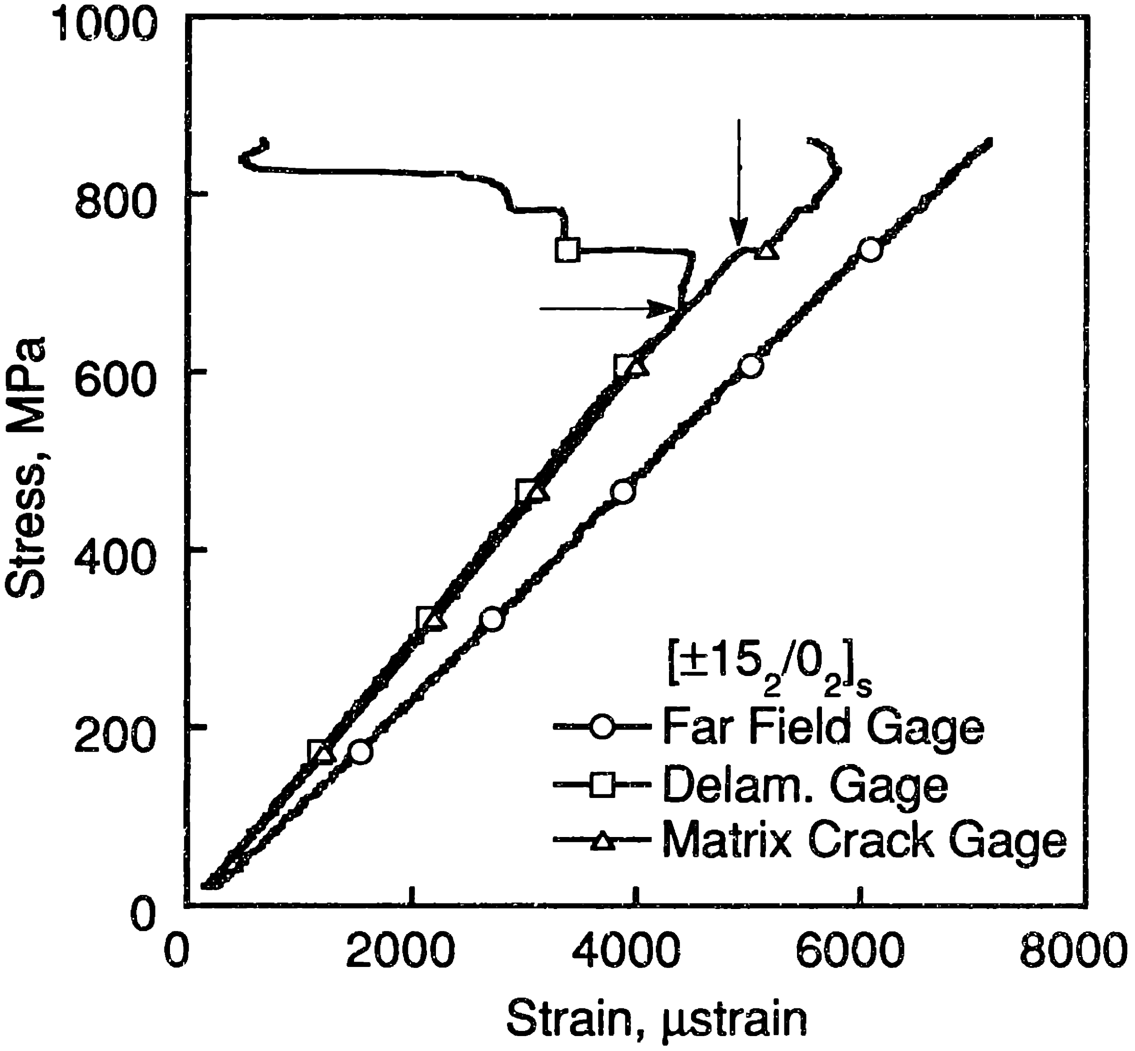

Figure 6.1 Stress-strain data for $[\pm15_2/0_2]_s$ specimen #1 with implant tested monotonically to failure.

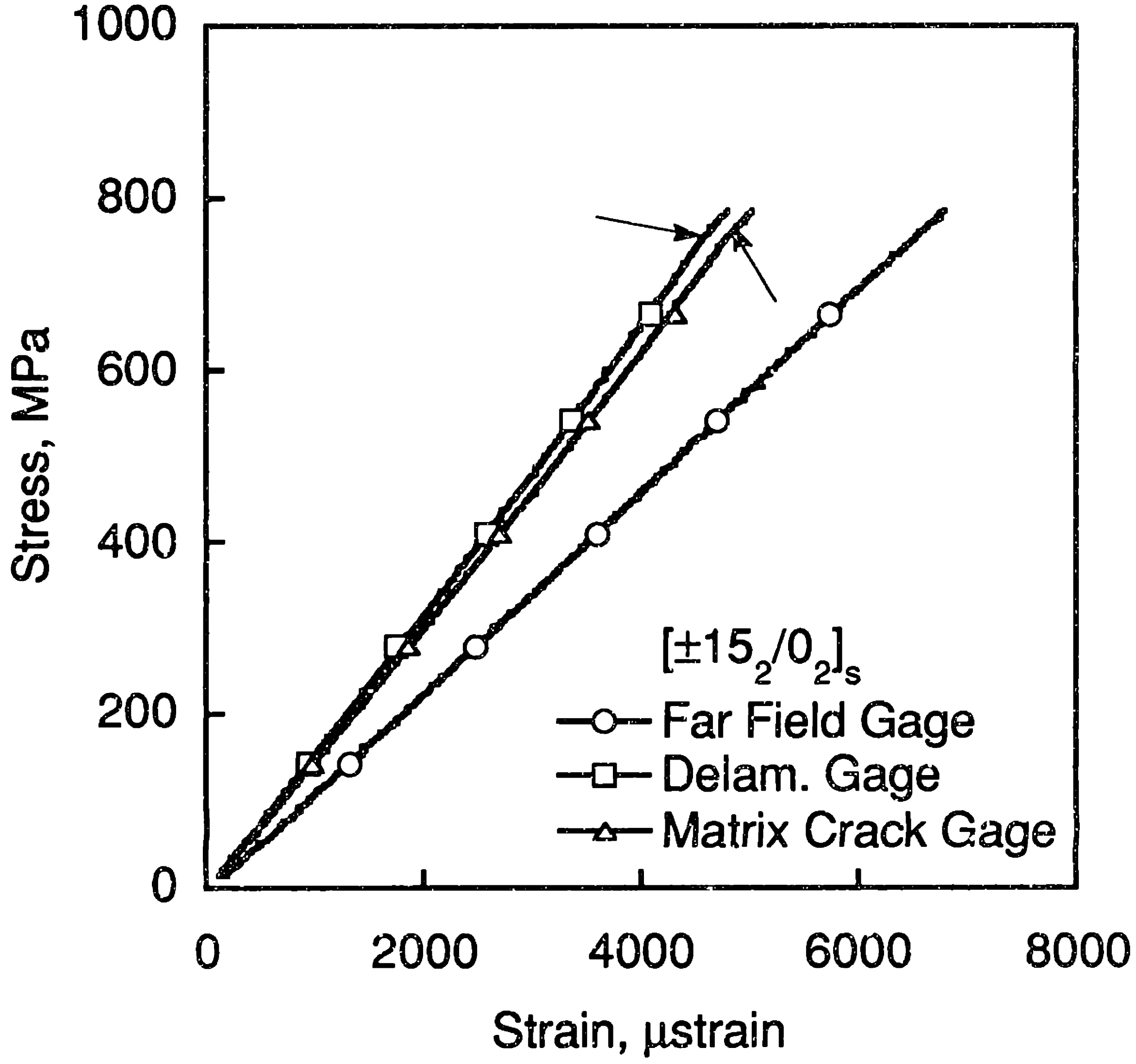

Figure 6.2 Stress-strain data for $[\pm 15_2/0_2]_s$ specimen #2 with implants obtained for the loading case which precedes the test to failure.

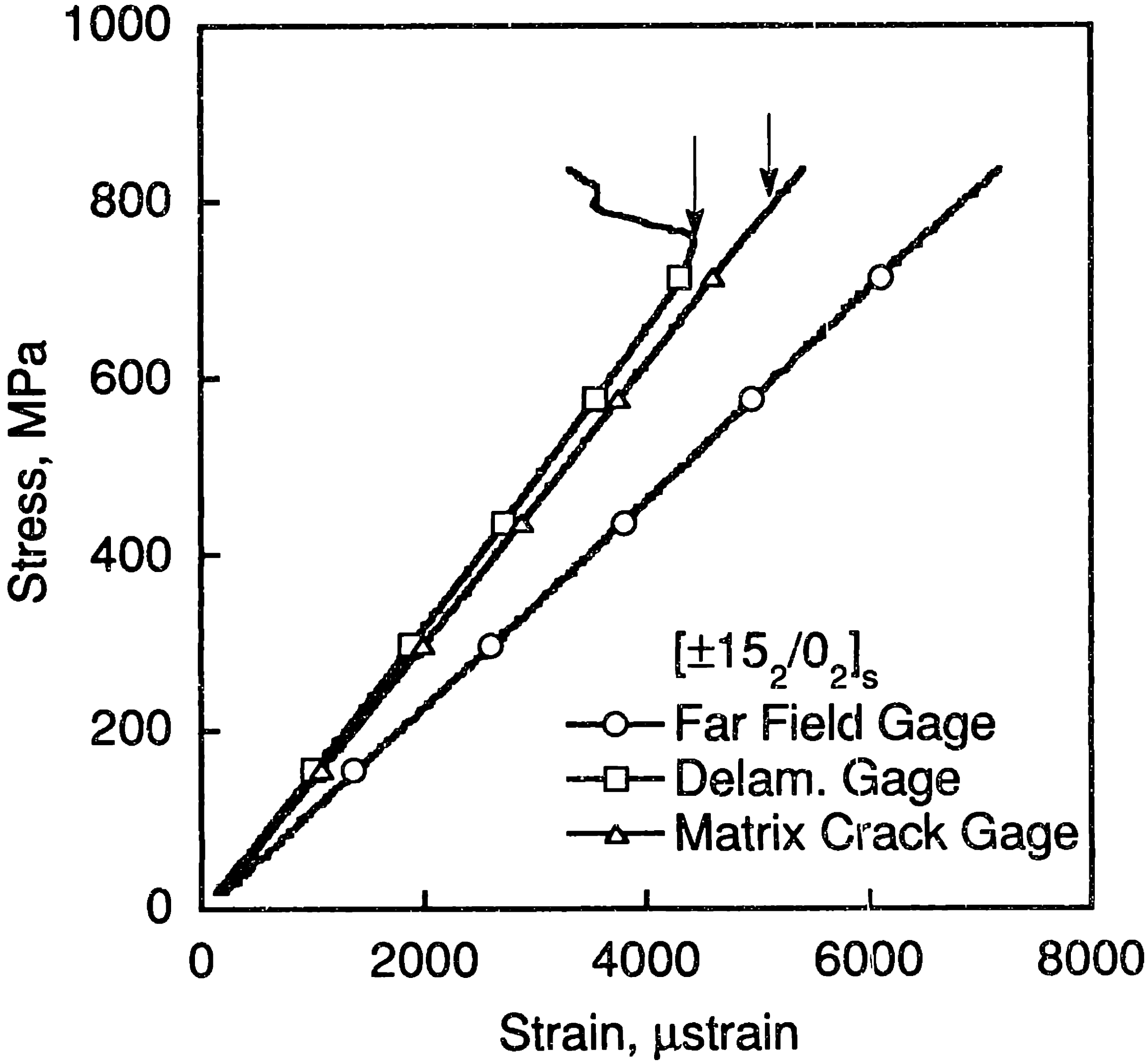

Figure 6.3 Stress-strain data for [±$15_2/0_2$]$_s$ specimen #2 with implant obtained on testing to failure.

these tests are shown in Figure 6.7.

These results show that there is a discontinuity that exists in the stress-strain data which is barely discernible in Figure 6.2, and may be placed at around 750 MPa, but more apparent in Figure 6.5, at about 630 MPa, which is about the same stress level at which the discontinuity was observed in the first specimen. The X-ray radiographs in Figure 6.4 and 6.7 both display growth of the delamination. The growth discernible from these radiographs along the delamination front has occurred in the vicinity of the free edge and no growth is observed near the matrix crack front region of the delamination. The delamination is observed to have grown by approximately 5 mm at the free edge region in both the cases. This growth reduces as the matrix crack front is approached and consequently it appears that the entire delamination front has changed from its initial 90° angle to the matrix crack front to a curved front. No secondary cracking is visible in the X-ray radiographs at this stage.

The stress-strain data obtained in the test of the specimen to failure indicates that the delamination front strain is the first to drop, followed by the strain read by the matrix crack gage at either the same stress level or a higher stress level and finally the far-field gage ceases to take data at failure. Even though growth of the delamination occurs, it does not grow unstably to the ends of the specimen and in almost all the cases it is accompanied with some fiber failure. The unflawed specimens [6] had delamination growth to the ends of the specimen and considerable amount of fiber failure was also observed implying that the delamination growth competes with with fiber failure. In fact, for unflawed specimens with a smaller value of n, i.e. $[\pm15/0]_s$ laminates (with n equal to one), the specimen failure was almost entirely due to fiber failure. The average failure strains for the unflawed specimens and specimens with implants are similar. The photograph of a typical failed specimen is shown in Figure 6.8

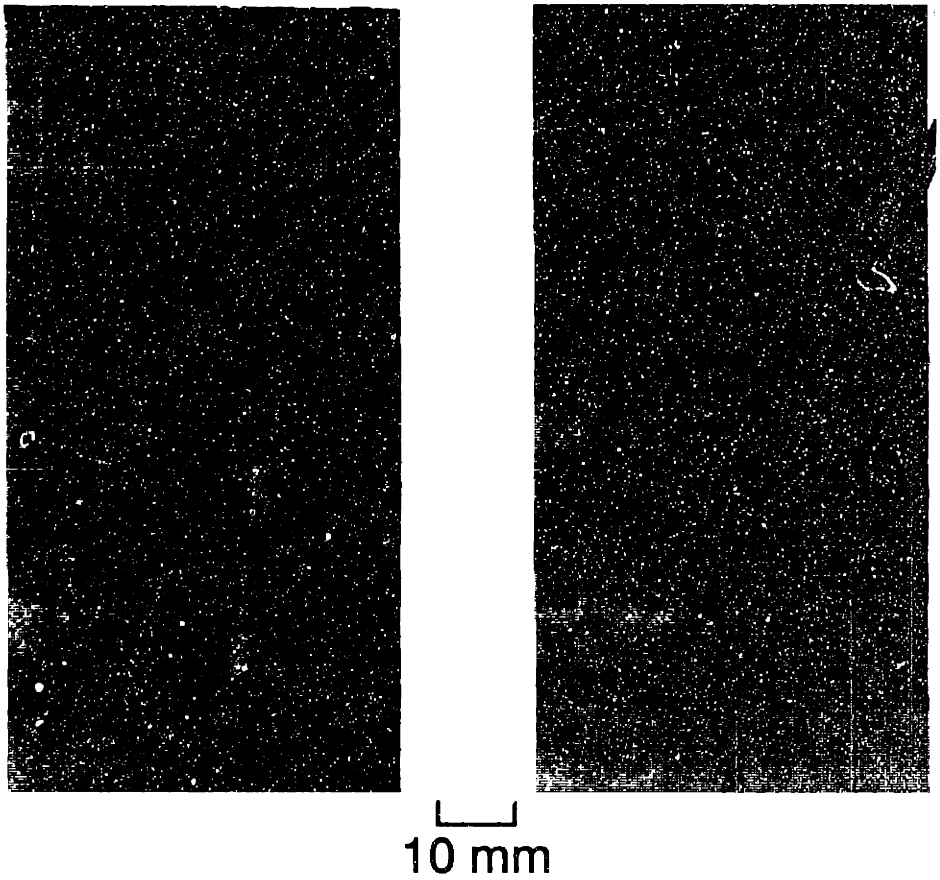

Figure 6.4 X-ray radiographs of $[\pm 15_2/0_2]_s$ specimen #2 with implant (*left*) before loading and (*right*) after loading to approximately 800 MPa.

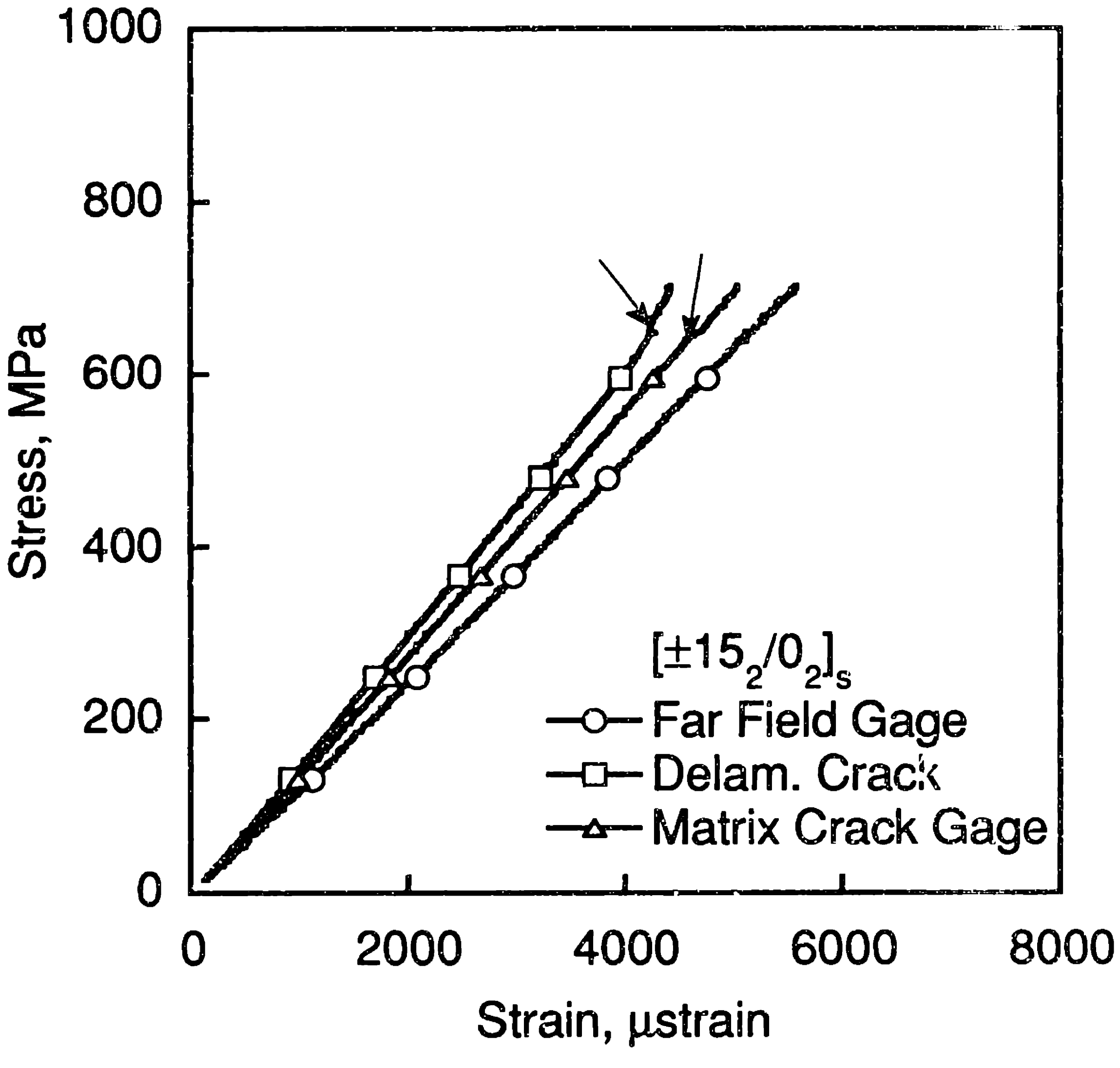

Figure 6.5 Stress-strain data for [$\pm15_2/0_2$]$_s$ specimen #3 with implant obtained for the loading case which precedes the test to failure.

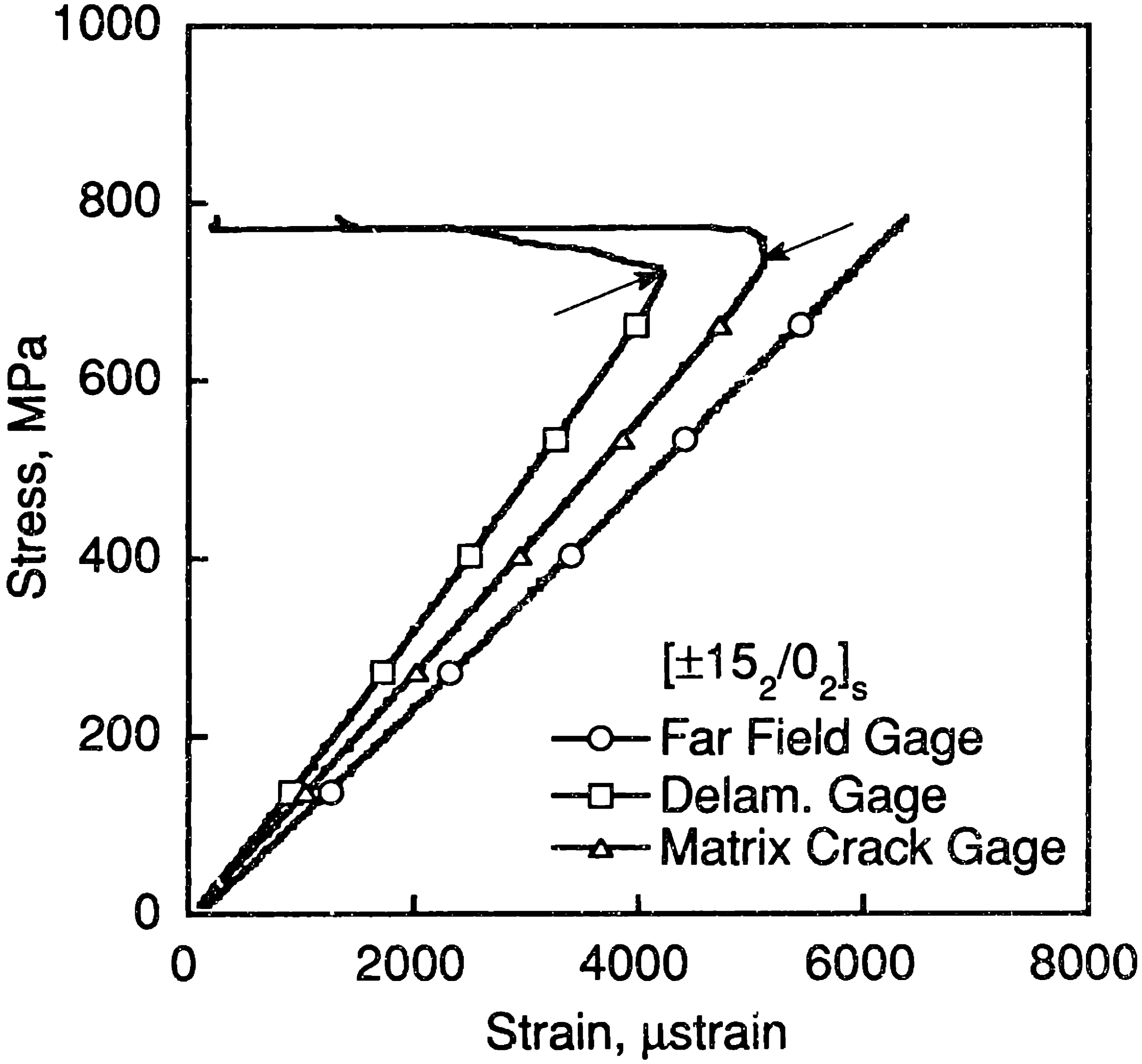

Figure 6.6 Stress-strain data for $[\pm 15_2/0_2]_s$ specimen #3 with implant obtained on testing to failure.

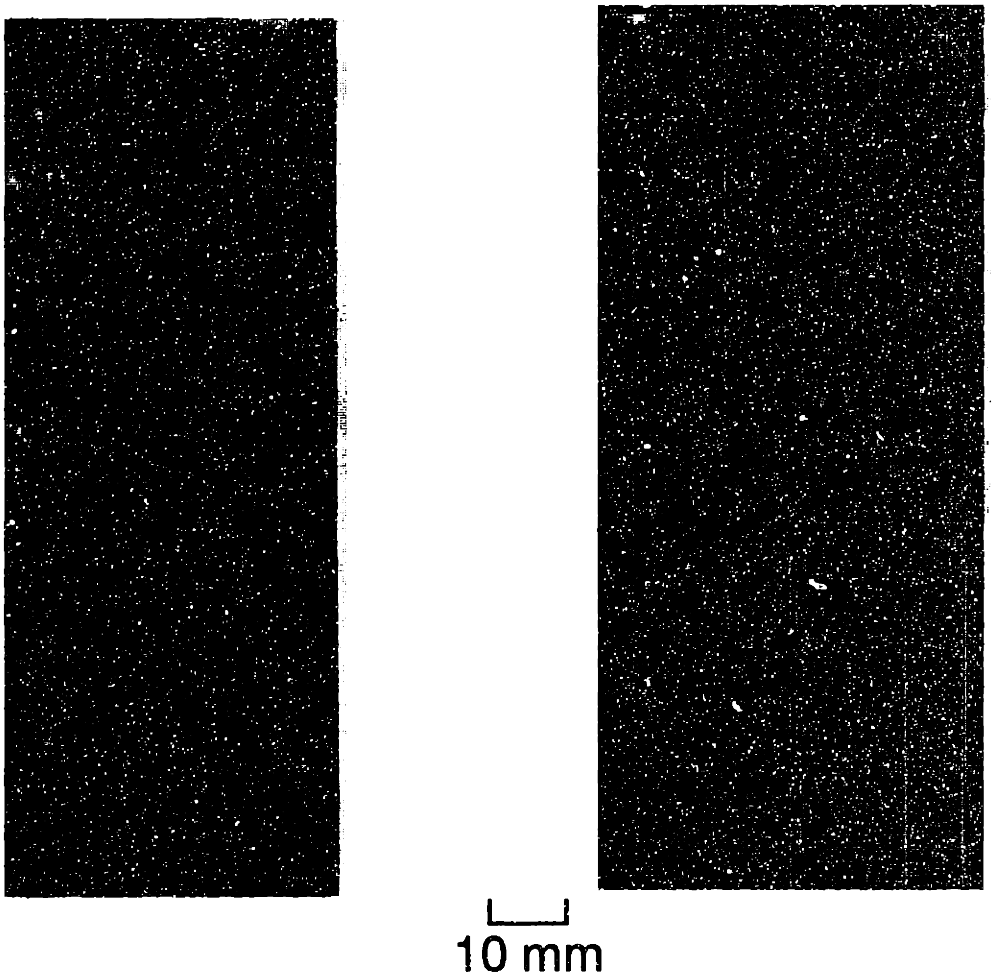

Figure 6.7 X-ray radiographs of $[\pm 15_2/0_2]_s$ specimen #3 with implants (*left*) before loading and (*right*) after loading to approximately 700 MPa.

where the fiber failure is visible at the center of the specimen.

The data from the first specimen of the $[\pm15_3/0_3]_s$ laminate with the implant is shown in Figure 6.9. This data exhibits a strange oscillation in the stresses during the test. The reasons for this are not quite clear, but one possible reason is the occurrence of secondary matrix cracking. However, such behavior was not observed in the remaining two specimens of this type. The data for the second and third specimens of this type obtained from the test which preceded the test to failure are shown in Figure 6.10 and Figure 6.13, respectively, and the results of the final test for these specimens are shown in Figure 6.11 and Figure 6.14, respectively. The X-ray radiographs taken between these two tests are shown in Figures 6.12 and 6.15, respectively. The data for these specimens is very similar to that for the $[\pm15_2/0_2]_s$ specimens and there is also no difference in the behavior of the delaminations as obtained from X-ray radiographs as the delamination is again seen to grow in the region of the delamination front located near the free edge of the laminate. Once again, the delamination extends about 5 mm along the free edge and this growth is seen to decrease as the matrix crack is approached. The delamination front hence appears to have re-oriented itself at an angle greater than 90° to the matrix crack and the front is now curved. A photograph of a typical failed $[\pm15_3/0_3]_s$ specimen with implant is shown in Figure 6.16. The implanted delamination is seen to grow to the ends of the specimen and the fiber failure observed is less than that observed in the $[\pm15_2/0_2]_s$ laminates and occurs at locations which vary from specimen to specimen. This failure is similar to that reported for the unflawed specimens in previous research [6].

The data for the $[\pm15_5/0_5]_s$ specimens differed from the earlier two types of specimens since some secondary cracking was observed in the -15° plies, within the delaminated region, from the X-ray radiographs and also from visual

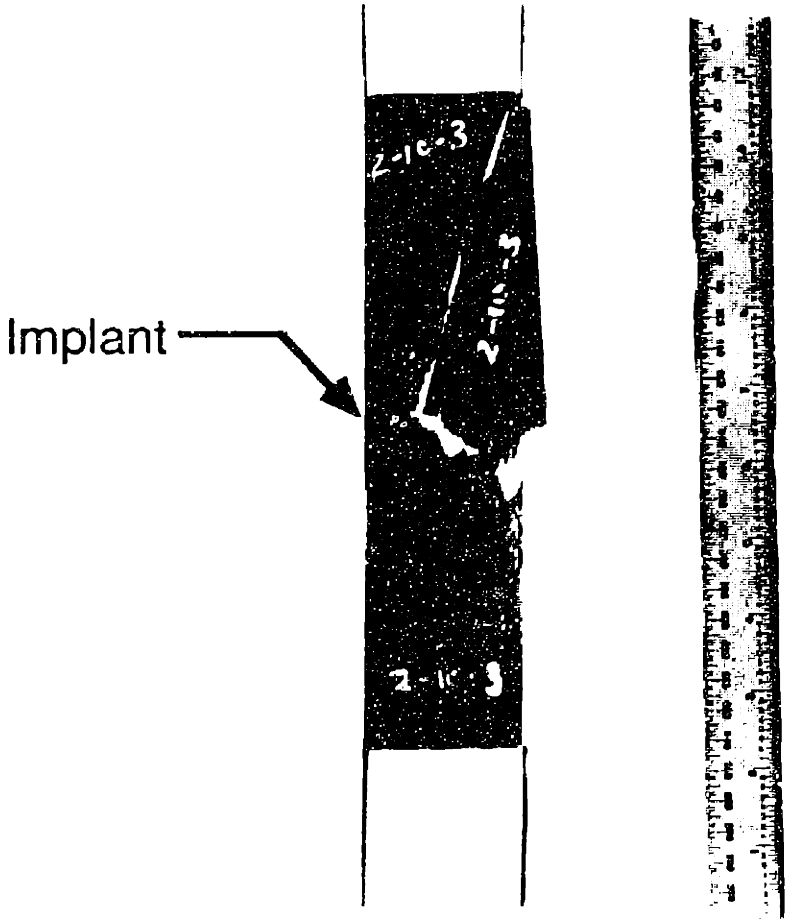

Figure 6.8 Photograph of typical failed $[\pm15_2/0_2]_s$ specimen with implant.

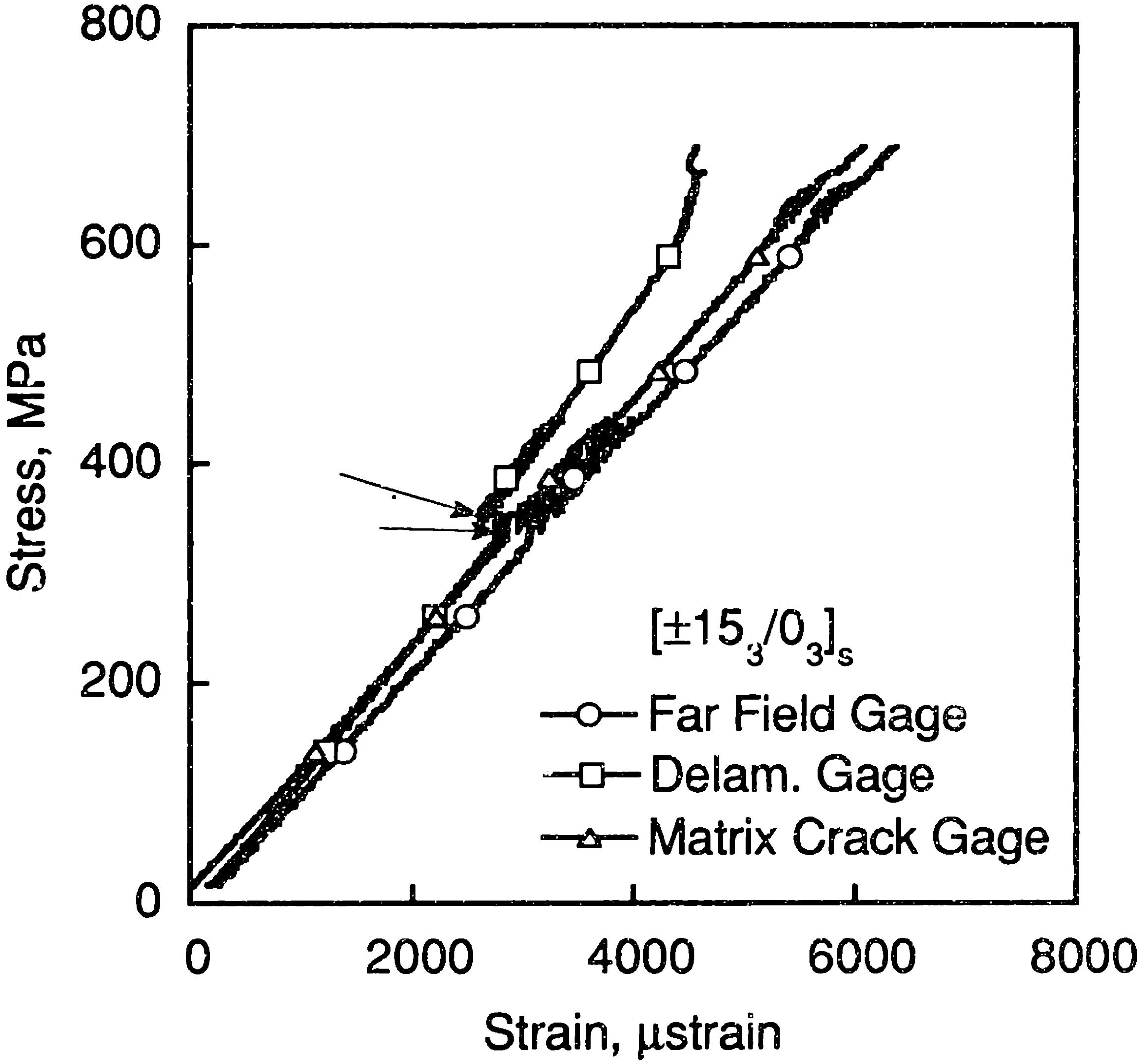

Figure 6.9 Stress-strain data for [$\pm15_3/0_3$]$_s$ specimen #1 tested monotonically to failure.

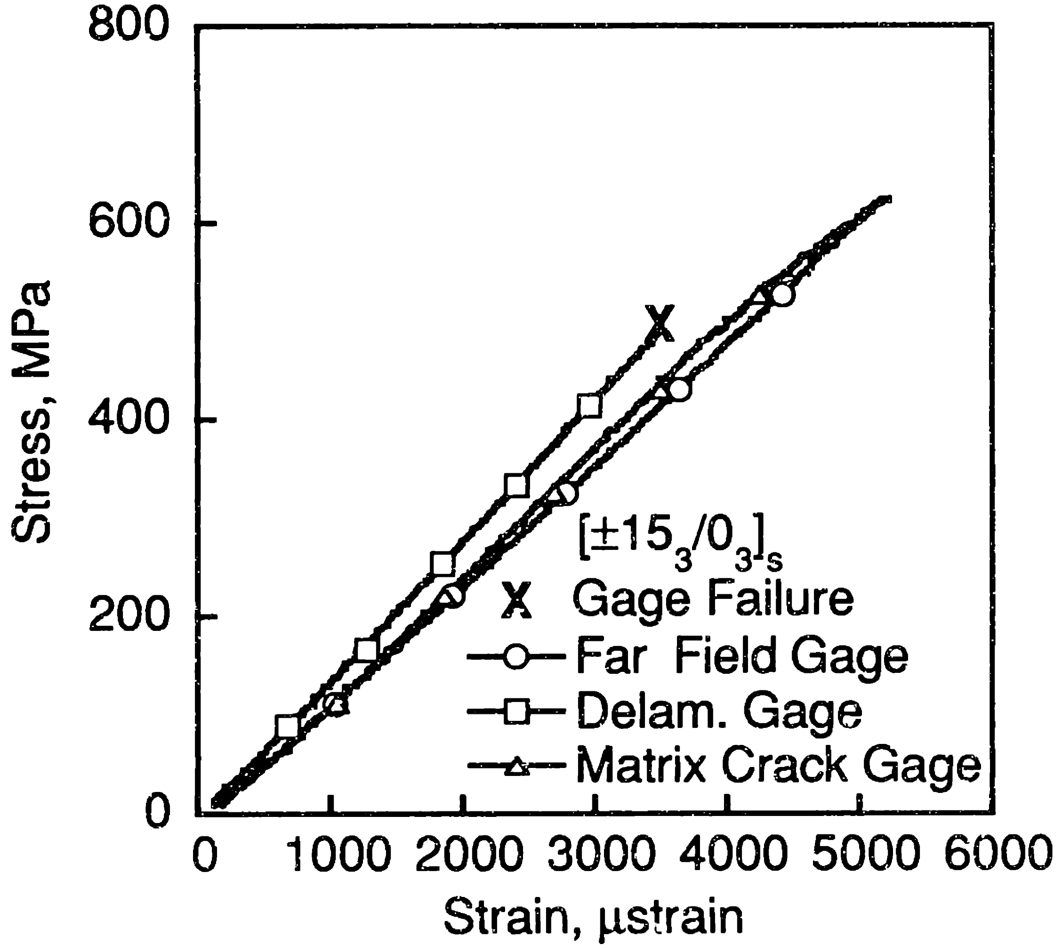

Figure 6.10 Stress-strain data for $[\pm15_3/0_3]_s$ specimen #2 with implant obtained for the loading case which precedes the test to failure.

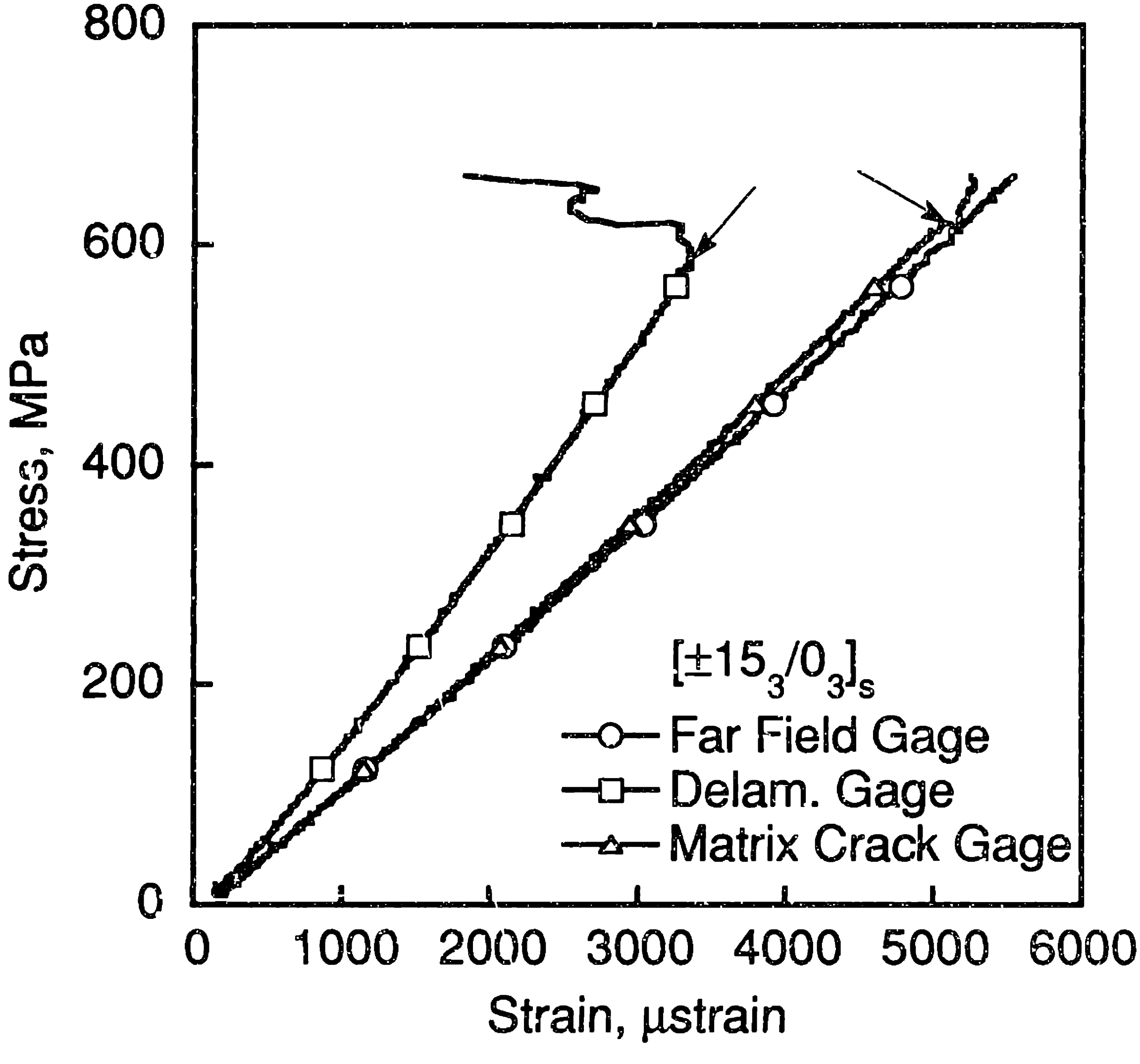

Figure 6.11 Stress-strain data for $[\pm15_3/0_3]_s$ specimen #2 with implant obtained on testing to failure.

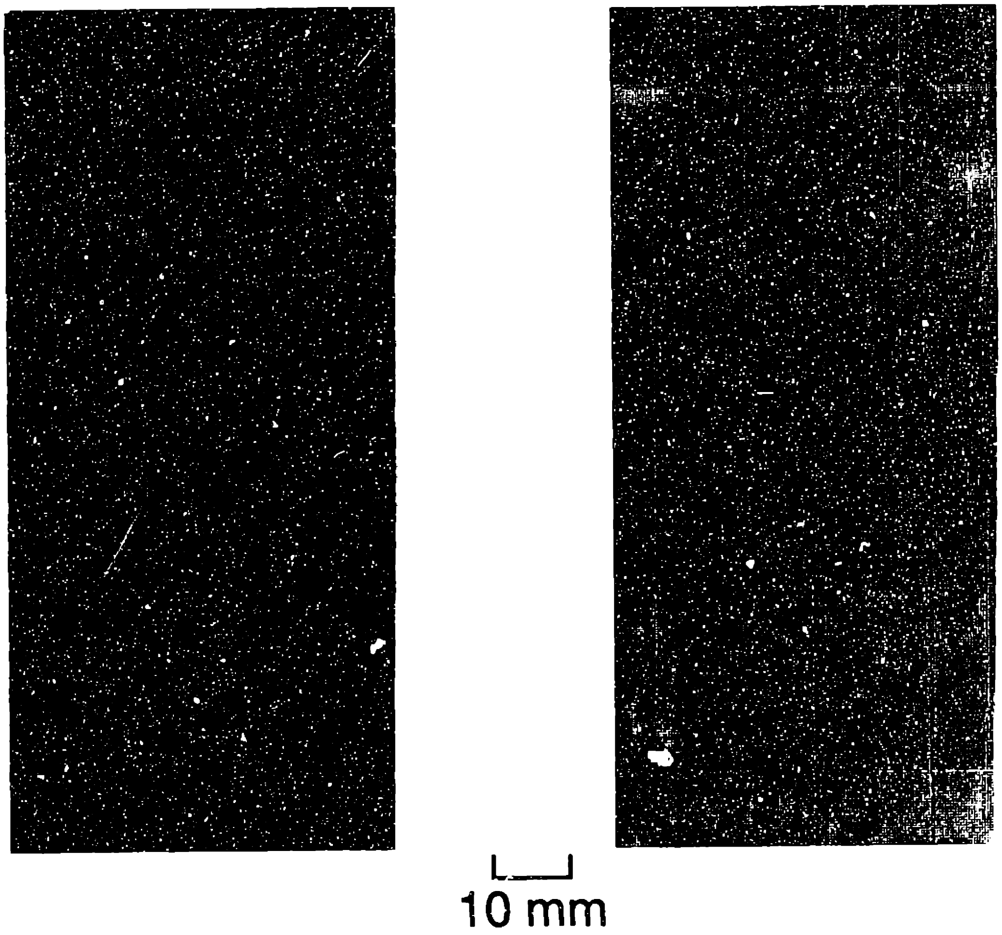

Figure 6.12 X-ray radiographs of $[\pm15_3/0_3]_s$ specimen #2 with implant (*left*) before loading and (*right*) after loading to approximately 650 MPa.

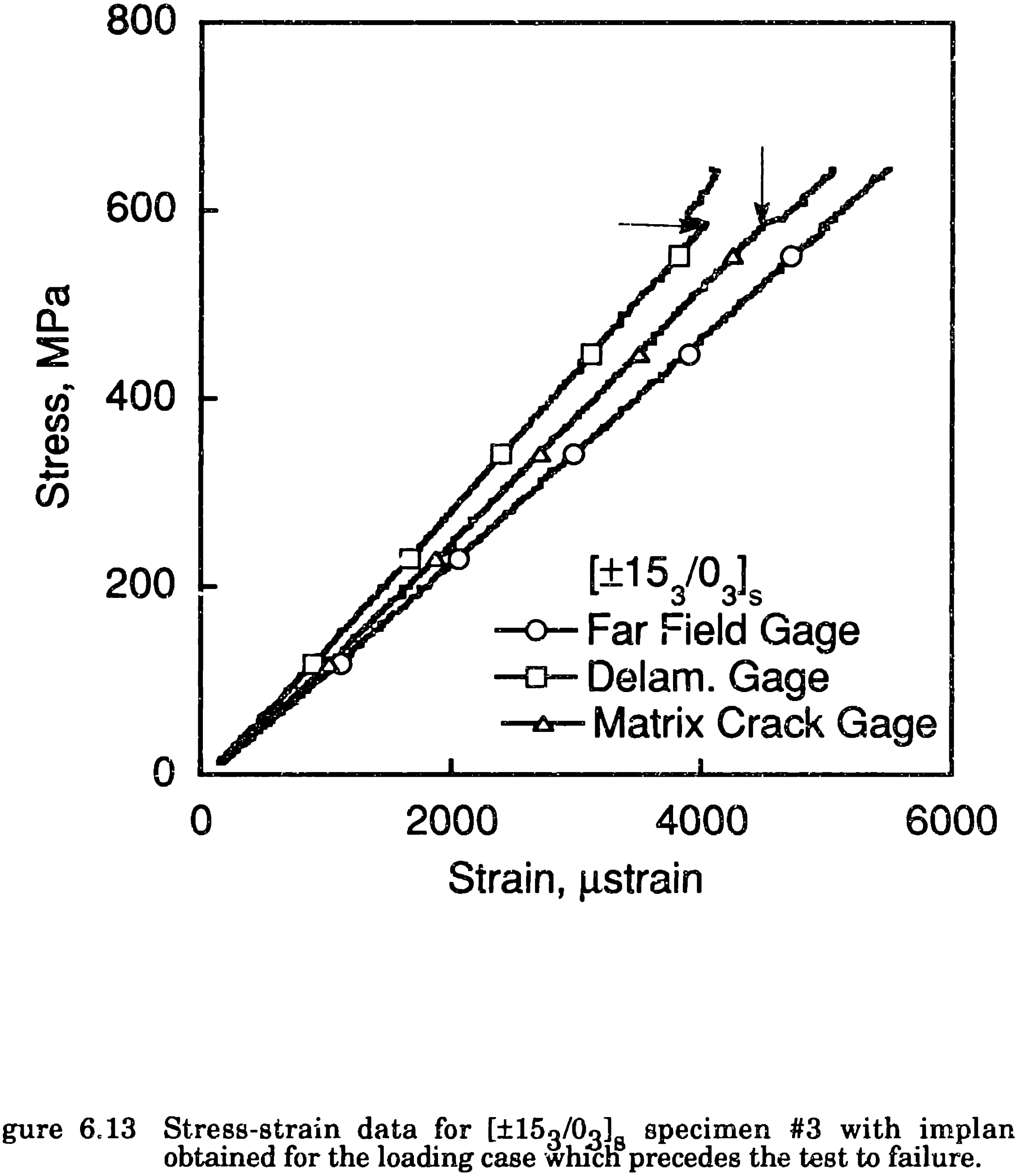

Figure 6.13 Stress-strain data for $[\pm 15_3/0_3]_s$ specimen #3 with implant obtained for the loading case which precedes the test to failure.

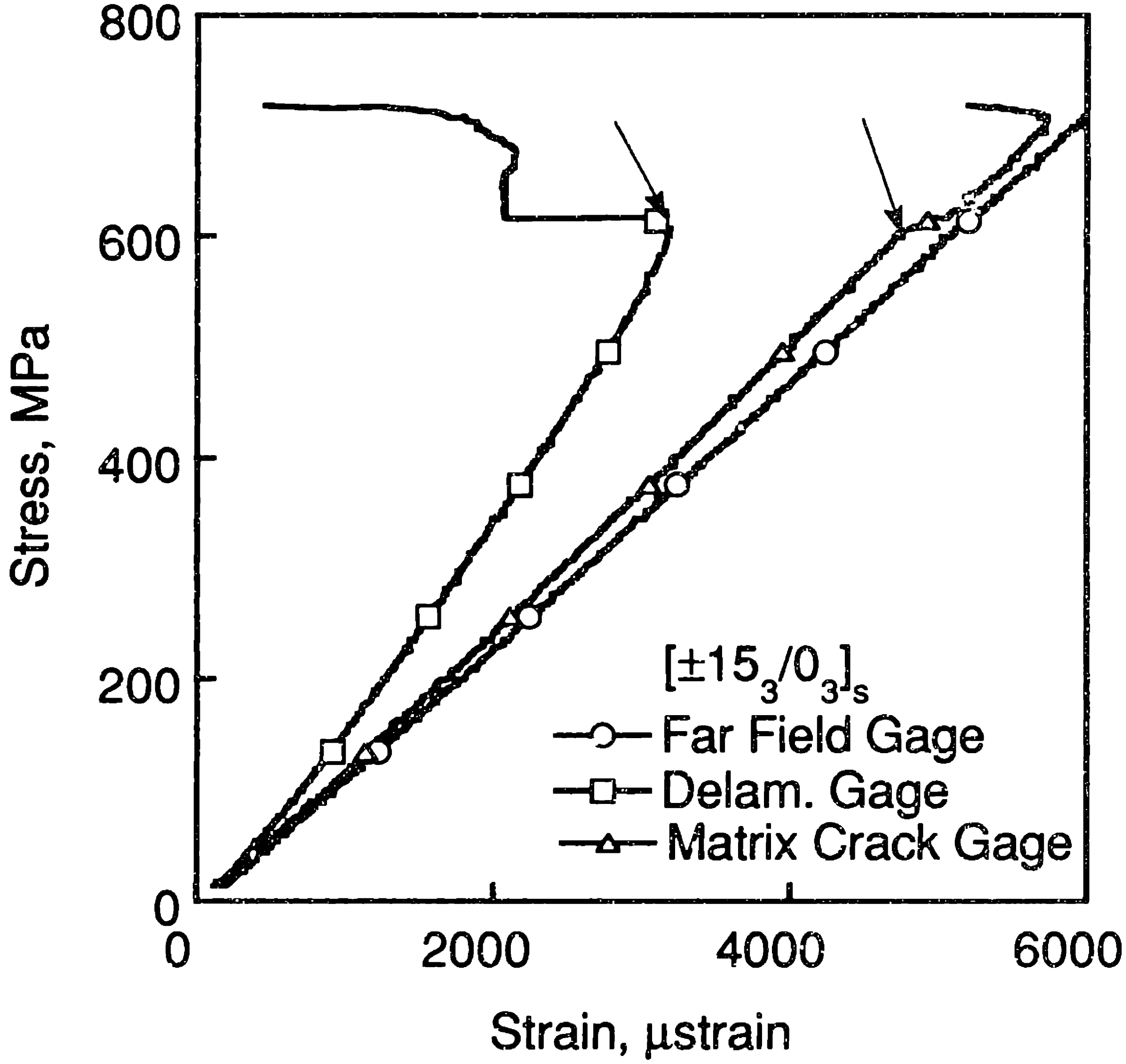

Figure 6.14 Stress-strain data for $[\pm15_3/0_3]_s$ specimen #3 with implaant obtained on testing to failure.

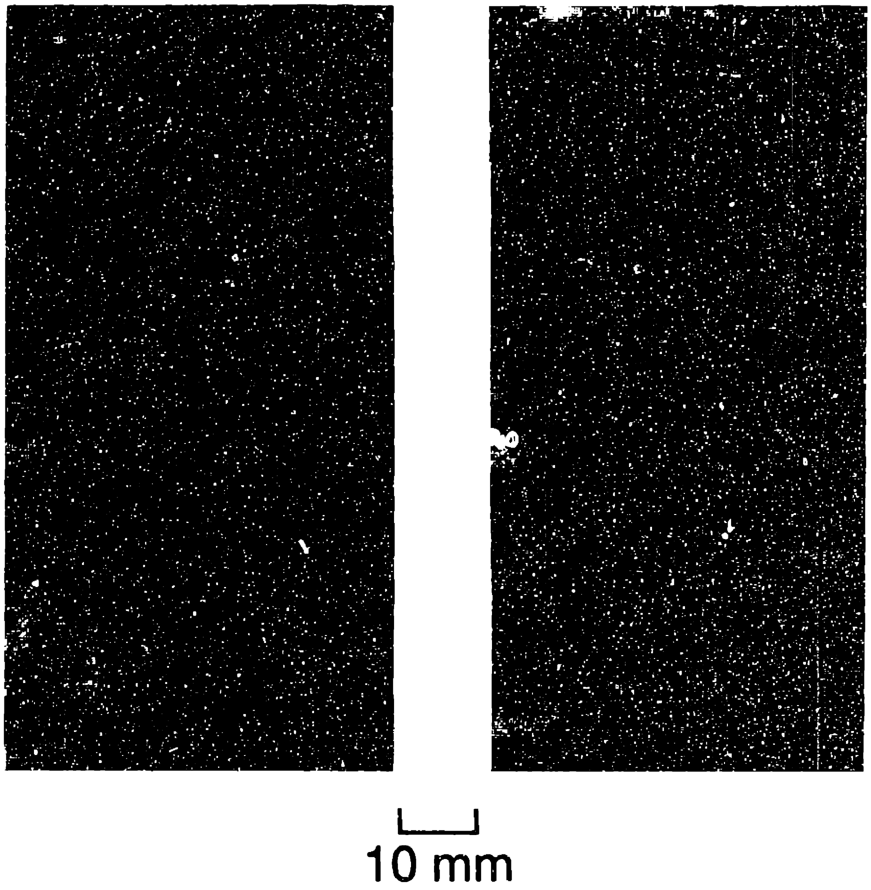

Figure 6.15 X-ray radiographs of $[\pm 15_3/0_3]_s$ specimen #3 with implant (*left*) before loading and (*right*) after loading to approximately 650 MPa.

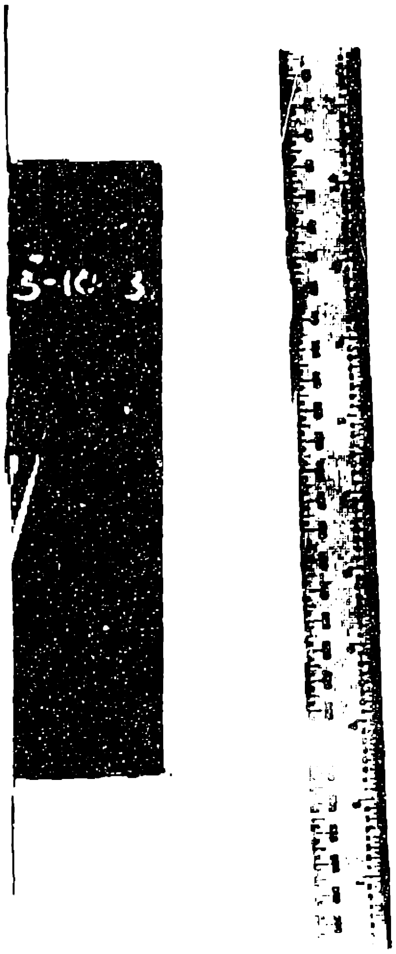

Figure 6.16 Photograph of typical failed $[\pm15_3/0_3]_s$ specimen with implant.

examination even before the testing of these specimens. The data obtained from the strain gages at the delamination front for the first specimen, shown in Figure 6.17, which was tested monotonically to failure, are not very informative because the readings of the gages at the delamination and matrix crack fronts have many discontinuities starting at about 200 MPa, which is very early in the loading history of the specimen. This indicates that there are some other forms of damage occurring at that stage. The test data for the second and third specimens of this type are not shown because these show the same characteristics as the data from the first specimen where discontinuities are observed from the first test in the series of incremental tests itself and these do not show up as any form of damage on the X-ray radiographs. However, the X-ray radiographs are shown in Figures 6.18 and 6.19. These indicate that after loading, the growth observed in the previous two laminates, $[\pm15_2/0_2]_s$ and $[\pm15_3/0_3]_s$, is missing and, instead, additional secondary matrix cracks in the -15° effective ply are seen to occur ahead of the implanted delamination and extend backwards and cross the delamination front within the -15° plies. In the case of the third specimen of this type the X-rays subsequent to loading of the specimen are inconclusive. In all cases, the final failure of these specimens still occurs by the growth of the implanted triangular delamination region itself, as shown by the photograph of a typical failed specimen in Figure 6.20, even though secondary matrix cracking that was discussed above also existed within the specimen. Almost no fiber breakage is observed in the failed specimen. This type of failure is similar to that observed in the unflawed specimens [1].

6.1.2 $[\pm15_2]_s$ laminates

The next set of tests involved the $[\pm15_2]_s$ specimens. Both unflawed specimens and specimens with implants were tested. The unflawed specimens

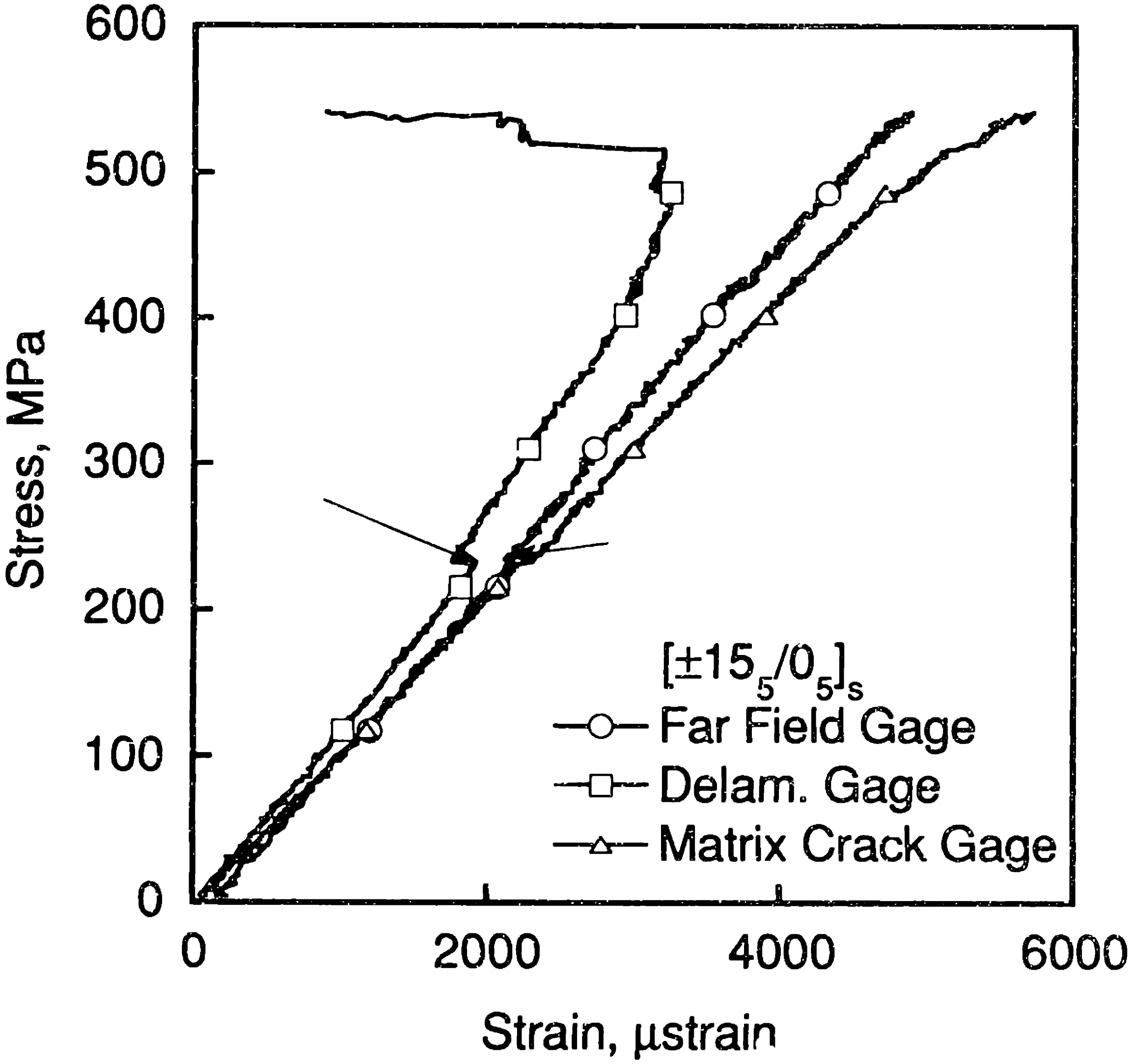

Figure 6.17 Stress-strain gage data for [±15$_5$/0$_5$]$_s$ specimen #1 tested monotonically to failure.

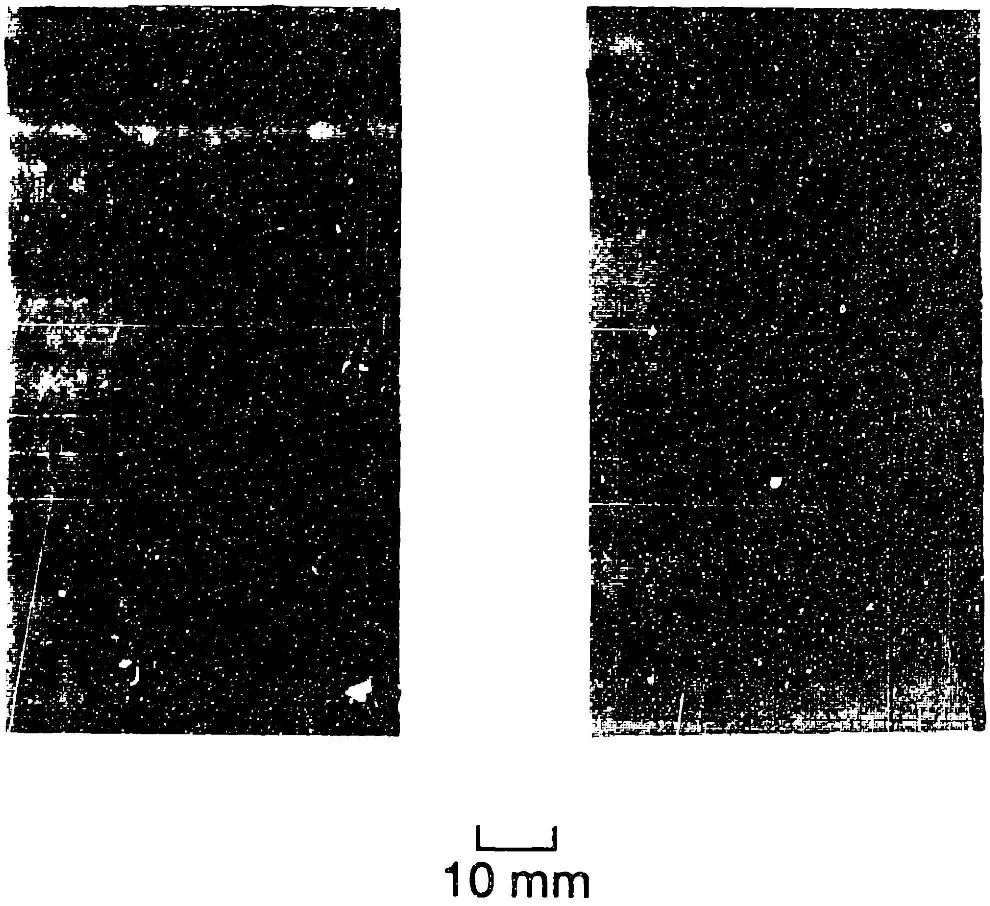

Figure 6.18 X-ray radiographs of $[\pm 15_5/0_5]_s$ specimen #2 with implant showing (*left*) secondary cracks before loading and (*right*) increased secondary cracking after loading to 400 MPa.

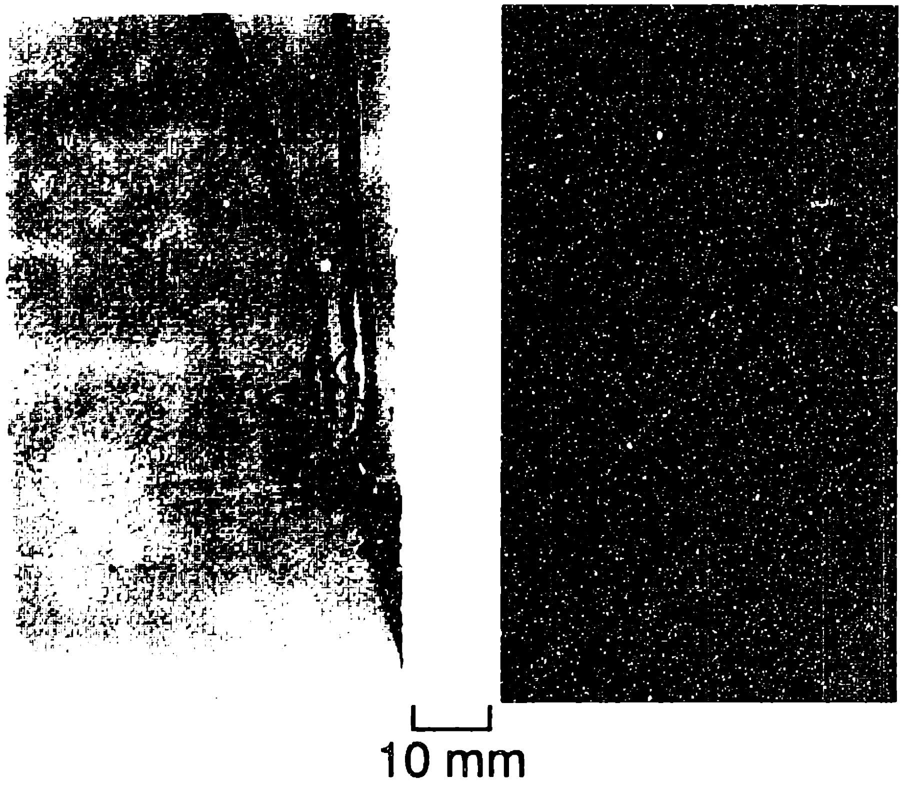

Figure 6.19 X-ray radiographs of $[\pm15_5/0_5]_s$ specimen #3 with implant (*left*) showing secondary cracks before loading and (*right*) subsequent to loading to 400 MPa (radiograph is inconclusive).

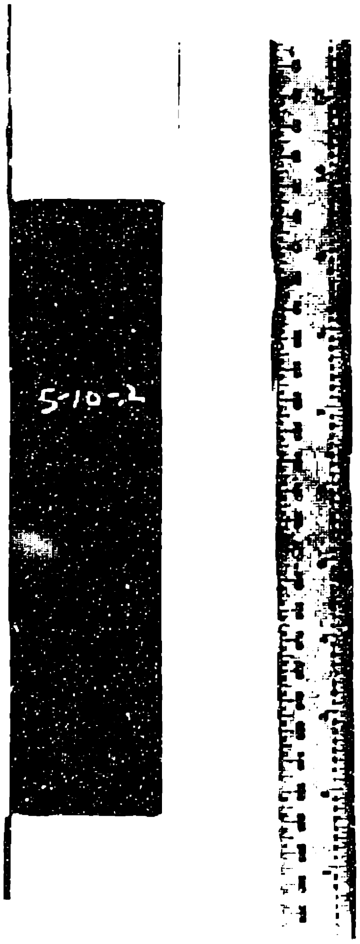

Figure 6.20 Photographs of failed $[\pm15_5/0_5]_s$ specimen with implants.

were tested since no previous test data was available for these laminates and these tests would help to determine whether the triangular-shaped delaminations were observed in these specific laminates as in the $[\pm 15_3]_s$ laminates discussed in Chapter three. The specimens with implants were expected to provide X-ray and strain data similar to that of the $[\pm 15_n/0_n]s$ specimens. The modulus and failure stresses and strains of the unflawed specimens are presented in Table 6.3. The modulus of these specimens as obtained from classical laminated plate theory is 116 MPa. The moduli of these specimens are within 5% of the theoretical values.

The unflawed $[\pm 15_2]_s$ specimens showed the formation of triangular delaminations as shown by a photograph of a failed specimen in Figure 6.21. In some cases, considerably more delamination and fiber damage was also observed in the failed specimen as shown in Figure 6.22. However, unlike the $[\pm 15_3]_s$ specimens discussed in Chapter three [6], the $[\pm 15_2]_s$ specimens did not show stable triangular delaminations. The triangular delaminations in all the cases grew unstably through the specimens and stopped at the tabs. In some cases, there was some fiber failure also seen and there was considerable amount of delamination. The growth of the delamination to the tabs was almost instantaneous and this resulted in a steep drop in the load carried by the specimens which was considered as failure of the specimen. The micrographs of the edges of the specimen taken after the failure of the specimen are shown in Figure 6.23. One of the micrographs shows that the delaminations occur symmetrically at both the top and bottom +15/-15 interfaces and the matrix crack occurs in both the top and bottom $[+15_2]$ sublaminate. The matrix crack profiles are curved in a manner similar to that observed by previous researchers for some other families of laminates [5]. The secondary matrix cracks that occur in the central $[-15_2]_s$ sublaminate during the failure process are also shown in

Table 6.3 Modulus[a] and failure stress and strain for unflawed $[\pm 15_2]_s$ specimens.

Specimen	Modulus (GPa)	Failure Strain (μstrain)	Failure Stress (MPa)
1	108	5560	610
2	111	6060	658
3	-[b]	-	601
4	113	5370	570
5	115	5600	639
Average	112 (2.7%)[c]	5648 (5.2%)	616 (5.5%)

[a] Theoretical value via classical laminated plate theory is 116 GPa.

[b] Could not be determined due to loss of strain gages during test.

[c] Values in parentheses are coefficients of variation.

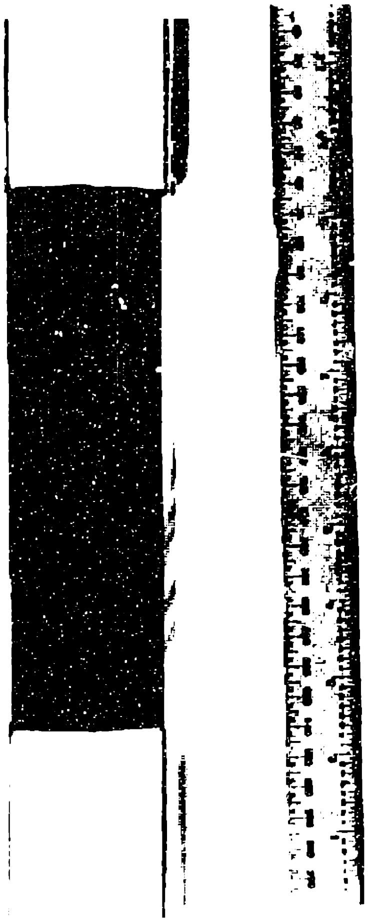

Figure 6.21 Post-failure photograph of an originally unflawed $[\pm 15_2]_S$ specimen showing triangular-shaped delaminations.

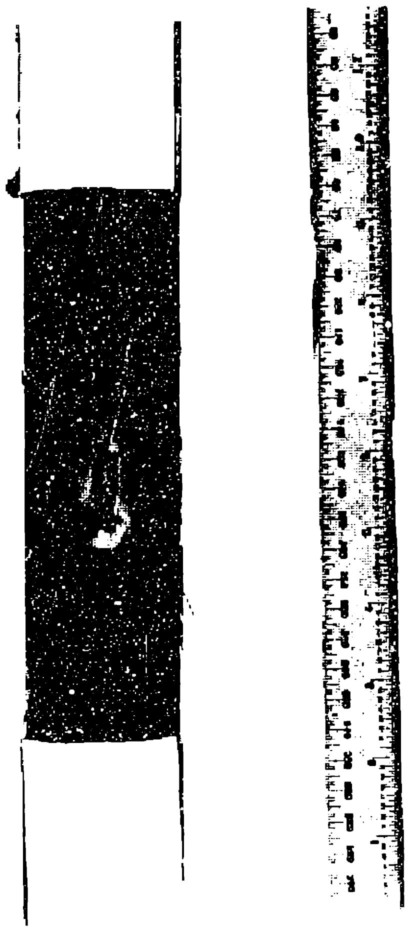

Figure 6.22 Post-failure photograph of an originally unflawed $[\pm 15_2]_s$ laminate showing triangular-shaped delaminations accompanied by fiber breakage.

Figure 6.23.

The modulus values and the failure stresses and strains for the $[\pm15_2]_s$ specimens with implants are given in Table 6.4. The modulus values for these specimens are within 4% (except in one case) of the values for this laminate obtained from classical laminated plate theory for the unflawed case. Therefore, the presence of the delamination does not alter the modulus of the laminate. The average failure stresses and strains for these laminates are within 4% of the values obtained for unflawed specimens. Hence, the presence of an implanted delamination has not affected the final failure of the laminate.

The $[\pm15_2]_s$ specimens with implants were tested incrementally to failure and X-ray radiographs were taken in a manner similar to the testing of the $[\pm15_n/0_n]_s$ specimens with implants. On subjecting the specimen to a far-field displacement, it was observed that the triangular delamination was lifted above the surface of the laminate. This opening up of the triangular piece was visible on the edge of the specimen, but no measurements of opening were taken. The implanted triangular region was seen to grow to the specimen tabs in an unstable manner, as in the case of the unflawed specimens. However, the stress-strain data shows that there is a discontinuity in the data obtained at the delamination and the matrix crack gage at about 350 MPa as seen in Figure 6.24. This discontinuity was observed in all the specimens of this kind at approximately the same value of stress. On taking an X-ray radiograph at that point, secondary cracking was observed to occur in the $[-15_2]_s$ sublaminate as can be seen in Figure 6.25. The secondary crack occurs at the free edge region ahead of the delamination front and extends backward across the delamination front into the delaminated region. The X-ray radiograph shows that the region between this secondary matrix crack and the original delamination front has also delaminated. It is, however, not clear whether this delamination first grew

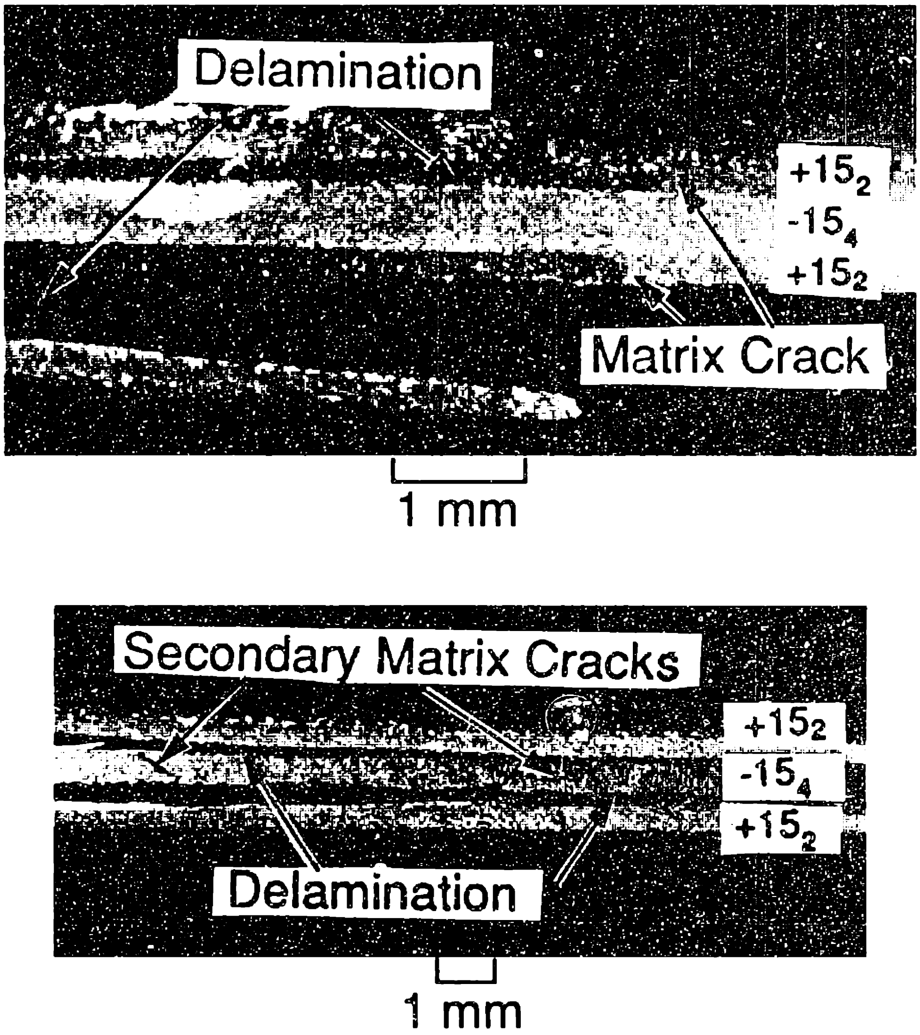

Figure 6.23 Post-failure micrographs of the edges of the originally unflawed $[\pm15_2]_s$ laminate exhibiting (*top*) a curved matrix crack profile and (*bottom*) secondary matrix cracking in the $[-15_4]$ sublaminate .

Table 6.4 Modulus[a] and Failure Stress and Strain for $[\pm 15_2]_s$ specimens with implants

Specimen	Modulus (GPa)	Failure Strain (μstrain)	Failure Stress (MPa)
1	102	6660	682
2	120	4950	572
3	111	5700	637
4	111	5560	613
Average	111 (6.6%)[b]	5718 (12.4%)	626 (7.3%)

[a] Theoretical value via classical laminated plate theory is 116 GPa

[b] Values in parentheses are coefficients of variation.

and the matrix crack formed subsequently or vice versa. This was a consistent feature of all the specimens of this type tested. The failure of the specimen, however, occurred by the growth of the implanted delamination to the ends of the specimen accompanied with some fiber failure as shown in the photograph of a typical failed specimen in Figure 6.26, The failure is similar to that observed in the unflawed specimens of this type.

6.2 Analytical Results

The analysis was performed for the case of a $[\pm15_2]_s$ laminate with implants. A quarter model of the laminate was used as discussed in Chapter four. The model, as shown in Figure 4.2, was subject to a displacement of $6.5\text{x}10^{-5}$ mm which is intended to produce a global axial strain of 1% (10,000 μstrain) within the specimen. The choice of applied strain is arbitrary since the model is linear and hence the results can be scaled to any desired value of strain. The local strains vary in the region around the delamination and the matrix crack, but in far-field regions (located at regions about 2.0 mm to 2.5 mm from the matrix crack front horizontally and about 2.0 mm to 2.5 mm vertically, as shown in Figure 6.27) it is expected that the global strain will be imposed on the specimen and hence the resulting stresses must compare well with the theoretical stresses obtained by classical laminated plate theory. Such stresses and strains were evaluated within some elements at the location shown in Figure 6.27. The stresses in these region matched the classical laminated plate theory within 3%-5% and the interlaminar stresses were approximately two orders of magnitude smaller than the in-plane stresses and hence could be approximated as zero. This verifies that the material properties and the applied loading conditions are those intended.

On subjecting the model to a far-field displacement, it was observed that

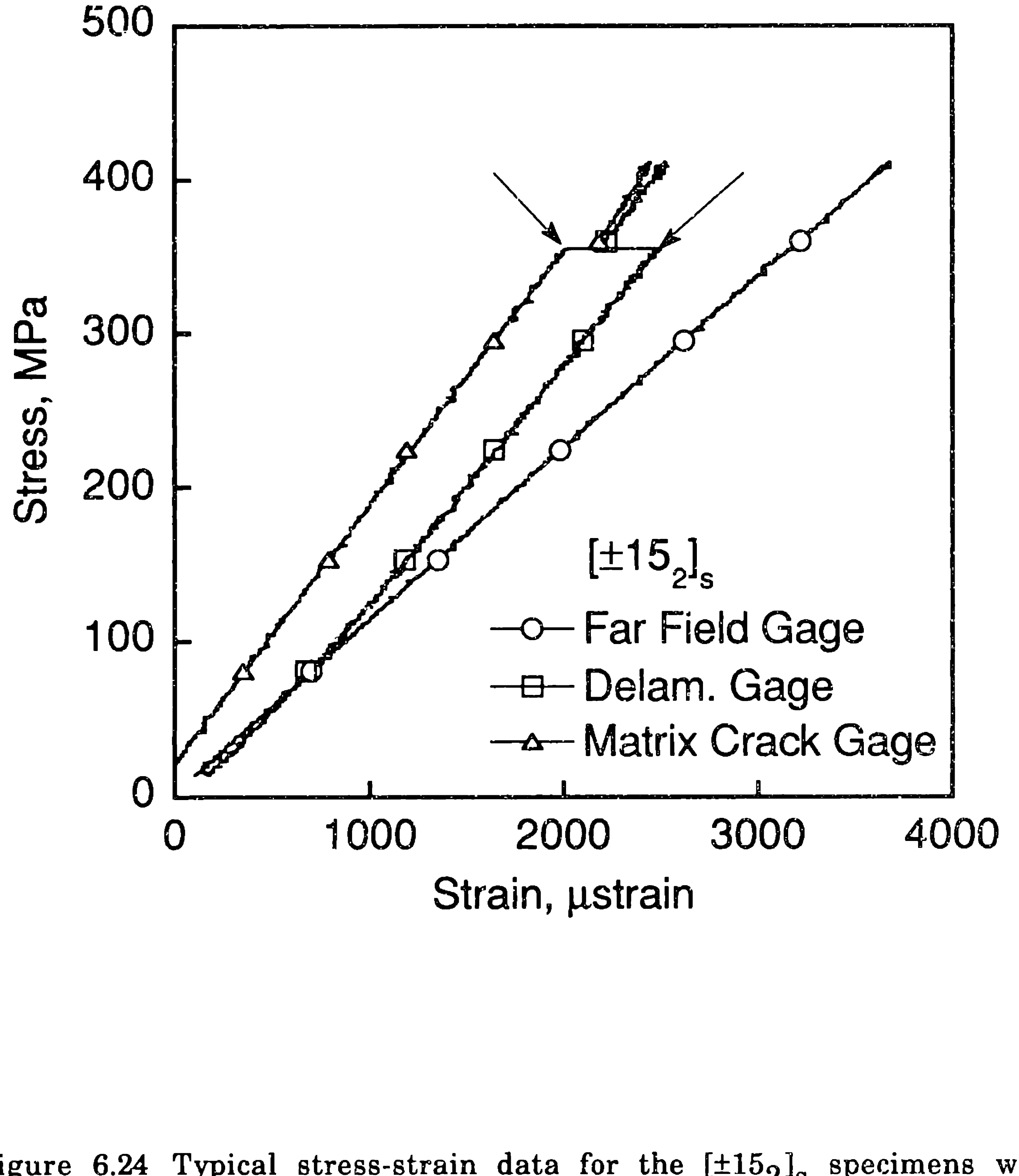

Figure 6.24 Typical stress-strain data for the [$\pm15_2$]$_s$ specimens with implants.

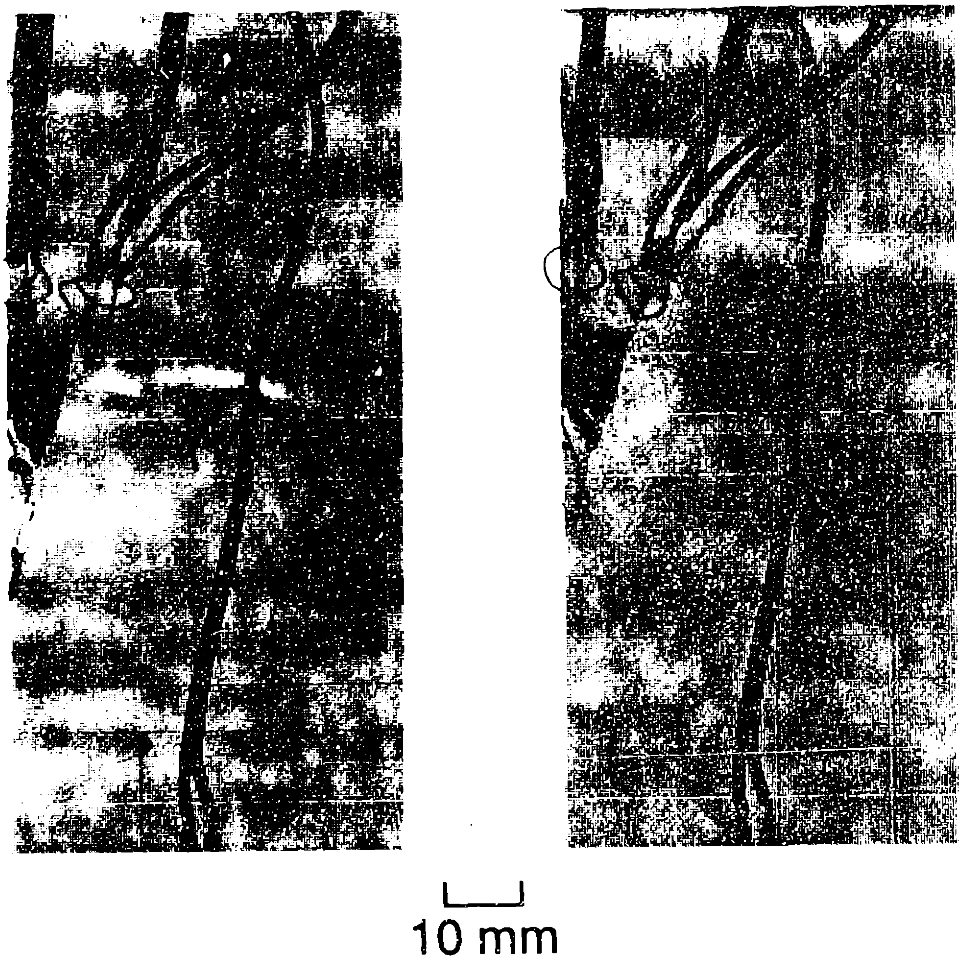

Figure 6.25 X-ray radiographs of $[\pm 15_2]_s$ specimens with implants (*left*) before testing and (*right*) after being loaded to approximately 300 MPa.

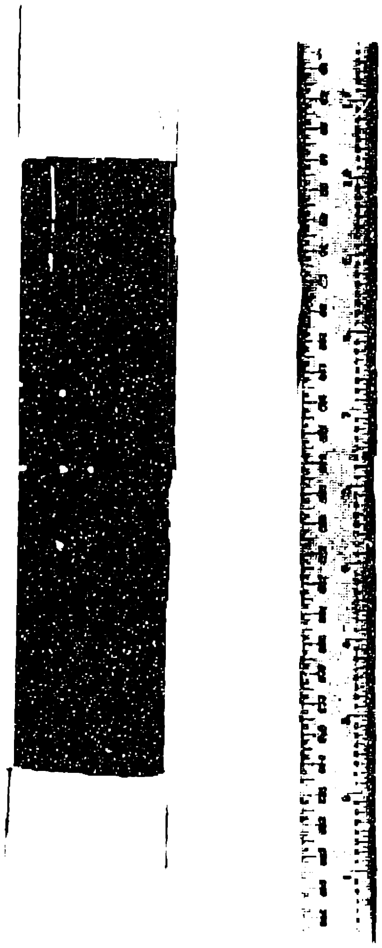

Figure 6.26 Photograph of failed $[\pm15_2]_s$ specimen with implants with the implanted delamination grown to the ends of the specimen.

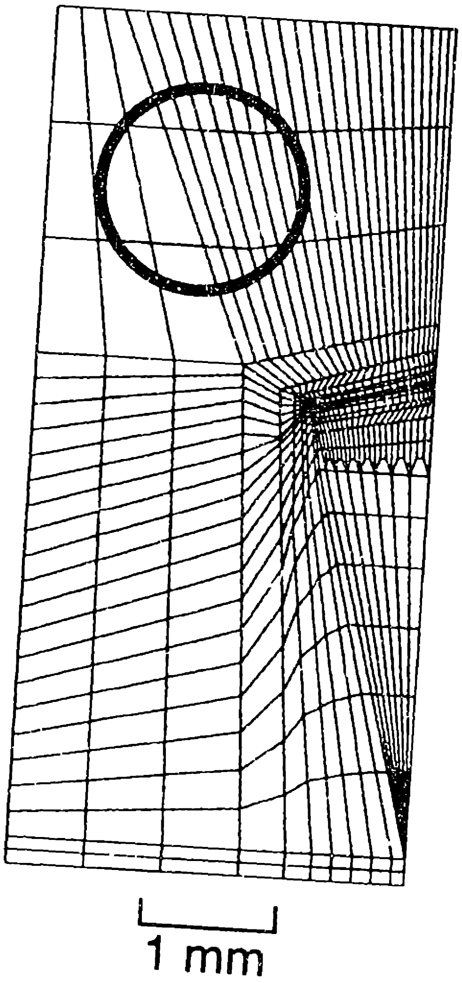

Figure 6.27 Locations in the finite element model at which the stresses are compared to the values obtained from classical laminated plate theory.

the triangular region opened up in a manner similar to that observed during testing of the specimen. A three-dimensional view of the undeformed mesh and an exaggerated deformed configuration (3X exaggeration) are shown in Figure 6.28. The delamination front is seen to open up and no crack surface interpenetration is observed to occur along the delamination front for any of the three orientations of the delamination shown in Figure 4.5. However, in the case of the 90° and 105° delamination orientations, the matrix crack surfaces were seen to interpenetrate. This interpenetration was localized around the matrix crack front alone and for regions away from the crack front, the surfaces of the matrix crack did not show any interpenetration. The top view of the $[+15_2]$ ply is shown in Figure 6.29 and, though the interpenetration is not apparent since it happens over an extremely small region, the matrix crack surfaces are seen to be close together in the region near the matrix crack tip but move apart at regions away from the matrix crack tip. This implies that for a matrix crack of the configuration assumed in the model, there is the likelihood of some friction at the tip of the matrix crack. Also, as the angle of the delamination changes from 90° to 105°, the matrix crack is observed to open up and the interpenetration is restricted to the top region of the matrix crack, i.e. the region of the matrix crack near the top surface of the laminate. When the delamination orientation is changed to 120° relative to the matrix crack, no interpenetration is observed at the matrix crack front.

The average failure strain of the unflawed $[\pm 15_2]_s$ specimens was about 5650 μstrain, as seen in Table 6.3, at which the triangular delaminations were seen to form and grow through the laminate. The results obtained from the finite element model are for an applied strain of 1%. These results are scaled to the observed failure strain of 5650 μstrain in order to examine the magnitudes of the energy release rates at the point of failure and to study how they compare

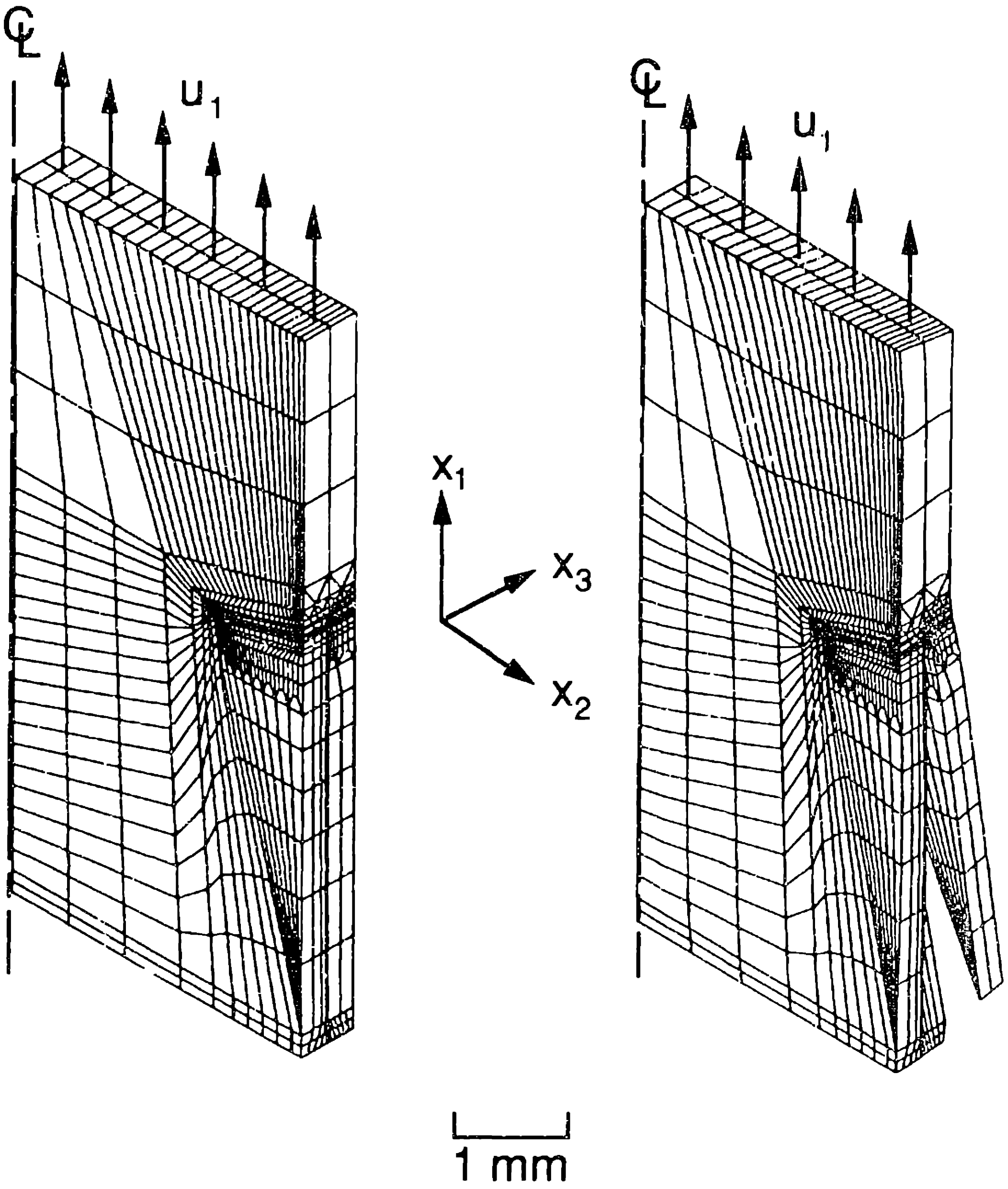

Figure 6.28 Three-dimensional mesh showing the (*left*) undeformed configuration and (*right*) deformed configuration (3X exaggeration) of the $[\pm 15_2]_s$ laminate at 1% strain.

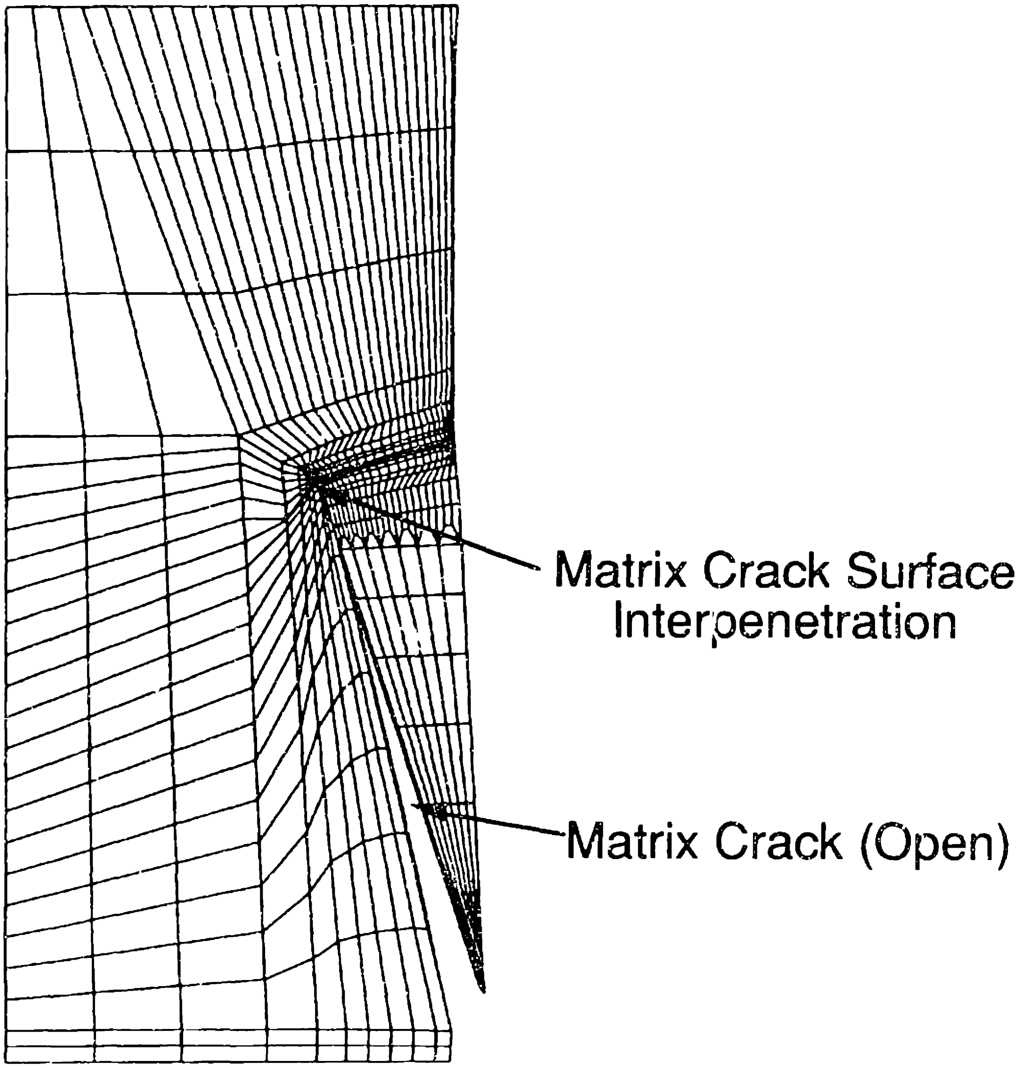

Figure 6.29 Top view of only the deformed [+15_2] sublaminate (3X exaggeration) with the matrix crack isolated from the finite element model of the [$\pm 15_2$]$_s$ laminate at 1% strain.

with observed critical values obtained in the literature [81] for the individual modes. The energy release rate scales as the square of the applied strain [[29]].

The results for the strain energy release rate for the delamination are presented along the s-axis, which is located along the delamination front as shown in Figure 6.30, and measures the distance from the matrix crack end of the delamination to any point on the delamination. The total length of the delamination is indicated by L_d, and it changes for different orientations of the delamination (1.04 mm for 90°, 1.15 mm for 105° and 1.41 mm for 120°).

The results for the total strain energy release rates for the three configurations of the delamination front are presented in Figure 6.31 using a nondimensional coordinate system where the distance, s, is non-dimensionalized by the length of the delamination front, L_d, so that it spans between 0 to 1 from the end of the delamination near the matrix crack to the end near the free edge. The same results are presented in Figure 6.32 as a function of the actual distance along the delamination front as measured from the free edge inwards. However, this does not convey any additional information regarding the distribution of the energy release rate in the three different orientations. The total energy release rate along the delamination front is observed to be highest near the free edge region and drops to lower values at regions closer to the matrix crack front. This is the trend observed for all the three delamination orientations. However, as the orientation of the delamination is changed from 90° to 105° to 120°, the magnitude of the energy release rate at the free edge is seen to drop, and the values away from that region are seen to increase. This process, in the model, of effectively tilting the delamination about the matrix crack front to angles greater than the 90° initial configuration is meant to approximate a possible manner of growth of the delamination where more growth occurs at regions near the free edge and less growth occurs at regions

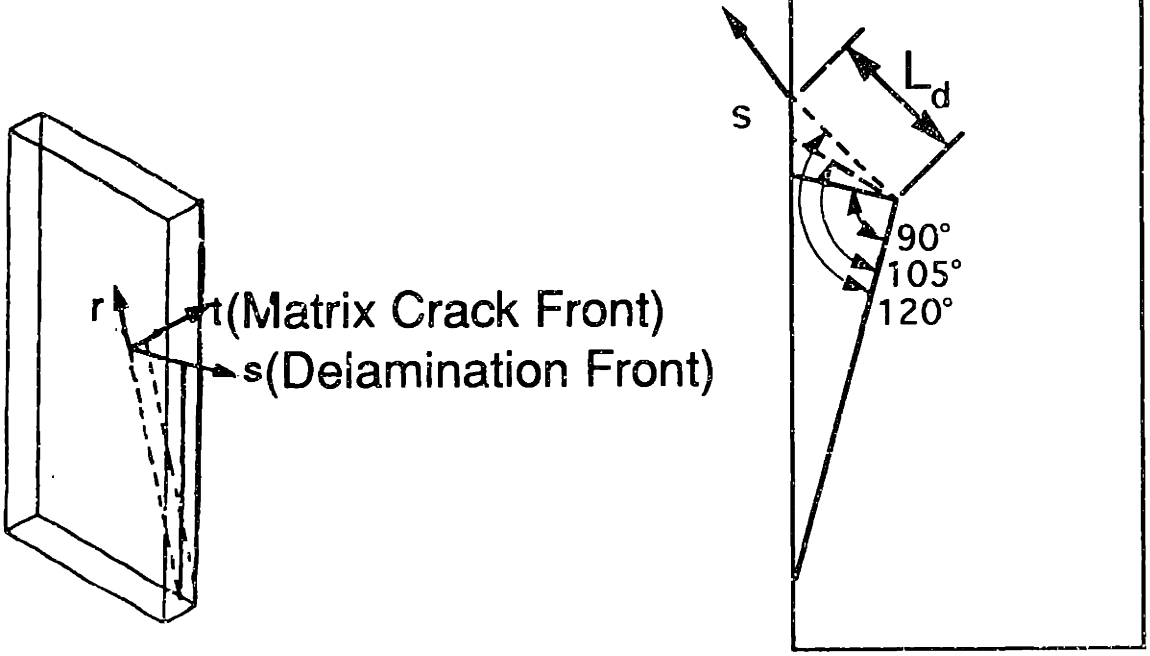

Front View

Figure 6.30 Coordinate system defined at the matrix and delamination fronts and used in the presentation of results.

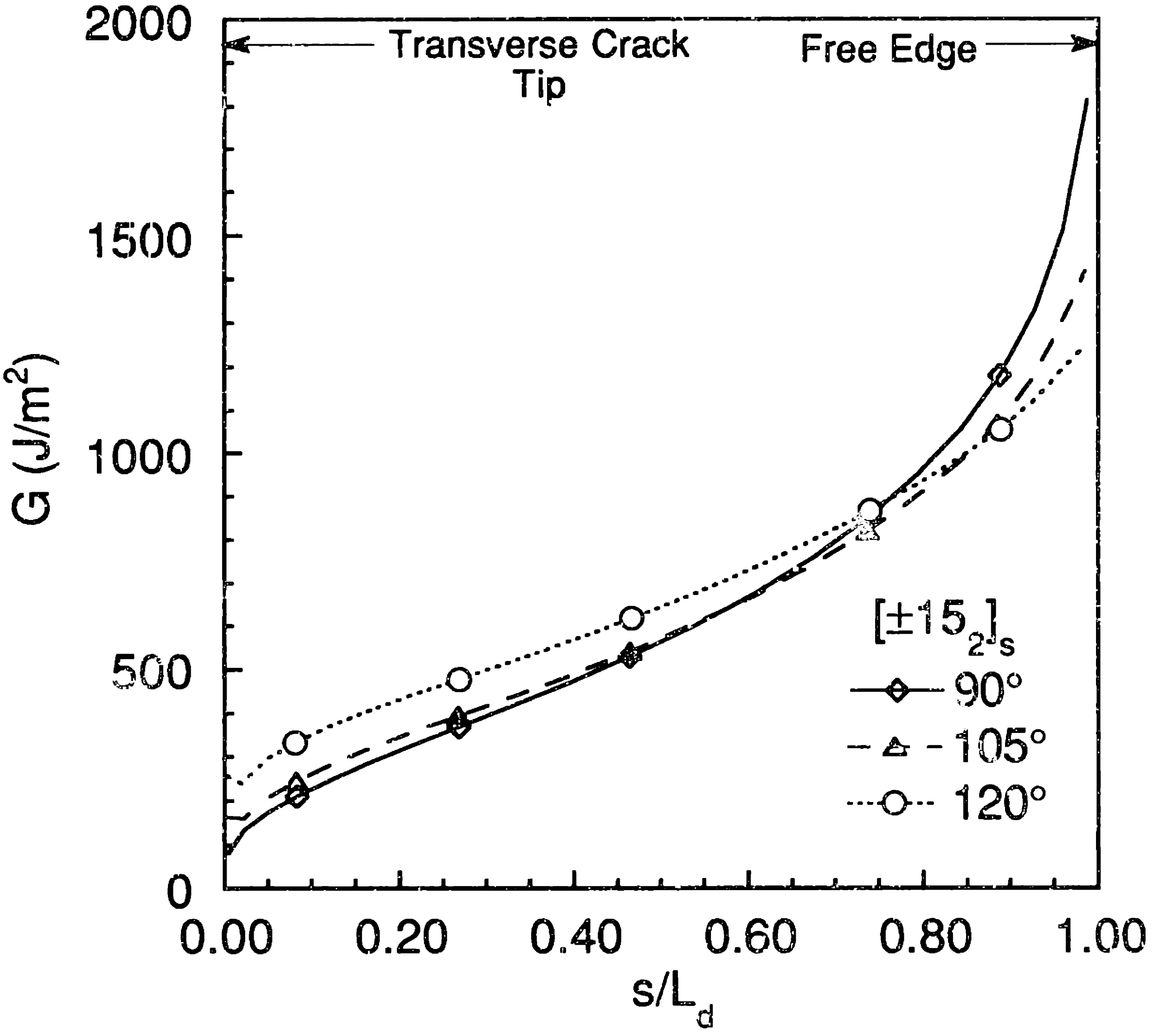

Figure 6.31 Total strain energy release rates along the delamination front as a function of the nondimensionalized distance at a strain level of 5650μstrain for different delamination orientations.

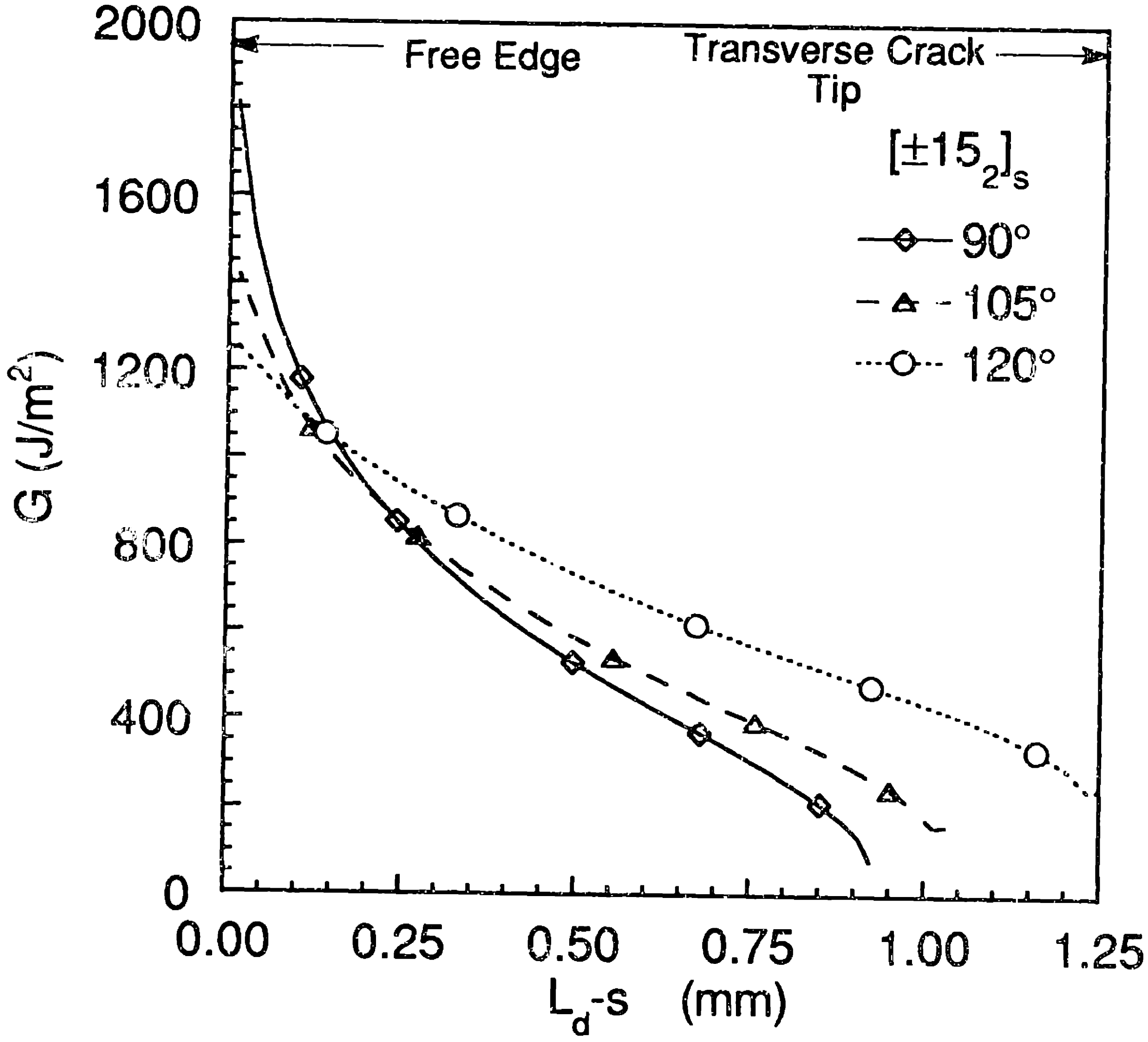

Figure 6.32 Total strain energy release rates as a function of the distance measured along the delamination front at a strain level of 5650μstrain for different orientations of the delamination.

away from the free edge. This simulation is justified if the growth is controlled by the total strain energy release rate, which is seen to be highest at the free edge and lowest near the matrix crack front. The energy release rate seems to become more uniform at higher angles of orientation

The individual components of the energy release rate are evaluated using the Equivalent Domain Integral approach in combination with the decomposition method. The results are presented in terms of the nondimensional coordinate system along the delamination front. Since no additional information was obtained from the plot of energy release rate against actual distance along the delamination front, similar plots are not presented separately. The mode 1, mode 2, and mode 3 data are presented in Figures 6.33, 6.34 and 6.35 (some graphs are presented twice as (a) or (b), on different scales to enable comparison with related graphs), respectively. Roman numerals I, II and III are not used to designate these modes, as they are only approximate modes as discussed in Chapters two and four. The critical values of these modes for AS4/3501-6, as obtained in the literature are [81], 200 J/m^2 for mode I, 525 J/m^2 for mode II and 832 J/m^2 for mode III. These critical values of the modal energy release rate are also plotted along with the modal strain energy release rates in Figures 6.33- 6.35 to provide a comparison of the relative magnitudes of the calculated values to a measured critical value and thus to aid in any conclusions to be drawn about the growth of the delamination. These critical values are determined from tests on unidirectional specimens and not from experiments on delamination at the interface of the +15/-15 plies which is of current interest. It has been observed that there could be a difference in the critical values for a delamination at a unidirectional interface as compared to one between plies of differing orientations of the same material [82]. This has not been considered here due to lack of adequate experimental data.

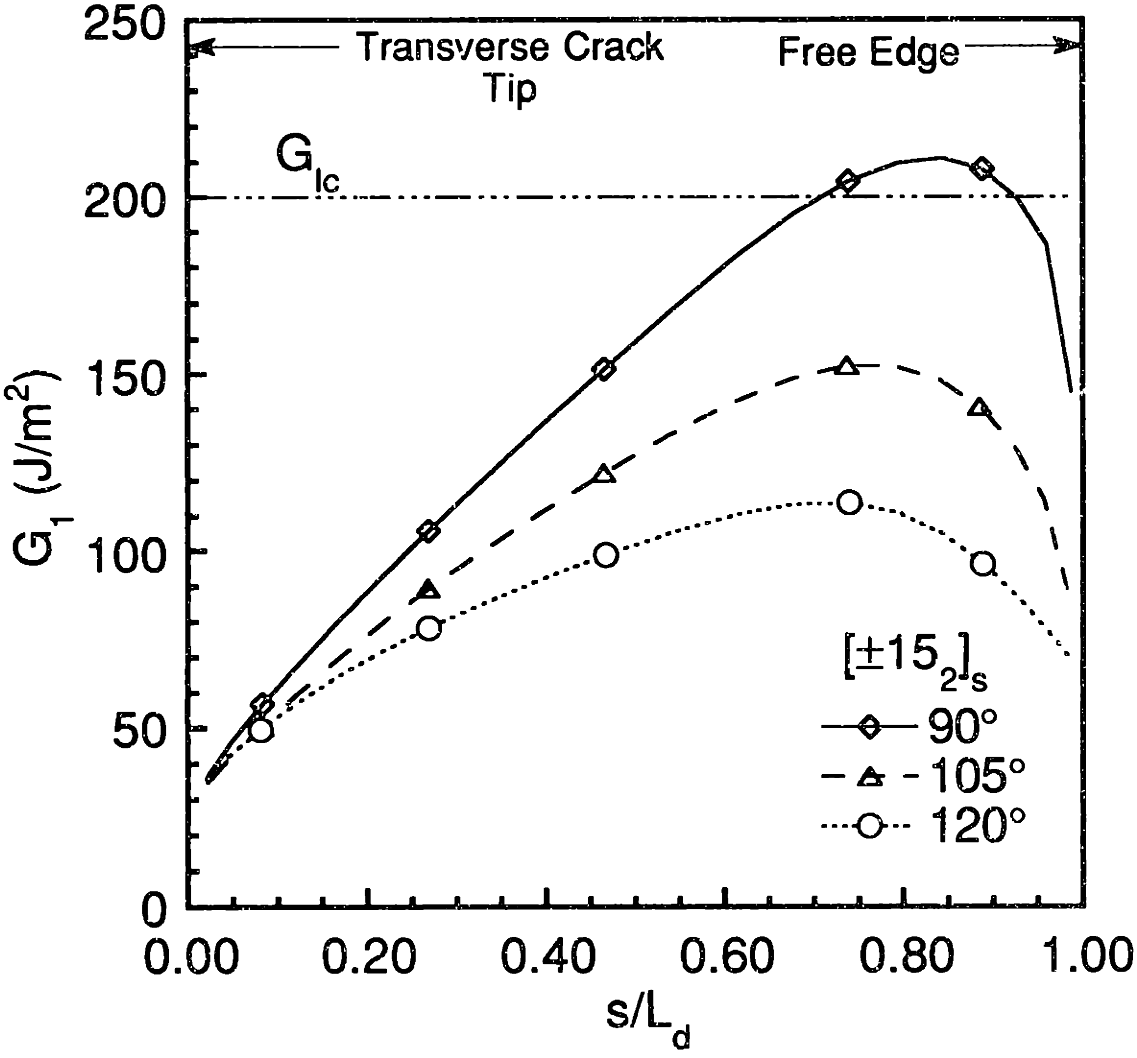

Figure 6.33a Mode 1 strain energy release rates along the delamination front in a $[\pm15_2]_s$ laminate as a function of the nondimensionalized distance for a strain level of 5650 μstrain for different delamination front orientations.

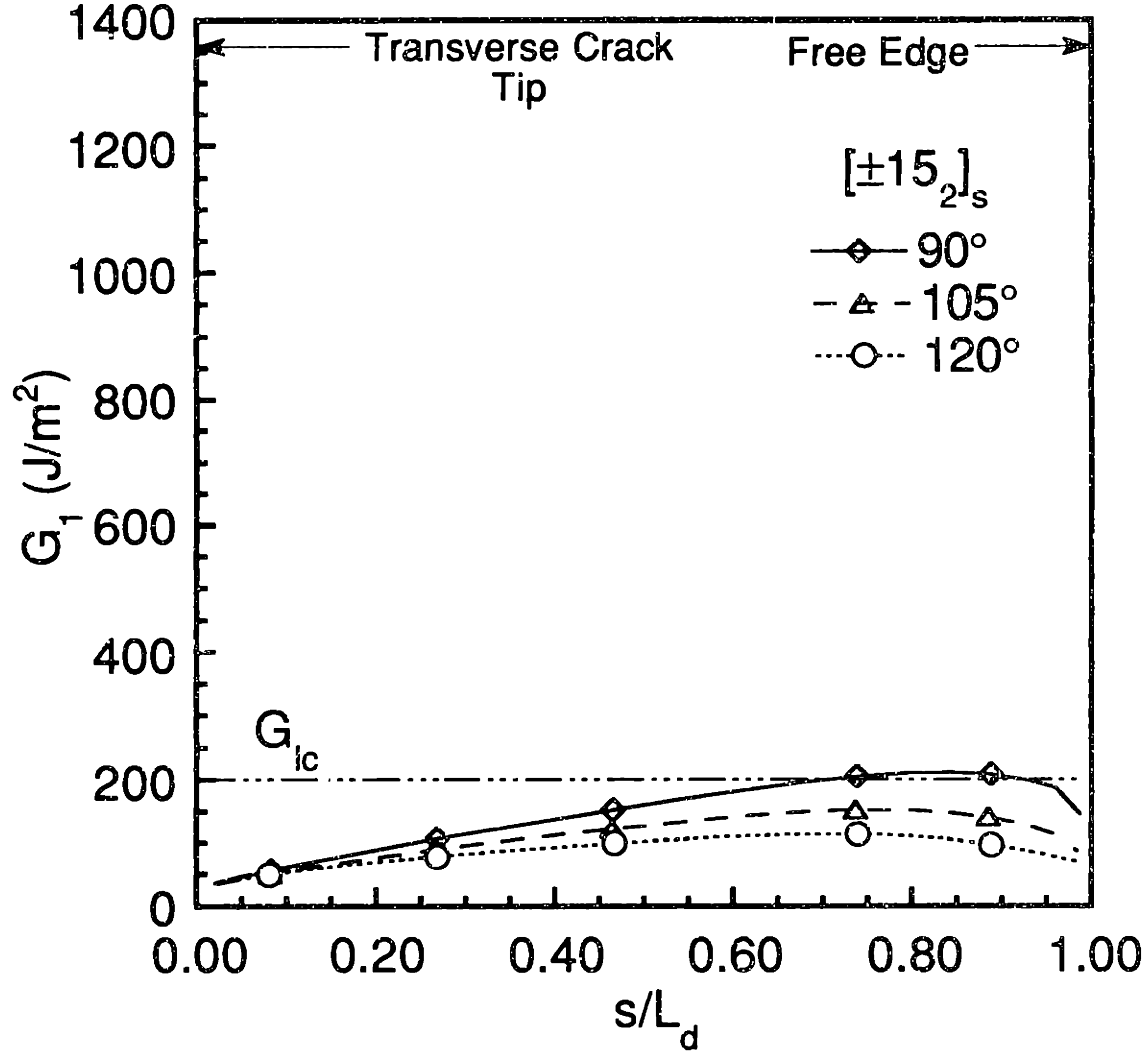

Figure 6.33b Mode 1 strain energy release rates along the delamination front in a $[\pm 15_2]_s$ laminate as a function of the nondimensionalized distance for a strain level of 5650 μstrain for different delamination front orientations (scale changed for comparative purposes).

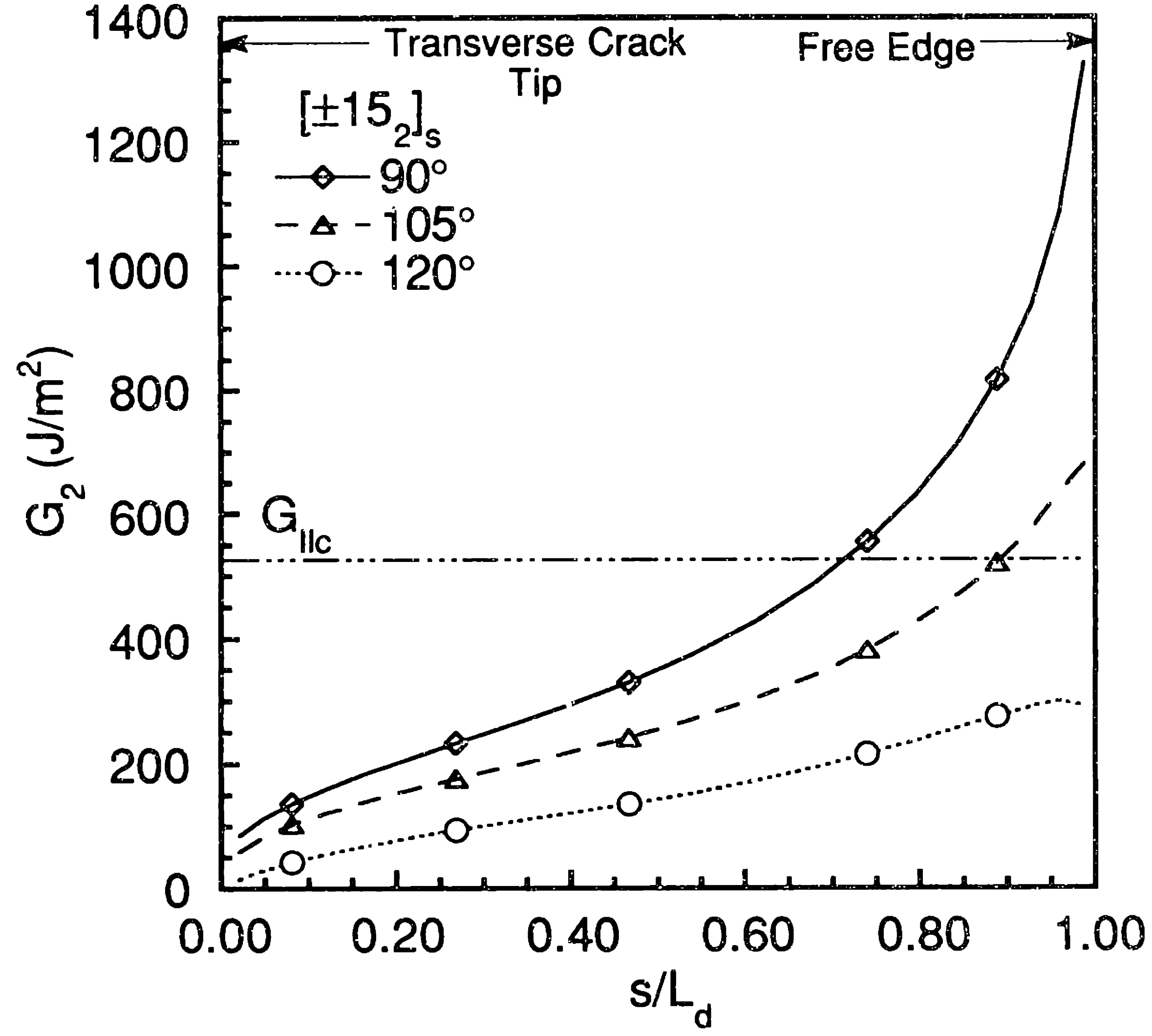

Figure 6.34 Mode 2 strain energy release rates along the delamination front in a $[\pm15_2]_s$ laminate as a function of the nondimensionalized distance for a strain level of 5650 μstrain for different delamination front orientations.

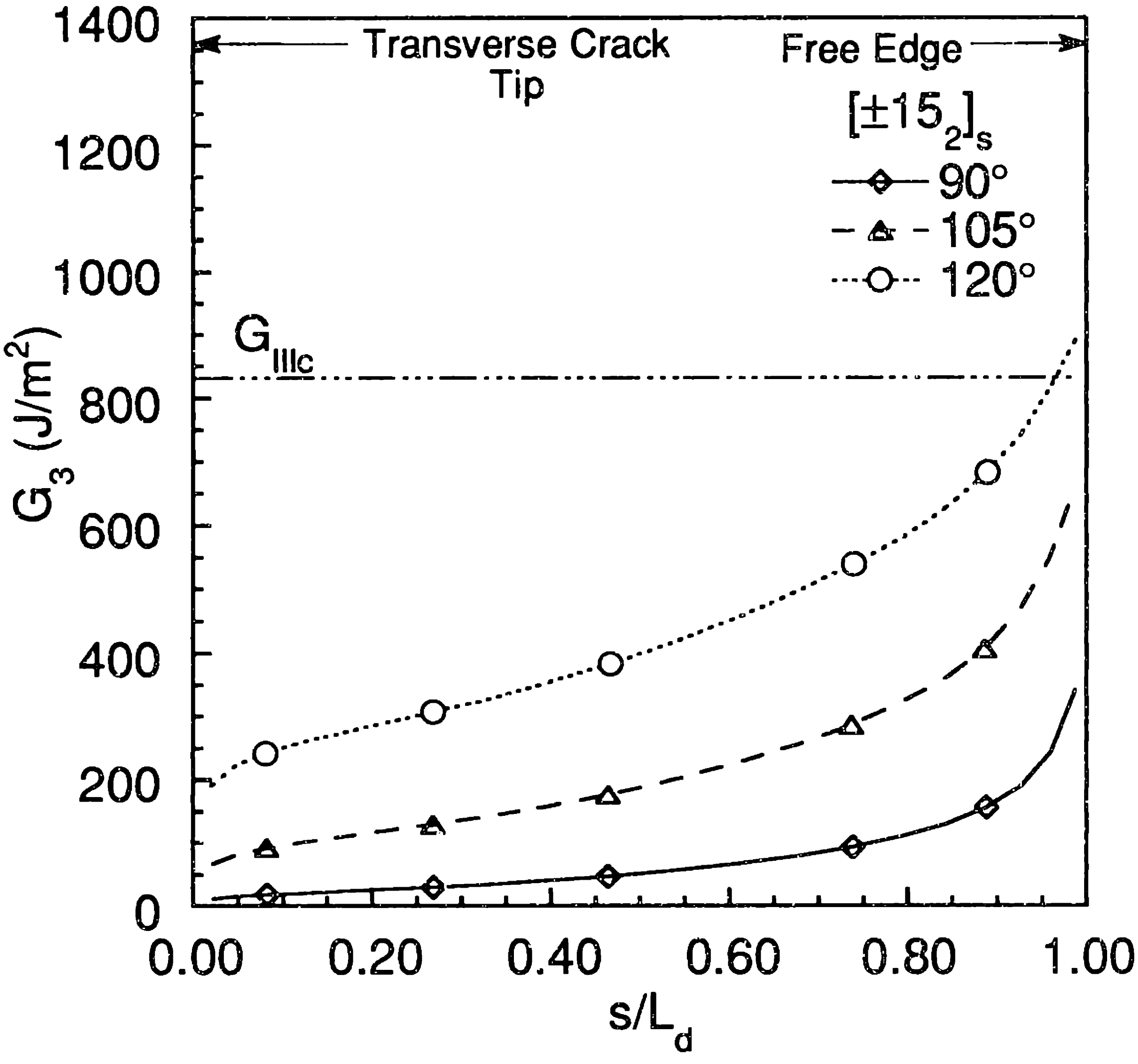

Figure 6.35 Mode 3 strain energy release rates along the delamination front in a $[\pm 15_2]_s$ laminate as a function of the nondimensionalized distance for a strain level of 5650 μstrain for different delamination orientations.

The values of mode 1 components are seen to decrease as the delamination orientation changes from 90° to 120°. The peak value of the mode 1 does not occur right at the free edge but slightly inside the delamination front and its value drops both near the free edge and the matrix crack front. The magnitude of the mode 1 components are lower than the mode 2 and mode 3 components. However, it is still comparable to the critical value of the mode 1.

The mode 2 and the mode 3 values have a distribution along the delamination front resembling the distribution of the total strain energy release rate. These modes have a peak value at the free edge region and their magnitudes reduce as the matrix crack front is approached. At a delamination orientation of 90°, the mode 2 value is substantially higher than the critical value of the energy release rate in the region near the free edges. As the orientation changes, the peak value sinks below the critical value for most of the delamination front.

The mode 3 results also have peak values at the delamination front near the free edge of the laminate. However, unlike the mode 2 energy release rate, the peak value is lowest for the 90° orientation and the peak value increases as the delamination changes orientation to the 120° angle. It must, however, be noted that the critical value of energy release rate for this mode is higher than that of the mode 2 case. Hence, despite the increase in the energy release rate as the delamination orientation changes from 90° to 120°, it does not rise significantly above the critical value.

The results for the strain energy release rate along the matrix crack are presented along the t-axis, shown in Figure 6.30, normalized by the effective ply thickness, T_{ply}. This axis measures the distance along the matrix crack front starting at the end of the matrix crack that is located near the delamination front. The length of the matrix crack is 0.268 mm, which is the same as the thickness, T_{ply}, of the $[+15_2]$ sublaminate. The energy release rate along the matrix crack front is presented for the case with the delamination orientation of 90° and 105° orientation shown in Figure 6.36. These two cases are presented separately from the 120° delamination orientation case because there is crack surface interpenetration observed in these two cases. The results from the linear finite element method used for the analysis neglects any contribution to the energy release rate from the frictional effect and therefore the energy release rate is only approximate and the error in the evaluation of the energy release rate is unknown. The total strain energy release rate along the matrix crack is presented in Figure 6.36 for these two cases as a function of a nondimensional parameter t/T_{ply}. In the case of the delamination oriented at 120° to the matrix crack, the total strain energy release rate is presented in Figure 6.37 and there is no crack surface interpenetration in this case. The energy release rate is highest at the top surface of the laminate and decreases at the region where the matrix crack makes contact with the delamination front. The peak energy release rate is small compared to the peak magnitude observed along the delamination front. However, its magnitude is comparable to the energy release rate observed along the other parts of the delamination. Even though there is crack surface interpenetration for the 90° and 105° case, the magnitude of the energy release rates obtained are very similar to that obtained for the 120° case.

It was suggested in Chapter three that the stress state around the delamination crack front at the free edge of the laminate may change significantly as the delamination changes orientation. This was considered to be a possible explanation for the observed secondary matrix cracking at the delamination front. However, it was found that the mesh around the delamination region was not refined enough to obtain smooth stress contours in that region. Some line contour plots have been plotted within a small region which includes about six elements around the delamination front as shown in

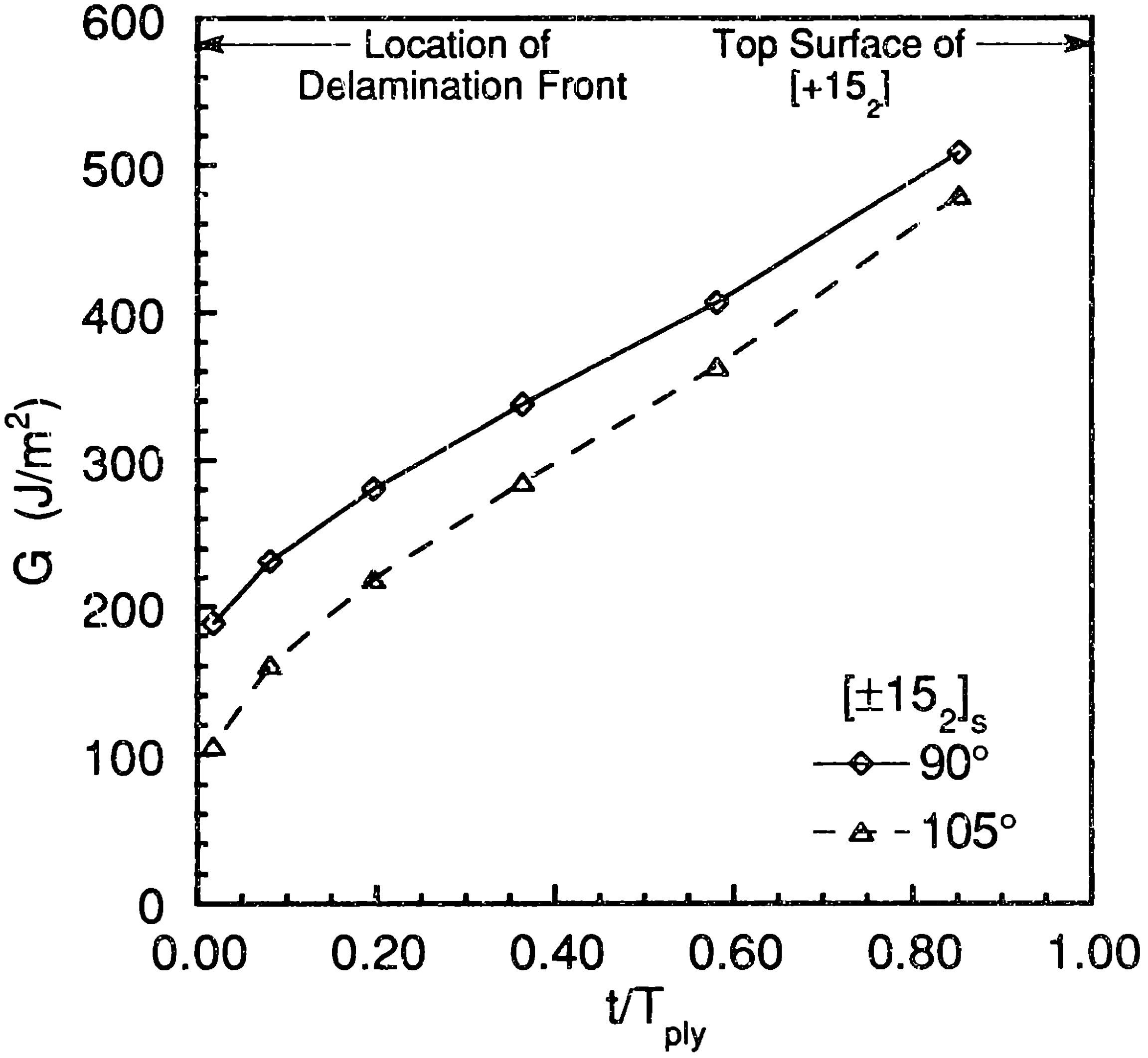

Figure 6.36a Total strain energy release rate along the matrix crack front for the cases of delamination oriented at 90° and 105° to the matrix crack in a $[\pm15_2]_s$ laminate at a strain level of 5650 μstrain for different delamination front orientations.

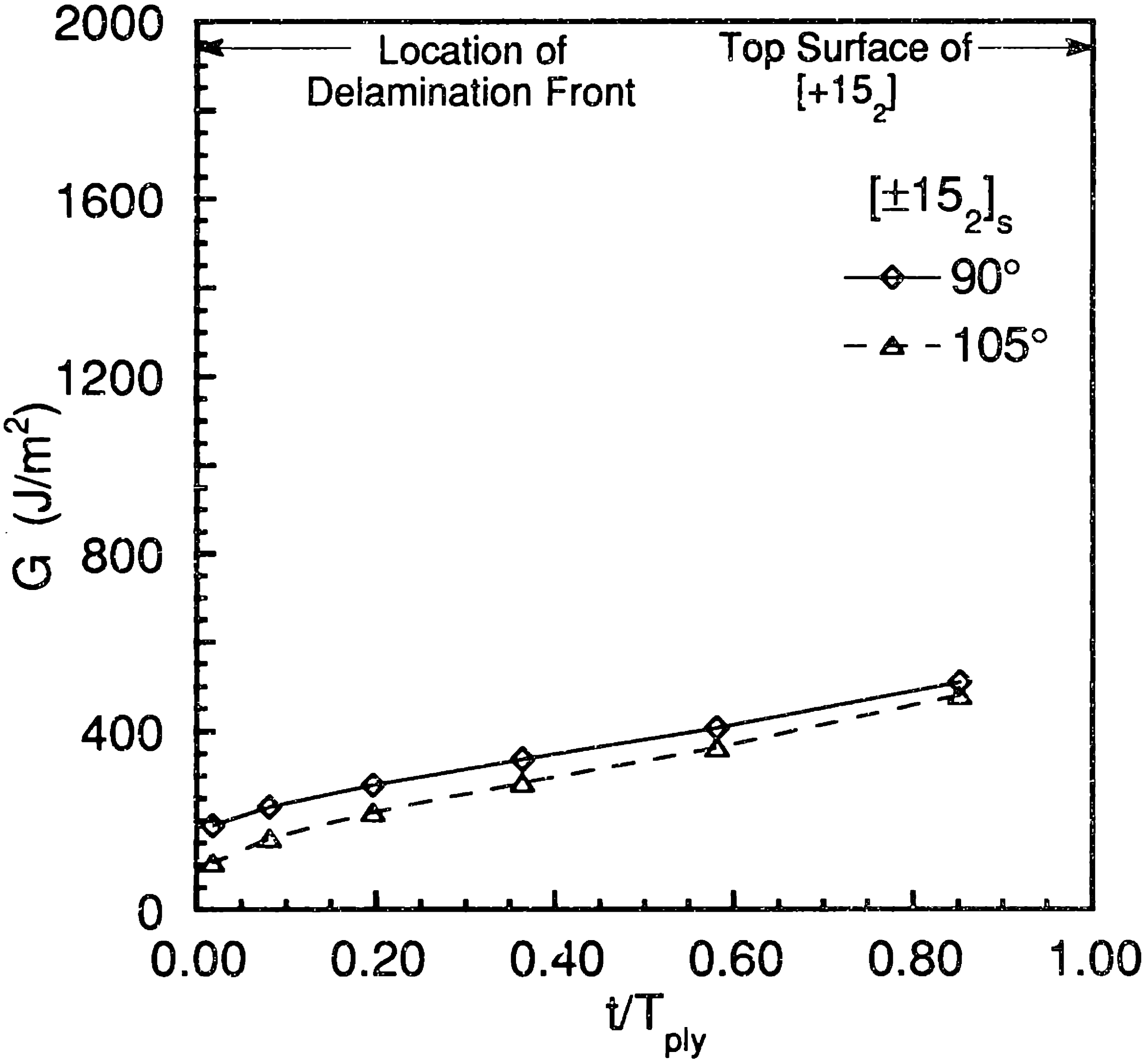

Figure 6.36b Total strain energy release rate along the matrix crack front for the cases of delamination oriented at 90° and 105° to the matrix crack in a $[\pm15_2]_s$ laminate at a strain level of 5650 μstrain for different delamination front orientations (scale changed for comparative purposes).

Figure 6.38. Only the results for the two stresses σ_{11} and σ_{13} are presented because these are the only stresses which have a significant magnitude at the free edge of the laminate. The contour plots for the stress σ_{11} normalized by the far-field value determined by the classical laminated plate theory within each ply (σ_{11} for both plies are identical) are presented in Figures 6.39, 6.40 and 6.41 for the 90°, 105° and 120° orientations, respectively. The contour plots for the stress σ_{13}, also normalized by the classical laminated plate theory values of σ_{11}, are presented in Figures 6.42, 6.43 and 6.44, respectively, for the 90°, 105° and 120° orientations. These contour plots, however, do not convey much information due to the inability of the mesh to accurately capture the stresses around the delamination front as seen by the discontinuities in the stress contour plots. There is hardly any discernible difference between the stress states for the 90°, 105° and 120° cases. Therefore, no conclusion can be drawn regarding any changes in the stress states at the free edge for different orientations of the delamination. Consequently, no conclusions can be drawn from this data regarding the secondary cracking which develops at the delamination front before failure of the laminate.

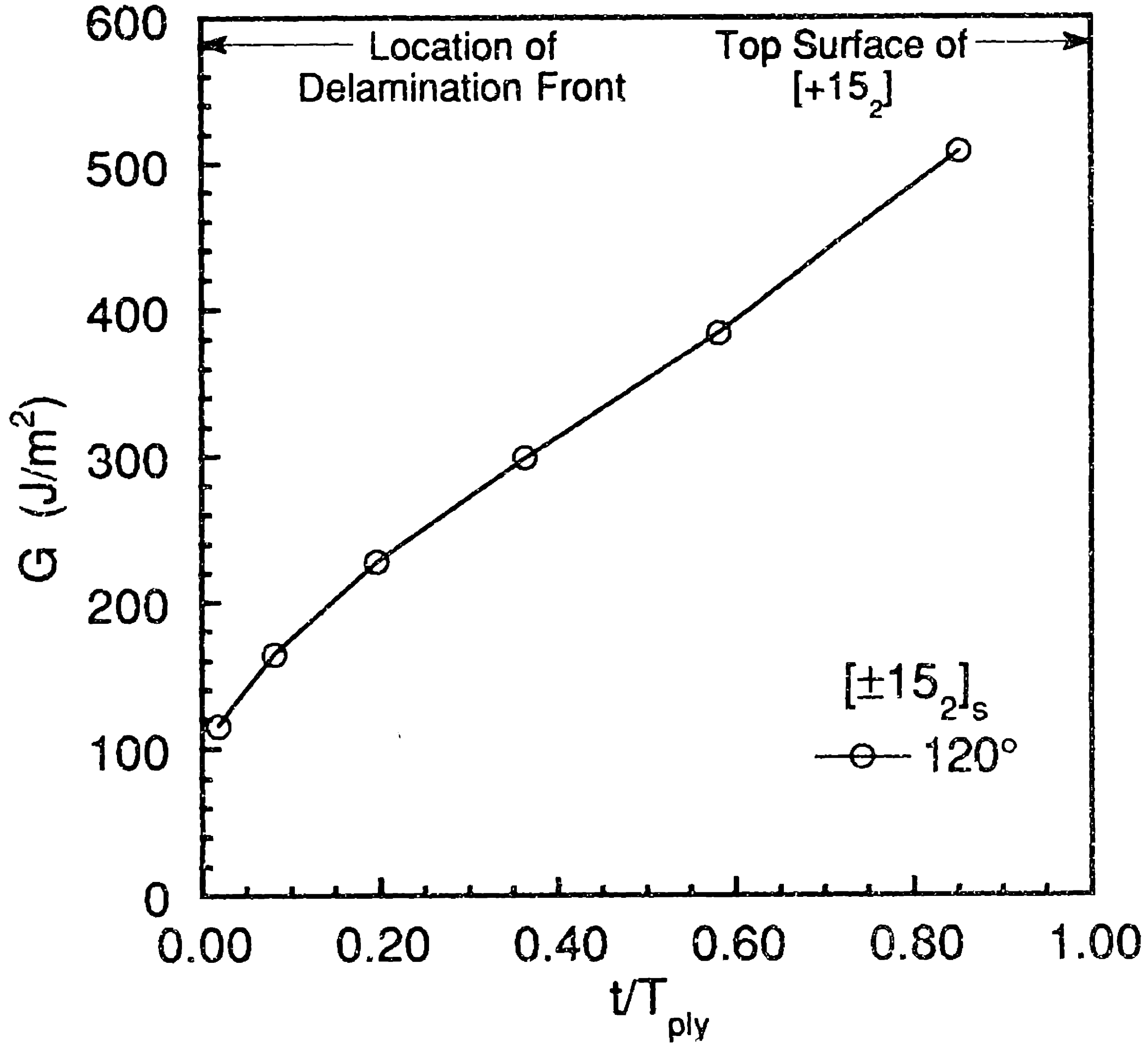

Figure 6.37a Total strain energy release rate along the matrix crack front for the cases of the delamination front oriented at 120° to the matrix crack in a $[\pm15_2]_s$ laminate at a strain level of 5650μstrain.

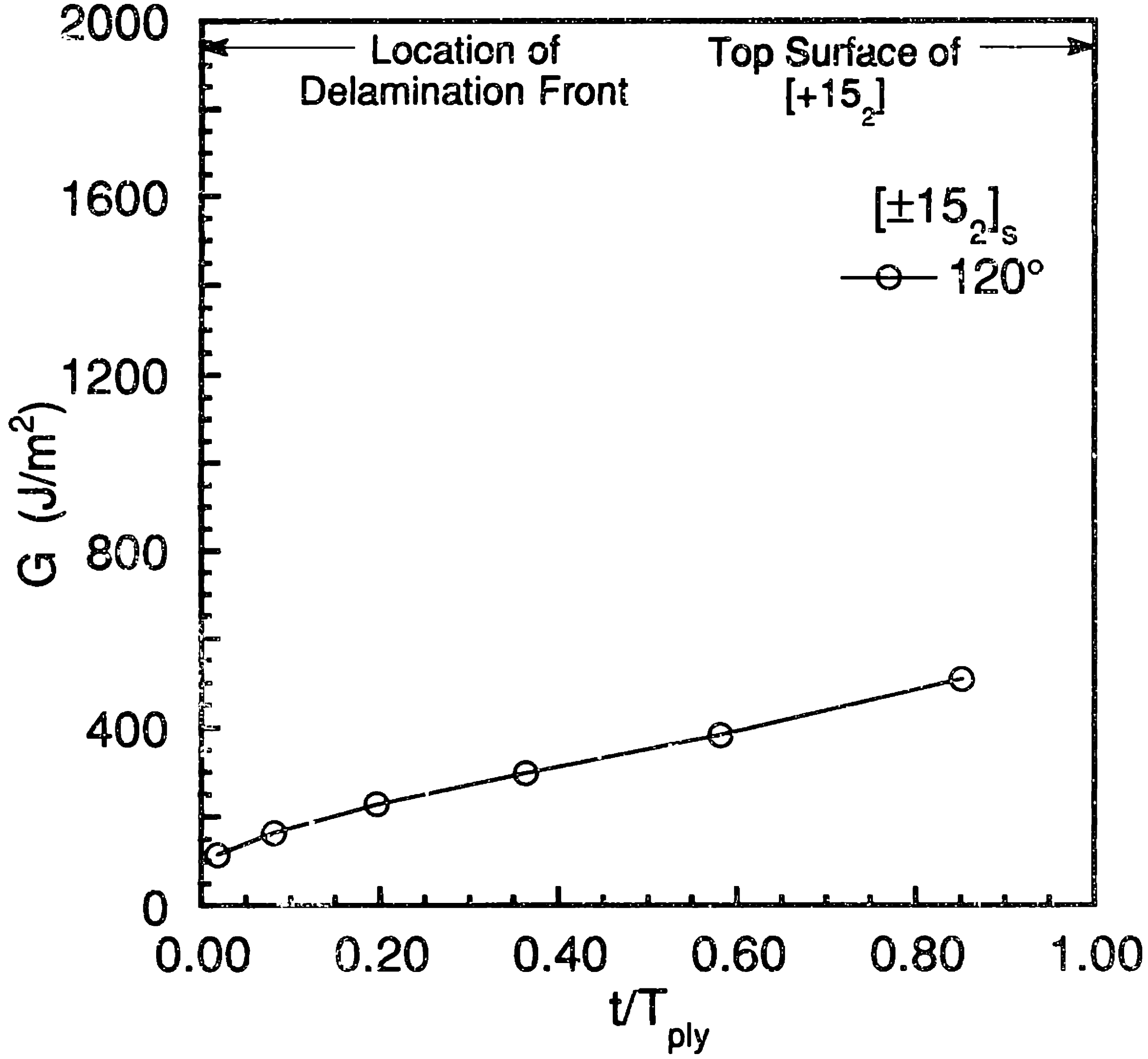

Figure 6.37b Total strain energy release rate along the matrix crack front for the cases of the delamination front oriented at 120° to the matrix crack in a $[\pm15_2]_s$ laminate at a strain level of 5650μstrain (scale changed for comparative purposes).

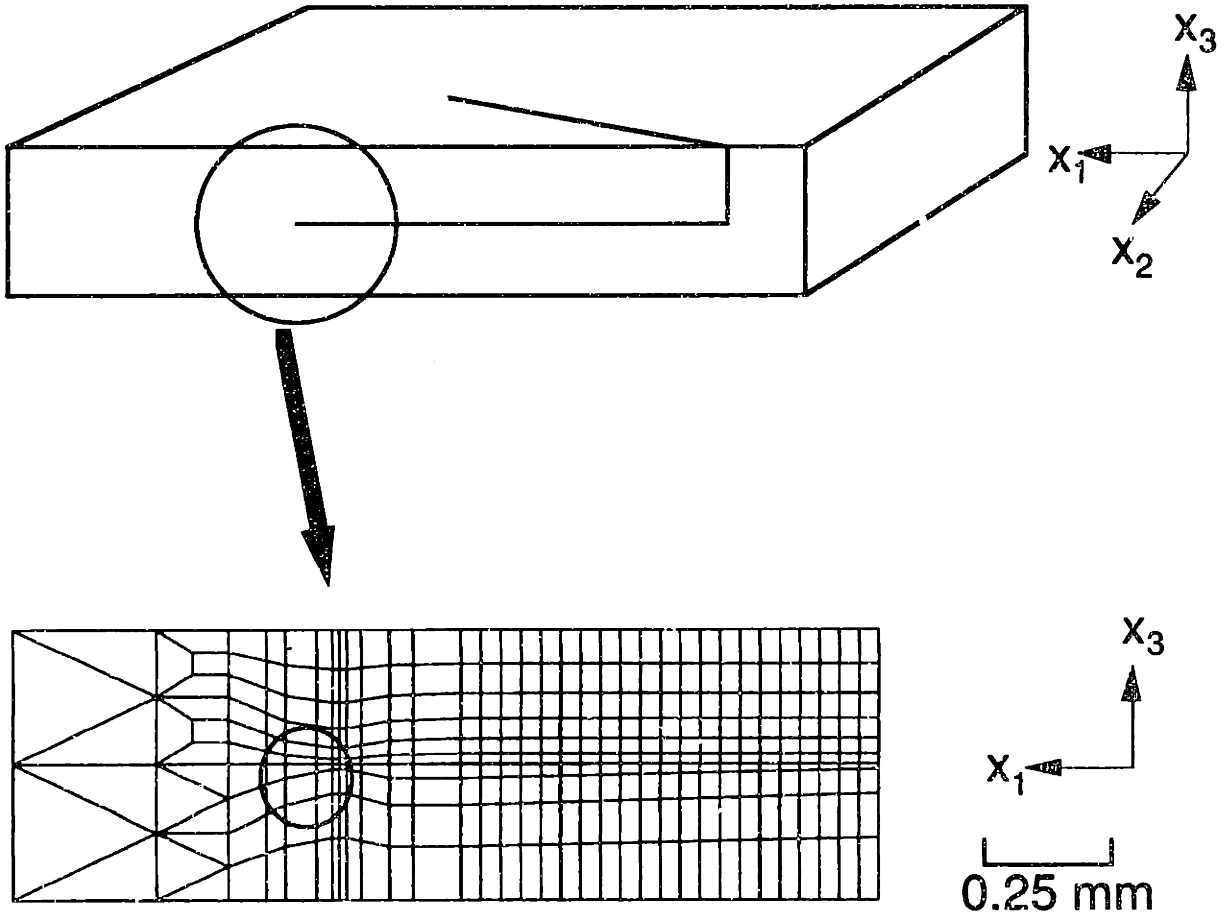

Figure 6.38 Diagrams showing (*top*) broad region around the delamination front which is selected in the finite element model to obtain stress contours, and (*bottom*) the specific elements around the crack tip region where the stress contours are evaluated.

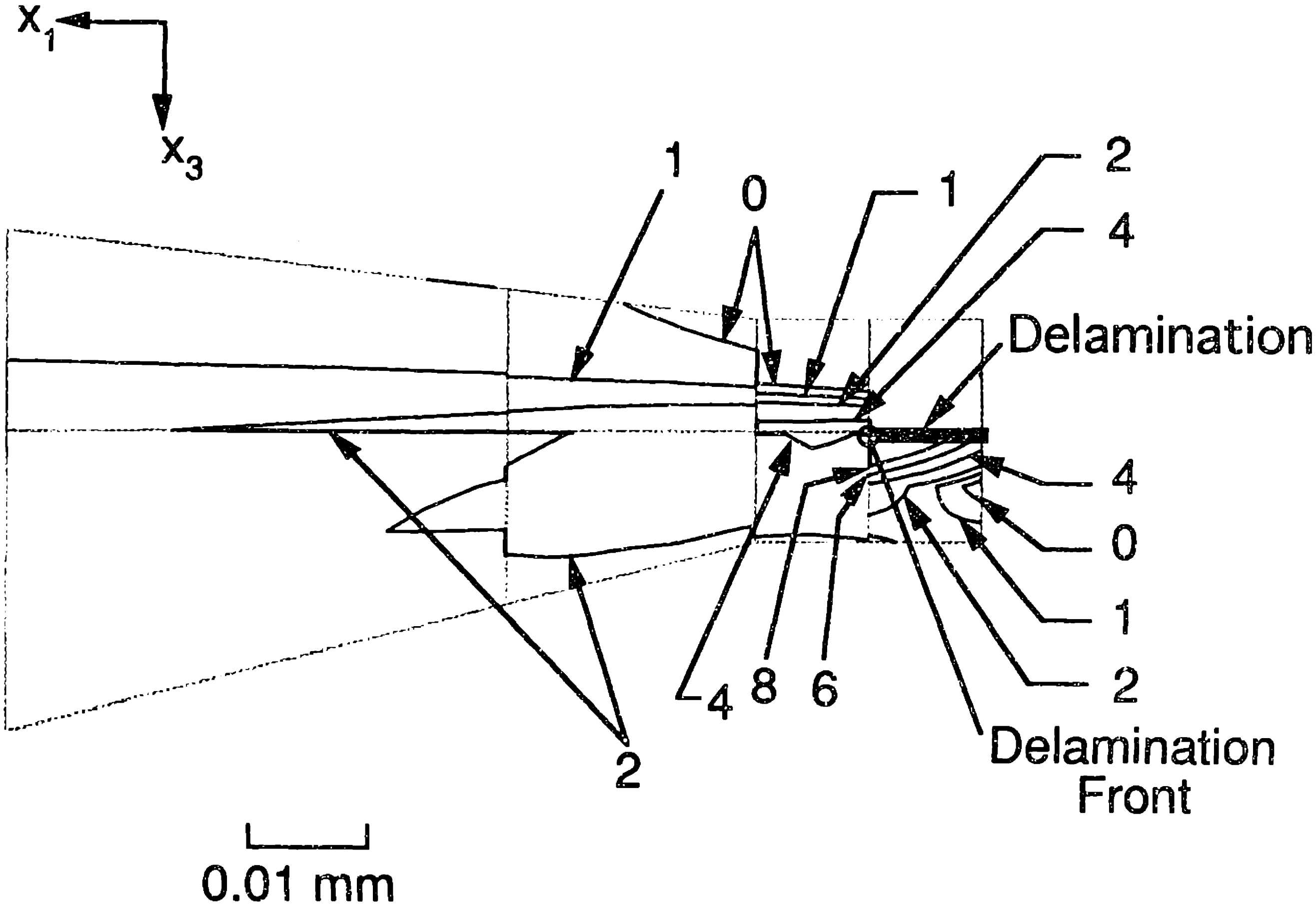

Figure 6.39 Contour plot, viewed at the free edge of the $[\pm 15_2]_s$ laminate with delamination front oriented at 90°, for the stress σ_{11} nondimensionalized by the far-field classical laminated plate theory value of σ_{11} (ply stress).

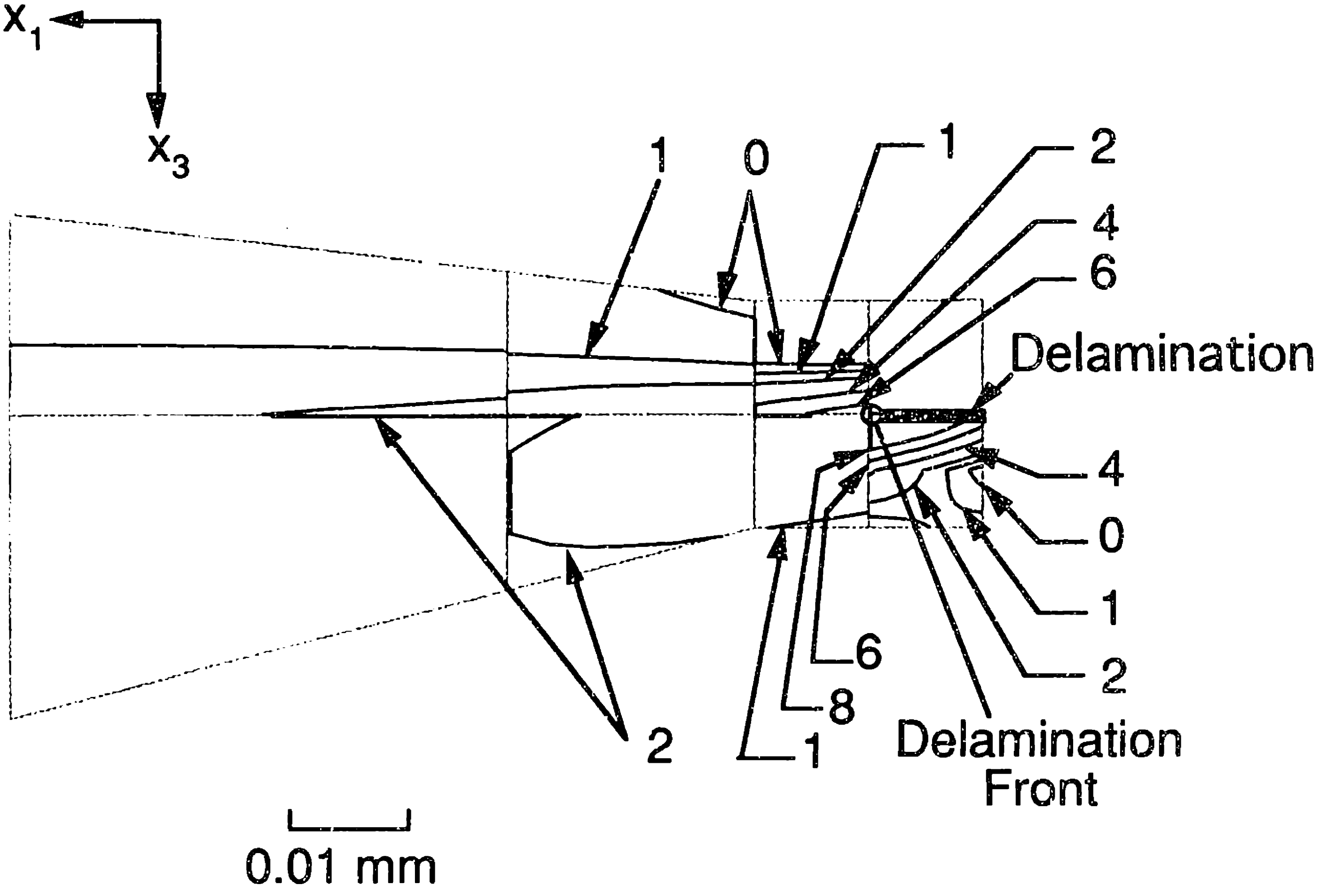

Figure 6.40 Contour plot, viewed at the free edge of the $[\pm15_2]_s$ laminate with delamination front oriented at 105°, for the stress σ_{11} nondimensionalized by the far-field classical laminated plate theory value of σ_{11} (ply stress).

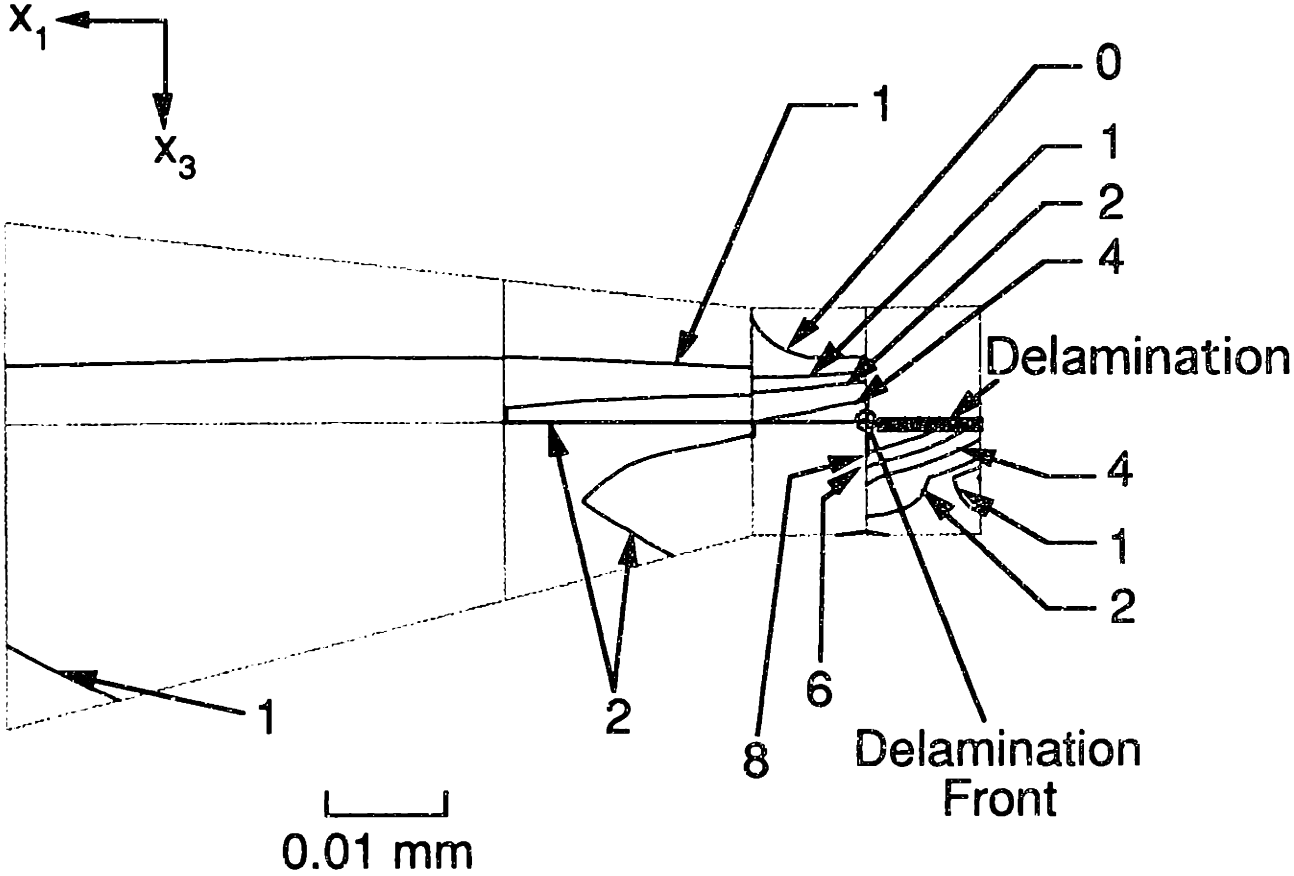

Figure 6.41 Contour plot, viewed at the free edge of the $[\pm15_2]_s$ laminate with delamination front oriented at 120°, for the stress σ_{11} nondimensionalized by the far-field classical laminated plate theory value of σ_{11} (ply stress).

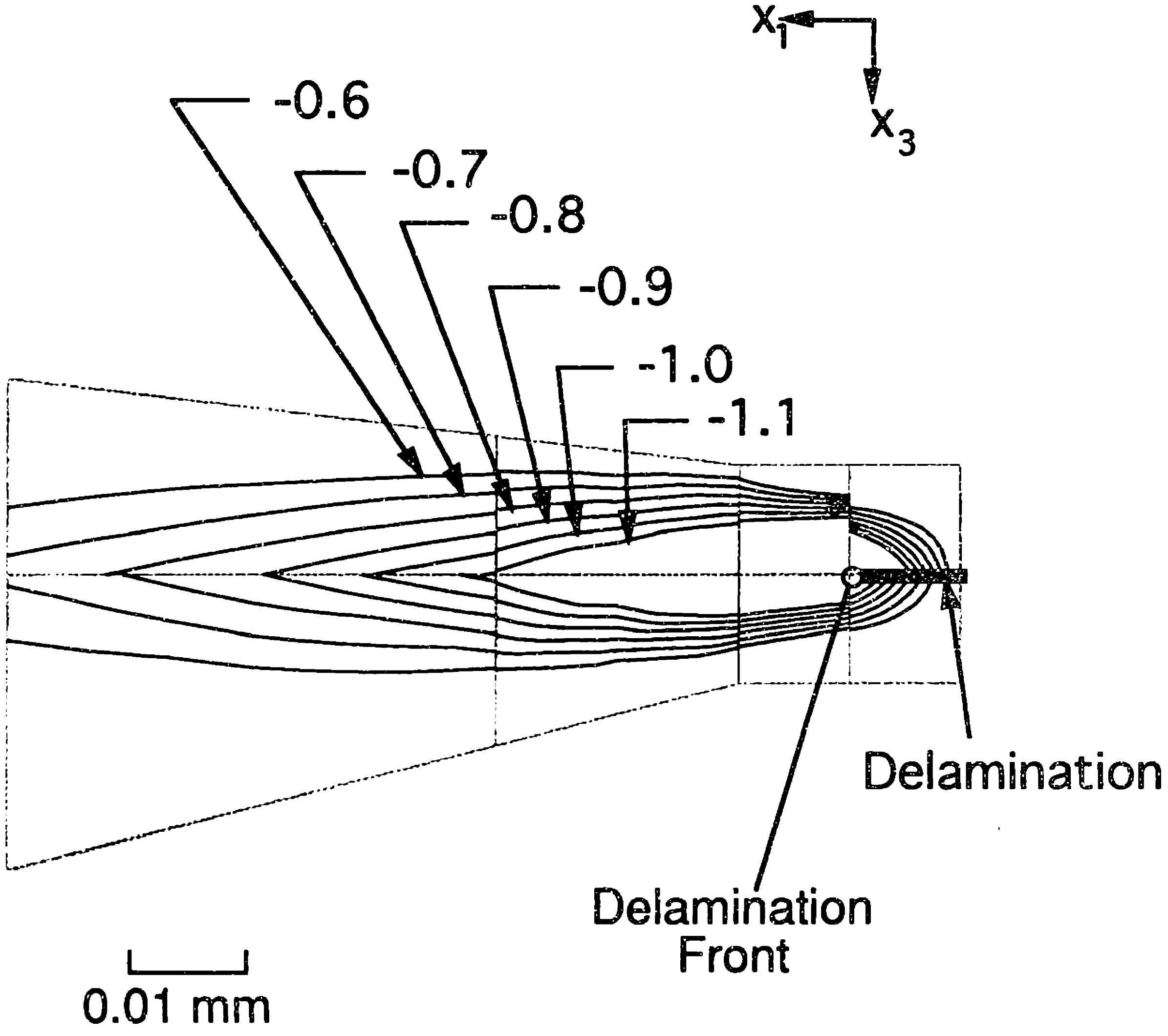

Figure 6.42 Contour plot, viewed at the free edge of the $[\pm 15_2]_s$ laminate with delamination front oriented at 90°, for the stress σ_{13} nondimensionalized by the far-field classical laminated plate theory value of σ_{11} (ply stress).

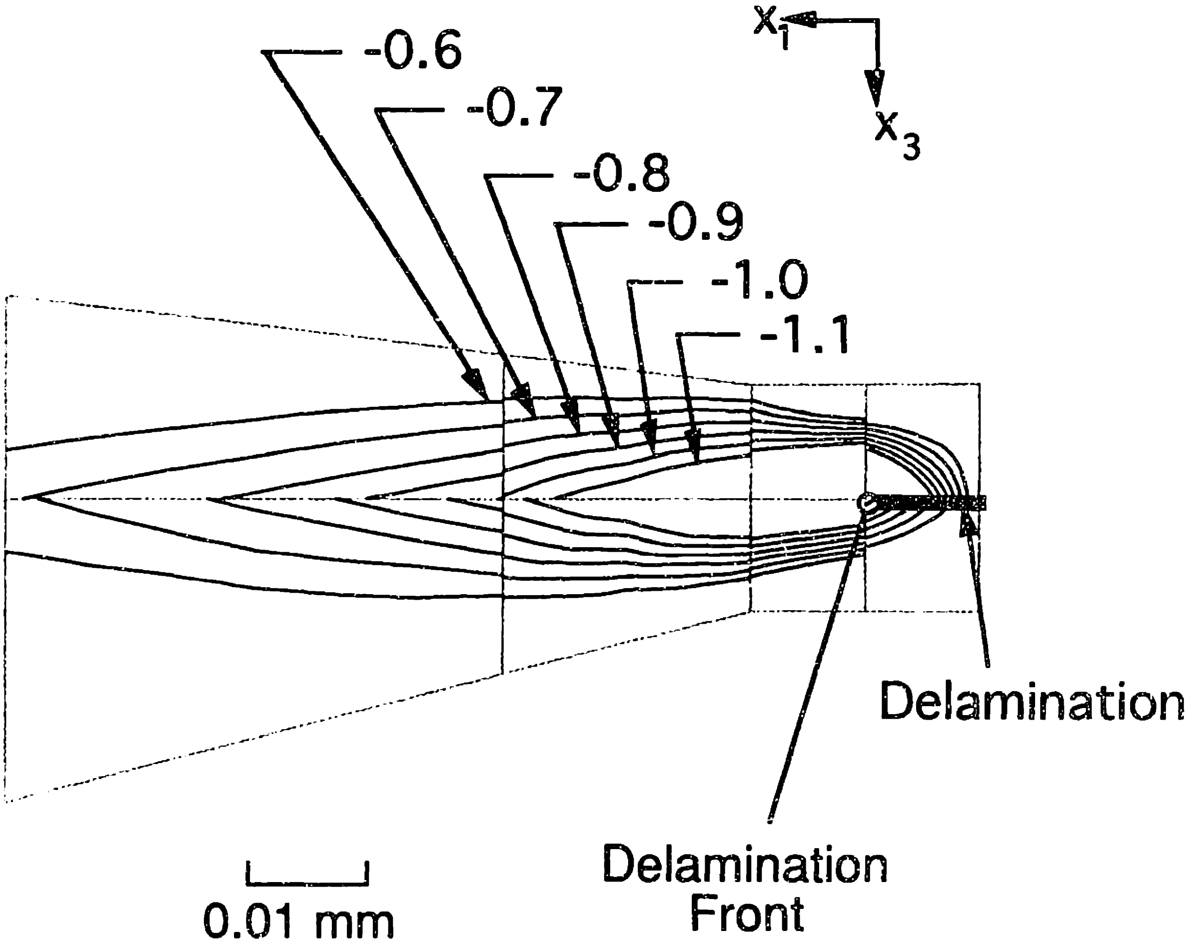

Figure 6.43 Contour plot, viewed at the free edge of the $[\pm 15_2]_s$ laminate with delamination front oriented at 105°, for the stress σ_{13} nondimensionalized by the far-field classical laminated plate theory value of σ_{11} (ply stress).

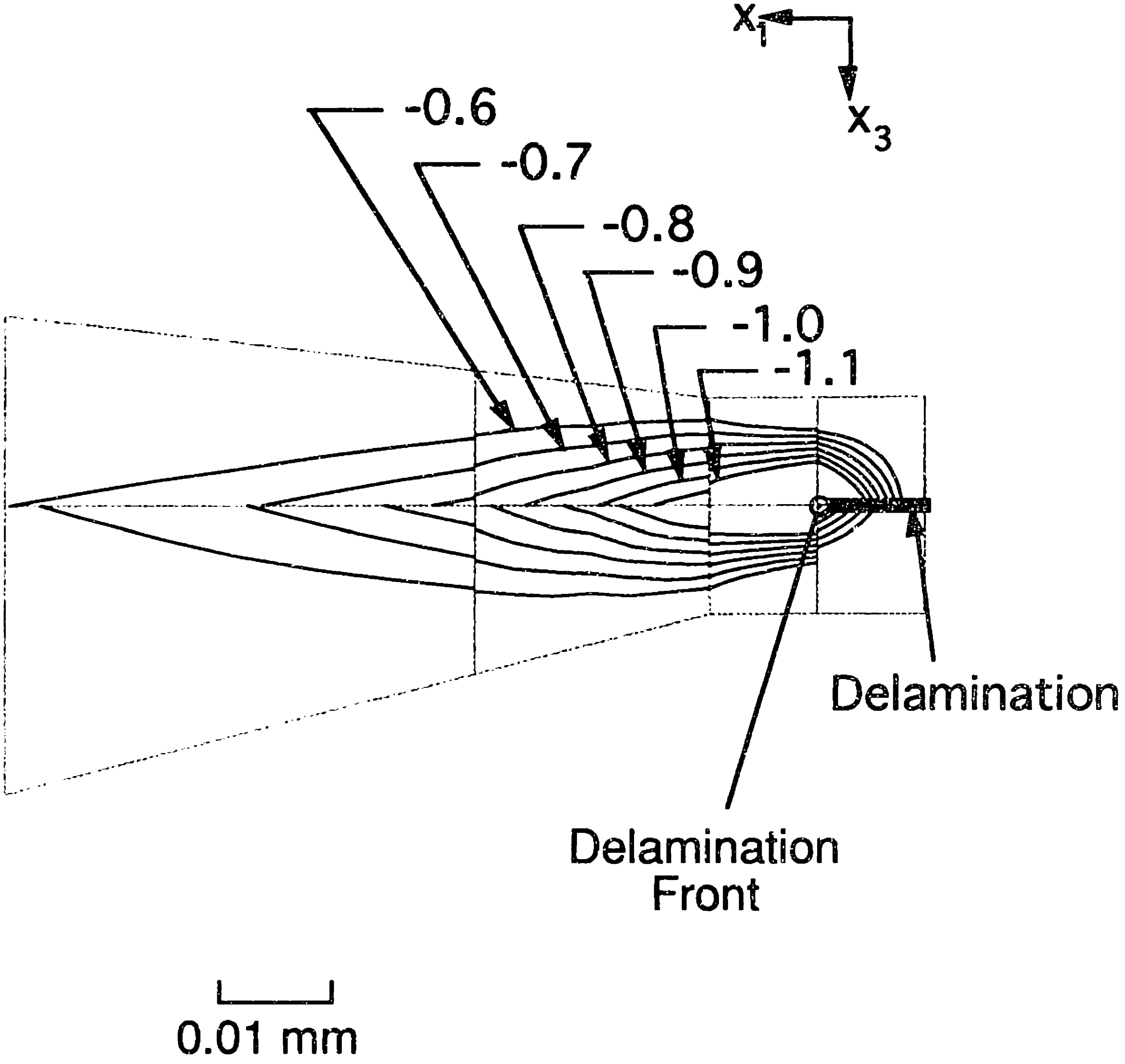

Figure 6.44 Contour plot, viewed at the free edge of the $[\pm 15_2]_s$ laminate with delamination front oriented at 120°, for the stress σ_{13} nondimensionalized by the far-field classical laminated plate theory value of σ_{11} (ply stress).

CHAPTER 7

DISCUSSION OF RESULTS

The results presented in the previous chapter are discussed in detail in this chapter. A comparison is made between the results of the specimens with implants and the unflawed specimens. The analytical model is assessed and the resulting predictions for the growth of the delamination from its initial configuration are compared to the experimental results. On the basis of these results, a mechanism for damage growth in these specimens is proposed.

7.1 Comparison of Unflawed Specimens and Specimens with Implants

The modulus of both the $[\pm15_n/0_n]_s$ and $[\pm15_2]_s$ specimens with implants matched the modulus values obtained for the unflawed specimens very closely. These results are also close to the values predicted by the classical laminated plate theory. Therefore, the presence of the implants did not alter the far-field stress-strain response of the specimens.

The failure strains and stresses of the $[\pm15_2/0_2]_s$, and $[\pm15_3/0_3]_s$ specimens with implants were also identical to those of the similar unflawed specimens. In the case of the $[\pm15_5/0_5]_s$ specimens, however, the failure stresses and strains are 20% lower than for the unflawed specimens which falls well beyond the experimental scatter of 10%. These $[\pm15_5/0_5]_s$ specimens with implants show some secondary cracking in the -15° plies within the delaminated region even before loading. This may be responsible for their early failure. These specimens also showed further secondary matrix cracking after loading, occurring ahead of the delamination front in the -15° ply and extending back across the delamination front into the delaminated region at stresses of about

350 to 400 MPa, before any delamination growth occurs. These secondary cracks are seen to occur in $[\pm 15_5/0_5]_s$ unflawed specimens only after the formation of a triangular-shaped delamination with a curved contour at stresses of about 500 MPa [6]. These stresses are significantly higher than those observed in the specimens with implants. It is not clear whether this premature secondary cracking is responsible for the lower failure strains observed in these specimens because this type of premature secondary cracking is also observed to occur in the $[\pm 15_2]_s$ specimens with implants where it does not alter the failure strains of these specimens as compared to the unflawed specimens.

Examination of the failed specimens indicates that there is a difference in the damage states observed in the $[\pm 15_n/0_n]_s$ laminates for different values of n. For n equal to two, fiber failure was observed in all the plies of the laminate and secondary cracking was observed in the -15° plies in and around the implanted delamination. The implanted delamination did not grow to the ends of the specimens. This type of failure is similar to that observed in unflawed specimens except that the delamination grows all the way to the tabs in the unflawed specimens [6]. For n equal to three, the implanted delamination grows to the tab and secondary cracking is observed in and around the delaminated region. Fiber failure is localized to some regions of the specimen outside the delaminated region and this type of failure is almost identical to that observed in unflawed specimens [6]. For n equal to five, the implanted delamination grows to the end of the specimen and secondary cracking is observed within the delaminated region only. This failure is very clean compared to the earlier type of specimens, with virtually no fiber failure at all, and is almost identical to that observed in unflawed laminates of this type [6].

The unflawed specimens of the $[\pm 15_2]_s$ laminates developed triangular-shaped delamination regions. These regions formed and grew almost instantaneously to the ends of the specimens at failure. No stable triangular delaminations were seen for these specimens before the failure load unlike the $[\pm15_3]_s$ specimens discussed in Chapter three. An examination of the failed specimens showed that there was secondary matrix cracking in the delaminated region and in some cases fiber failure in all the plies, outside the delaminated region. Since no damage was observed before failure, it appears that the formation of the secondary cracking and the formation of the triangular-shaped delamination both occur virtually simultaneously at failure.

The $[\pm15_2]_s$ specimens with implants also fail in an almost identical manner to the unflawed specimens with the growth of the implanted delamination to the ends of the specimen, accompanied with fiber failure at various locations in the plies outside the region of delamination. The failure strains and stresses for the unflawed specimens and specimens with implants are also virtually the same. However, in the case of the specimens with implants, the secondary cracking is seen to occur before any delamination growth occurs. Since the triangular-shaped delamination is already present, it therefore appears that the stress state may be suitable for the formation of secondary matrix cracks before the growth of the delamination.

In summary, the implanted specimens simulate the behavior of unflawed specimens quite well in most cases in terms of modulus (and general stress-strain behavior), failure stresses and strains, as well as the damage states observed subsequent to failure. In some cases, though the damage at final failure resembles that in the unflawed specimens, the intermediate damage does not occur in the same order that is observed in the unflawed specimens. This is described further in section 7.3 where the growth of implanted delaminations is discussed.

7.2 Assessment of the Analytical Model

The deformed finite element model, as shown in Figure 6.28, indicates that the delaminated region deforms in a manner which lifts it above the surface of the laminate, as was observed in the experiments. The top view of the +15° ply also shows that the matrix crack has a tendency to open up at regions away from the matrix crack front. However, near the matrix crack front, the crack surfaces are very close to each other and, for a delamination oriented at 90° to the matrix crack, interpenetration of crack surfaces is predicted at the crack tip elements. As the delamination angle is changed to 105°, interpenetration is restricted to the region where the matrix crack front meets the top surface of the $[+15_2]$ ply. Interpenetration is not predicted by the model for the 120° case. This interpenetration is likely to depend on both the crack front and crack profile characteristics. Since both these profiles are modelled as straight lines in the present model, it is not known whether crack surface contact does occur in the actual specimens where the crack profile is curved and the shape of the crack front is unknown. Therefore, the curved crack profile needs to be modelled. If interpenetration is still predicted by the model, a nonlinear analysis may be necessary to analyze the problem.

The far-field stress values determined from the model at the locations shown in Figure 6.24 are seen to be similar to those determined from classical laminated plate theory. This implies that the model is sufficiently large enough that regions termed as 'far-field' are not affected by the presence of the delamination. It needs to be pointed out that only a quarter model of the laminate has been made for the current study. Therefore, the boundary condition imposed on the laminate implies that the centerline of the laminate shown in Figure 6.27 does not move in the x_2-direction. While this boundary condition is true in the case of an unflawed laminate, it is not completely true in the case of a laminate with triangular-shaped delaminations where some shearing is likely to occur. However, for "small" delamination sizes (in the present case with a ratio of less than a third for the intrusion to width ratio) the conditions termed as far-field are much the same as that for an unflawed laminate. Also, imposing this boundary condition reduced the model from a half model to a quarter model resulting in considerable reduction in computation time. The use of this boundary condition was then justified by comparing the results for the stresses to those obtained via classical laminated plate theory.

The results that are presented for the energy release rate are obtained only using the Equivalent Domain Integral method. The modes are separated using the mode decomposition technique. As discussed earlier, this method is capable of evaluating the total strain energy release rate correctly. However, it has been shown to be valid in conjunction with the decomposition method to separate the modes only in cases where the oscillatory singularity does not exist. In the present case, the oscillatory singularity has a nonzero value, yet this method has been used to separate the modes for two reasons. The first reason is that the oscillatory singularity in the present context is quite small, as is presented further on in the text. Second, it was shown in the example of the $[\pm 75_2]_s$ laminate in Chapter four that the trends of the individual modes of energy release rate as obtained from the Equivalent Domain Integral approach are very similar to the trends that are obtained by the Crack Opening Displacement approach on ignoring the presence of the oscillatory singularity. This similarity in trends between the results obtained by the two approaches does not validate either method but indicates consistency between the results obtained by two independent methods. Since there are no theoretical definitions of modes that exist in the cases with oscillatory singularities, there are no comparisons that could be made to validate these modes.

The Crack Opening Displacement approach which accounts for the presence of the oscillatory singularity has not been used in the present context for a number of reasons as elaborated here. The method had been developed for the case of generalized plane strain. The present conditions along the delamination front are more representative of a full three-dimensional problem and cannot be considered as plane strain or generalized plane strain. Second, there are three different configurations of the delamination front analyzed. This means that the delamination is located between two anisotropic materials whose properties change in the three cases relative to the orientation of the delamination front as it is changed from 90° to 120°. In the initial configuration, the plies above (+15°) and below (-15°) the delamination have an orientation of 0° and -30° relative to the x'_1-direction respectively, as shown in Figure 7.1. When the delamination is reoriented such that it subtends an angle of 105° or 120° with the matrix crack, the material orientation of the effective ply above the delamination is -15° or -30°, and the material orientation of the effective ply below the delamination crack is -45° or -60°, respectively. This implies that the oscillatory singularity at the delamination front changes at the delamination front for the three cases modelled. Any use of a new definition of modes discussed in Chapter four or the use of the results from the COD approach needs to consider this factor, the consequences of which are not understood. The oscillatory singularities δ are evaluated for each of these cases using the method described in Chapter four. The magnitudes of the oscillatory singularities are 0.0298, 0.0194 and 0.0232 for the delamination oriented at 90°, 105° and 120° to the matrix crack, respectively. It is seen that in all the cases, the oscillatory singularity is extremely small compared to the maximum possible value of 0.175. The problem of dealing with even a constant oscillatory singularity was itself termed as an unresolved issue and hence the consequences of a changing oscillatory singularity are unknown.

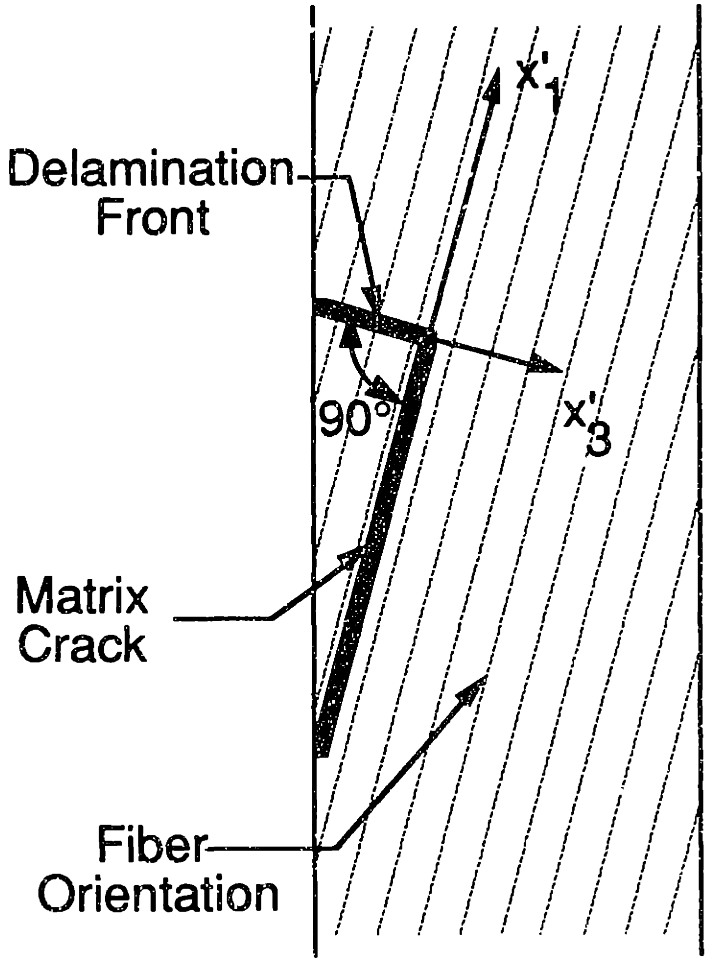

Figure 7.1 Orientation of the top ply relative to the local x'_1-axis at the delamination front for the delamination oriented at 90° relative to the matrix crack.

Since the magnitude of the oscillatory singularity was small, the conventional approach of the Equivalent Domain Integral along with the decomposition approach appeared to be the most feasible method of observing the trends displayed by the individual modes of the energy release rate. The modes obtained are not necessarily representative of the actual physical processes that occur at the crack front. However, from the research available to date, this was the most efficient method that was identified by the author to provide a separation of the total energy release rate into component modes using the same basis as in isotropic materials. These modes are therefore presented as possible measures of the processes occurring at the crack tip. This is an active research issue which needs to be further resolved before a physical meaning can be attached to the "modes" that have been obtained by the current study.

The implanted delamination front does start out as a straight line at right angles to the matrix crack. But, as the implanted delamination grows, it is no longer a straight line as it does not grow equally at all points of the implant. However, this growth is modelled by a straight line in the current work. This is representative of the approximate manner in which the delamination grows due to complexities involved in modelling the curved delamination front. The modelling of the curved delamination front is a recommended step for future studies in the growth of the delamination front.

The stresses at the delamination front were also examined for different orientations of the delamination. The nonzero stresses at the free edges of the specimen were examined. The results for the stresses shown in Figures 6.39 through 6.44 indicate that the mesh is still quite coarse since the stresses are discontinuous across elements. No discernible difference exists between the stresses examined at the free edge, to which the formation of the matrix cracks could be attributed. This may imply three possibilities: one, the mesh needs further refinement to detect any differences between the different orientations; or, two, the matrix crack could initiate at some point on or in the neighborhood of the delamination front, not at the free edge; or, three, the curved nature of the delamination not modelled in the current study may be the reason sufficient stresses arise to cause secondary cracks. Therefore, the mesh must be refined in future studies and the changes in stresses at the delamination front in regions away from the free edge must be examined.

7.3 Manifestations of Damage Growth from Implanted Configuration

The experimental results obtained for the growth of implanted triangular-shaped delaminations are compared here with the predictions from the analytical results. Although the implants were placed in both the $[\pm15_n/0_n]_s$ specimens and the $[\pm15_2]_s$ specimens, the growth of the implanted delaminations without the early formation of any secondary cracking occurred only in the $[\pm15_n/0_n]_s$ laminates. The unflawed $[\pm15_2]_s$ specimens showed formation of triangular-shaped delamination which grew instantaneously to the ends of the specimens. No stable delaminations were observed and hence no X-ray radiographs of the intermediate stages are available. Therefore, the analytical results obtained for the growth of a triangular-shaped delamination in a $[\pm15_2]_s$ laminate are used to explain the results of experimentally observed stable delamination growth in the $[\pm15_n/0_n]_s$ laminates. This may be done since the unflawed specimens of the $[\pm15_n]_s$ or $[\pm15_n/0_n]_s$ laminate families show the same characteristic delamination, i.e. the delamination is always located at the +15/-15 interface and the matrix crack is always within the +15° sublaminate. The delamination front observed in the naturally occurring delamination configuration is also observed to be curved irrespective of the presence of the additional 0° plies (as was seen in Chapter two). Furthermore, the classical laminated plate theory stresses within the individual plies are very similar between the two laminates. These values, as a percentage of the far-field stress, $\bar{\sigma}_{11}$ applied to the laminate, are compared in Table 7.1. The stresses in the 15° plies of the two laminates vary from each other only by the small transverse stresses which exist in the $[\pm 15_n/0_n]_s$ laminates and are absent in the $[\pm 15_n]_s$ laminates. In addition, the failed specimens of both these laminates show similar characteristics, indicating a similar mechanism underlying the failure behavior of these two types of specimens. Thus, the delamination growth in the $[\pm 15_2]_s$ laminates is likely to have undergone the same growth patterns observed in the $[\pm 15_n/0_n]_s$ laminates, however, in an unstable manner. The explanations offered, therefore, also pertain to the $[\pm 15_2]_s$ laminates despite the unstable nature of the growth in that case.

The analytical results for the total strain energy release rate were presented in Figure 6.29. These results are for an applied far-field strain of 5650 μstrain, which is the average failure strain for the unflawed $[\pm 15_2]_s$ laminates that were tested in the current study. At this failure strain, triangular delaminations were seen to form and simultaneously grow to the ends of the specimen in the experiments. The results were presented for this strain so that the energy release rate values obtained at this strain may be compared to the critical energy release rates available in the literature.

From these results, it is seen that the energy release rate at the delamination front is highest at the free edge region and drops considerably at the matrix crack front region. This implies that the delamination front would have a tendency to grow from the region near the free edge. The process of growth is approximated by tilting the delamination front about the matrix crack so that the maximum amount of growth is at the free edge and there is no growth at the matrix crack. As the delamination orientation is changed to 105°, the energy

Table 7.1 Classical laminated plate theory stresses in the plies of $[\pm 15_n]_s$ and $[\pm 15_n/0_n]_s$ laminates in the laminate axes as a ratio of the far-field laminate stress ($\bar{\sigma}_{11}$)

Stress Ratio	$[\pm 15_n]_s$		$[\pm 15_n/0_n]_s$		
	+15°	-15°	+15°	-15°	0°
$\sigma_{11}/\bar{\sigma}_{11}$	1.00	1.00	0.94	0.94	1.12
$\sigma_{22}/\bar{\sigma}_{11}$	0	0	0.02	0.02	-0.04
$\sigma_{12}/\bar{\sigma}_{11}$	0.23	-0.23	0.21	-0.21	0

release rate still maintains its relative distribution along the delamination front, being highest at the free edge region and lowest near the matrix crack. However, the magnitude of the energy release rate at the free edge is lower than that observed for the 90° case and it is marginally higher along the other regions of the delamination front. Further growth is simulated by tilting the delamination to an angle of 120° relative to the matrix crack. The energy release rate is seen to drop again near the free edge and it is seen to increase along other regions of the delamination front in what appears to be a tendency of the strain energy release rate to become more uniform along the entire delamination front.

This implies that a delamination that starts from the initial configuration chosen should have a tendency to start growth near the free edges and the growth should be such that the delamination would have a tendency to build up a more uniform energy release rate along the delamination front. There is, however, a decrease in the energy release rate associated with this simulated growth for a given far-field value of strain. Therefore, as the delamination grows, it is possible that the criterion governing the growth of the delamination may no longer be satisfied at some points along the delamination front, and it would tend to stop growing. This assumes the absence of any additional form of damage such as secondary cracking which are not addressed in this model.

The energy release rate along the matrix crack tip in the initial configuration is about a third of that observed along the delamination front. Hence, any growth of damage that occurs would have to be along the delamination front. This is, however, true only if the critical values of energy release rate are similar for the delamination crack and the matrix crack. There is no data available for the critical values for the matrix crack in AS4/3501-6 graphite/epoxy but, from the data available for T300/934 graphite/epoxy [53], the critical values for matrix cracks are seen to be of the same order ($G_{Ic,}$ G_{IIc} are

160 J/m^2, 500 J/m^2 respectively, and no data is available for G_{IIIc}) as for the delamination cracks in that material. Though the numerical values for AS4/3501-6 may be different from these, it appears that, at least in thermoset graphite/epoxy composites, there is no significant difference in the critical values of energy release rate for delamination cracks and matrix cracks. Therefore, the small energy release rate at the matrix crack front implies that the delamination front is more likely to grow over the matrix crack front. There is no significant change in the total energy release rate along the matrix crack front as the delamination changes orientation, though the results for the 90° and 105° case are only approximate. As mentioned earlier, the specific detail of the energy distribution may be dependent on the exact crack profile or crack front which are not modelled in the current study. Hence, the energy release rate along the matrix crack front is used only for an order of magnitude comparison study.

The strain gages at the delamination front and at the matrix crack front were intended to be indicators of any changes in the damage from the initial configuration. The magnitude of the strain measured by these gages is not of much importance, but the discontinuities observed in the data are expected to be the indicators of any local changes in damage. The $[\pm15_2/0_2]_s$ specimens and $[\pm15_3/0_3]_s$ specimens showed similar behavior, with a discontinuity observed in the delamination gage data before a discontinuity was registered in the gage located at the matrix crack front. This is experimental evidence that delamination growth near the free edge occurred before either the matrix crack or the delamination near the matrix crack front had any growth. This evidence corroborates the predictions obtained from the analytical model.

The X-ray radiographs of the $[\pm15_2/0_2]_s$ and $[\pm15_3/0_3]_s$ specimens confirm this by showing that delamination growth has occurred along the delamination front near the free edge region. In all the cases studied there was no growth visible at either the matrix crack front, or the regions of the delamination around the matrix crack front. The resulting delamination front after growth is seen to have an approximately curved contour. Therefore, the observed delamination growth from the initial configuration matches the trends proposed from the analytical results. These results indicate that the implanted delamination grows in a manner as to approach the naturally observed delamination configuration described in Chapter three and shown in Figure 3.1. One of the X-ray radiographs shown in Figure 6.7 has been shown again with an additional outline, in Figure 7.2, and this resembles the naturally observed configuration in Figure 3.1 quite closely.

The failure of the specimen occurs subsequent to this initial growth of the delamination. The stress versus strain data of the $[\pm 15_2/0_2]_s$ and $[\pm 15_3/0_3]_s$ specimens taken up to failure indicates that the strain from the gage at the delamination front is the first to drop, followed by a drop in the strain read by the gage at the matrix crack front at either the same stress level or at a slightly higher stress level. Finally, the far-field gage ceases to take data at failure. This indicates that further activity occurs in the region around the delamination front before failure of the laminate since the far-field gage is virtually unaffected prior to failure. It is inconclusive as to whether the discontinuity observed in the strain gage data, after growth is observed from X-ray radiographs, implies further delamination growth or formation of secondary cracks.

Unlike the earlier two laminates, the $[\pm 15_5/0_5]_s$ specimens do not show such delamination growth. These specimens have initial damage in the form of secondary cracks in the -15° plies in the delaminated region visible after the cure. Further secondary cracking is seen to occur at low loads ahead of the delamination front as described in section 7.1. It may be inferred that secondary cracking which occurs in the specimens with implants may be due to the thicker

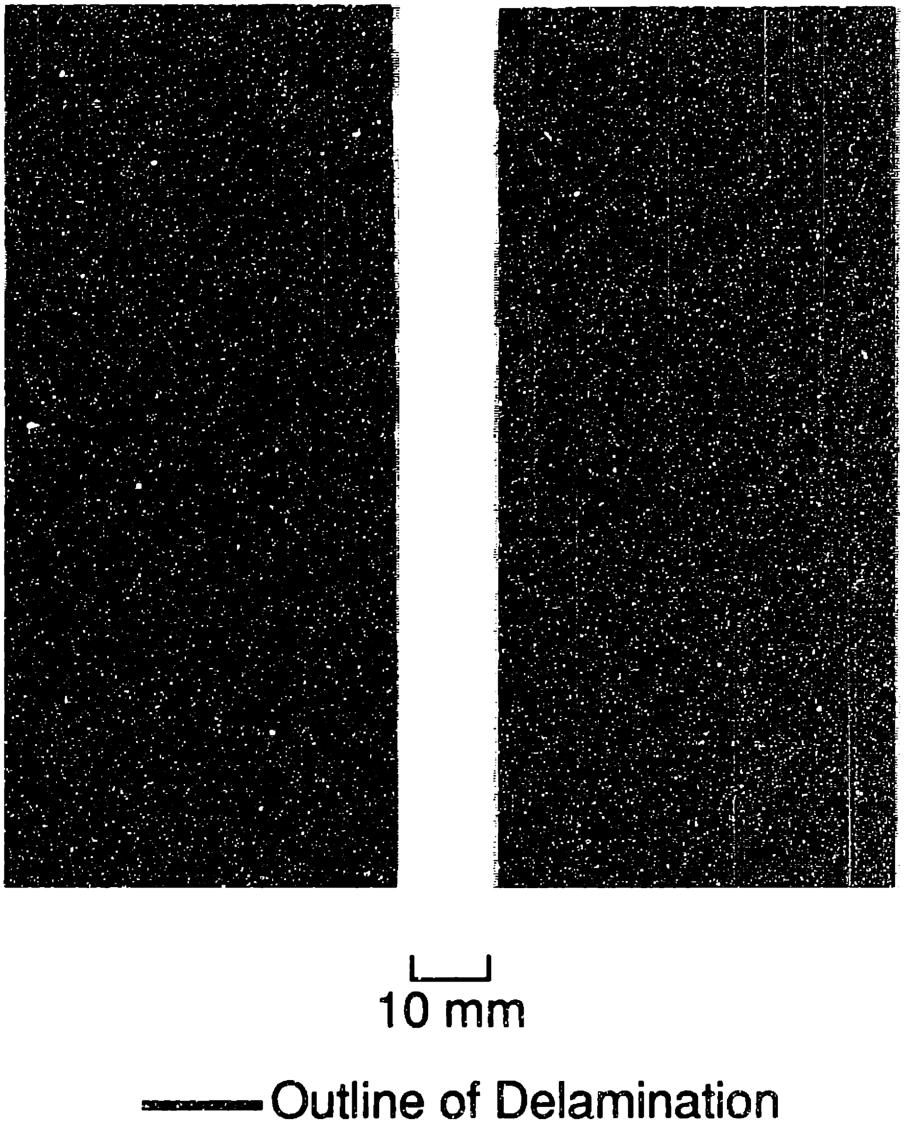

Figure 7.2 X-ray radiograph with the delaminated region outlined (*left*) before and (*right*) after growth of the implanted delamination in a $[\pm 15_2]_s$ laminate.

effective plies. It has been shown [3, 4] that laminates with thicker effective plies (i.e. for larger values of n in laminates such as $[\pm 15_n/0_n]_s$) are more prone to matrix cracking at the free edges and this itself, or coupled with the residual stresses from the cure cycle, could be a possible reason for the cracks observed after the cure. Another possible reason for the occurrence of secondary matrix cracks that form on loading the laminate is that the size of the delamination is larger than that occurring naturally in unflawed specimens without any secondary cracking. Hence, the stress state at this delamination front is likely to be different than that observed in the natural configuration and it is likely that this contributes to the formation of secondary matrix cracks. There is, however, no proof for this hypothesis, but, such premature secondary cracking is also observed to occur in the $[\pm 15_2]_s$ specimens with implants at loads where no damage was observed in the unflawed specimens.

In summary, both the analytical predictions and experimental results indicate that any growth of the implanted delamination configuration manifests itself at the delamination front near the free edge. Experimentally it is also observed that consequent to this growth, the delamination resembles the stable delamination configuration which appears in the unflawed specimens.

7.4 Proposed Growth Mechanism

A growth mechanism is proposed based on the analytical and experimental evidence obtained from the current study for the occurrence of the stable triangular-shaped delaminations and their subsequent growth.

There are four stages which can be identified in the failure process of the composite laminates. The first stage is the initiation of damage, which usually occurs at the free edge of the laminate and is microscopic in nature. The nature of this initiation may be controlled by the defects present at or near the edges of the laminate. The second stage is the propagation of this initial damage to a stable damage configuration consisting of a triangular-shaped delamination bordered by a matrix crack. This damage is macroscopic in nature, but the size of this damage may vary depending on the edge defects or internal defects that may exist in the laminate. The third stage involves the formation of secondary matrix cracking in the plies adjacent to the delamination, in the vicinity of the delamination front. The last stage involves the unstable growth of the triangular-shaped delamination usually to the ends of the specimens, and sometimes accompanied by fiber failure in the laminate.

The initiation of damage and consequent formation of the initial configuration in an unflawed specimen is still a debated issue as mentioned in Chapter two. Experimentally, it has been shown that delamination initiation can occur at the free edges of the $[\pm 15_n/0_n]_s$ series of laminates before any matrix cracking occurs. This is an edge delamination restricted to the free edge of the specimen. It has also been shown earlier, by implanting delaminations alone without matrix cracks [6], that a delamination without a matrix crack tends to develop a matrix crack adjoining it very early in the loading, prior to any delamination growth, thus producing a configuration approximately similar to the initial configuration adopted in this study.

Another alternative mechanism that has been shown analytically to be feasible in $[0_n/\pm\theta_n]_s$ laminates is the formation of the matrix crack and the growth of a delamination initiating from the intersection of the matrix crack and developing into a triangular-shaped delamination [29]. This has not been experimentally observed in static tensile testing, but has been observed under conditions of tensile fatigue loading. This also would lead to the formation of a situation similar to the initial configuration adopted in this study.

Whatever the mechanism responsible for the formation of the damage state consisting of the delamination bordered by a matrix crack, such a damage state is approximated by the initial configuration that has been adopted in the present study. The conditions at this initial configuration are such that the growth is energetically feasible due to the steep energy release rates along the delamination front near the free edge. This results in the growth of the delamination in that region only. The energy release rate at the matrix crack front and the delamination front adjacent to the matrix crack region are much lower and hence conditions are not conducive to growth. This manner of growth of the delamination results in a curved delamination front. This resulting delamination front has a significantly lower peak energy release rate at the free edge, which is insufficient to satisfy the criterion responsible for growth. Hence this is more stable than the initial configuration. This is the reason for the appearance of these types of delaminations in the course of testing of unflawed specimens. Also, since the energy release rate is more uniformly distributed in this new configuration, when the applied strain is increased the entire delamination front has a tendency to propagate. However, an intermediate stage with secondary cracking also appears at this stage before the delamination propagates in an unstable fashion.

In order to obtain further insight into this proposed mechanism the individual modes of the energy release rate are examined. As described earlier, there are uncertainties in the physical implications of these, hence it needs to be pointed out that the proposed growth mechanism was developed with the aid of only the total energy release rate.

The peak value of mode 1 data does not occur at the free edge, but a short distance away from the free edge along the delamination front, and its value drops both at the free edge and at the matrix crack front. The peak magnitude of the mode 1 energy release rate is substantially less than the those of the other modes, but it is still comparable to the critical value in mode I. So it plays an important part if the failure criteria which govern the growth depend on the ratio (G_1/G_{Ic}) rather than the absolute magnitude of G_1 alone.

The mode 2 and the mode 3 values have a peak value at the free edge region and their magnitudes are reduced as the matrix crack front is approached. At a delamination orientation of 90°, the mode 2 value is substantially higher than the critical value of the mode II energy release rate in the region near the free edges. This indicates that conditions for growth are most conducive in this region of the delamination. As the delamination changes orientation to 120°, this component of the energy release rate drops substantially. While the magnitude of this particular mode is higher than the mode 1 values, the critical value for this mode is also higher than in mode 1.

The mode 3 results also have peak values at the delamination front near the free edge of the laminate with the peak value being lowest for the 90° orientation and the peak value increasing as the delamination changes orientation to the 120° angle. Therefore, as the delamination changes orientation, this mode makes the delamination more prone to growth. However, the critical value of the energy release rate in this mode is higher than either the critical values in mode 1 or 2. Hence, even if the entire energy carried by the mode 2 were transferred into mode 3, the higher value of G_{IIIc} as compared to G_{IIc} could be another possible reason for the slowdown or stop in the growth of a delamination.

A common method of employing the energy release rates to predict growth of the delamination involves the use of a criterion which incorporates all the energy release rates as well as the critical values of the individual modes. In order to predict mixed mode failure in composite materials, the criteria available in the literature may be generalized as:

$$\left(\frac{G_I}{G_{Ic}}\right)^p + \left(\frac{G_{II}}{G_{IIc}}\right)^q + \left(\frac{G_{III}}{G_{IIIc}}\right)^r \geq 1 \tag{7.1}$$

where the parameters p, q and r are determined from experiments. There is no available research which provides a mixed mode criterion for crack growth involving all three modal components. But for crack growth in mode I and II alone, the suggestion of p and q both equal to unity has been given [83]. The results are presented here for this criterion extended to include r equal to unity. Since these criteria are based on curve fits, there is a possibility that p, q and r could have non-integer values which are greater than unity. Therefore, as an approximation to this case, another criterion with p, q and r all equal to two is also presented here to examine any possible changes in the proposed growth mechanism due to a change in the criterion adopted.

The results for the first criterion used viz.:

$$\frac{G_1}{G_{Ic}} + \frac{G_2}{G_{IIc}} + \frac{G_3}{G_{IIIc}} = C_1 \tag{7.2}$$

are presented in Figure 7.3. For regions along the delamination front where C_1 is greater than or equal to unity, the conditions are presumed to be suitable for the growth of the delamination front. The results for the second criterion used viz.:

$$\left(\frac{G_1}{G_{Ic}}\right)^2 + \left(\frac{G_2}{G_{IIc}}\right)^2 + \left(\frac{G_3}{G_{IIIc}}\right)^2 = C_2 \tag{7.3}$$

are presented in Figure 7.4. This quadratic criterion was chosen as an approximation to the case where the indices p, q and r may have values greater

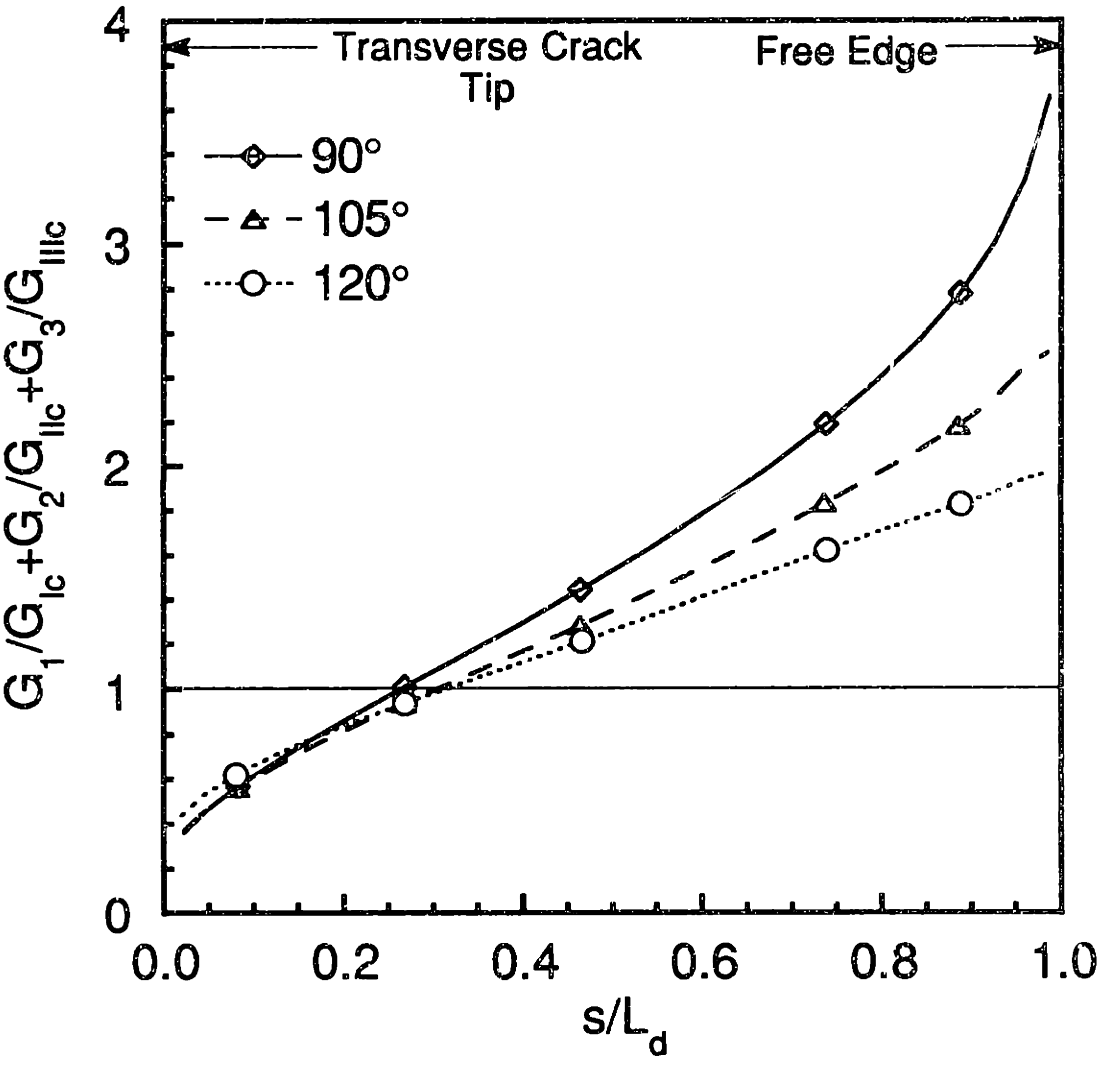

Figure 7.3 Results for a $[\pm 15_2]_s$ laminate from the application of a linear growth criterion to the components of the energy release rate along the delamination front for different delamination orientations.

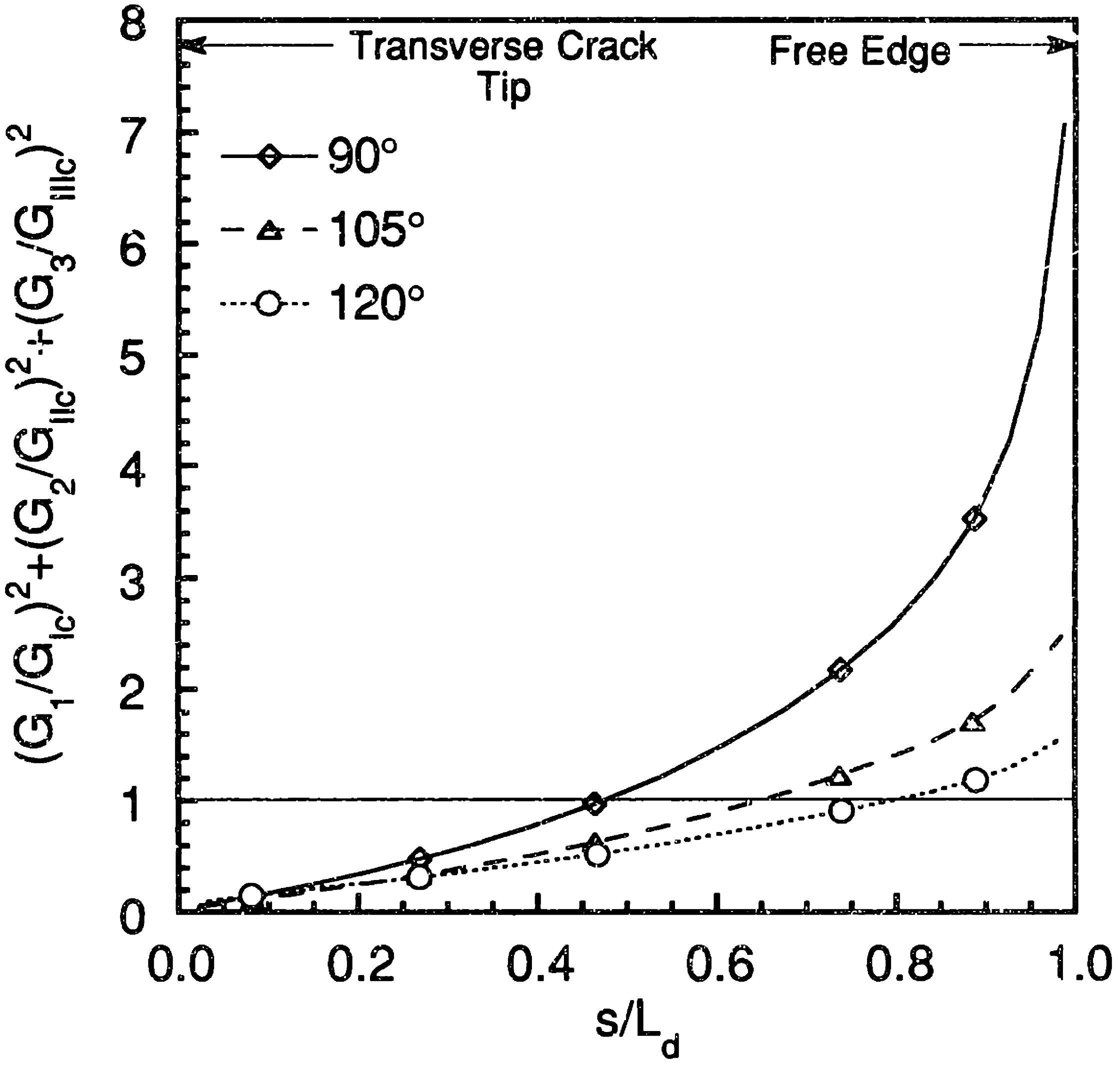

Figure 7.4 Results for a $[\pm 15_2]_s$ laminate from the application of a quadratic growth criterion to the components of the energy release rate along the delamination front for different delamination orientations.

than unity. Once again, growth is presumed to occur where C_2 is greater than or equal to unity along the delamination front.

Both these results show the same trend as shown by the total strain energy release rate. That is, the growth criterion is satisfied at the delamination front in the regions near the free edge as the value of C_1 and C_2 are greater than unity. As the orientation of the delamination changes, the values of C_1 and C_2 are seen to decrease and, in the present study, they stay above the value of unity indicating that the growth is therefore likely to occur near the free edges and the delamination is likely to grow in a manner which is approximated by tilting about the matrix crack front. In some cases, the tilting of the delamination may result in the value of C_1 and C_2 lying below unity which would result in arrest of the delamination growth, since the criteria for growth are no longer satisfied.

The triangular-shaped delamination has also been studied by O'Brien [29]. A simple formula has been proposed to evaluate the global energy release rate for this type of delamination, which was discussed in detail in Chapter two. This equation (2.5) has been used here to evaluate the total energy release rate for the triangular region. This equation is repeated here:

$$G = \frac{\varepsilon^2 t_{Lam}}{2m}\left(\frac{L}{a}\right)\left[E_{Lam} - \frac{1}{(Ba+C)} + \frac{Ba}{(Ba+C)^2}\right] \tag{2.5}$$

where,

$$B = \frac{1}{2}\left(\frac{1}{t_{LD}E_{LD}} - \frac{1}{t_{Lam}E_{Lam}}\right)\left(\frac{t}{L}\right) \tag{2.6}$$

and

$$C = \frac{1}{E_{Lam}} \tag{2.7}$$

For the $[\pm15_2]_s$ laminate, the E_{Lam} is equal to 116.1 GPa. In the delaminated region, assuming that only the $[-15_2]_s$ sublaminate carries the load, the modulus E_{LD} is 59.7 GPa. For the case with 90°, 105° and 120° orientations of the delamination, the values of a are 4 mm, 4.2 mm and 4.7 mm, respectively. The expression in equation (2.5) already assumes that one delamination exists on each free edge. The existence of symmetric delaminations through the thickness of the specimen can be accounted by letting the value of the parameter m equal to 2. The resulting total energy release rates for the 90°, 105° and 120° orientations are 1162 J/m^2, 1126 J/m^2 and 1045 J/m^2 respectively. These values are closer to the peak values than the average values of the energy release rates as observed in the present study. Though the differences between the energy release rate in the three orientations are quite small (less than 10%), the trend shown by these values indicate that the total strain energy reduces as the delamination changes orientation. However, as observed from the distribution of the total energy release rate, only the peak values at the free edge region dropped, but the energy release rate actually increased at regions away from the free edge. Therefore, evaluation of only a global energy release rate could possibly mask the underlying mechanisms involved.

This study of triangular-shaped compound delaminations indicates the criticality of the delamination front in the failure of the $[\pm15_n/0_n]_s$ and the $[\pm15_n]_s$ specimens. The existence of the matrix crack and its interaction with the delamination front are not as responsible for the damage growth and failure as is the interaction of the delamination front with the free edge of the laminate. This can be inferred from the experimental evidence and by considering the three different cases that are modelled to simulate the actual growth. The case of the delamination front angled at 120° to the matrix crack is considered to be the best of the three approximations to the naturally occurring curved configuration. The energy release rate obtained for this case is lower at the free edge region of the delamination front as compared to the other orientations of the delamination approximated by the 90° and 105° configurations. The resulting delamination at an angle of 120° is, therefore, less likely to satisfy any growth criterion which may be satisfied by the higher energy release rates in the 90° and 105° cases. Hence, it may be inferred that the final configuration is more stable than the implanted configuration simulated in the study. This is one reason why only delaminations with this curved front are observed during the testing of the unflawed laminates.

It may also be concluded that an increase in the interlaminar fracture toughness would be sufficient to delay the unstable growth of this delamination, at least until the energy release rate at the matrix crack front reached the value critical for that growth. With the straight profile assumed for the matrix crack in the current study, it is observed that the peak energy release rate at the matrix crack, in the 120° configuration, is about half that at the delamination front. Hence, even if further delamination growth was delayed by increasing the interlaminar fracture toughness, there may be some growth observed when the criterion for growth is satisfied by the energy release rate at the matrix crack front. Even in such a case, without sufficient experimentation it is difficult to judge whether the matrix crack alone is likely to grow. If, however, such matrix crack growth does occur, previous experiments have observed, by implanting matrix cracks which extend beyond the delamination, that the delamination follows the matrix crack to recreate the natural triangular-shaped compound delamination state [1]. Therefore, an unstable propagation of the matrix crack could result in the failure of the specimen with the same triangular-shaped delamination, although at a higher load.

It therefore appears that if the delamination initiates and a triangular-shaped stable delamination is formed despite interlaminar toughening, then the growth of the triangular delamination will occur, if not by the growth of the delamination front, then by the growth of the matrix crack at a higher load level. Hence, the manifestation of the final failure would still involve the growth of triangular-shaped delaminations to the ends of the specimen and the post mortem examination of the specimens would not reveal whether the unstable growth was caused by the delamination front or matrix crack first reaching the critical growth point. In light of this, it is therefore necessary to consider both the delamination and the matrix crack in predicting growth and in trying to prevent such growth. Techniques for preventing the initiation of delamination itself may thus provide a better means to improve the ultimate failure load of the laminate than techniques for controlling the growth.

CHAPTER 8

CONCLUSIONS AND RECOMMENDATIONS

The growth of delaminations to form stable triangular-shaped compound delaminations has been studied both experimentally and analytically. The data obtained from this study have resulted in the following conclusions and recommendations.

8.1 Conclusions

The conclusions presented here address the formation and growth of delaminations in unflawed specimens and in specimens with implants, along with the predictions from the model used in the analysis.

1. The macroscopic stable damage observed in unflawed $[\pm 15_n]_s$, $[\pm 15_n/0_n]_s$ and $[0_n/\pm 15_n]_s$ specimens during tensile testing, is in the form of a triangular-shaped compound delamination at the +15/-15 interface. One side of the damage is a delamination with a curved front, the other side of the triangle is a matrix crack with a curved profile occurring in the $[+15]_n$ effective ply in the $[\pm 15_n]_s$ and $[\pm 15_n/0_n]_s$ laminates and in the $[-15]_{2n}$ effective ply in $[0_n/\pm 15_n]_s$ specimens.

2. The macroscopic failure process in $[\pm 15_n]_s$, $[\pm 15_n/0_n]_s$ and $[0_n/\pm 15_n]_s$ unflawed laminates consists of the formation of the stable triangular-shaped delamination, followed by secondary cracking in the adjoining $[-15]_n$ effective plies in the $[\pm 15_n]_s$ and $[\pm 15_n/0_n]_s$ laminates and in the $[+15]_n$ effective plies in the $[0_n/\pm 15_n]_s$ laminates, followed by the unstable

growth of this triangular-shaped delamination.

3. Secondary cracks in the $[-15_n]_s$ effective plies in the $[\pm 15_n]_s$ and $[\pm 15_n/0_n]_s$ laminates, may form prior to unstable delamination growth, but the effects of these on the growth of the delamination are not known.

4. The $[\pm 15_2/0_2]_s$ and $[\pm 15_3/0_3]_s$ laminates with implants simulate the failure stresses and strains observed in the unflawed laminates. The delamination growth from the implanted configuration also occurs in such a manner that the resulting delamination resembles the naturally observed configuration. This also implies that the implanted configuration may be an intermediate stage in the formation of the natural triangular configuration in unflawed specimens.

5. The X-ray radiographs and the stress-strain data both indicate that the naturally observed delamination develops from the implanted configuration by delamination growth near the free edge and not near the matrix crack region. This is corroborated by the analytical results which show that the value of the total strain energy release rate peaks at the delamination front near the free edge and drops rapidly towards the matrix crack front.

6. The peak value of the total strain energy release rate decreases and the energy release rate becomes more uniform as the angle subtended by the delamination front with the matrix crack in the different models increases.

7. The observed stable delamination configuration in unflawed specimens occurs due to delamination growth in regions with higher energy release rate resulting in a curved configuration with a more uniform energy release rate along its front. This configuration has a lower peak energy release rate.

8. The total energy release rate is predicted to have a higher maximum value along the delamination front as compared to the matrix crack front and the growth of the delamination front and the absence of growth at the matrix crack front in the X-ray radiographs are attributed to this.

9. For the straight matrix crack profile analyzed, the strain energy release rate at the matrix crack tip is highest at the top of the laminate and not at the intersection with the delamination front.

10. The matrix crack as modelled shows crack tip interpenetration at low delamination angle and opens up at higher delamination angles.

11. An increase in the interlaminar toughness may not be sufficient to prevent the unstable growth of a triangular-shaped delamination, though it might delay such a growth, as growth of the damage could occur at higher loads as a consequence of the growth of the matrix crack front.

12. The individual "modes" obtained by ignoring the oscillatory singularity for a crack between two anisotropic bimaterials display a trend which is similar to the modes determined by conventional methods used in isotropic materials.

13. There is seen to be a shift in the strain energy release rate from mode 2 into mode 3 as the delamination is tilted from the initial configuration to subtend higher angles with the matrix crack front. This may also contribute to the arrest of the delamination front in the observed stable configuration.

14. The total energy release rate obtained by a new method based on the crack opening displacement behind the crack front was seen to compare well with that obtained by the equivalent domain integral approach.

15. The individual modes obtained by the equivalent domain integral using the decomposition approach display the same trend along the delamination front as the modes obtained by the crack opening displacement approach, neglecting the oscillatory singularity. The magnitudes of the individual modes, however are not the same.

8.2 Recommendations

Based on the results obtained and the issues raised in some aspects of the analysis and experiments, the following recommendations are made for future work in this area:

1. Further study must address the consequences of ignoring the oscillatory singularities and the effect on the computation of individual modes of energy release rate.

2. Analytical techniques need to be developed to enable the verification of

modes that may be obtained by the different techniques of mode separation.

3. Techniques must be developed to record the actual growth of the delamination from the initiation phase (microscopic) to the stable triangular-shaped delamination (macroscopic) phase.

4. The unstable growth of the delamination needs to be studied along with the consequences of the secondary matrix cracks on the failure process.

5. The growth of implants of various sizes with the initial configuration of triangular-shaped delamination must be studied experimentally to examine whether the proposed mechanism is independent of size.

6. The growth of implanted delamination fronts with different initial configurations, including delamination fronts subtending acute angles with the matrix crack front, need to be examined to determine if the initial orientation dictates the formation of the natural configuration from the implanted configuration and whether such growth is possible only from select configurations.

7. Specimens with implanted small penny-shaped delaminations only, and specimens with only a matrix crack must be used to determine if the naturally observed configuration could be developed from either case. This could show what the consequence of an initial damage or edge defects of either kind has on the damage configuration formed.

8. The curved delamination front and the curved matrix crack profile observed in experiments need to be properly modelled to obtain the actual energy release rate predictions. These need to be compared to the energy release rate from the approximate models to determine the level of modelling necessary for such problems.

9. The reasons for the occurrence of the secondary matrix cracking after the formation of the triangular-shaped delamination need to be investigated along with its effects on the growth.

10. The critical values of the energy release rate at interfaces involving other angles than unidirectional need to be determined.

11. A criterion for crack growth based on energy release rate involving all the three modes of energy release rate needs to be developed and tested for both delamination cracks as well as matrix cracks.

12. A global-local approach may be needed to refine the mesh near the crack fronts and obtain the stresses more accurately to determine any changes in the stress state as the delamination grows.

APPENDIX A

FORTRAN SOURCE CODE

In this software, the Equivalent Domain Integral (EDI) approach is used to calculate the energy release rate around the crack tip region of a general three-dimensional crack. The crack tip stresses, strains and displacements, that are available around the crack tip region from any analysis can be utilized. In the present study, the same program is used to obtain the energy release rate at both the delamination front and the matrix crack front. This program is based on the method discussed in references [47, 50].

The option of dividing the total energy release rate into individual components using the decomposition method is provided in this program. However, the modes are accurate only for cracks in isotropic materials or in bimaterials with no oscillatory singularities. In the case of a bimaterial with oscillatory singularities, the total energy is unambiguous, but the individual "modes" that are obtained are not defined analytically and hence there is no means by which they may be verified as described in Chapter two. The modes are only approximate and may change with the size of the crack tip element.

The inputs required by this program are the displacements at the nodes, and the stresses and strains. In the case where the data is obtained from finite element packages, good results are obtained by using the stresses and strains at the integration points of the elements located at the crack front. This data is to be provided in two files: 'top.dat' provides the data for elements on the region above the crack, and 'bot.dat' provides similar data for elements below the crack.

The output can be found in the file 'Gmodes.dat', where the total G and the individual modes are provided along the crack front. The data is provided at discrete points along the crack front.

```
C******************************************************************************C
C------------------------------------------------------------------------------C
C    PROGRAM for:  Equivalent Domain Integral  &  Decomposition Method         C
C                       Author: Narendra V. Bhat
C                       Date: 3rd September 1993
C------------------------------------------------------------------------------C
C******************************************************************************C
              Copyright c 1993 Massachusetts Institute of Technology

Permission to use, copy and modify this software and its documentation for internal
purposes only and without fee is hereby granted provided that the above copyright
notice and this permission appear on all copies of the code and supporting
documentation.  For any other use of this software, in original and modified form,
including but not limited to, adaptation as the basis of a commercial software or
hardware product, or distribution in whole or in part, specific prior permission
and/or the appropriate license must be obtained from MIT.  This software is provided
"as is" without any warranties whatsoever, either express or implied, including but
not limited to the implied warranties of merchantability and fitness for a particular
purpose   This software is a research program, and MIT does not represent that it is
free of errors or bugs or suitable for any particular task.
C
C
C     This program evaluates the EQUIVALENT DOMAIN INTEGRAL for the 3D case and
C     separates the modes by the DECOMPOSITION METHOD given in Raju and Sivakumar
C
C     This is the program which assumes a ring of square elements around
C     the crack tip, It tackles both the top and bottom regions simultaneously
C
C     DATA FILES REQD:    top.dat
C                         bot.dat
C
C     The program picks up the ring consisting of two elements from top.dat
C     and two elements from bot.dat simultaneously and then prepares the symmetric
C     and antisymmetric components required to determine the components of G.
C
C     OUTPUT FILES:      Gmodes.dat
C
C     This output file contains all the necessary info for every ring. The midpoint
C     coordinate of the ring, width of ring and the GI GII GIII and G.
C     This program uses a circular shape function to evaluate the EDI
C     and uses the 4 crack tip singular elements only.
C
C
      IMPLICIT DOUBLE PRECISION (A-H,O-Z)
      PARAMETER(NOD=20,IPTS=3,INTG=27,NELEM=2,KELEM=2*NELEM)
      REAL*8 XN(KELEM,NOD,3),U(KELEM,NOD,3),SIG(KELEM,3,3,INTG)
      REAL*8 STR(KELEM,3,3,INTG),X(NOD,3)
      REAL*8 UI(NOD,3),SIGI(3,3,INTG),STRI(3,3,INTG),WI(INTG)
      REAL*8 UII(NOD,3),SIGII(3,3,INTG),STRII(3,3,INTG),WII(INTG)
      REAL*8 UIII(NOD,3),SIGIII(3,3,INTG),STRIII(3,3,INTG),WIII(INTG)
      REAL*8 SIGOI(IPTS,IPTS),SIGOII(IPTS,IPTS),SIGOIII(IPTS,IPTS)
      REAL*8 PLACE(IPTS),WGT(IPTS),S(KELEM,NOD)
      REAL*8 GI(100),GII(100),GIII(100),WIDTH(100)
      COMMON /GAUSS/PLACE,WGT
      COMMON /SFUNC/S,F
      OPEN(UNIT=2,FILE='Gmodes.dat',STATUS='UNKNOWN')
      OPEN(UNIT=3,FILE='top.dat',STATUS='OLD')
      OPEN(UNIT=4,FILE='bot.dat',STATUS='OLD')
C
C     Variables
C     ----------
C
```

```
C     NELEM :  Number of elements around the crack tip.
C     X     :  Matrix containing nodal coordinates
C              X(NOD,1)=x-coordinate of node NOD
C              X(NOD,3)=y-coordinate of node NOD
C     U     :  Matrix containing nodal coordinates
C              U(NOD,1)=x-displacement (u) of node NOD
C              U(NOD,2)=y-displacement (v) of node NOD
C     SIG   :  Matrix containing stresses at integration points
C              SIG(1,1,INTG)=sigma11 @ integration pt INTG etc.
C     STR   :  Matrix containing stresses at integration points
C              STR(1,1,INTG)=epsilon11 @ integration pt INTG etc.
C     SIGI  :  SIG I counterpart of the stresses etc.
C
C     Nodal and Integration Point numbering scheme follows ADINA:
C     -------------------------------------------------
C
C     3-POINT GAUSSIAN INTEGRATION
C
      PLACE(1)=-SQRT(3./5.)
      PLACE(2)= 0.
      PLACE(3)=+SQRT(3./5.)
      WGT(1)=5./9.
      WGT(2)=8./9.
      WGT(3)=5./9.
C
C
      READ(3,*) NRING1
      READ(4,*) NRING2
      IF(NRING1.NE.NRING2) THEN
      WRITE(6,*) '**ERROR !! TOP AND BOTTOM RINGS HAVE UNEQUAL ELEM**'
      ELSE
      NRING=NRING1
      ENDIF
C
            DO 5 ITMP=1,NRING
               GI(ITMP)=0.0
               GII(ITMP)=0.0
               GIII(ITMP)=0.0
               WIDTH(ITMP)=0.0
 5    CONTINUE
C
                  DO 7 IELEM=1,KELEM
                     DO 7 INOD=1,NOD
                        S(IELEM,INOD)=0.0
 7                CONTINUE
C      Nikishkov's paper S-function given by (c), CIRCULAR  ALONG THE CRACK FRONT
C
C     Element 1
            S(1,6)=.0
            S(1,14)=1.0
            S(1,7)=.0
            S(1,18)=0.
            S(1,19)=0.
            S(1,13)=0.
            S(1,15)=0.
C     Element 2
            S(2,5)=.0
            S(2,16)=1.0
            S(2,8)=.0
            S(2,17)=0.
            S(2,20)=0.
            S(2,13)=0.
            S(2,15)=0.
C     Element 3
```

```
            S(3,6)=.0
            S(3,14)=1.0
            S(3,7)=.0
            S(3,18)=0.
            S(3,19)=0.
            S(3,13)=0.
            S(3,15)=0.
C     Element 4
            S(4,5)=.0
            S(4,16)=1.0
            S(4,8)=.0
            S(4,17)=0.
            S(4,20)=0.
            S(4,13)=0.
            S(4,15)=0.
C
      DO 1111 IRING=1,NRING
C
C     Step 1: Read the finite element data from file : INP.DAT
C
      CALL INPUT(IRING,XN,U,SIG,STR,F)
        WIDTH(IRING)=(3./2.)*F
C
C     Step 2: Pick up one element at a time and evaluate its contribution
C             to GI and GII.
      DO 10 NEL=1,(KELEM)
C
C     Step 3: Preprocess the data separating into I,II.
C
         CALL PREPROC(NEL,XN,U,SIG,STR,X,UI,SIGI,STRI,WI,
     &           UII,SIGII,STRII,WII,UIII,SIGIII,STRIII,WIII)
C
         CALL EVG(NEL,X,UI,SIGI,STRI,WI,SIGOI,GIQ)
         CALL EVG(NEL,X,UII,SIGII,STRII,WII,SIGOII,GIIQ)
         CALL EVG(NEL,X,UIII,SIGIII,STRIII,WIII,SIGOIII,GIIIQ)
C
        GI(IRING)=GIQ+GI(IRING)
        GII(IRING)=GIIQ+GII(IRING)
        GIII(IRING)=GIIIQ+GIII(IRING)
c
      sloc=0.0
c         Gtot=GI(iring)+GII(iring)+GIII(iring)
c         Gttemp=GIQ+GIIQ+GIIIQ
c         write(6,501) NEL,GIQ,GIIQ,GIIIQ,Gttemp
c
 10   CONTINUE
 1111 CONTINUE
C
      wide=0.0
      WRITE(2,*)'-------------------------------------------------------
     &------------------------------'
      WRITE(2,*)'RING       GI       GII         GIII          G
     &    Location     Element-width'
      WRITE(2,*)'-------------------------------------------------------
     &------------------------------'
      DO 500 ITMP=1,NRING
         wide=wide+width(itmp)
         sloc=wide-0.5*width(itmp)
         Gtot=GI(itmp)+GII(itmp)+GIII(itmp)
         WRITE(2,501) itmp,GI(itmp),GII(itmp),GIII(itmp),Gtot,
     &sloc,width(itmp)

 500  CONTINUE
 501             format(1x,I2,4(2x,E11.4),3x,E11.4,3x,E11.4)
```

```
      CLOSE(UNIT=2)
      END
C     --------end of MAIN PROGRAM------
C
C     -----------------------------------
      SUBROUTINE EVG(NEL,X,U,SIG,STR,W,SIGO,GQ)
C     -----------------------------------
C     This subroutine evaluates the two components of Gi;i=I,II. In the
C     derivation it is seen that the integral for GI(or GII) is divided
C     into two parts.  This evaluates both these parts, GF1 and GF2.
C
      IMPLICIT DOUBLE PRECISION(A-H,O-Z)
      PARAMETER(NOD=20,IPTS=3,INTG=27,NELEM=2,KELEM=2*NELEM)
      REAL*8 X(NOD,3),U(NOD,3),SIG(3,3,INTG),STR(3,3,INTG),W(INTG)
      REAL*8 SIGO(IPTS,IPTS),S(KELEM,NOD)
      COMMON /SFUNC/S,F
C
       CALL EVGF1(NEL,X,U,SIG,STR,W,GF1)
C      The calling of GF2 is not necessary unless there are "non-elastic" strains
C      CALL EVGF2(NEL,X,U,SIG,STR,W,SIGO,GF2)
C
      GQ=(GF1)/F
C
      RETURN
      END
C
C     ----------------------------------------
      SUBROUTINE EVGF1(NEL,X,U,SIG,STR,W,GF1)
C     ----------------------------------------
C     This subroutine evaluates the first of the two integrals needed to
C     evaluate GI(or GII), denoted by GF1.
C                               GF1= Rl*Sl    (sum over 'l', the node#)
C     Here Rl is evaluated for each node. But, since Rl is an integral, at
C     each node, 'l' Rl has to be integrated over the gaussian points. Here
C     instead of evaluating Rl completely for a given 'l', it will be
C     evaluated for all 'l' at a given integration point and then the process
C     is repeated for all integration points.
C
      IMPLICIT DOUBLE PRECISION (A-H,O-Z)
      PARAMETER(NOD=20,IPTS=3,INTG=27,NELEM=2,KELEM=2*NELEM)
      REAL*8 DN(NOD,3),R(NOD)
      REAL*8 X(NOD,3),U(NOD,3),SIG(3,3,INTG),STR(3,3,INTG),W(INTG)
      REAL*8 PLACE(IPTS),WGT(IPTS),S(KELEM,NOD)
      REAL*8 XI(NOD),YI(NOD),ZI(NOD)
      COMMON /GAUSS/PLACE,WGT
      COMMON /SFUNC/S,F
      COMMON /COOR/XI,YI,ZI
      DATA XI/1,-1,-1,1,1,-1,-1,1,0,-1,0,1,0,-1,0,1,1,-1,-1,1/
      DATA YI/1,1,-1,-1,1,1,-1,-1,1,0,-1,0,1,0,-1,0,1,1,-1,-1/
      DATA ZI/1,1,1,1,-1,-1,-1,-1,1,1,1,1,-1,-1,-1,-1,0,0,0,0/
C
C     Initializations
      INT=0
      GF1=0.0
      DV=0.0
      VOLUME=0.0
      DO 5 IFLAG=1,NOD
         R(IFLAG)=0.0
 5    CONTINUE
C
      DO 10 INTI=1,IPTS
         PXI=PLACE(INTI)
         DO 20 INTJ=1,IPTS
            PET=PLACE(INTJ)
```

```
            DO 30 INTK=1,IPTS
               PRO=PLACE(INTK)
               INT=INT+1
C
            CALL DERV(X,PXI,PET,PRO,DETJ,DN)
            CALL EVALR(INT,X,U,W,SIG,DN,R)
            DV=(WGT(INTI)*WGT(INTJ)*WGT(INTK)*ABS(DETJ))
            VOLUME=VOLUME+DV
C
C
            DO 40 I=1,NOD
               GF1=GF1+R(I)*S(NEL,I)*DV
c
c
 40         CONTINUE
 30          CONTINUE
 20        CONTINUE
 10      CONTINUE
C
               RETURN
               END
C
C     ------------------------------------
      SUBROUTINE EVALR(INT,X,U,W,SIG,DN,R)
C     -------------------------------------
C     This subroutine evaluates the matrix R, for all 8 nodes at
C     one integration point, thus enabling easy evaluation
C     of the first integral GF1 evaluated at one integration point.
C
      IMPLICIT DOUBLE PRECISION (A-H,O-Z)
      PARAMETER(NOD=20,IPTS=3,INTG=27,NELEM=2,KELEM=2*NELEM)
      REAL*8      X(NOD,3),U(NOD,3),SIG(3,3,INTG),W(INTG)
      REAL*8      DN(NOD,3),R(NOD),B(3)
C
C     Finding R for all the 20 Nodes, at a given integration point,
C     because, the DN, BI etc have been evaluated at one integration
C     point (PXI,PET) only.
C
      DO 5 I=1,3
               B(I)=BI(U,DN,I)
  5    CONTINUE

      DO 10 L=1,NOD
C     Initializations
      T=0.0
C
C     This summation for T, is to account for all the stresses, s11,s22....
         DO 20 I=1,3
         DO 20 J=1,3
               T=SIG(I,J,INT)*DN(L,J)*B(I)+T
 20      CONTINUE
          R(L)=-(W(INT)*DN(L,1)-T)
 10   CONTINUE
C
      RETURN
      END
C
C     -------------------
      FUNCTION BI(U,DN,I)
C     -------------------
      IMPLICIT DOUBLE PRECISION (A-H,O-Z)
      PARAMETER(NOD=20)
      REAL*8      DN(NOD,3),U(NOD,3)
      BI=0.0
```

```
C
      DO 10 J=1,NOD
         BI=BI+DN(J,1)*U(J,I)
 10   CONTINUE
C
      RETURN
      END
C
C     -----------------------------------
      SUBROUTINE DERV(X,PXI,PET,PRO,DETJ,DN)
C     ------------------------------------
C     This subroutine finds the GLOBAL DERIVATIVES OF N (wrt X and Y)
C     at a given integration  point (PXI,PET)
C
      IMPLICIT DOUBLE PRECISION (A-H,O-Z)
      PARAMETER(NOD=20)
      REAL*8      ND(NOD,3),JINV(3,3),DN(NOD,3)
      REAL*8      X(NOD,3)
C
      CALL JACOBI(PXI,PET,PRO,X,ND,JINV,DETJ)
C
      DO 10 NODE=1,NOD
      DO 10 K=1,3
         DN(NODE,K)=ND(NODE,1)*JINV(K,1)
     &              +ND(NODE,2)*JINV(K,2)
     &              +ND(NODE,3)*JINV(K,3)
 10   CONTINUE
C
      RETURN
      END
C
C     ---------------------------------------------
      SUBROUTINE JACOBI(PXI,PET,PRO,X,ND,JINV,DETJ)
C     ----------------------------------------------
C     This subroutine evaluates the jacobian, inverse jacobian and
C     determinant of the jacobian at a given integration pt.(PXI,PET,PRO)
C
      IMPLICIT DOUBLE PRECISION (A-H,O-Z)
      PARAMETER(NOD=20)
      REAL*8  ND(NOD,3),J(3,3),JINV(3,3),X(NOD,3)
C
C     Initialization
      DO 10 I=1,3
      DO 10 K=1,3
            J(I,K)=0.0
 10   CONTINUE
C
      CALL NATDERV(PXI,PET,PRO,ND)
C
      DO 20 I=1,3
         DO 30 K=1,3
            DO 40 NODE=1,NOD
               J(I,K)=J(I,K)+ND(NODE,I)*X(NODE,K)
 40         CONTINUE
 30      CONTINUE
 20   CONTINUE
C
      DETJ=J(1,1)*(J(2,2)*J(3,3)-J(3,2)*J(2,3))
     &     -J(1,2)*(J(2,1)*J(3,3)-J(3,1)*J(2,3))
     &     +J(1,3)*(J(2,1)*J(3,2)-J(3,1)*J(2,2))
C
      JINV(1,1)= (1./DETJ)*(J(2,2)*J(3,3)-J(3,2)*J(2,3))
      JINV(2,1)=-(1./DETJ)*(J(2,1)*J(3,3)-J(3,1)*J(2,3))
      JINV(3,1)= (1./DETJ)*(J(2,1)*J(3,2)-J(3,1)*J(2,2))
```

```
      JINV(1,2)=-(1./DETJ)*(J(1,2)*J(3,3)-J(3,2)*J(1,3))
      JINV(2,2)= (1./DETJ)*(J(1,1)*J(3,3)-J(3,1)*J(1,3))
      JINV(3,2)=-(1./DETJ)*(J(1,1)*J(3,2)-J(3,1)*J(1,2))
      JINV(1,3)= (1./DETJ)*(J(1,2)*J(2,3)-J(2,2)*J(1,3))
      JINV(2,3)=-(1./DETJ)*(J(1,1)*J(2,3)-J(2,1)*J(1,3))
      JINV(3,3)= (1./DETJ)*(J(1,1)*J(2,2)-J(2,1)*J(1,2))
C
      RETURN
      END
C
C     ------------------------------------
      SUBROUTINE NATDERV(PXI,PET,PRO,ND)
C     -------------------------------------
C     This Subroutine evaluates the NATURAL DERIVATIVES (wrt PXI,PET) of the
C     shape functions.  They are evaluated for a given GAUSSIAN POINT.
C
      IMPLICIT DOUBLE PRECISION (A-H,O-Z)
      PARAMETER(NOD=20)
      REAL*8    ND(NOD,3)
      REAL*8    XI(NOD),YI(NOD),ZI(NOD)
      COMMON /COOR/XI,YI,ZI
C
         A11=(1.-PXI*PXI)
         A22=(1.-PET*PET)
         A33=(1.-PRO*PRO)
C
      DO 10 I=1,NOD
         A1=1.+PXI*XI(I)
         A2=1.+PET*YI(I)
         A3=1.+PRO*ZI(I)
         B1=XI(I)*XI(I)
         B2=YI(I)*YI(I)
         B3=ZI(I)*ZI(I)
         BB=B1*B2*B3
         CC=A1+A2+A3-3.
C
C     The derivative of N wrt PXI
         ND(I,1)=(1./8.)*(A2*A3)*(XI(I)*BB)*(CC-2.+A1)+
     &         (1./4.)*(A33*XI(I)*A2*(1-B3)+
     &                 A22*A3*XI(I)*(1-B2)+
     &                 (-2.*PXI)*A2*A3*(1-B1))
C     The derivative of N wrt PET
         ND(I,2)=(1./8.)*(A1*A3)*(YI(I)*BB)*(CC-2.+A2)+
     &         (1./4.)*(A33*A1*YI(I)*(1-B3)+
     &                 (-2.*PET)*A3*A1*(1-B2)+
     &                 A11*YI(I)*A3*(1-B1))
C     The derivative of N wrt PXI
         ND(I,3)=(1./8.)*(A1*A2)*(ZI(I)*BB)*(CC-2.+A3)+
     &         (1./4.)*((-2.*PRO)*A1*A2*(1-B3)+
     &                 A22*ZI(I)*A1*(1-B2)+
     &                 A11*A2*ZI(I)*(1-B1))
C
 10   CONTINUE
C
      RETURN
      END
C
C     ----------------------------------
      SUBROUTINE NSHAPES(PXI,PET,PRO,SMAT,SVAL)
C     ---------------------------------
C     This subroutine returns the value(SVAL) of a parameter at
C     a point (PXI,PET) when the nodal values(SMAT) of a parameter
C     are fed in.
C
```

```
      IMPLICIT DOUBLE PRECISION (A-H,O-Z)
      PARAMETER(NOD=20)
      REAL*8 N(NOD),SMAT(NOD),XI(NOD),YI(NOD),ZI(NOD)
      COMMON /COOR/XI,YI,ZI
C
C     Initializations
      SVAL=0.0
C
         A11=(1.-PXI*PXI)
         A22=(1.-PET*PET)
         A33=(1.-PRO*PRO)
C
C     The Shape function N:
C     This Shape function has been taken from Leslie-Banks Sills paper
C
      DO 10 I=1,NOD
         A1=1.+PXI*XI(I)
         A2=1.+PET*YI(I)
         A3=1.+PRO*ZI(I)
         B1=XI(I)*XI(I)
         B2=YI(I)*YI(I)
         B3=ZI(I)*ZI(I)
C
         N(I)=(1./8.)*(A1*A2*A3)*
     &         (XI(I)*PXI+YI(I)*PET+ZI(I)*PRO-2.)*(B1*B2*B3)+
     &          (1./4.)*A33*A1*A2*(1-B3)+
     &          (1./4.)*A22*A3*A1*(1-B2)+
     &          (1./4.)*A11*A2*A3*(1-B1)
         SVAL=SVAL+N(I)*SMAT(I)
C
 10   CONTINUE
      RETURN
      END
C
C     ------------------------------------
      SUBROUTINE INPUT(IRING,XN,U,SIG,STR,F)
C     ------------------------------------
C     This subroutine reads the data from the adina output file
C
      IMPLICIT DOUBLE PRECISION (A-H,O-Z)
      PARAMETER(NOD=20,IPTS=3,INTG=27,NELEM=2,KELEM=2*NELEM)
      REAL*8 XN(KELEM,NOD,3),U(KELEM,NOD,3),SIG(KELEM,3,3,INTG)
      REAL*8 STR(KELEM,3,3,INTG)
      REAL*8 XT(NOD),YT(NOD),YINT(INTG,INTG),XINT(INTG,INTG)
      REAL*8 PLACE(IPTS),WGT(IPTS)
      COMMON /GAUSS/PLACE,WGT
C
C     This input is specialized to read in 4 elements at a time, and it
C     picks2 elements from the previous ring everytime (except of course
C     the first time) so that the G values can be obtained the most number
C     of times with the given number of elements.
C
C     Angle
      PI=4*ATAN(1.)
C     The angle is 90deg between delamination and transverse crack
       rthe=15*(PI/180.)
C     The angle is 105deg between delamination and transverse crack
C      rthe=30*(PI/180.)
C     The angle is 120deg between delamination and transverse crack
C       rthe=45*(PI/180.)
      wrthe=15
C-------------------------------------------------------------
      if (iring.eq.1) then
      write(6,*) ' have you got the correct angle; angle= ',wrthe
```

```
      endif
C----------------------------------------------------------------
      DO 10 IELEM=1,KELEM
         IF(IELEM.LE.NELEM) THEN
          DO 25 NODE=1,NOD
       READ(3,*)JUNK,xt1,xt2,xt3,ut1,ut2,ut3
             CALL ROTVEC(rthe,xt1,xt2,xt3,xtemp1,xtemp2,xtemp3)
             CALL ROTVEC(rthe,ut1,ut2,ut3,utemp1,utemp2,utemp3)
             XN(IELEM,NODE,3)=xtemp3
             XN(IELEM,NODE,1)=xtemp2
             XN(IELEM,NODE,2)=-xtemp1
             U(IELEM,NODE,3)=utemp3
             U(IELEM,NODE,1)=utemp2
             U(IELEM,NODE,2)=-utemp1
 25       CONTINUE
          DO 35 INT=1,INTG
C     This data is read for the left hand cracktip of the full model
      READ(3,*)JUNK,JUNK,JUNK,t11,t22,t33,t23,t13,t12
             CALL ROTTENS(rthe,t11,t22,t33,t23,t13,t12,
     &                 tsi11,tsi22,tsi33,tsi23,tsi13,tsi12)
             SIG(IELEM,3,3,INT)=tsi33
             SIG(IELEM,1,1,INT)=tsi22
             SIG(IELEM,2,2,INT)=tsi11
             SIG(IELEM,1,2,INT)=-tsi12
             SIG(IELEM,2,3,INT)=-tsi13
             SIG(IELEM,1,3,INT)=tsi23
 35       CONTINUE
          DO 45 INT=1,INTG
C     This data is read for the top elements
      READ(3,*)JUNK,JUNK,JUNK,t11,t22,t33,t23,t13,t12
             CALL ROTTENS(rthe,t11,t22,t33,t23,t13,t12,
     &                 tsi11,tsi22,tsi33,tsi23,tsi13,tsi12)
             STR(IELEM,3,3,INT)=tsi33
             STR(IELEM,1,1,INT)=tsi22
             STR(IELEM,2,2,INT)=tsi11
             STR(IELEM,1,2,INT)=-tsi12
             STR(IELEM,2,3,INT)=-tsi13
             STR(IELEM,1,3,INT)=tsi23
 45       CONTINUE
         ELSE
          DO 225 NODE=1,NOD
       READ(4,*)JUNK,xt1,xt2,xt3,ut1,ut2,ut3
             IF(NODE.GE.1)  MNODE=NODE+4
             IF(NODE.GE.5)  MNODE=NODE-4
             IF(NODE.GE.9)  MNODE=NODE+4
             IF(NODE.GE.13) MNODE=NODE-4
             IF(NODE.GE.17) MNODE=NODE
c
             CALL ROTVEC(rthe,xt1,xt2,xt3,xtemp1,xtemp2,xtemp3)
             CALL ROTVEC(rthe,ut1,ut2,ut3,utemp1,utemp2,utemp3)
             XN(IELEM,MNODE,3)=xtemp3
             XN(IELEM,MNODE,1)=xtemp2
             XN(IELEM,MNODE,2)=-xtemp1
             U(IELEM,MNODE,3)=utemp3
             U(IELEM,MNODE,1)=utemp2
             U(IELEM,MNODE,2)=-utemp1
c
 225       CONTINUE
C
C     This data is read for the bottom elements
          IM=0
          DO 335 INT=1,INTG
          READ(4,*)JUNK,JUNK,JUNK,t11,t22,t33,t23,t13,t12
             CALL ROTTENS(rthe,t11,t22,t33,t23,t13,t12,
```

```
     &                 tsi11,tsi22,tsi33,tsi23,tsi13,tsi12)
             MINT=ABS(4+6*IM-INT)
             IM=INT/3
C
             SIG(IELEM,3,3,MINT)=tsi33
             SIG(IELEM,1,1,MINT)=tsi22
             SIG(IELEM,2,2,MINT)=tsi11
             SIG(IELEM,1,2,MINT)=-tsi12
             SIG(IELEM,2,3,MINT)=-tsi13
             SIG(IELEM,1,3,MINT)=tsi23
 335     CONTINUE
C
          IM=0
          DO 445 INT=1,INTG
          READ(4,*)JUNK,JUNK,JUNK,t11,t22,t33,t23,t13,t12
             CALL ROTTENS(rthe,t11,t22,t33,t23,t13,t12,
     &                 tsi11,tsi22,tsi33,tsi23,tsi13,tsi12)
             MINT=ABS(4+6*IM-INT)
             IM=INT/3
C
             STR(IELEM,3,3,MINT)=tsi33
             STR(IELEM,1,1,MINT)=tsi22
             STR(IELEM,2,2,MINT)=tsi11
             STR(IELEM,1,2,MINT)=-tsi12
             STR(IELEM,2,3,MINT)=-tsi13
             STR(IELEM,1,3,MINT)=tsi23
 445       CONTINUE
      ENDIF
C
C     This evaluates the width of the elements along the crack front:
C     f  =area under the S curve (see ref.)
          f=(2./3.)*sqrt((xn(1,6,1)-xn(1,7,1))**2 +
     &                  (xn(1,6,2)-xn(1,7,2))**2 +
     &                  (xn(1,6,3)-xn(1,7,3))**2 )
C
 10   CONTINUE
C
      RETURN
      END
C
C     -----------------------------------------------------------------
      SUBROUTINE PREPROC(IELEM,XN,U,SIG,STR,X,UI,SIGI,STRI,WI,
     &          UII,SIGII,STRII,WII,UIII,SIGIII,STRIII,WIII)
C     ------------------------------------------------------------------
C     This subroutine processes the stress and strain data at the integration
C     points to give, the stress and strain data in appropriate I and II forms
C     and also the strain energy densities, WI and WII.
C
      IMPLICIT DOUBLE PRECISION (A-H,O-Z)
      PARAMETER(NOD=20,IPTS=3,INTG=27,NELEM=2,KELEM=2*NELEM)
      REAL*8 XN(KELEM,NOD,3),U(KELEM,NOD,3),SIG(KELEM,3,3,INTG)
      REAL*8 STR(KELEM,3,3,INTG)
      REAL*8 X(NOD,3)
      REAL*8 UI(NOD,3),SIGI(3,3,INTG),STRI(3,3,INTG),WI(INTG)
      REAL*8 UII(NOD,3),SIGII(3,3,INTG),STRII(3,3,INTG),WII(INTG)
      REAL*8 UIII(NOD,3),SIGIII(3,3,INTG),STRIII(3,3,INTG),WIII(INTG)
C
C     Initializations
      IF (IELEM.LE.2) THEN
         JELEM=IELEM+2
      ELSE
         JELEM=IELEM-2
      ENDIF
C
```

```
      DO 10 INT=1,INTG
         WI(INT)=0.0
         WII(INT)=0.0
         WIII(INT)=0.0
 10   CONTINUE
C
         DO 20 NODE=1,NOD
            UI(NODE,1)=0.5*(U(IELEM,NODE,1)+U(JELEM,NODE,1))
            UI(NODE,2)=0.5*(U(IELEM,NODE,2)-U(JELEM,NODE,2))
            UI(NODE,3)=0.5*(U(IELEM,NODE,3)+U(JELEM,NODE,3))
            UII(NODE,1)=0.5*(U(IELEM,NODE,1)-U(JELEM,NODE,1))
            UII(NODE,2)=0.5*(U(IELEM,NODE,2)+U(JELEM,NODE,2))
            UII(NODE,3)=0.5*(0)
            UIII(NODE,1)=0.5*(0)
            UIII(NODE,2)=0.5*(0)
            UIII(NODE,3)=0.5*(U(IELEM,NODE,3)-U(JELEM,NODE,3))
C
C     *********DELAMINATION: PENETRATION CHECK********
C     The node #'s 5,16,8 should always have a +ve value for COD and for
C     interpenetration not to occur.
C    The node #'s 6,14,7 should always have a 0 value, for they are at the crack tip
and
C     the COD is 0.
            if ((ielem.eq.1).and.(node.eq.20)) then
            WRITE(6,420) UI(5,2),UI(16,2),UI(8,2),UI(13,2),UI(15,2),
     &                   UI(6,2),UI(14,2),UI(7,2)
 420        FORMAT(1X,8(E14.7,3X))
            endif
C     **************************************************
            X(NODE,1)=XN(IELEM,NODE,1)
            X(NODE,2)=XN(IELEM,NODE,2)
            X(NODE,3)=XN(IELEM,NODE,3)
c---------
C     This is for finding out what the order of the gap introduced
C     between the elements is.
C
C           if ((ielem.le.2).and.(node.eq.20)) then
C            diff1=XN(IELEM,8,1)-XN(JELEM,8,1)
C            diff2=XN(IELEM,8,2)-XN(JELEM,8,2)
C            diff3=XN(IELEM,8,3)-XN(JELEM,8,3)
C            WRITE(6,*) 'ielem=',ielem
C            WRITE(6,420) diff1,diff2,diff3
C            endif
c---------
 20      CONTINUE
C
      DO 30 INT=1,INTG
              SIGI(1,1,INT)=0.5*(SIG(IELEM,1,1,INT)+
     &                           SIG(JELEM,1,1,INT))
              SIGI(2,2,INT)=0.5*(SIG(IELEM,2,2,INT)+
     &                           SIG(JELEM,2,2,INT))
              SIGI(3,3,INT)=0.5*(SIG(IELEM,3,3,INT)+
     &                           SIG(JELEM,3,3,INT))
              SIGI(2,3,INT)=0.5*(SIG(IELEM,2,3,INT)-
     &                           SIG(JELEM,2,3,INT))
              SIGI(1,3,INT)=0.5*(SIG(IELEM,1,3,INT)+
     &                           SIG(JELEM,1,3,INT))
              SIGI(1,2,INT)=0.5*(SIG(IELEM,1,2,INT)-
     &                           SIG(JELEM,1,2,INT))
              SIGII(1,1,INT)=0.5*(SIG(IELEM,1,1,INT)-
     &                           SIG(JELEM,1,1,INT))
              SIGII(2,2,INT)=0.5*(SIG(IELEM,2,2,INT)-
     &                           SIG(JELEM,2,2,INT))
              SIGII(3,3,INT)=0.5*(0)
```

```
            SIGII(2,3,INT)=0.5*(0)
            SIGII(1,3,INT)=0.5*(0)
            SIGII(1,2,INT)=0.5*(SIG(IELEM,1,2,INT)+
     &                        SIG(JELEM,1,2,INT))
            SIGIII(1,1,INT)=0.5*(0)
            SIGIII(2,2,INT)=0.5*(0)
            SIGIII(3,3,INT)=0.5*(SIG(IELEM,3,3,INT)-
     &                        SIG(JELEM,3,3,INT))
            SIGIII(2,3,INT)=0.5*(SIG(IELEM,2,3,INT)+
     &                        SIG(JELEM,2,3,INT))
            SIGIII(1,3,INT)=0.5*(SIG(IELEM,1,3,INT)-
     &                        SIG(JELEM,1,3,INT))
            SIGIII(1,2,INT)=0.5*(0)
C
            SIGI(3,2,INT)= SIGI(2,3,INT)
            SIGI(3,1,INT)= SIGI(1,3,INT)
            SIGI(2,1,INT)= SIGI(1,2,INT)
            SIGII(3,2,INT)= SIGII(2,3,INT)
            SIGII(3,1,INT)= SIGII(1,3,INT)
            SIGII(2,1,INT)= SIGII(1,2,INT)
            SIGIII(3,2,INT)= SIGIII(2,3,INT)
            SIGIII(3,1,INT)= SIGIII(1,3,INT)
            SIGIII(2,1,INT)= SIGIII(1,2,INT)
C
            STRI(1,1,INT)=0.5*(STR(IELEM,1,1,INT)+
     &                        STR(JELEM,1,1,INT))
            STRI(2,2,INT)=0.5*(STR(IELEM,2,2,INT)+
     &                        STR(JELEM,2,2,INT))
            STRI(3,3,INT)=0.5*(STR(IELEM,3,3,INT)+
     &                        STR(JELEM,3,3,INT))
            STRI(2,3,INT)=0.5*(STR(IELEM,2,3,INT)-
     &                        STR(JELEM,2,3,INT))
            STRI(1,3,INT)=0.5*(STR(IELEM,1,3,INT)+
     &                        STR(JELEM,1,3,INT))
            STRI(1,2,INT)=0.5*(STR(IELEM,1,2,INT)-
     &                        STR(JELEM,1,2,INT))
            STRII(1,1,INT)=0.5*(STR(IELEM,1,1,INT)-
     &                        STR(JELEM,1,1,INT))
            STRII(2,2,INT)=0.5*(STR(IELEM,2,2,INT)-
     &                        STR(JELEM,2,2,INT))
            STRII(3,3,INT)=0.5*(0)
            STRII(2,3,INT)=0.5*(0)
            STRII(1,3,INT)=0.5*(0)
            STRII(1,2,INT)=0.5*(STR(IELEM,1,2,INT)+
     &                        STR(JELEM,1,2,INT))
            STRIII(1,1,INT)=0.5*(0)
            STRIII(2,2,INT)=0.5*(0)
            STRIII(3,3,INT)=0.5*(STR(IELEM,3,3,INT)-
     &                        STR(JELEM,3,3,INT))
            STRIII(2,3,INT)=0.5*(STR(IELEM,2,3,INT)+
     &                        STR(JELEM,2,3,INT))
            STRIII(1,3,INT)=0.5*(STR(IELEM,1,3,INT)-
     &                        STR(JELEM,1,3,INT))
            STRIII(1,2,INT)=0.5*(0)
C
            STRI(3,2,INT)= STRI(2,3,INT)
            STRI(3,1,INT)= STRI(1,3,INT)
            STRI(2,1,INT)= STRI(1,2,INT)
            STRII(3,2,INT)= STRII(2,3,INT)
            STRII(3,1,INT)= STRII(1,3,INT)
            STRII(2,1,INT)= STRII(1,2,INT)
            STRIII(3,2,INT)= STRIII(2,3,INT)
            STRIII(3,1,INT)= STRIII(1,3,INT)
            STRIII(2,1,INT)= STRIII(1,2,INT)
```

```
C
               DO 40 I=1,3
               DO 40 J=1,3
               WI(INT)=SIGI(I,J,INT)*STRI(I,J,INT)*0.5+WI(INT)
               WII(INT)=SIGII(I,J,INT)*STRII(I,J,INT)*0.5+WII(INT)
               WIII(INT)=SIGIII(I,J,INT)*STRIII(I,J,INT)*0.5+WIII(INT)
  40           CONTINUE
C
 30     CONTINUE
C
C
      RETURN
      END
C
C     ---------------------------------------
      SUBROUTINE ROTVEC(THETA,T1,T2,T3,X1,X2,X3)
C     ---------------------------------------
C     This subroutine results in vector x* which are obtained by rotation
C     of vectors t* by an angle 'theta' about the 1-axis by an angle -(90+theta)
C
      IMPLICIT DOUBLE PRECISION (A-H,O-Z)
      REAL*8 NINTY
C
      PI=4*ATAN(1.)
      NINTY=PI/2.0
      angle=(theta+ninty)*(180/PI)
      C=COS(-1*(THETA+NINTY))
      S=SIN(-1*(THETA+NINTY))
      X3=T3*(C)+T2*(S)
      X2=T2*(C)-T3*(S)
      X1= T1
C
      RETURN
      END
C
C     ---------------------------------------------------
      SUBROUTINE  ROTTENS(THETA,T11,T22,T33,T23,T13,T12,
     &                    X11,X22,X33,X23,X13,X12)
C     ---------------------------------------------------
C
C     This subroutine results in the rotation of a tensor t** about the 1 axis
C     by an angle -(90+theta) to get a tensor x**
C
      IMPLICIT DOUBLE PRECISION (A-H,O-Z)
      REAL*8 NINTY
C
      PI=4*ATAN(1.)
      NINTY=PI/2.0
      C=COS(-1*(THETA+NINTY))
      S=SIN(-1*(THETA+NINTY))
      X33=T33*(C**2)+T22*(S**2)+T23*(2*C*S)
      X22=T33*(S**2)+T22*(C**2)+T23*(-2*C*S)
      X11=T11
      X12=T12*(C)+T13*(-S)
      X13=T12*(S)+T13*(C)
      X23=T33*(-C*S)+T22*(C*S)+T23*(C**2-S**2)
C
      RETURN
      END
C

C     This subroutine evaluates the second of the two integrals needed to
C     evaluate GI(or GII).
     ---------------------------------------
```

```
      SUBROUTINE EVGF2(NEL,X,U,SIG,STR,W,SIGO,GF2)
     ----------------------------------------
C     This subroutine evaluates the second of the two integrals needed to
C     evaluate GI(or GII).
C     Note*****THIS INTEGRAL IS NEEDED ONLY IF THERE ARE PLASTIC STRAINS, ELSE THIS
C              INTEGRAL SUMS TO ZERO OVER THE ENTIRE DOMAIN
C
      IMPLICIT DOUBLE PRECISION (A-H,O-Z)
      PARAMETER(NOD=20,IPTS=3,INTG=27,NELEM=2,KELEM=2*NELEM)
      REAL*8 X(NOD,3),U(NOD,2),SIG(2,2,INTG),STR(2,2,INTG),W(INTG)
      REAL*8 YNODE(NOD),SIGO(2,2),Y(INTG)
      REAL*8 PLACE(IPTS),WGT(IPTS),S(KELEM,NOD),STEMP(NOD)
      COMMON /GAUSS/PLACE,WGT
      COMMON /SFUNC/S,F
C
      T1=0.0
      T2=0.0
      INT=0
C
C     Evaluation of the co-ordinate Y at the integration points
C     and the function S in the center of an element.
C
C     Writing the Y-coordinates into another matrix for sending it to
C     NSHAPES and finding the Y-coordinate at the integration points.
      DO 5 I=1,NOD
         YNODE(I)=X(I,2)
         STEMP(I)=S(NEL,I)
 5    CONTINUE

      DO 10 INTI=1,IPTS
         DO 20 INTJ=1,IPTS
                     INT=INT+1
                     PXI=PLACE(INTI)
                     PET=PLACE(INTJ)
                     CALL NSHAPES(PXI,PET,YNODE,Y(INT))
 20      CONTINUE
 10      CONTINUE
                     CALL NSHAPES(0.,0.,STEMP,SO)
C
               DO 30 I=1,2
                  DO 40 J=1,2
                     T2=T2+SIGO(I,J)*
     &                    ( (STR(I,J,2)-STR(I,J,3)) * (Y(3)-Y(1))+
     &                      (STR(I,J,1)-STR(I,J,4)) * (Y(4)-Y(2)) )
 40                  CONTINUE
 30                  CONTINUE
C
                     T1=(  (W(2)-W(3))*(Y(3)-Y(1))
     &                               +(W(1)-W(4))*(Y(4)-Y(2)))
C
                     GF2=-(SQRT(3.)/2.)*(T1-T2)*SO
      RETURN
      END
C
C     -----------------------------------
      SUBROUTINE POLAR(IELEM,RAD,THE,Y,X)
C     ------------------------------------
C     This subroutine converts cartesian coordinat parameters to polar
C     coordinate parameters
C
      IMPLICIT DOUBLE PRECISION (A-H,O-Z)
      PI=4.*ATAN(1.)
      IF(X.EQ.0) THEN
         IF(Y.EQ.0) THEN
```

```
            THE=0.0
         ELSE
            IF(Y.GT.0) THEN
               THE=PI/2.
            ELSE
               THE=-PI/2.
            ENDIF
         ENDIF
      ELSE
         GOTO (10,20,30,40)IELEM
 10      THE=ATAN(Y/X)
         GOTO 50
 20      THE=PI+ATAN(Y/X)
         GOTO 50
 30      THE=ATAN(Y/X)
         GOTO 50
 40      THE=-PI+ATAN(Y/X)
      ENDIF

 50   RAD=SQRT(Y**2+X**2)
      RETURN
      END
C
```

APPENDIX B

APPLICATION OF DECOMPOSITION METHOD TO INTERFACE CRACKS

The decomposition method is an approach which has been used to separate the energy release rate into individual component modes in isotropic materials. However, its application to separate modes for cracks at bimaterial interfaces has not been addressed in the literature. It has been discussed earlier in Chapter two that cracks at bimaterial interfaces could have oscillatory singularities, in which case there is no unique definition of modes. However, there are combinations of bimaterials without oscillatory singularities, if the constitutive properties of the materials satisfy certain conditions as described in Chapter four. For such bimaterial combinations, there exist unique definitions for modes. However, the ability of the decomposition method to separate the total energy release rate into these modes is not clear. This problem has not been addressed in available literature, but generalizations which imply the inability of the decomposition method to separate modes in bimaterials may be seen in the literature [48]. Contrary to these implications in the literature, a brief proof is provided in this appendix to show that the decomposition approach is capable of obtaining the individual modes of energy release rate in the case of a crack between two isotropic materials (i.e. a bimaterial) without oscillatory singularities.

In the case of an interface crack between bimaterials without oscillatory singularities, it has been shown that the near-tip fields (stresses, strains and displacements) in the two materials do not interact with each other in the sense that, apart from the stress intensity factors, the field within each material is independent of the modulus of the other material. Thus, the structure of the field in each solid is identical to those for a crack in the corresponding homogeneous material [40, 77]. If such a crack were subject to a mixed mode loading, then the near-tip stresses can be written as [76],

$$\sigma_{11} = \frac{K_I}{\sqrt{2\pi r}}\left(\cos\frac{\theta}{2}\right)\left(1 - \sin\frac{\theta}{2}\sin\frac{3\theta}{2}\right) - \frac{K_{II}}{\sqrt{2\pi r}}\left(\sin\frac{\theta}{2}\right)\left(2 + \cos\frac{\theta}{2}\cos\frac{3\theta}{2}\right) \qquad (B.1)$$

$$\sigma_{22} = \frac{K_I}{\sqrt{2\pi r}}\left(\cos\frac{\theta}{2}\right)\left(1 + \sin\frac{\theta}{2}\sin\frac{3\theta}{2}\right) + \frac{K_{II}}{\sqrt{2\pi r}}\left(\sin\frac{\theta}{2}\right)\left(\cos\frac{\theta}{2}\cos\frac{3\theta}{2}\right) \qquad (B.2)$$

$$\sigma_{12} = \frac{K_I}{\sqrt{2\pi r}}\left(\sin\frac{\theta}{2}\right)\left(\cos\frac{\theta}{2}\right)\left(\cos\frac{3\theta}{2}\right) + \frac{K_{II}}{\sqrt{2\pi r}}\left(\cos\frac{\theta}{2}\right)\left(1 - \sin\frac{\theta}{2}\sin\frac{3\theta}{2}\right) \qquad (B.3)$$

The strains can be found by using the constitutive relations :

$$\varepsilon_{11} = \left(\frac{1}{E}\right)(\sigma_{11} - \nu\sigma_{22}) \qquad (B.4)$$

$$\varepsilon_{22} = \left(\frac{1}{E}\right)(\sigma_{22} - \nu\sigma_{11}) \qquad (B.5)$$

$$\varepsilon_{12} = \frac{\sigma_{12}}{G} \qquad (B.6)$$

and the near-tip displacements are [76]:

$$u_1 = \frac{K_I}{G}\sqrt{\frac{r}{2\pi}}\cos\left(\frac{\theta}{2}\right)\left[1 - 2\nu + \sin^2\frac{\theta}{2}\right] + \frac{K_{II}}{G}\sqrt{\frac{r}{2\pi}}\sin\left(\frac{\theta}{2}\right)\left[2 - 2\nu + \cos^2\frac{\theta}{2}\right] \qquad (B.7)$$

$$u_2 = \frac{K_I}{G}\sqrt{\frac{r}{2\pi}}\sin\left(\frac{\theta}{2}\right)\left[2 - 2\nu - \cos^2\frac{\theta}{2}\right] + \frac{K_{II}}{G}\sqrt{\frac{r}{2\pi}}\cos\left(\frac{\theta}{2}\right)\left[-1 + 2\nu + \sin^2\frac{\theta}{2}\right] \qquad (B.8)$$

where

$$\begin{aligned} E, \nu &= E_1, \nu_1 \quad for \ \ 0 < \theta \le \pi \\ &= E_2, \nu_2 \quad for \ \ -\pi \le \theta < 0 \end{aligned} \qquad (B.9)$$

The subscripts 1 and 2 on E and v refer to the two materials.

If these stresses, strains and displacements are used in the J-integral, then the total G is obtained:

$$J = G = \int_{\Gamma_\varepsilon} \left[W n_1 - \sigma_{ij} \frac{\partial u_i}{\partial x_1} n_j \right] d\Gamma \tag{B.10}$$

where,
$$W = \int^{\varepsilon_{ij}} \sigma_{ij}\, d\varepsilon_{ij} = \frac{1}{2}\left(\sigma_{11}\varepsilon_{11} + \sigma_{22}\varepsilon_{22} + 2\sigma_{12}\varepsilon_{12}\right) \tag{B.11}$$

The stresses, strains and displacements can be divided into components σ^I, ε^I and u^I, which are the symmetric components and contribute to mode I only and σ^{II}, ε^{II} and u^{II} which are the asymmetric components which contribute to mode II only, as follows:

$$\begin{aligned} \{\sigma\} &= \left\{\sigma^I\right\} + \left\{\sigma^{II}\right\} \\ &= \frac{1}{2}\begin{Bmatrix} \sigma_{11}(\theta) + \sigma_{11}(-\theta) \\ \sigma_{22}(\theta) + \sigma_{22}(-\theta) \\ \sigma_{12}(\theta) - \sigma_{12}(-\theta) \end{Bmatrix} + \frac{1}{2}\begin{Bmatrix} \sigma_{11}(\theta) - \sigma_{11}(-\theta) \\ \sigma_{22}(\theta) - \sigma_{22}(-\theta) \\ \sigma_{12}(\theta) + \sigma_{12}(-\theta) \end{Bmatrix} \end{aligned} \tag{B.12}$$

$$\begin{aligned} \{\varepsilon\} &= \left\{\varepsilon^I\right\} + \left\{\varepsilon^{II}\right\} \\ &= \frac{1}{2}\begin{Bmatrix} \varepsilon_{11}(\theta) + \varepsilon_{11}(-\theta) \\ \varepsilon_{22}(\theta) + \varepsilon_{22}(-\theta) \\ \varepsilon_{12}(\theta) - \varepsilon_{12}(-\theta) \end{Bmatrix} + \frac{1}{2}\begin{Bmatrix} \varepsilon_{11}(\theta) - \varepsilon_{11}(-\theta) \\ \varepsilon_{22}(\theta) - \varepsilon_{22}(-\theta) \\ \varepsilon_{12}(\theta) + \varepsilon_{12}(-\theta) \end{Bmatrix} \end{aligned} \tag{B.13}$$

$$\begin{aligned} \{u\} &= \left\{u^I\right\} + \left\{u^{II}\right\} \\ &= \frac{1}{2}\begin{Bmatrix} u_1(\theta) + u_2(-\theta) \\ u_1(\theta) - u_2(-\theta) \end{Bmatrix} + \frac{1}{2}\begin{Bmatrix} u_1(\theta) - u_2(-\theta) \\ u_1(\theta) + u_2(-\theta) \end{Bmatrix} \end{aligned} \tag{B.14}$$

If the individual components are used in the J-integral then,

$$G_I = \int_{\Gamma_\varepsilon} \left[W^I n_1 - \sigma_{ij}^I \frac{\partial u_i^I}{\partial x_1} n_j \right] d\Gamma \tag{B.15}$$

$$G_{II} = \int_{\Gamma_\varepsilon} \left[W^{II} n_1 - \sigma_{ij}^{II} \frac{\partial u_i^{II}}{\partial x_1} n_j \right] d\Gamma \tag{B.16}$$

where

$$W^I = \int_0^{\varepsilon_{ij}^I} \sigma_{ij}^I \, d\varepsilon_{ij}^I \tag{B.17}$$

and

$$W^{II} = \int_0^{\varepsilon_{ij}^{II}} \sigma_{ij}^{II} \, d\varepsilon_{ij}^{II} \tag{B.18}$$

The integrals in equations (B.15 and B.16) are evaluated around a unit circle, i.e. Γ_ε is the circumference of a circle of unit radius, as shown in Figure B.1. This integration results in the individual energy release rate modes:

$$G_I = \frac{1}{4}\left(\frac{1}{E_1} + \frac{1}{E_2}\right) K_I^2 \tag{B.19}$$

and

$$G_{II} = \frac{1}{4}\left(\frac{1}{E_1} + \frac{1}{E_2}\right) K_{II}^2 \tag{B.20}$$

It is seen in equation (B.19) that the mode I energy release rate is dependent only on the mode I stress intensity factor. Similarly, from equation (B.20), the mode II energy release rate is dependent only on the mode II stress intensity factor. From these results, it may be inferred that the decomposition method has successfully separated the energy release rate into two components, one dependent on mode I only and the other on mode II only. Furthermore, these results are identical to those obtained by separating the modes by the virtual crack closure method in reference [84] for the individual modes of the energy release rate for interface cracks. Hence, the decomposition method is capable of separating the individual modes of energy release rate for bimaterial interface cracks where the oscillatory singularity is nonexistent.

The method has been presented here for a two-dimensional case only for convenience of presentation. The proof may, however, be easily extended to the three-dimensional case.

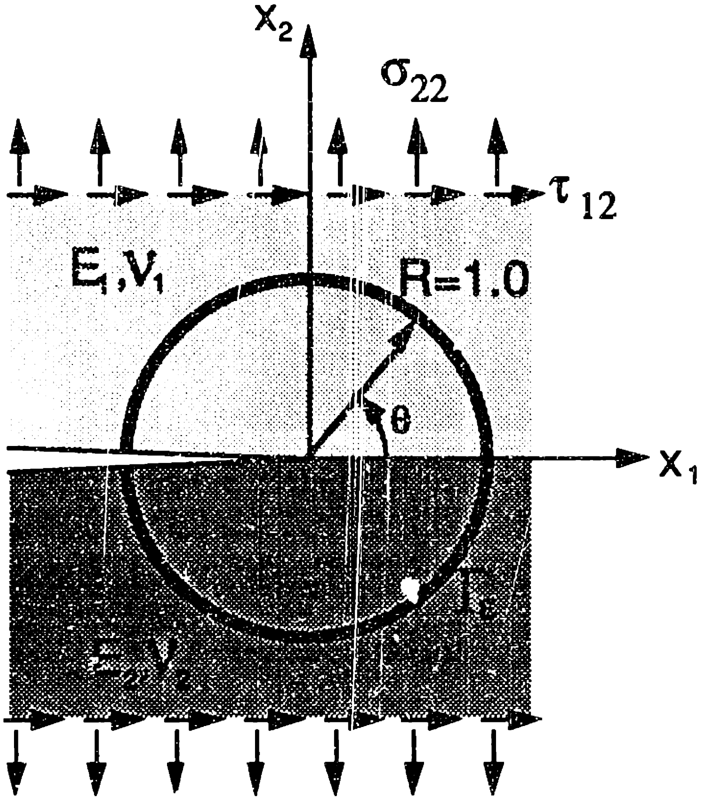

Figure B.1 Crack located at a bimaterial interface subjected to mixed mode loading.

REFERENCES

1. Brewer, J. C. and Lagace, P. A., "Failure of Graphite/Epoxy Induced by Delamination", *22nd International SAMPE Technical Conference*, Boston, 1990.

2. Carlsson, L. A. and Pipes, R. B., *Experimental Characterization of Advanced Composite Materials*, Prentice-Hall, New Jersey, 1987.

3. Crossman, F. W., Warren, W. J., Wang, A. S. D., and Law, G. E., Jr., "Initiation and Growth of Transverse Cracks and Edge Delamination in Composite Laminates, Part2, Experimental Correlation", *Journal of Composite Materials Supplement*, Vol. 14, 1980, pp. 88-107.

4. Crossman, F. W. and Wang, A. S. D., "The dependence of Transverse Cracking and Delamination on Ply Thickness in Graphite/Epoxy Laminates", in *Damage in Composite Materials, ASTM STP 775*, ed. Reifsnider, K. L., American Society for Testing and Materials, 1982, pp. 118-139.

5. O'Brien, T. K. and Hooper, S. J., "Local Delamination in Laminates with Angle Ply Matrix Cracks: Part I, Tension Tests and Stress Analysis", 104076, NASA, 1991.

6. Brewer, J. C., "Failure of Graphite/Epoxy Induced by Delamination", Massachusetts Institute of Technology, Ph.D. Thesis, 1988.

7. Wang, S. S., "Delamination Crack Growth in Unidirectional Fiber-Reinforced Composites under Static and Cyclic Loading", in *Compoiste Materials: Testing and Design(Fifth Conference),ASTM STP 674*, American Society for Testing and Materials, 1979, pp. 642-663.

8. Pipes, B. R. and Pagano, N. J., "Interlaminar Stresses in Composite Materials Under Uniform Axial Extension", *Journal of Composite Materials*, Vol. 4, October, 1970, pp. 538-548.

9. Lagace, P. A., "Delamination in Composites: Is Toughness the Key", *SAMPE Journal*, Vol. 22, 1986, pp. 53-60.

10. McManus, H. L., "Failure Modes in a Family of Graphite-Epoxy Laminates", Massachusetts Institute of Technology, S.M. Thesis, 1981.

11. Jackson, A. C., "Testing of the L-1011 Advanced Composite Vertical Fin", *Sixth Conference on Figrous Composites in Structural Design, AMMRC-MS-83-2*, 1983, pp. 53-70.

12. Wilkins, D. J., Eisenmann, J. R., Camin, R. A., and Margolis, W. S., "Characterizing Delamination Growth in Graphite/Epoxy", in *Damage in Composite Materials, ASTM STP 775*, ed. Reifsnider, K. L., American Society for Testing and Materials, 1982, pp. 168-183.

13. Wang, A. S. D. and Crossman, F. W., "Some New Results on Edge Effect in Symmetric Composite Laminates", *Journal of Composite Materials*, Vol. 11, January, 1977, pp. 92-106.

14. Rybicki, E. F., "Approximate Three-Dimensional Solutions for Symmetric Laminates under In-Plane Loading", *Journal of Composite Materials*, Vol. 5, July, 1971, pp. 354-360.

15. Garg, A. C., "Delamination -A Damage Mode in Composite Structures", *Engineering Fracture Mechanics*, Vol. 29, No. 5, 1988, pp. 557-584.

16. Hsu, P. W. and Herakovich, C. T., "Edge Effects in Angle-Ply Composite Laminates", *Journal of Composite Materials*, Vol. 11, October, 1977, pp. 422-428.

17. Kassapoglou, C. and Lagace, P. A., "An Efficient Method for the Calculation of Interlaminar Stresses in Composite Materials", *Journal of Applied Mechanics*, Vol. 53, December, 1986, pp. 744-750.

18. Wang, S. S. and I., C., "Boundary-Layer Effects in Composite Laminates Part-1. Free Edge Stress Singularities", *Journal of Applied Mechanics*, Vol. 49, September, 1982, pp. 541-548.

19. Wang, S. S. and Choi, I., "Boundary-Layer Effects in Composite Laminates Part-2. Free Edge Stress Solutions and Basic Characteristics", *Journal of Applied Mechanics*, Vol. 49, September, 1982, pp. 549-560.

20. Brewer, J. C. and Lagace, P. A., "Quadratic Stress Criterion for Initiation of Delamination", *Journal of Composite Materials*, Vol. 22, December, 1988, pp. 1141-1135.

21. Kim, R. Y. and Soni, S. R., "Experimental and Analytical Studies of the Onset of Delamination in Laminated Composites", *Journal of Composite Materials*, Vol. 18, January, 1984, pp. 70-80.

22. Vizzini, A. and Lagace, P. A., "An Elastic Foundation Model to Predict the Growth of Delaminations", *Journal of Composite Technology and Research*, Vol. 11, No. 3, 1989, pp. 81-86.

23. Sih, G. C. and Chen, E. P., ed. *Cracks in Composite Materials*, 6 vols. Vol. 6, Martinus Nijhoff Publishers, 1981.

24. Irwin, G. R., "Fracture", *Handbuch der Physik*, Vol. 6, 1958, pp. 551-590.

25. Griffith, A. A., "The Phenomenon of Rupture and Flow in Solids", *Philosophical Transactions of the Royal Society*, Vol. A-221, 1920, pp. 163-197.

26. Wang, A. S. D. and Crossman, F. W., "Initiation and Growth of Transverse Cracks and Edge Delamination in Composite Laminates, Part1, An Energy Method", *Journal of Composite Materials Supplement*, Vol. 14, 1980, pp. 71-87.

27. Wang, A. S. D., "Growth Mechanism of Transverse Cracks and Ply Delamination in Composite Laminates", *ICCM-III*, Paris, 1980, pp. 170-183.

28. Rybicki, E. F., Schmueser, D. W., and Fox, J., "An Energy Release Rate Approach for Stable Crack Growth in Free-Edge Delamination Problem", *Journal of Composite Materials*, Vol. 11, October, 1977, pp. 470-487.

29. O'Brien, T. K., "Local Delamination in Laminates with Angle Ply Matrix Cracks: Part II, Delamination Fracture Analysis and Fatigue Characterization", TM 104076, NASA, 1991.

30. Ashizawa, M., "Fast Interlaminar Fracture of a Compressively Loaded Composite Containing a Defect", *Fifth DOD/NASA Conference on Fibrous Composites in Structural Design*, New Orleans, LA, 1981,

31. Whitcomb, J. D., "Finite Element Analysis of Instability Related Delamination Growth", *Journal of Composite Materials*, Vol. 14, September, 1981, pp. 403-426.

32. Gillespie, J. W., Jr. and Pipes, R. B., "Compressive Strength of Composite Laminates with Interlaminar Defects", *Composite Structures*, Vol. 2, No. 1, 1984, pp. 49-69.

33. Flanagan, G., "Two-Dimensional Delamination Growth in Composite Laminates Under Compression Loading", in *Composite Materials: Testing and Design (Eighth Conference), ASTM STP 972*, ed. Whitcomb, J. D., American Society for Testing and Materials, Philadelphia, 1988, pp. 180-190.

34. Wang, A. S. D., Crossman, F. W., and Law, G. E., Jr., "Interlaminar Failure in Epoxy Based Composite Laminates", *29th Meeting of the Mechanical Failures Prevention Group*, 1979.

35. O'Brien, T. K., “Characterization of Delamination Onset and Growth in a Composite Laminate”, in *Damage in Composite Materials, ASTM STP 775*, ed. Reifsnider, K. L., American Society for Testing and Materials, 1982, pp. 282-297.

36. O'Brien, T. K., "Mixed-Mode Strain-Energy-Release Rate Effects on Edge Delamination in Composites", TM 84592, NASA, 1983.

37. Salpekar, S. A. and O'Brien, T. K., "Combined Effect of Matrix Cracking and Stress-Free Edge on Delamination", TM 102591, NASA, 1990.

38. Williams, W. L., "The Stresses Around a Fault or Crack in Dissimilar Media", *Bulletin of the Seismological Society of America*, Vol. 49, 1959, pp. 199-204.

39. Rice, J. R., "Elastic Fracture Mechanics Concepts for Interfacial Cracks", *Journal of Applied Mechanics*, Vol. 55, March, 1988, pp. 98-103.

40. Suo, Z., "Singularities, Interfaces and Cracks in Dissimilar Anisotropic Media", *Proceedings of the Royal Society of London*, Vol. A, No. 427, 1990, pp. 331-358.

41. Wang, S. S. and Choi, I., "The Interface Crack Between Dissimilar Anisotropic Composite Materials", *Journal of Applied Mechanics*, Vol. 50, No. 3, March, 1983, pp. 169-178.

42. Wang, S. S. and Choi, I., "The Interface Crack Behavior in Dissimilar Anisotropic Composites Under Mixed-Mode Loading", *Journal of Applied Mechanics*, Vol. 50, No. 3, March, 1983, pp. 179-183.

43. Wang, S. S., "Fracture Mechanics for Delamination Problems in Composite Materials", *Journal of Composite Materials*, Vol. 17, May, 1983, pp. 210-223.

44. Clements, D. L., "A Crack Between Dissimilar Anisotropic Media", *International Journal of Engineering and Science*, Vol. 9, No. 2, 1971, pp. 257-265.

45. Banks-Sills, L., "Application of the Finite Element Method to Linear Elastic Fracture Mechanics", *Applied Mechanics Review*, Vol. 44, No. 10, 1991, pp. 447-461.

46. Li, F. Z., Shih, C. F., and Needleman, A., "A Comparison of Methods for Calculating Energy Release Rates", *Engineering Fracture Mechanics*, Vol. 21, No. 2, 1985, pp. 405-421.

47. Nikishkov, G. P. and Atluri, S. N., "Calculation of Fracture Mechanics Parameters for an Arbitrary Three-Dimensional Crack, by the 'Equivalent Domain Integral' Method", *International Journal for Numerical Methods in Engineering*, Vol. 24, No. 9, 1987, pp. 1801-1821.

48. Chen, K. L. and Atluri, S. N., "Comparison of Different Methods of Evaluation of Weight Functions for 2-D Mixed Mode Fracture Analyses", *Engineering Fracture Mechanics*, Vol. 34, No. 4, 1989, pp. 935-956.

49. Raju, I. S. and Shivakumar, K. N., "An Equivalent Domain Integral Method in the Two-Dimensional Analysis of Mixed Mode Crack Problems", *Engineering Fracture Mechanics*, Vol. 37, No. 4, 1990, pp. 707-725.

50. Shivakumar, K. N. and Raju, I. S., "An Equivalent Domain Integral Method for Three Dimensional Mixed Mode Fracture Problems", *Engineering Fracture Mechanics*, Vol. 42, No. 6, 1992, pp. 935-959.

51. Raju, I. S., Crews, J. H., Jr., and Aminpour, M. A., "Convergence of Strain Energy Release Rate Components for Edge-Delaminated Composite Laminates", 89135, NASA, April, 1987.

52. Sun, C. T. and Manoharan, M. G., "Strain Energy Release Rates of an Interfacial Crack Between Two Orthotropic Solids", *Journal of Composite Materials*, Vol. 23, May, 1989, pp. 460-478.

53. Wang, A. S. D., Kishore, N. N., and Feng, W. W., "On Mixed Mode Fracture in Off-Axis Unidirectional Graphite/Epoxy Composites", *ICCM -IV*, Tokyo, 1982, pp. 599-606.

54. Donaldson, S. L., "Fracture Toughness Testing of Graphite/Epoxy and Graphite/Peek Composites", *Composites*, Vol. 16, No. 2, April, 1985, pp. 103-112.

55. Williams, J. G., "Fracture Tests for Mixed Mode Failure of Composite Laminates", *International Journal of Fracture* , Vol. 36, pp. 101-119.

56. Suo, Z., "Delamination Specimens for Orthotropic Materials", *Journal of Applied Mechanics*, Vol. 57, September, 1990, pp. 627-634.

57. Carlsson, L. A., Gillespie, J. W., Jr., and Pipes, R. B., "On the Design and Analysis of the End Notched Flexure (ENF) Specimen for Mode II Testing", *Journal of Composite Materials*, Vol. 20, November, 1986, pp. 594-604.

58. Arcan, M., Hashin, Z., and Voloshin, A., "A Method to Produce Uniform Plane Stress States with Applications to Fiber-Reinforced Materials", *Experimental Mechanics*, Vol. 18, April, 1978, pp. 141-146.

59. Charalambides, P. G., Lund, J., Evans, A. G., and McMeeking, R. M., "A Test Specimen for Determining the Fracture Resistance of Bimaterial Interfaces", *Journal of Applied Mechanics*, Vol. 56, March, 1989, pp. 77-82.

60. Wang, T. C. and Suo, Z., "Experimental Determination of Interfacial Toughness Using Brazil-Nut-Sandwich", *Acta Metallurgica*, Vol. 38, 1990, pp. 1279-1290.

61. Donaldson, S. L., "Mode III Interlaminar Fracture Characterization of Composite Materials", University of Dayton, Ohio, M.S.Thesis Thesis, 1987.

62. Robinson, P. and Song, D. Q., "A Modified DCB Specimen for Mode I Testing of Multidirectional Laminates", *Journal of Composite Materials*, Vol. 26, No. 11, 1992, pp. 1554-1577.

63. Barsoum, R. S., "Finite Element Application in the Fracture Analysis of Composite Materials - Delamination", in *Key Engineering Materials*, ed. Armanios, E. A., Vol. 37, Trans Tech Publications, Switzerland, 1989, pp. 35-58.

64. Olsson, R., "Factors Influencing the Interlaminar Fracture Toughness and its Evaluation in Composites", FFA TN 1991-34, FFA, The Aeronautical Research Institute of Sweden, 1991.

65. Davies, P. and Benzeggagh, M. L., "Interlaminar Mode I Fracture Testing", in *Application of Fracture Mechanics to Composite Materials*, ed. Friedrich, K., 6 vols. Composite Materials Series. Vol. 6, Elsevier, New York, 1989, pp. 82-107.

66. Carlsson, L. A. and Gillespie, J. W., Jr., "Mode-II Interlaminar Fracture of Composites", in *Application of Fracture Mechanics to Composite Materials*, ed. Friedrich, K., 6 vols. Composite Materials Series. Vol. 6, Elsevier, New York, 1989, pp. 114-154.

67. Wisnom, M. R., "On the Increase in Fracture Energy with Thickness in Delamination of Unidirectional Glass Fibre-Epoxy with Cut Central Plies", *Journal of Reinforced Plastics and Composites*, Vol. 11, August, 1992, pp. 897-909.

68. Liechti, K. M. and Chai, Y.-S., "Asymmetric Shielding in Interfacial Fracture Under Inplane Shear", EMRL 89/4, University of Texas at Austin, Austin, Texas, 1989.

69. Liechti, K. M. and Chai, Y.-S., "Biaxial Loading Experiments for Determining Interfacial Toughness", *Journal of Applied Mechanics*, Vol. 58, September, 1991, pp. 680-687.

70. Lagace, P. A., "Delamination Fracture Under Tensile Loading", *Sixth Conference on Fibrous Composites in Structural Design*, New Orleans, 1983, pp. IX53-70.

71. Lagace, P. A. and Bhat, N. V., "On the Prediction of Delamination Initiation", *International Conference on Advanced Composites, Advanced Composites '93*, University of Wollongong, Sydney, Australia, 1993.

72. Bathe, K. J., *ADINA-Automatic Dynamic Incremental Nonlinear Analysis System*, Adina Engineering Inc., USA, 1990.

73. Salpekar, S. A. and O'Brien, T. K., "Analysis of Matrix Cracking and Local Delamination in $(0/\theta/-\theta)_s$ Graphite/Epoxy Laminates Under Tension Load", *ICCM VIII*, Honolulu, 1991.

74. O'Brien, T. K., “Analysis of Local Delaminations and Their Influence on Composite Laminate Behavior”, in *Delamination and Debonding of Material, ASTM STP 876*, ed. Johnson, W. S., American Society for Testing and Materials, 1985.

75. deLorenzi, H. G., "On The Energy Release Rate and the J-Integral for 3-D Crack Configurations", *International Journal of Fracture*, Vol. 19, 1982, pp. 183-193.

76. Ishikawa, H., Kitagawa, H., and Okamura, H., "J Integral of a Mixed Mode Crack and its Application", *3rd International Conference on Mechanical Behavior of Materials,ICM 3*, Cambridge,England, 1979, pp. 447-455.

77. Bassani, J. L. and Qu, J., "Finite Crack on Bimaterial and Bicrystal Interfaces", *Journal of Mechanics and Physics of Solids*, Vol. 37, No. 4, 1989, pp. 435-453.

78. Weems, D. B., "The Effect of Thick Interlaminar Shear Layers on the Behavior of Graphite/Epoxy Laminates", TELAC Report 87-4, Massachusetts Institute of Technology, February, 1987.

79. Lagace, P. A., Brewer, J. C., Varnerin, C., and Beaumont, M., "TELAC Manufacturing Course Notes", TELAC Report 88-4B, Massachusetts Institute of Technology, 1990.

80. Vizzini, A. J., "An Effecient Algorithm to Characterize Stress/Strain Data Using Piecewise Linear Curves", *Journal of Testing and Evaluation*, Vol. 20, No. 2, March, 1992, pp. 126-131.

81. Becht, G. and Gillespie, J. W., "Numerical and Experimental Evaluation of the Mode III interlaminar fracture toughness of Composite Materials", *Polymer Composites*, Vol. 10, No. 5, 1989, pp. 293-304.

82. Rubbrecht, P. and Verpoest, I., "The Size of The Plastic Zone in Front of an Advancing Delamination at an Interface with Dissimilar Fibre Orientation", *International Conference on Composite Materials, IX*, Madrid, Spain, 1993, pp. 708-715.

83. Johnson, W. S. and Mangalgiri, P. D., "Influence of the Resin on Interlaminar Mixed Mode Fracture", in *Toughened Composites, ASTM STP 937*, ed. Johnston, N. J, American Society for Testing and Materials, Philadelphia, 1987, pp. 295-319.

84. Hutchinson, J. W. and Suo, Z., "Mixed Mode Cracking in Layered Materials", in *Advances in Applied Mechanics*, ed. Hutchinson, J. W. and Wu, T. Y., Vol. 29, Academic Press, 1991.